

Synthesis, Characterization and Reactivity of pincerMOFs

Dissertation

Presented in Partial Fulfillment of the Requirements for the Degree Doctor of Philosophy

in the Graduate School of The Ohio State University

By

Abebu Amare Kassie

Graduate Program in Chemistry

The Ohio State University

2020

Dissertation Committee

Casey R. Wade, Advisor

Yiying Wu

Christo S. Sevov

Copyrighted by
Abebu Amare Kassie
2020

Abstract

Metal-organic frameworks (MOFs) are porous, crystalline materials assembled from organic linkers and metal ions/clusters via solvothermal, mechanochemical, sonochemical, microwave-assisted or electrochemical methods. The structure and function of MOFs can be tuned for a desired application by changing the organic bridging ligands and/or inorganic constituents. As a result, MOFs have emerged as an important class of materials for applications in gas storage and separation, drug delivery, sensing and heterogeneous catalysis. Their well-defined structures, large internal surface area, permanent porosity and stability have attracted a great deal of interest for catalyst design with beneficial features of both homogeneous and heterogeneous catalysts.

This thesis describes the immobilization of catalytically active diphosphine pincer complexes in MOFs as metallolinkers and the effect of site isolation on their stability and reactivity. Diphosphine pincer complexes are ubiquitous in homogeneous catalysis and are known to catalyze a wide range of organic transformations. However, these pincer-based catalysts can suffer from various deactivation processes such as dimerization, ligand decomposition, or reaction with solvent conditions in the homogeneous solution. Hence, immobilization of diphosphine pincer complexes in a rigid porous solid framework can help to stabilize key reactive intermediates in catalytic steps. Moreover, heterogenization

of catalyst species in MOFs can improve selectivity and activity over homogeneous catalysts with the added advantages of easy catalyst separation and recyclability.

Zr MOFs assembled from diphosphine pincer complexes have shown remarkably improved stability and catalytic activity compared to homogeneous counterparts. A Zr MOF with linkers based on Pd aryl diphosphinite (POCOP-Pd) pincer complexes proved to be an effective and recyclable catalyst for transfer hydrogenation of unsaturated organic substrates, terminal alkyne hydration and intramolecular hydroarylation of alkynes. On the other hand, the homogeneous analogue suffered from deactivation processes under the catalytic conditions used for transfer hydrogenation and alkyne hydration reactions. Moreover, solubility limitations encountered in the homogeneous catalysis during intramolecular hydroarylation reactions are obviated with the heterogeneous catalyst.

A Zr MOF has been constructed from Co^{III} *bis*(diarylphosphino)-diaminopyridine (PNNNP- Co^{III}) pincer complexes and shown to undergo postsynthetic metal exchange (PSME), allowing access to MOFs that are difficult or impossible to assemble via the conventional solvothermal conditions. PSME was used to generate Zr MOFs containing PNNNP-M (M = Rh, Pt) metallolinkers by exchanging Co for Rh and Pt at the PNNNP-Co linker sites. The mechanism of PSME was investigated by EPR and ^{31}P NMR spectroscopy and is proposed to involve initial reduction of Co^{III} to Co^{II} .

An isostructural series of Zr MOFs have been synthesized from PNNNP-Ru metallolinkers and are observed to exhibit different reactivity depending on the ancillary ligands coordinated to the Ru sites. Deprotonation/dearomatization of the PNNNP linker followed by carbonyl ligand abstraction from the Ru centers generates a MOF that

catalyzes hydrosilylation of aldehydes with triethylsilane. An analogous homogeneous pincer complex shows inferior catalytic activity under the optimized conditions, highlighting the benefits of immobilizing reactive catalytic intermediates in a rigid framework to improve catalytic efficiency.

Dedication

“Family is not an important thing.

It’s everything.” Michael J. Fox

To my family

Acknowledgments

First and foremost, I would like to thank my advisor Prof. Casey Wade for his guidance, mentorship and support throughout this long journey. His immense chemical knowledge and enthusiasm for science has been the major source of energy that kept me going even at times research seemed frustrating. His meticulous approach to details and aspiration for excellence has helped me become a better version of myself and grow as an independent thinker. I also thank him for allowing me to work on a really challenging and rewarding project. I envision team pincerMOF growing big and making significant contributions to the scientific community.

My special gratitude goes to my undergrad advisor Prof. Dasan Thamattoor who inspired me to pursue a career in chemistry. I thank you a million times for believing in me and making me feel smart even at times I doubt myself.

I would also like to thank Prof. Christine Thomas for being a great source of help. I am appreciative of your precious time spent on writing reference letters. Also, holiday and summer season parties have been great, and I just wish there would be more of them before I head to my next stop.

A huge thank you goes to the Wade lab former and current members. The long journey to a PhD would have been painful without the culture of great support and care we have in the Wade lab. First, I want to thank Alex, who I shared both office and hood when I started

the experience of a PhD student. The stories we shared, the science talks we had, and your sense of humor still resonate with me. I am so grateful for our friendship and thank you for being a humble and truly caring friend. Thank you for words of courage during the time of necessity.

To Ben, thank you for being a great source of knowledge and I enjoyed very much all the interesting scientific discussions we have had. To Katie: thank you for being the best colleague one could ever ask for. Your willingness to help and listen has made the frustrating times in lab more bearable. Also, thank you for all the science talks, suggestions when needed, and more importantly for being a very caring and pleasant person to work with. To Amy: I am so grateful you chose to join our lab. It has been a pleasure working with you and thank you for making my last year of grad school enjoyable. To Mamdud: Your kindness and willingness to help is so amazing and I thank you for that.

To Qiao, Jordan, Josh and Sean: You guys are very kind and smart, and I enjoyed working with you all. To Josh: I thought teaching lab while writing my thesis would be difficult and less enjoyable. However, working with you has made my last year of teaching as a graduate student a pleasure. Thank you for understanding and taking care of most of the grading responsibilities. To Jordan: your excitement for science is incredible. You bring positive/happy spirit to our lab and I am glad that I got to know you. To Sean: You are the sweetest and smartest undergrad that our lab has been blessed with. And thank you so much for all the donuts.

I would also like to thank all the Thomas lab members for being so supportive and helpful.

Finally, I would like to thank my family and friends who have been a great support system. To Tata: Thank you for your unconditional love, prayer and raising me with characters that I still embrace and maintain. To my sisters, Welala, Etalem and Lackech, thank you for your love and support. I am also blessed with brothers who played a crucial role for me to be where I am now. Tadie (source of inspiration and father figure), Metalem and Eristu are my heroes. To Tsige, Atakilt, Yaye, Wube and Menberu: thank you for all the love and support during my transition to abroad. And thank you for making my stay in Addis enjoyable. I am also grateful to have Atsi, Tringo and Teshu here in the U.S. Living away from home is a challenge but having you here is a world to me. Jalene: you have been there during the good and bad times in this entire process, which signifies the true meaning of friendship. I am truly grateful for our friendship. Haime, Shimelis, Abreham and Bizuye thank you for being a great support system during this long journey.

Vita

EDUCATION

Ph.D., Inorganic Chemistry, The Ohio State University, Columbus, OH

B.A. with Honors in Chemistry, Colby College, Waterville, ME, 2014

IB, Waterford Kamhlaba UWC of Southern Africa, Mbabane, Swaziland, 2009

Publications

- Kassie, A. A.; Duan, P.; Gray, M. B.; Schmidt-Rohr, K.; Woodward, P. M.; Wade, C. *Organometallics* **2019**, 38, 3419-3428.
- Kassie, A. A.; Duan, P.; McClure, E.; Schmidt-Rohr, K.; Woodward, P.; Wade, C. R. *Inorg. Chem.*, **2019**, 58, 3227–3236.
- Reiner, B. R.; Kassie, A. A.; Wade, C. R. *Dalton Trans.* **2019**, 48, 9588-9595.
- Kassie, A. A.; Wade, C.R.; Duan, P.; Schmidt-Rohr K. *Front. Chem.* **2018**
Conference Abstract: (NOBCChE) 45th Annual Conference
- Burgess, S. A.; Kassie, A. A.; _Baranowski, S. A.; _Fritzsching, K. J.; Schmidt-Rohr, K.; _Brown, C. B.; Wade, C.R. *J. Am. Chem. Soc.* **2016**, 138, 1780.

Fields of Study

Major Field: Chemistry

Table of Contents

Abstract	ii
Dedication	v
Acknowledgments	vi
Vita	ix
List of Tables.....	xiii
List of Figures	xiv
Chapter 1. Introduction.....	1
1.1 Bridging homogeneous and heterogeneous catalysis.....	1
1.2 Metal-Organic Frameworks (MOFs)	3
1.3 Catalysis with MOFs.....	5
1.4 Immobilizing diphosphine pincer complexes in MOFs.....	9
Chapter 2: Synthesis, characterization and reactivity of Zr MOFs assembled from POCOP-Pd metallolinkers	17
2.1 Introduction	18
2.2 Synthesis and characterization of POCOP-Pd pincer complexes.....	19
2.3 Synthesis and characterization of 2-PdX	22
2.4. Catalytic activity of 2-PdX.....	25
2.5 Postsynthetic ligand exchange at Pd.....	26
2.6 Catalytic study of 2-PdTFA	27
2.7 Conclusions	33
2.8 Experimental.....	34
Chapter 3: Broad scope catalytic activity of POCOP-Pd pincer complexes immobilized in a Zr MOF	45
3.1 Introduction	45
3.2 Synthesis and characterization of 2-PdBF ₄	46
3.3 Transfer hydrogenation of aldehydes.....	52
3.4 Transfer hydrogenation of alkene, alkyne and nitroarene substrates.....	53
3.5 Terminal alkyne hydration	57
3.6 Intramolecular alkyne hydroarylation.....	60
3.7 Conclusions	62

3.8 Experimental.....	63
Chapter 4: Synthesis and reactivity of PNNNP-Co ^{III} pincer complexes immobilized in a Zr MOF	67
4.1 Introduction	68
4.2 Synthesis and characterization of PNNNP-CoCl ₃ pincer complexes	70
4.3 Synthesis and characterization of 6-CoCl ₃	71
4.4 Postsynthetic metal exchange (PSME)	81
4.5 Conclusions	94
4.6 Experimental.....	95
Chapter 5: Synthesis, characterization and reactivity of isostructural Zr MOFs assembled from PNNNP-Ru pincer complexes	103
5.1 Introduction	104
5.2 Synthesis and characterization of PNNNP-Ru metallolinkers	106
5.3 Synthesis and characterization of Zr MOFs containing PNNNP-Ru metallolinkers	112
5.4 Postsynthetic activation of 9-RuCl(CO) ₂	123
5.5 Catalytic hydrosilylation studies.....	126
5.5 Conclusions	129
5.6 Experimental.....	130
Bibliography.....	140
Appendix.....	163
Permissions to Reprint.....	163

List of Tables

Table 1. Catalytic transfer hydrogenation of aldehydes	29
Table 2. Transfer hydrogenation of aldehydes	53
Table 3. Transfer hydrogenation of alkene, alkyne and nitroarene substrates	55
Table 4. Catalytic hydration of alkynes	58
Table 5. Synthesis of simple coumarins via intramolecular hydroarylation.....	61
Table 6. Catalytic Hydrosilylation of aryl aldehydes	126

List of Figures

Figure 1. Cartoon scheme depicting solvothermal self-assembly of MOFs	3
Figure 2. Removal of H ₂ O molecules from HKUST-1 with high vacuum and heat.....	6
Figure 3. Illustration of some commonly used strategies to incorporate catalytically active sites in MOFs.	7
Figure 4. General structure of pincer complexes	9
Figure 5. General structure of diphosphine pincer complexes.....	10
Figure 6. a) A Co MOF assembled from PCP-PdCl metallolinkers b) Framework structure of NU-1000 c) POCOP-IrH ₂ complex immobilized on NU-1000 node.....	14
Figure 7. PNP-Ru(CO)HCl encapsulation in UiO-66 and CO ₂ hydrogenation with Ru@UiO-66.	14
Figure 8. a) ¹ H and b) ³¹ P{ ¹ H} NMR spectra of ^t Bu ₄ (1-PdI) and H ₄ (1-PdI).	21
Figure 9. a) Experimental and simulated SPXRD patterns of 2-PdX (synchrotron radiation, λ = 0.413959 Å). b) Framework structure of 2-PdX . Linker disorder has been omitted for clarity. c) View of a portion of the framework showing ovoidal pores. d) Hexanuclear Zr clusters ([Zr ₆ O ₄ (OH) ₄](CO ₂) ₁₂). e) PXRD patterns (Cu-Kα radiation, λ = 1.5418 Å) for samples of 2-PdX that are “as synthesized”, soaked in 0.1 M NaOH and 1 M HNO ₃ , and activated by heating under vacuum.	23
Figure 10. a) TGA data for a sample of 2-PdX measured at a ramp rate of 5 °C/min under flowing N ₂ (50 mL/min). b) N ₂ adsorption isotherms measured at 77 K for samples of 2-PdX and 2-PdTFA after desolvation at 100 °C and 10 ⁻⁴ torr.....	24
Figure 11. a) Solid-state ³¹ P NMR spectra of 2-PdX and H ₄ (1-PdI). Asterisks (*) are used to denote spinning side bands. b) ³¹ P{ ¹ H} NMR spectra of H ₄ (1-PdI) (DMSO-d ₆) and 2-PdX (CF ₃ COOH/C ₆ D ₆).	25
Figure 12. a) PXRD patterns (Cu-Kα radiation, λ = 1.5418 Å) for samples of 2-PdX and 2-PdTFA before and after catalysis. b) Solid-state ³¹ P NMR spectra of 2-PdTFA before and after catalysis. Asterisks (*) are used to denote spinning side bands.	27
Figure 13. Solid-state ¹³ C NMR spectra of H ₄ (1-PdI), 2-PdX , and 2-PdTFA before and after catalysis.....	30
Figure 14. a) ¹ H NMR spectrum (CD ₃ OD) of (<i>p</i> - ^t BuO ₂ CPh)(O)OCD ₃ . b) ³¹ P { ¹ H} NMR spectra for (<i>p</i> - ^t BuO ₂ CPh)(O)OCD ₃ (CD ₃ OD) and ^t Bu ₄ (1-PdTFA) (CDCl ₃)	32
Figure 15. ³¹ P{ ¹ H} NMR spectra (CF ₃ COOH/C ₆ D ₆) of 2-PdX and 2-PdI	47
Figure 16. ¹ H NMR spectrum (CF ₃ COOH/C ₆ D ₆) of 2-PdI	48
Figure 17. a) XRF spectra of 2-PdI and 2-PdBF₄ . b) XPS spectra of 2-PdX , 2-PdI and 2-PdBF₄ showing the iodine 3d _{3/2} and 3d _{5/2} region.....	48
Figure 18. ³¹ P{ ¹ H} NMR spectra (CF ₃ COOH/C ₆ D ₆) of 2-PdBF₄ and ^t Bu ₄ (1-PdBF ₄). ...	49
Figure 19. ¹ H NMR spectra (CF ₃ COOH/C ₆ D ₆) of 2-PdBF₄ and ^t Bu ₄ (1-PdBF ₄)......	50

Figure 20. a) N ₂ adsorption isotherms measured at 77 K for 2-PdX , 2-PdI and 2-PdBF₄ after desolvation at 100 °C and 10 ⁻⁴ torr for 16 h. b) PXRD patterns (Cu-Kα radiation, λ = 1.5418 Å) of 2-PdI and 2-PdBF₄ before and after activation.	51
Figure 21. a) PXRD patterns (Cu-Kα radiation, λ = 1.5418 Å) of 2-PdBF₄ before and after transfer hydrogenation of styrene. b) ³¹ P{ ¹ H} NMR spectra of ^t Bu ₄ (1-PdBF ₄) before and after transfer hydrogenation reactions.	56
Figure 22. a) PXRD patterns (Cu-Kα radiation, λ = 1.5418 Å) of 2-PdBF₄ before and after phenylacetylene hydration (Run 5). b) Recyclability plot for hydration of phenylacetylene with 2-PdBF₄ . c) ³¹ P{ ¹ H} NMR spectrum of ^t Bu ₄ (1-PdBF ₄) after phenylacetylene hydration attempt in THF/H ₂ O.....	59
Figure 23. a) ¹ H NMR spectra (acetone-d ₆) of ^t Bu ₄ (5-CoCl ₃) and H ₄ (5-CoCl ₃). b) ³¹ P{ ¹ H} NMR spectra of ^t Bu ₄ PNNNP, ^t Bu ₄ (5-CoCl ₃) and H ₄ (5-CoCl ₃).	71
Figure 24. a) Final Rietveld refinement profile of 6-CoCl₃ from SPXRD data (λ = 0.412697 Å). b) Framework structure of 6-CoCl₃ . The blue octahedra represent [Zr ₆ O ₄ (OH) ₄] ¹²⁺ clusters. c) Structure of the D _{4h} [Zr ₆ O ₄ (OH) ₄ (OAc) ₄] ⁸⁺ secondary building units.	72
Figure 25. [5-CoCl ₃] ⁴⁺ linker (left) and Zr ₆ cluster (right) rigid bodies used for Rietveld refinement of 6-CoCl₃ in the <i>P6</i> space group.....	74
Figure 26. Square planar diphosphine pincer metallolinkers and framework structure adopted by the isostructural series of Zr pincer MOFs 2-PdX , 7-PdX , and 7-PtX	74
Figure 27. Solid-state ³¹ P NMR spectra for as-synthesized 6-CoCl₃ and 6-CoCl₃(MeOH) with magic-angle spinning (MAS) and total suppression of spinning sidebands (TOSS).	75
Figure 28. ³¹ P{ ¹ H} NMR spectra (CF ₃ CO ₂ H/C ₆ D ₆) of 6-CoCl₃ , 6-CoCl₃(MeOH) and H ₄ (5-CoCl ₃).	77
Figure 29. ¹ H NMR spectrum (CF ₃ CO ₂ H/C ₆ D ₆) of as synthesized 6-CoCl₃	78
Figure 30. a) TGA data for a sample of 6-CoCl₃ measured at a ramp rate of 5 °C/min under flowing N ₂ (50 mL/min). b) N ₂ adsorption isotherm measured at 77 K for 6-CoCl₃(MeOH) after desolvation at 100 °C and 10 ⁻⁴ torr.....	79
Figure 31. Acid-digested a) ¹ H and b) ³¹ P{ ¹ H} NMR spectra (CF ₃ CO ₂ H/C ₆ D ₆) of 6-CoCl₃(MeOH) after activation.	80
Figure 32. a) XRF spectra and b) PXRD patterns (Cu-Kα radiation, λ = 1.5418 Å) of 6-CoCl₃ before and after heating at 85 °C in DMF at different reaction time.	81
Figure 33. a) ³¹ P{ ¹ H} NMR spectra for reactions between ^t Bu ₄ (5-CoCl ₃) and [Rh(nbd)Cl] ₂ with and without Et ₃ N, and reaction of ^t Bu ₄ PNNNP with [Rh(nbd)Cl] ₂ in DMSO. b) ³¹ P{ ¹ H} NMR spectra of ^t Bu ₄ (5-CoCl ₃) before and after heating in DMSO at 85 °C, and after reaction with Et ₃ N at room temperature.	84
Figure 34. a) X-band EPR spectra of 6-CoCl₃(MeOH) before and after reaction with Et ₃ N in THF. Spectra were recorded at 10 K. Microwave frequency = 9.385 GHz, power = 0.002 mW, modulation amplitude = 0.8 mT/100 kHz. b) PXRD patterns (Cu-Kα radiation, λ = 1.5418 Å) of 6-CoCl₃(MeOH) before and after reaction with Et ₃ N at 60 °C in THF.....	85
Figure 35. a) XRF spectra and kinetic plot showing the rate of Rh/Co PSME in 6-CoCl₃(MeOH) . b) Solid-state ³¹ P NMR spectra of 6-RhCl and 6-RhCl(NEt₃) with MAS and TOSS.	86

Figure 36. a) Solid-state ^{31}P NMR spectra for samples of 6-RhCl(Et₃N) generated by Rh/Co PSME of 6-CoCl₃(MeOH) with [Rh(nbd)Cl] ₂ and 1 or 3 equiv. of Et ₃ N per Co. b) PXRD patterns (Cu-K α radiation, $\lambda = 1.5418 \text{ \AA}$) of the product obtained upon reaction of 6-CoCl₃(MeOH) with [Rh(nbd)Cl] ₂ in DMF. NP = nanoparticles.	88
Figure 37. a) PXRD patterns (Cu-K α radiation, $\lambda = 1.5418 \text{ \AA}$) for 6-RhCl , 6-RhCl(NEt₃) , 6-PtCl , and 6-PtRh . b) CO adsorption isotherms measured for 6-CoCl₃(MeOH) and 6-RhCl at 303 K. c) Solid-state ^{31}P NMR spectrum of 6-RhCl after CO adsorption measurement with MAS and TOSS. d) ATR-IR spectra of 6-RhCl before and after CO adsorption measurement.	89
Figure 38. a) SEM images of 6-CoCl₃ , 6-RhCl and 6-PtCl . b) Elemental mapping of Zr and Co in 6-CoCl₃ , Zr and Rh in 6-RhCl , and Zr and Pt in 6-PtCl using EDX.	90
Figure 39. a) XRF spectra before and after the Pt/Co exchange reaction used to generate 6-PtCl . b) Kinetic plot derived from XRF data measured for Pt/Co exchange reaction. c) Solid-state ^{31}P NMR spectrum of 6-PtCl with MAS and TOSS.	91
Figure 40. a) $^{31}\text{P}\{^1\text{H}\}$ NMR spectra (CF ₃ CO ₂ H/C ₆ D ₆) of 6-CoCl₃(MeOH) , 6-PtCl and 6-PtRh . Asterisks (*) are used to denote ^{195}Pt satellites. b) XRF spectra before and after the Pt/Co and Rh/Co exchange reactions used to generate 6-PtRh	93
Figure 41. ^1H NMR spectrum of $^t\text{Bu}_4(5\text{-RuH}(\text{CO})(\text{PPh}_3))$ in DMSO-d ₆	107
Figure 42. $^{31}\text{P}\{^1\text{H}\}$ NMR spectra of $^t\text{Bu}_4(5\text{-RuH}(\text{CO})(\text{PPh}_3))$ and $\text{H}_4(5\text{-Ru}(\text{TFA})(\text{CO})(\text{PPh}_3))$ in DMSO-d ₆	108
Figure 43. ^1H NMR spectrum of $\text{H}_4(5\text{-Ru}(\text{TFA})(\text{CO})(\text{PPh}_3))$ in DMSO-d ₆	109
Figure 44. ^1H NMR spectra of $^t\text{Bu}_4(5\text{-RuCl}(\text{CO})_2)$ and $\text{H}_4(5\text{-RuCl}(\text{CO})_2)$ in DMSO-d ₆	110
Figure 45. $^{31}\text{P}\{^1\text{H}\}$ NMR spectra of $^t\text{Bu}_4(5\text{-RuCl}(\text{CO})_2)$, $\text{H}_4(5\text{-RuCl}(\text{CO})_2)$ and <i>cis/trans</i> - $\text{H}_4(5\text{-RuCl}_2(\text{CO}))$ in DMSO-d ₆	111
Figure 46. ^1H NMR spectrum of <i>cis/trans</i> - $\text{H}_4(5\text{-RuCl}_2(\text{CO}))$ in DMSO-d ₆	112
Figure 47. a) PXRD patterns (Cu-K α radiation, $\lambda = 1.5418 \text{ \AA}$) for 8-RuCl₂(CO) , 9-RuCl(CO)₂ and 10-RuCl₂(CO) . b) Rietveld refinement profile of 8-RuCl₂(CO) from SPXRD data ($\lambda = 0.414536 \text{ \AA}$). c) Framework structure of 8-RuCl₂(CO) . d) Structure of the D _{4h} [Zr ₆ O ₄ (OH) ₄ (OAc) ₄] ⁸⁺ secondary building units.	114
Figure 48. a) Solid-state ^{31}P NMR spectra of 8-RuCl₂(CO) , 9-RuCl(CO)₂ and 10-RuCl₂(CO) . Asterisks (*) mark spinning side bands. b) CsF- and acid-digested $^{31}\text{P}\{^1\text{H}\}$ NMR spectra of 8-RuCl₂(CO) , 9-RuCl(CO)₂ and 10-RuCl₂(CO) . 8-RuCl₂(CO) was digested with CsF/DMSO-d ₆ /D ₂ O while 9-RuCl(CO)₂ and 10-RuCl₂(CO) were digested with CF ₃ CO ₂ H/DMSO-d ₆	115
Figure 49. CsF-digested ^1H NMR spectrum (DMSO-d ₆ /D ₂ O) of 8-RuCl₂(CO) after MeOH solvent exchange.....	116
Figure 50. a) ATR-IR spectra of 8-RuCl₂(CO) , 9-RuCl(CO)₂ and 10-RuCl₂(CO) . b) N ₂ adsorption isotherms at 77 K for samples of 8-RuCl₂(CO) , 10-RuCl₂(CO) and 9-RuCl(CO)₂ after desolvation at 100 °C and 10 ⁻⁴ torr. TGA for samples of 8-RuCl₂(CO) (c), 9-RuCl(CO)₂ (d), and 10-RuCl₂(CO) (e) measured at a ramp rate of 5 °C/min under flowing N ₂ (50 mL/min).	117
Figure 51. Solid-state ^{13}C NMR spectra of 8-RuCl₂(CO) (a), 9-RuCl(CO)₂ (b), 10-RuCl₂(CO) (c), and 10-RuCl₂(CO) (d) synthesized using HCO ₂ H as a modulator.	

Quantitative multiCP ^{13}C NMR spectra of without (blue line) and with (red line) recoupled ^1H dipolar dephasing, recorded at 14 kHz MAS. The spectrum in red shows nonprotonated carbons and highly mobile segments. (e) Solid-state ^{31}P NMR spectrum for **10-RuCl₂(CO)** synthesized using HCO_2H as a modulator with MAS and TOSS. (f) $^{31}\text{P}\{^1\text{H}\}$ NMR spectrum for reaction supernatant of **8-RuCl₂(CO)**..... 118

Figure 52. Acid-digested ^1H NMR spectrum ($\text{CF}_3\text{CO}_2\text{H}/\text{DMSO-d}_6$) of **9-RuCl(CO)₂** after THF washing..... 119

Figure 53. a) PXRD patterns (Cu-K α radiation, $\lambda = 1.5418 \text{ \AA}$) for activated samples of **8-RuCl₂(CO)**, **9-RuCl(CO)₂** and **10-RuCl₂(CO)**. b) PXRD patterns for as synthesized, THF and MeOH solvent exchanged samples of **9-RuCl(CO)₂**. c) ATR-IR spectra for **9-RuCl(CO)₂** before and after activation. d) Acid-digested $^{31}\text{P}\{^1\text{H}\}$ NMR spectrum ($\text{CF}_3\text{CO}_2\text{H}/\text{DMSO-d}_6$) of **9-RuCl(CO)₂** after activation..... 121

Figure 54. Acid-digested ^1H NMR spectrum ($\text{CF}_3\text{CO}_2\text{H}/\text{DMSO-d}_6$) of **9-RuCl(CO)₂** after activation..... 122

Figure 55. a) ATR-IR spectra for **9-RuCl(CO)₂**, **9a-RuCl(CO)₂**, and **9b-RuCl(CO)**. b) PXRD patterns (Cu-K α radiation, $\lambda = 1.5418 \text{ \AA}$) for **9-RuCl(CO)₂**, **9a-RuCl(CO)₂**, and **9b-RuCl(CO)** before catalysis and after catalytic run 4. c) ATR-IR spectra for **9b-RuCl(CO)** before and after catalysis, and after catalyst regeneration with Me_3NO . d) ATR-IR spectra for homogeneous complexes of $^1\text{Bu}_4(5\text{-RuCl(CO)}_2)$, $^1\text{Bu}_4(5\text{a-RuCl(CO)}_2)$, and $^1\text{Bu}_4(5\text{b-RuCl(CO)})$ 125

Chapter 1. Introduction¹

1.1 Bridging homogeneous and heterogeneous catalysis

We have witnessed some tremendous developments in catalysis, including the direct conversion of N₂ and H₂ to ammonia using iron catalysts, the polymerization of olefins with Ziegler-Natta catalysts, and the selective production of gasoline from methanol using zeolite catalysts. Catalysis plays a central role in improving the efficiency of energy storage/conversion processes and preparation of fine and bulk chemicals that are directly or indirectly linked to the necessity and advancement of our society. Approximately 90 % of chemical reactions in industry are carried out with the assistance of catalysts, highlighting the need for new catalyst design principles that improve efficiency, selectivity, stability and sustainability.¹ Furthermore, the development of efficient catalytic processes are crucial to mitigate environmental pollution, with existing autocatalytic converters technology as one practical example.¹⁻³

There are two major classifications of catalysts: heterogeneous (solid catalysts) and homogeneous (uniformly mixed with reactants in gas or liquid phases) catalysts, each with their own advantages and disadvantages. Heterogeneous catalysts can often withstand harsh catalytic conditions and are easily separated from a reaction mixture by filtration or centrifugation. These features make them attractive from economic and environmental

¹References in this dissertation follow the style and format of the Journal of the American Chemical Society

perspectives.^{4,5} As a result, approximately 90% of industrial catalytic processes are carried out using heterogeneous catalysts.⁴ This means that only a small fraction of industrial chemical processes use homogeneous catalysts even though they can offer higher activity and selectivity.⁴ Hydroformylation of terminal alkenes to aldehydes is by far the most widely employed industrial application of homogeneous catalysis. Their use in this transformation stems from the selectivity obtained by tuning ligand and metal identity. For example, substituting Co for Rh has led to a significant selectivity improvement toward linear aldehydes, although the scarcity and high price of Rh raises concerns.⁶ This example illustrates the power of understanding structure-function relationships at a molecular level to tune a catalyst for a particular application. However, the advantages that homogeneous catalysts offer are often diminished by their poor stability under harsh catalytic conditions and difficulty to separate from the reaction medium. Methods such as membrane separation, polymer grafting, and functionalization of polysilane dendrimers with catalytically active metals have been used to enhance the separation process for homogeneous catalysis, but efficiency of separation is still often inadequate.^{4,7-9}

As mentioned previously, the large dependence of industrial chemical production on heterogeneous catalysts is related to their stability and recyclability. However, reaction mechanisms in heterogeneous systems are often difficult to elucidate and may not be well-understood.⁵ Mechanistic investigations are complicated by factors such as an inhomogeneous distribution of active sites, poorly defined coordination environments, and the role of interactions between the support and catalyst species. A lack of understanding about the structure and electronic environment of catalytically active sites can limit rational

optimization for activity and/or selectivity improvements. Therefore, ideal catalyst design principles will strive to combine the beneficial characteristics of homogeneous and heterogeneous catalysis.

1.2 Metal-Organic Frameworks (MOFs)

MOFs are crystalline, porous coordination polymers assembled from organic linkers and metal ions/clusters (Figure 1). These metal ions/clusters are often referred to as secondary building units (SBUs). Organic linkers usually contain functional groups such as carboxylates, amines, pyrazolates, trizolates, or tetrazolates that permit self-assembly with the SBUs.^{10–13} The general solvothermal synthesis shown in Figure 1 is the most commonly employed method of MOF assembly, although mechanochemical, sonochemical, microwave-assisted and electrochemical methods have also been used.

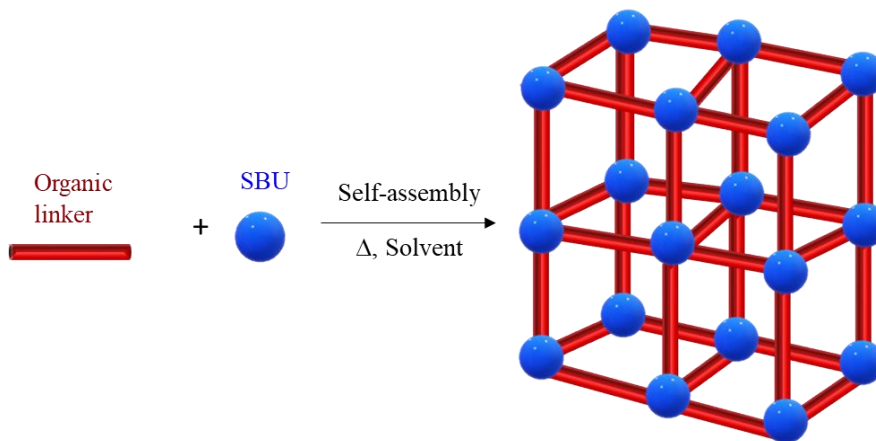


Figure 1. Cartoon scheme depicting solvothermal self-assembly of MOFs

The choice of SBUs, organic linkers and synthesis conditions including solvent, modulator, temperature, and reaction time are key factors that influence the framework topology, porosity, and stability of MOFs.^{14–18} The matching of linker functional group and metal ion based upon hard/soft acid/base principles can confer a MOF with good chemical and

thermal stability. For example, the exceptional chemical and thermal stability of Zr MOFs constructed from organic linkers with carboxylate functional groups is attributed to the strong interaction between Zr^{4+} and carboxylate O atoms.¹⁹

The multitude of available organic linkers and inorganic building units provides access to MOFs with a variety of topologies and functions. As result, the chemistry of MOFs has experienced explosive growth and interest for applications in gas storage²⁰ and separation²¹, drug delivery²², sensing²³ and catalysis²⁴. The interest in MOFs for catalytic application stems from their well-defined structures that resemble homogeneous catalysts and large internal surface areas. Currently, many industrial processes use zeolites (microporous aluminosilicate) as heterogeneous catalysts;²⁵ however, their chemical diversity is limited due to their solely inorganic nature.²⁶ In addition, MOFs can accommodate large substrates because of their high internal surface areas (up to $\sim 10000 \text{ m}^2\text{g}^{-1}$) compared to zeolites (usually $< 700 \text{ m}^2\text{g}^{-1}$).²⁷⁻²⁹ Heterogeneous catalysts based on mesoporous silica supports often suffer from instability and low catalytic activity owing to their amorphous pore channels.²⁶ Hence, MOFs offer a great opportunity to bridge the heterogeneous nature and porosity of zeolites and other solid supports with the tunability of homogeneous catalysts.

Several methods are available to determine the structure, composition and porosity of MOFs.^{30,31} Single crystal X-ray diffraction (SXRD) is an ideal method for structure determination. However, the quality or size of MOF crystallites may not be suitable for SXRD analysis, and instead, powder X-ray diffraction (PXRD) in combination with other analytical techniques is frequently used to elucidate structure and composition. In addition,

FT-IR, UV-Vis, X-ray fluorescence spectroscopy (XRF), X-ray photoelectron spectroscopy (XPS), inductively coupled plasma-optical emission spectroscopy (ICP-OES), elemental analysis, and solution- or solid-state multinuclear NMR spectroscopy methods are used to corroborate composition and structure. Scanning electron microscopy (SEM) and transmission electron microscopy (TEM) techniques can also help to determine morphology and particle size. Thermogravimetric analysis (TGA) provides information about the volatility of MOF components as a function of temperature and the loss of solvent guest molecules from MOF pores or channels is often used as a qualitative measure of MOF porosity. Surface area data are usually obtained using N₂ adsorption isotherms at 77 K and application of Brunauer-Emmett-Teller (BET) theory. In cases, where desolvation causes framework collapse, supercritical CO₂ and lyophilization can be used to prevent or minimize framework collapse. In addition, dye sorption has been used to determine MOF porosity.^{32,33}

1.3 Catalysis with MOFs

There are four main approaches that have been used to incorporate catalytically active species within MOFs: SBU activation, catalyst encapsulation, postsynthetic modification of organic linkers or SBUs, and the use of linkers as intrinsic catalysts species. In addition to providing framework support, the metal node of a MOF can serve as an active site for catalysis.³⁴ The removal of ancillary ligands such as coordinated solvent molecules from the node upon heating under high vacuum creates coordinatively unsaturated Lewis acidic metal sites.³⁵⁻³⁹

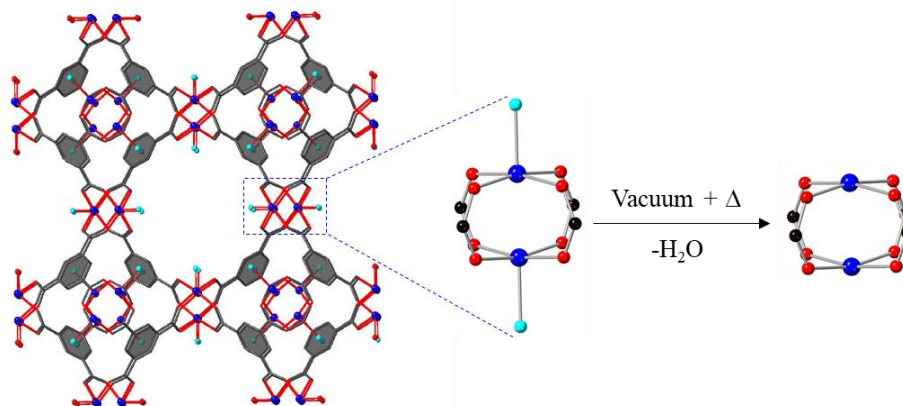


Figure 2. Removal of H₂O molecules from HKUST-1 with high vacuum and heat.^{35,40}

Kaskel and coworkers showed that axially-coordinated H₂O molecules could be removed from HKUST-1 (Cu₃(BTC)₂ (H₂O)₃ (BTC = benzene 1,3,5-tricarboxylate)) to generate coordinatively unsaturated Cu²⁺ Lewis acid sites, and the activated MOF catalyzed cyanosilylation of benzaldehyde (Figure 2).^{35,40} Moreover, rationally engineered or unintended defect sites at MOF SBUs have shown interesting Lewis and Brønsted acid catalytic activities.^{41–44} Reaction time, temperature, and various acid modulators have been used to introduce and control defects in MOFs, particularly those containing hexanuclear Zr SBUs.^{45–47} The major drawbacks of using SBUs for catalysis are the limitation on metal identity and the number of coordination sites available. In addition, the procedures used to generate coordinatively unsaturated sites at the metal node might compromise the structural integrity of the MOF.

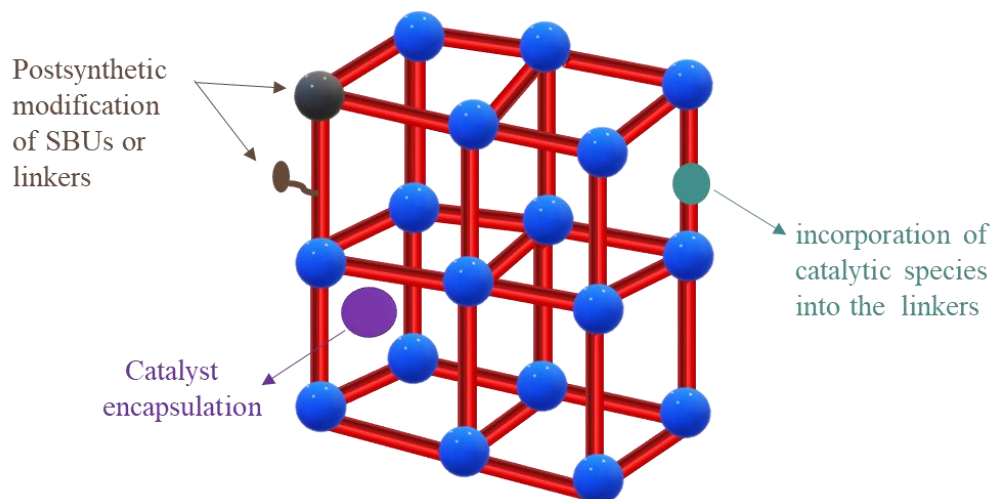


Figure 3. Illustration of some commonly used strategies to incorporate catalytically active sites in MOFs.

Encapsulation of molecular or nanoparticle catalysts within MOF pores has resulted in materials with high catalytic efficiency, stability and reusability (Figure 3). There have been numerous reports on MOF-encapsulated Pd,⁴⁸ Pt,⁴⁹ and Au⁵⁰ nanoparticles that demonstrate high catalytic activity and recyclability for various organic transformations. Molecular catalysts such as porphyrin complexes,⁵¹ and even enzymes,⁵² have been immobilized in MOFs and shown superior catalytic activity and reusability compared to their homogeneous counterparts. The drawbacks of catalyst encapsulation include a high risk of catalyst leaching and diminished accessible surface area for substrate/product diffusion. However, the former challenge has been addressed through careful selection of MOFs with appropriate pore aperture sizes and catalytic conditions that prevent catalyst species from leaching.⁵³⁻⁵⁵

Postsynthetic modification of organic linkers or inorganic nodes via covalent attachment or grafting is a widely used approach to incorporate catalytically active species in MOFs (Figure 3).^{33,56-63} Postsynthetic modification is particularly appealing when a

catalyst is incompatible with solvothermal synthesis conditions or precatalyst activation steps are required. Férey and coworkers grafted ethylenediamine on coordinatively unsaturated Cr³⁺ sites in MIL-101(Cr) (MIL = Materials Institute Lavoisier) to generate catalytically active sites for the Knoevenagel condensation of benzaldehyde with ethyl cyanoacetate.⁶⁴ Another study from the Farrusseng group showed that (Fe)MIL-101-NH₂, assembled from amine-functionalized linkers, could be modified to incorporate Ni species that catalyze ethylene dimerization.⁶⁵ Lin and coworkers have shown that metalating the SBUs of Zr MOFs with MgMe₂ generates materials that catalyzes hydroboration and hydroamination reactions.⁶² These are only a few examples among many seminal reports that demonstrate postsynthetic modification of MOFs as a versatile approach to design heterogeneous catalysts.

Catalytically active species can also be incorporated as an integral part of the organic linker during MOF self-assembly (Figure 3).^{10,66-75} Integrating the catalyst species into the organic linker results in a homogeneous distribution of active sites and does not greatly impact substrate accessible surface area. However, in most cases, precatalyst activation procedures are required because catalytically active metal centers become coordinatively saturated under MOF synthesis conditions. Metalloporphyrin and metallosalen complexes have been widely studied as metallolinkers, and the corresponding MOFs have shown significantly better stability and catalytic activity than homogeneous analogues.^{66,74,76-79} For example, Cui et. al. reported a Cd MOF assembled from Co-salen metallolinkers that catalyzes hydrolytic kinetic resolution of racemic epoxides with higher enantioselectivity (up to 99.5 % ee) than the monomeric analogue.⁸⁰ In addition, Zhou and

coworkers showed that a Zr MOF PCN-222(Fe) (PCN = porous coordination network) constructed from Fe-porphyrin linkers exhibits biomimetic catalytic activity for peroxidase-like oxidation reactions.⁸¹ Pincer complexes have also been used as metallolinkers in MOFs, resulting in materials that with better catalytic stability, reactivity and recyclability than homogeneous analogues.^{82–87}

1.4 Immobilizing diphosphine pincer complexes in MOFs

The chemistry of pincer complexes has been the focus of much attention in the homogeneous catalysis community owing to their stability and tunable electronic and steric properties.^{88–94} Pincer ligands can support a wide range of metals (soft/hard Lewis acids) by judicious choice of Z, X and E components (Figure 4).

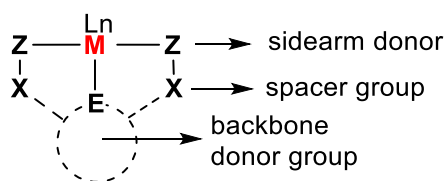


Figure 4. General structure of pincer complexes

Pincer complexes commonly contain P,⁹⁵ N,⁹⁶ S,⁹⁷ Si,⁹⁸ or O⁹⁹ groups as chelating side arms (Z) and N,¹⁰⁰ C,¹⁰¹ Si,¹⁰² P,¹⁰³ B,¹⁰⁴ Al,¹⁰⁵ Sb¹⁰⁶ as backbone donor elements (E). The spacer component (X) is often constructed from O,¹⁰⁷ NH,⁹¹ CH₂,¹⁰¹ or phosphine¹⁰⁸ groups. Pincer complexes with P and S sidearm donor atoms support late transition metals because of their tendency to behave as soft Lewis bases while N and O donor sites favor mid or early, electropositive transition metals.^{88,109} In addition to tuning Z, X, E components, the ability to vary metal identity while keeping other components constant offers a wide scope of systematic studies for a given ligand platform.

Diphosphine pincer complexes with CH₂, O, NH spacers and pyridine/arene backbones support a broad range of transition metals that have shown interesting reactivity and catalytic activity.^{90-95,110} The general structure and commonly used abbreviations for this class of diphosphine pincer complexes are shown in Figure 5.

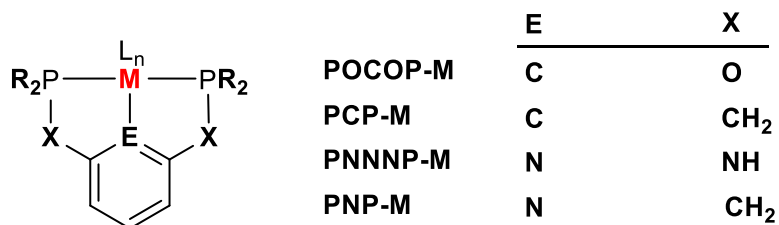
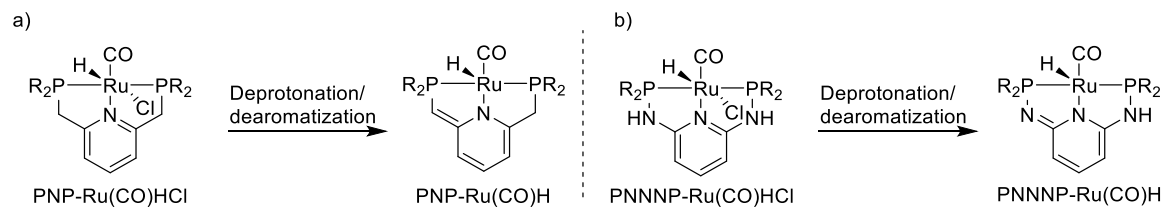


Figure 5. General structure of diphosphine pincer complexes.

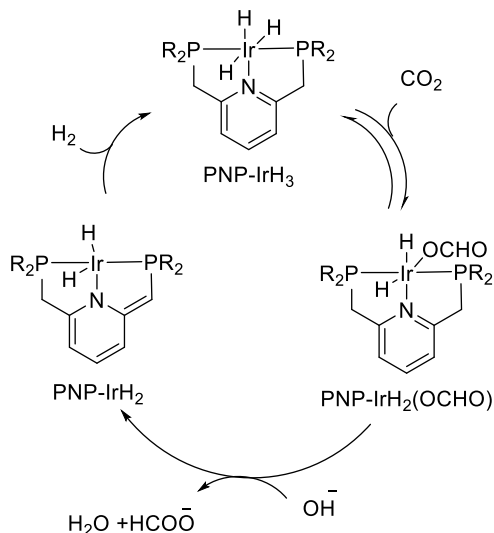
The spacer type, phosphine substituents, backbone, and metal identities are key factors that influence the reactivity of diphosphine pincer complexes. For example, catalytic reactions with PNP and PNNNP pincer complexes have been proposed to involve metal-ligand cooperativity (MLC) via deprotonation/dearomatization of CH₂ and NH spacers respectively.^{91,111} Representative examples of PNP-Ru and PNNNP-Ru pincer complexes that illustrate deprotonation/dearomatization reactions are depicted in Scheme 1. Milstein and others have proposed MLC mechanisms for dehydrogenation, hydrogenation, and hydroboration reactions catalyzed by PNP-Ru pincer complexes.¹¹¹



Scheme 1. Illustration of deprotonation/dearomatization reactions for PNP-Ru (a) and PNNNP-Ru (b) pincer complexes

Nozaki and coworkers reported a highly active PNP-IrH₃ catalyst for CO₂ hydrogenation

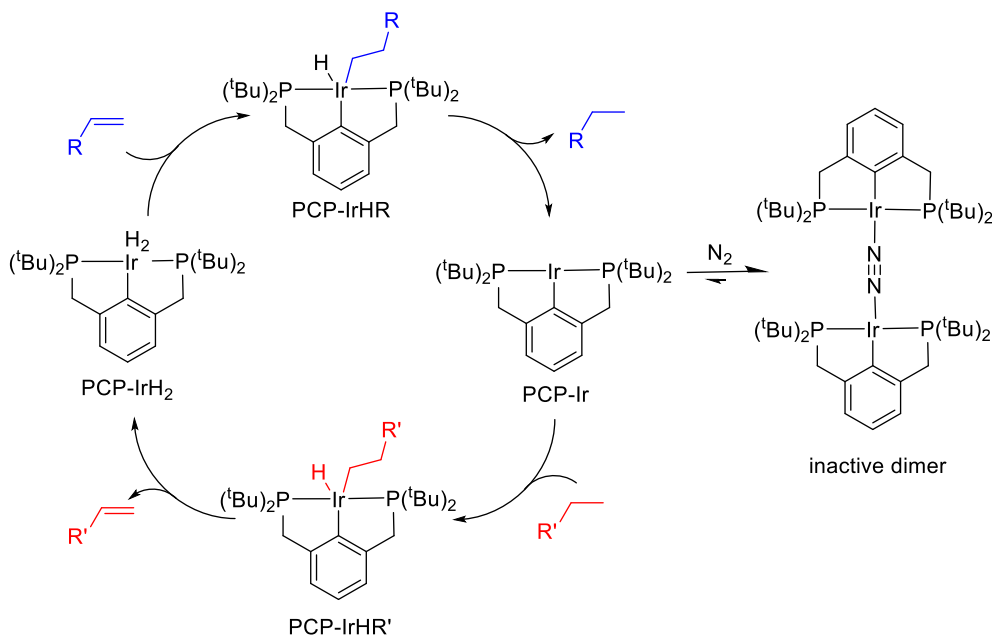
that is proposed to involve a similar type of MLC mechanism (Scheme 2).¹¹² In addition, Huang and others have proposed deprotonation/dearomatization mechanisms for catalytic reactions with PNNNP-based pincer complexes.^{91,113–117}



Scheme 2. Proposed mechanism for CO₂ hydrogenation by PNP-IrH₃

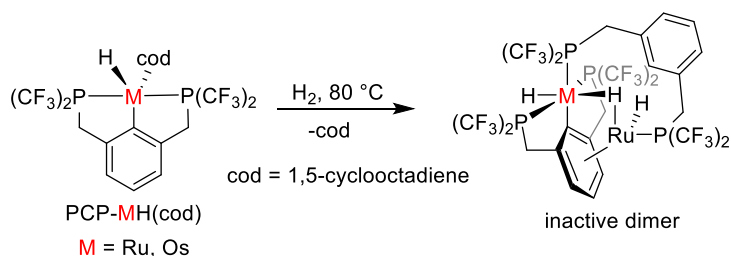
Goldman, Brookhart, Ozerov and others have shown that PCP and POCOP based Ir pincer complexes catalyze organic transformations such as alkane dehydrogenation, carbonyl hydrogenation, olefin isomerization, and C-H borylation reactions.^{92,101,107,118} However, the optimal activity of these pincer complexes is often attained under rigorously inert atmospheres to prevent unwanted side reactions and bimolecular deactivation pathways. For example, Jensen and coworkers showed that a PCP-IrH₂ pincer complex was highly effective for catalytic transfer dehydrogenation of alkanes as long as the reactions were carried out under Ar atmosphere (Scheme 3).^{119,120} However, the catalytic activity dropped significantly when reactions were carried out under N₂ rather than Ar atmosphere. A highly reactive, 14-electron PCP-Ir species is thought to be a key

intermediate in the catalytic cycle, and the formation of an inactive, N₂-bridged dimer from the reactive intermediate has been proposed to be responsible for the decrease in catalytic activity.



Scheme 3. Dimerization of Ir-PCP intermediate in the presence of N₂

Roddick and coworkers have reported that PCP-M (M = Ru, Os) pincer complexes also catalyze alkane dehydrogenation. However, the catalytic efficiency of these complexes is hampered by inactive dimer formation and thermal decomposition under the catalytic conditions (Scheme 4).^{121,122} Although pincer complexes exhibit better stability relative to organometallic complexes containing mono- and bi-dentate ligands, the examples provided here illustrate that reactive intermediates in catalytic steps can still suffer from deactivation pathways. Hence, developing methods that protect these reactive intermediates from undergoing deactivation during catalysis could significantly boost their activity and utility.



Scheme 4. Dimerization of PCP-MH(cod) (M = Ru, Os) pincer complexes

Heterogenization of pincer complexes on solid surfaces has been shown to be a viable approach to increase stability and recyclability while maintaining high activity and selectivity.^{9,123,124} Challenging organic transformations are also often catalyzed by scarce transition metals such as Pd, Pt, Ru, Rh, Ir, making catalyst recyclability essential for sustainable utilization of these metals. PCP-Ir and POCOP-Ir pincer complexes supported on silica, γ -alumina, and Merrifield resin have been shown to benefit from catalyst recyclability while providing comparable catalytic activity to homogeneous analogues.¹²³ Huang and coworkers have also reported a significant improvement in catalytic formic acid dehydrogenation activity for PNNNP-Ru pincer complexes bound to a porous organic polymer.¹²⁴ With their well-defined structures and tunable properties, MOFs offer a unique platform to isolate and protect active sites from deactivation processes such as dimerization or decomposition. Moreover, immobilization of catalytically active species in MOFs may impart new modes of reactivity or selectivity owing to the confined pore environment.^{49,85} Although the chemistry of pincer complexes has rapidly developed for homogeneous catalysis, there are relatively few reports of MOFs containing pincer complexes.^{55,82–87,125–128} Humphrey and coworkers reported a Co MOF assembled from PCP-Pd pincer metallolinkers that is selective for adsorption of CO₂ over CO (Figure 6a).¹²⁷

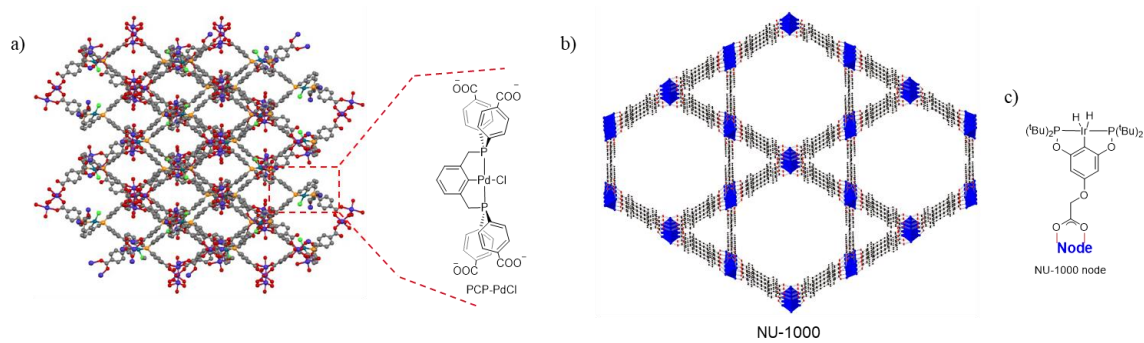


Figure 6. a) A Co MOF assembled from PCP-PdCl metallolinkers¹²⁷ b) Framework structure of NU-1000 c) POCOP-IrH₂ complex immobilized on NU-1000 node⁸⁴

In addition, Hupp and coworkers showed that POCOP-IrH₂ pincer complexes immobilized in NU-1000 via solvent assisted ligand incorporation onto Zr₆ SBUs resulted in a material that catalyzes gas-phase hydrogenation of ethene to ethane (Figure 6b).⁸⁴ Recently, Byers and coworkers reported the encapsulation of PNP-Ru(CO)HCl pincer complexes in UiO-66 (UiO = University of Oslo) via an aperture opening process that involves linker dissociation and association mechanisms in protic solvents (Figure 7).⁵⁵

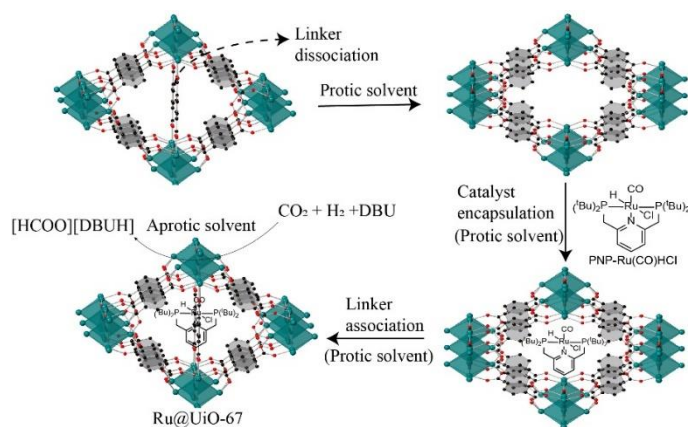


Figure 7. PNP-Ru(CO)HCl encapsulation in UiO-66 and CO₂ hydrogenation with Ru@UiO-66.⁵⁵

The resulting material, Ru@UiO-66, was an effective and recyclable catalyst for CO₂

hydrogenation in aprotic solvents. On the other hand, the homogeneous complex showed a significant decline in activity in recycling experiments owing to bimolecular decomposition processes. Interestingly, catalytic studies in the presence of thiol poisons showed that Ru@UiO-66 was more resistant to thiol poisoning than the homogeneous complex. This example illustrates how MOFs can serve as protecting groups to prevent reactive catalysts from deactivation by exogenous species.

Chapters 2 and 3 of this thesis describe the synthesis, characterization and catalytic study of Zr MOFs constructed from POCOP-Pd pincer metallolinkers. Chapter 2 discusses postsynthetic oxidative ligand exchange reactions at Pd sites using $\text{PhI}(\text{TFA})_2$ ($\text{TFA} = \text{CF}_3\text{CO}_2^-$) to generate a recyclable MOF catalyst for transfer hydrogenation of aldehydes. Chapter 3 illustrates an alternative precatalyst activation approach using NOBF_4 to produce a MOF catalyst that demonstrates broad scope catalytic activity for transfer hydrogenation of unsaturated organic substrates, alkyne hydration and intramolecular alkyne hydroarylation. The catalytic activity of these MOFs has been compared with homogeneous analogues to identify the effects of catalyst immobilization.

Chapter 4 describes the assembly and reactivity of a Zr MOF containing PNNNP- Co^{III} pincer complexes. Postsynthetic metal exchange (PSME) reactions at the PNNNP- Co^{III} pincer sites both in the MOF and homogeneous complex analogue are discussed. The reduction of Co^{III} to Co^{II} under mild reducing conditions allowed substitution of Co by Rh and Pt to generate MOFs containing PNNNP-M (Rh, Pt) pincer complexes. In addition, the chapter provides experimental details that support the proposed mechanism of the metal exchange reactions.

Chapter 5 describes the synthesis, characterization and reactivity of three isostructural Zr MOFs assembled from PNNNP-Ru pincer metallolinkers bearing different combinations of ancillary ligands. Reactivity differences observed among these isostructural MOFs are discussed. A series of postsynthetic precatalyst activation procedures involving deprotonation/dearomatization and removal of carbonyl ligands were used to generate an active and recyclable MOF catalyst for hydrosilylation of aryl aldehydes with triethylsilane.

Chapter 2: Synthesis, characterization and reactivity of Zr MOFs assembled from POCOP-Pd metallolinkers

Portions of this chapter have been described in *J. Am. Chem. Soc.* **2016**, 138, 1780-1783.

Contribution: I carried out the catalytic and reactivity studies presented in this chapter and contributed to the ICP-OES, TEM and solid-state NMR characterization.

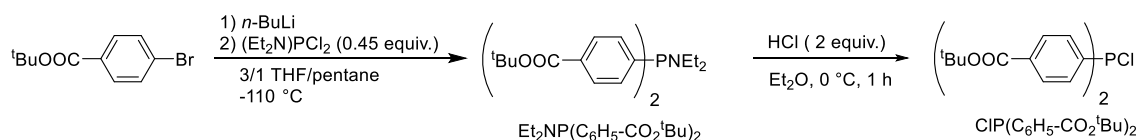
2.1 Introduction

As described in Chapter 1, diphosphine pincer ligands have been widely used in homogeneous catalysis owing to their rigid coordination, tunability, and stability.^{92,111,129–133} They support a wide range of transition metals, allowing access to different modes of reactivity by varying metal identity. In particular, Pd diphosphine pincer complexes have been shown to catalyze a number transformations including C–C cross coupling,^{134–137} aldol and Michael reactions,^{138–140} allylation of aldehydes, imines and CO₂,^{141–146} and hydrogenation.^{147–149} MOFs assembled from catalytically active Pd diphosphine pincer complexes have the potential to maintain the high activity and selectivity of homogeneous catalysts while providing catalyst stability, easy product separation, and recyclability. However, only a few examples of such materials have been reported.^{85,127,150,151} Our approach to the assembly of MOFs containing diphosphine pincer complexes relies on the synthesis of diphosphine pincer metallolinkers followed by a solvothermal reaction with a metal salt. This approach is appealing owing to the uniformity of catalytic sites and decreased likelihood of catalyst leaching.

This chapter describes the synthesis, characterization and reactivity of Zr MOFs constructed from Pd diphosphinite metallolinkers (POCOP-Pd). Synthetic strategies have been developed to assemble a Zr MOF, **2-PdX** (X = Cl, I), from H₄(1-PdI) metallolinkers under solvothermal conditions (Scheme 7). Initial catalytic studies revealed that **2-PdX** is an ineffective catalyst for transfer hydrogenation of benzaldehyde. The low catalytic activity of **2-PdX** is attributed to strongly bound I⁻ ligands at the Pd centers. Consequently, exchanging the I⁻ ligands for more weakly coordinating anions is expected to increase

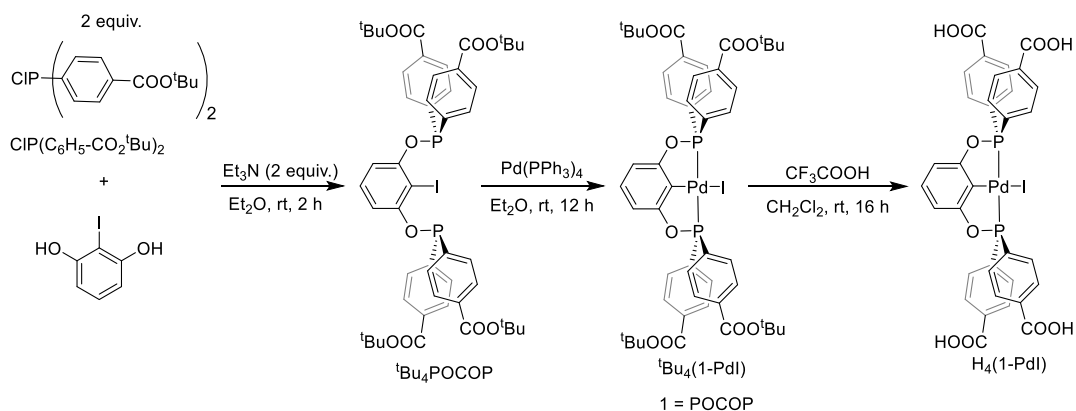
catalytic activity. Indeed, **2-PdTFA**, prepared from reaction of **2-PdX** with $\text{PhI}(\text{TFA})_2$ ($\text{TFA} = \text{CF}_3\text{COO}$) via oxidative $\text{I}^-/\text{CF}_3\text{COO}^-$ ligand exchange, proved to be an effective and recyclable catalyst for transfer hydrogenation of both aryl and aliphatic aldehydes. On the other hand, the homogeneous analogue **^tBu₄(1-PdTFA)** suffered from decomposition under the catalytic conditions and exhibited poor activity demonstrating the benefits of immobilizing active species in MOFs.

2.2 Synthesis and characterization of POCOP-Pd pincer complexes



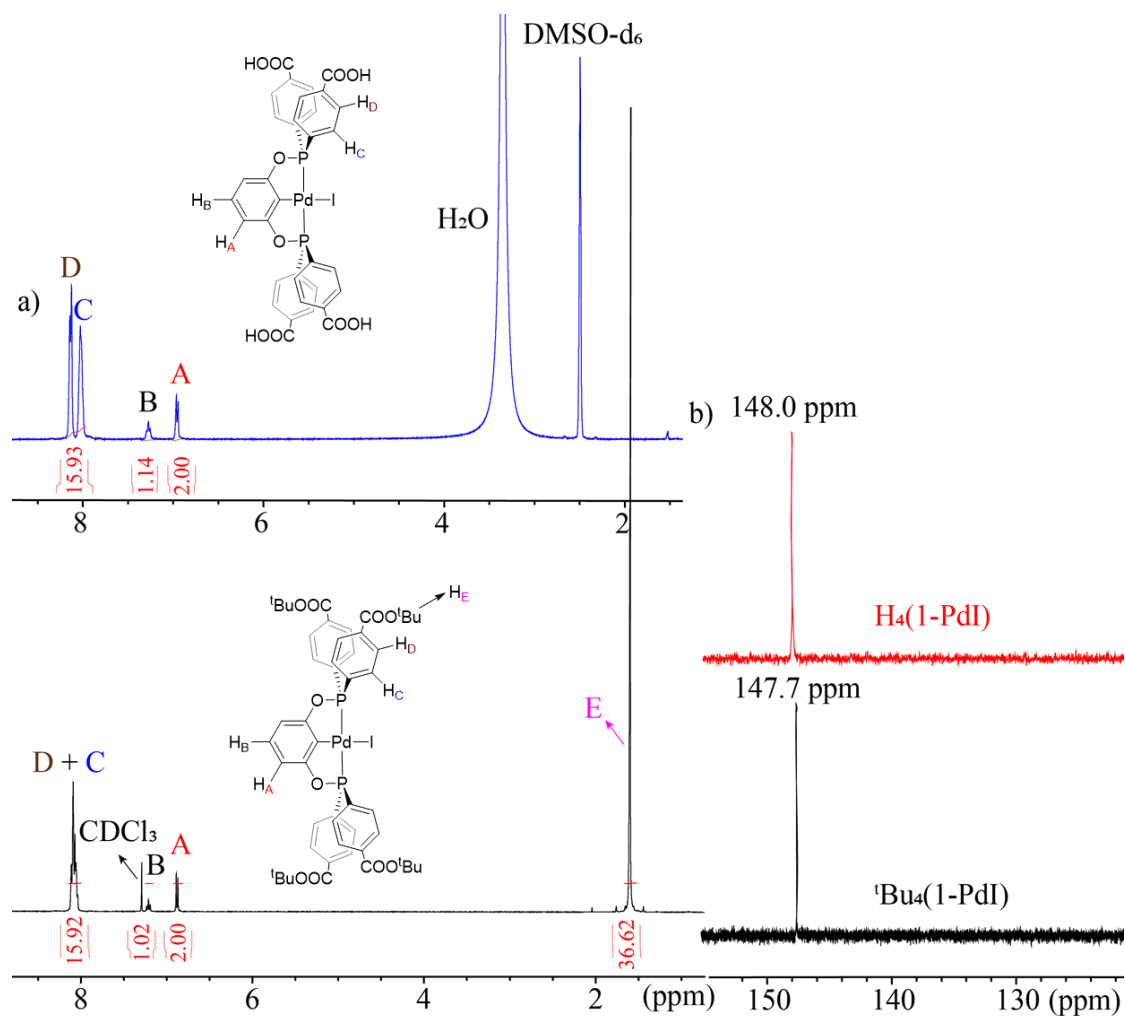
Scheme 5. Synthesis of ligand precursors

Precursors to the POCOP-Pd pincer complexes were prepared following reported procedures with slight modification.¹⁵⁰ Reaction of tert-butyl-4-bromobenzoate with ⁿBuLi followed by $\text{Et}_2\text{N}(\text{P})\text{Cl}_2$ at $-110\text{ }^\circ\text{C}$ produced $\text{Et}_2\text{NP}(\text{C}_6\text{H}_5\text{-CO}_2\text{tBu})_2$ as a white solid in 70 % yield (Scheme 5). The fate of this reaction is highly dependent on reaction temperature and quality of ⁿBuLi. The desired temperature, $-110\text{ }^\circ\text{C}$, must be carefully maintained using an ethanol/liquid N_2 bath prepared from absolute ethanol. $\text{ClP}(\text{C}_6\text{H}_5\text{-CO}_2\text{tBu})_2$ has been prepared from reaction of $\text{Et}_2\text{NP}(\text{C}_6\text{H}_5\text{-CO}_2\text{tBu})_2$ with $\text{HCl}/\text{Et}_2\text{O}$ as shown in Scheme 5.

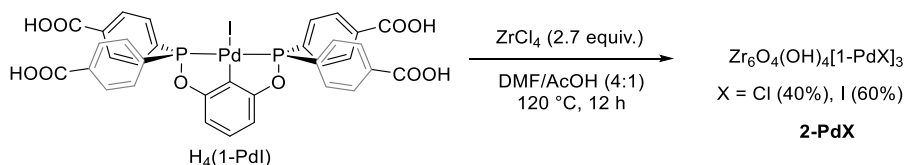


Scheme 6. Synthesis of POCOP-PdI pincer complexes

The ${}^t\text{Bu}_4\text{POCOP}$ pincer ligand was synthesized from reaction of $\text{CIP}(\text{C}_6\text{H}_5\text{-CO}_2{}^t\text{Bu})_2$ with 2-iodoresorcinol in the presence of triethylamine (Et_3N). In situ ${}^{31}\text{P}$ NMR is used to confirm formation of the ${}^t\text{Bu}_4\text{POCOP}$ ligand ($\delta = 110$ ppm). Without further purification, a diethyl ether (Et_2O) solution of ${}^t\text{Bu}_4\text{POCOP}$ was treated with $\text{Pd}(\text{PPh}_3)_4$ to generate ${}^t\text{Bu}_4(1\text{-PdI})$ ($1 = \text{POCOP}$) as a bright yellow powder in 70 % yield (Scheme 6). The ${}^{31}\text{P}$ NMR spectrum of ${}^t\text{Bu}_4(1\text{-PdI})$ shows a single resonance at 147.7 ppm, consistent with pincer ligand chelation to Pd (Figure 8b). The ${}^1\text{H}$ NMR spectrum shows all the expected resonances for ${}^t\text{Bu}_4(1\text{-PdI})$ (Figure 8a). Subsequent, deprotection of the tert-butyl ester groups from ${}^t\text{Bu}_4(1\text{-PdI})$ using $\text{CF}_3\text{CO}_2\text{H}/\text{CH}_2\text{Cl}_2$ furnished the target metallolinker $\text{H}_4(1\text{-PdI})$ as a bright yellow powder in 94 % yield. The structure of $\text{H}_4(1\text{-PdI})$ was established by ${}^1\text{H}$ and ${}^{31}\text{P}$ NMR spectroscopy analysis as well as elemental analysis (Figure 8).



2.3 Synthesis and characterization of 2-PdX



Scheme 7. Synthesis of 2-PdX

A mixture of $\text{H}_4(1\text{-PdI})$ and ZrCl_4 in 4/1 (v/v) DMF/AcOH was sealed in a 20 mL vial and heated at 120 °C for 12 h resulting in formation of **2-PdX** as an off-white microcrystalline powder (Scheme 7). The structure of **2-PdX** has been determined from synchrotron powder X-ray diffraction (SPXRD) data (Figure 9a). Indexing provided a cubic unit cell ($a = 16.724 \text{ \AA}$) with $Pm\text{-}3$ as the most likely space group (Figure 9b). The structural model of **2-PdX** shows $[\text{Zr}_6\text{O}_4(\text{OH})_4]^{12+}$ octahedra connected by $[1\text{-PdX}]^{4-}$ linkers that span each face of the cubic unit cell, generating ovoidal pores $\sim 16 \text{ \AA} \times 10 \text{ \AA}$ in diameter. Moreover, in the $Pm\text{-}3$ space group, the $[1\text{-PdX}]^{4-}$ linkers are four-fold disordered as a consequence of the crystallographic mirror plane normal to the a-axis and the C_{2v} molecular symmetry of the linker which gives rise to non-crystallographic rotational disorder.

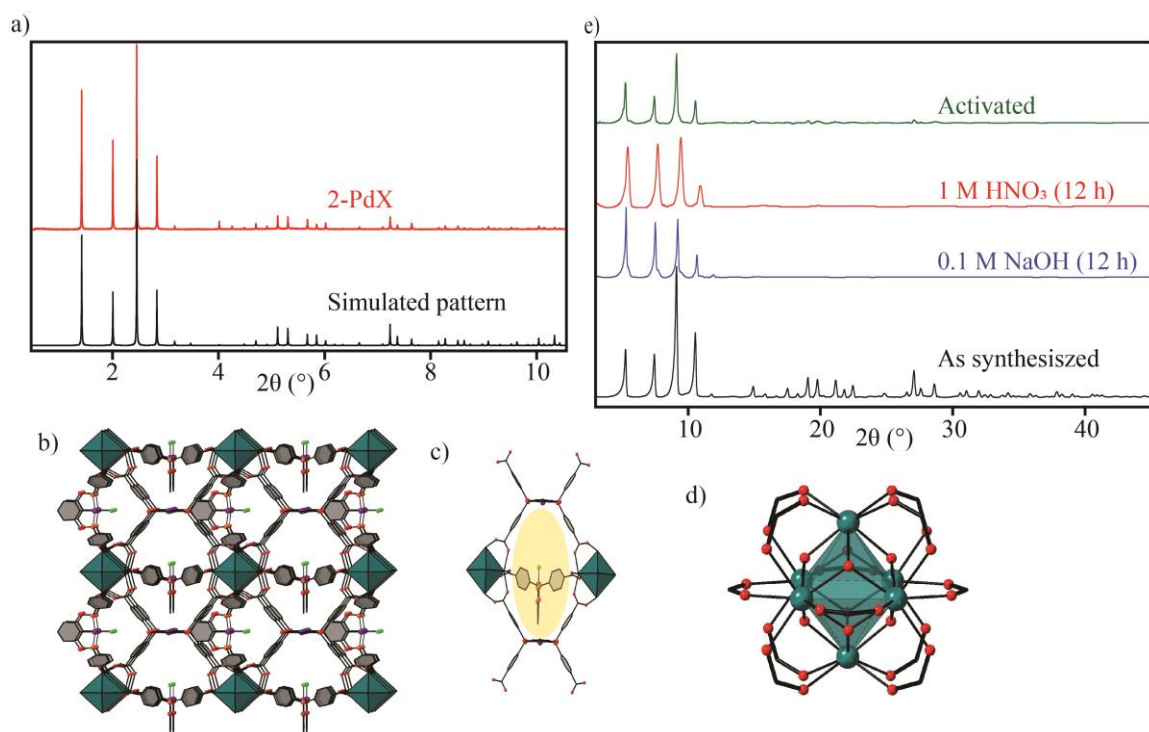


Figure 9. a) Experimental and simulated SPXRD patterns of **2-PdX** (synchrotron radiation, $\lambda = 0.413959 \text{ \AA}$). b) Framework structure of **2-PdX**. Linker disorder has been omitted for clarity. c) View of a portion of the framework showing ovoidal pores. d) Hexanuclear Zr clusters ($[\text{Zr}_6\text{O}_4(\text{OH})_4](\text{CO}_2)_{12}$). e) PXRD patterns (Cu-K α radiation, $\lambda = 1.5418 \text{ \AA}$) for samples of **2-PdX** that are “as synthesized”, soaked in 0.1 M NaOH and 1 M HNO₃, and activated by heating under vacuum.

Similar to other Zr-based MOFs, **2-PdX** displays exceptional chemical stability.^{152–154} The material is stable for weeks under ambient conditions and retains crystallinity upon exposure to strong acid (1 M HNO₃) and base (0.1 M NaOH) (Figure 9e). In line with the predicted porous structure of **2-PdX**, thermogravimetric analysis (TGA) shows ~25 wt. % mass loss at 250 °C arising from occluded solvent (Figure 10a). A sample of **2-PdX** was activated by heating in vacuum (10^{-4} torr) at 150 °C for 12 h, and an apparent Brunauer-Emmett-Teller (BET) surface area of $1164 \text{ m}^2 \text{ g}^{-1}$ was calculated from a N₂ adsorption isotherm measured at 77 K (Figure 10b). Elemental analysis of an activated sample of **2-**

PdX revealed the presence of a significant amount of Cl (1 wt. %) and a lower than expected I content (6.5 wt. % versus 15 wt. %) based on the presence of $[1\text{-PdI}]^{4-}$ linkers.

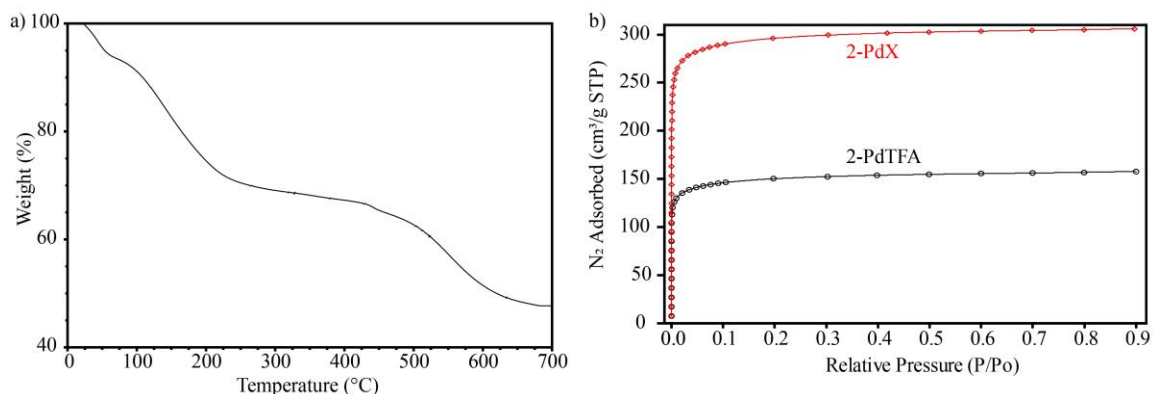


Figure 10. a) TGA data for a sample of **2-PdX** measured at a ramp rate of 5 °C/min under flowing N₂ (50 mL/min). b) N₂ adsorption isotherms measured at 77 K for samples of **2-PdX** and **2-PdTFA** after desolvation at 100 °C and 10⁻⁴ torr.

Thus, the use of ZrCl₄ in the solvothermal synthesis appears to result in partial ligand exchange at Pd and a halide occupancy of ~60% I and ~40% Cl. Attempts to circumvent halide disorder by using a Cl-exchanged linker H₄(1-PdCl) were unsuccessful as no crystalline products could be obtained. The solid-state ³¹P NMR spectrum of **2-PdX** shows a major resonance (96%) centered at 150 ppm, which is close to that observed for H₄(1-PdI) (148 ppm) in DMSO-*d*₆ solution (Figure 11a). The ~40% Cl occupancy in **2-PdX** is corroborated by the asymmetry of the main resonance which suggests overlap of two signals with similar chemical shift. Furthermore, the ³¹P NMR spectrum of an acid-digested sample of **2-PdX** shows the presence of both Pd-Cl and Pd-I species (Figure 11b). The solid-state ³¹P spectrum of **2-PdX** also shows the presence of an unidentified species giving rise to a small resonance (4%) centered at 93 ppm.

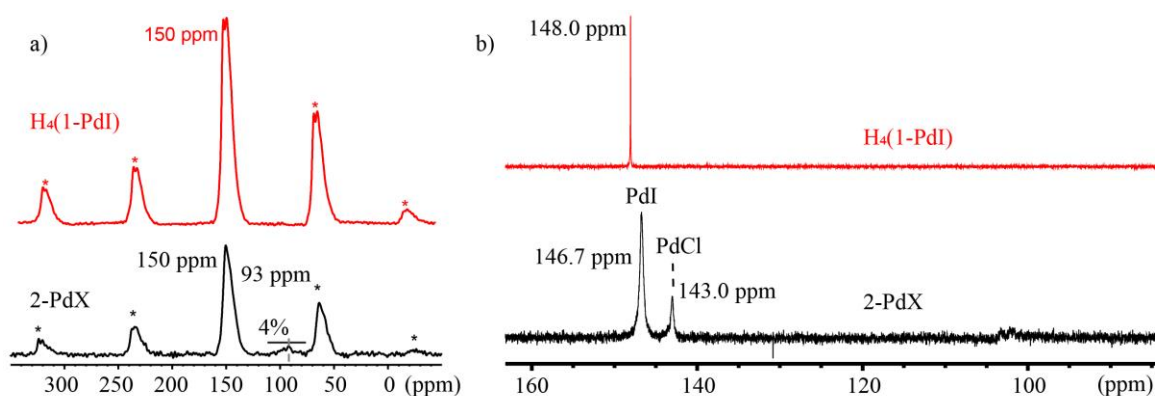
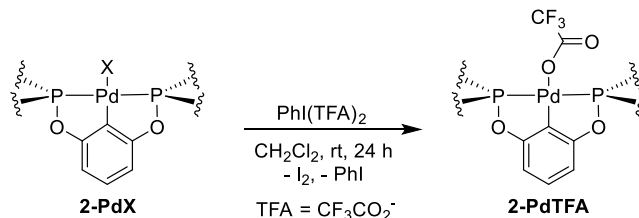


Figure 11. a) Solid-state ^{31}P NMR spectra of **2-PdX** and $\text{H}_4(1\text{-PdI})$. Asterisks (*) are used to denote spinning side bands. b) $^{31}\text{P}\{^1\text{H}\}$ NMR spectra of $\text{H}_4(1\text{-PdI})$ (DMSO-d_6) and **2-PdX** ($\text{CF}_3\text{COOH}/\text{C}_6\text{D}_6$).

2.4. Catalytic activity of **2-PdX**

Catalytic transfer hydrogenation of organic substrates with sacrificial hydrogen donors such as alcohols or formic acid is a mild and convenient alternative to direct hydrogenation with H_2 .¹⁵⁵ Pd diphosphine pincer complexes have been shown to catalyze chemoselective transfer hydrogenation of α,β -unsaturated ketones using *n*-butanol as a hydrogen source.^{147,149} Consequently, we decided to investigate the activity and recyclability of **2-PdX** as a catalyst for transfer hydrogenation. Given the chemical stability of **2-PdX**, transfer hydrogenation reactions were tested in aqueous solvent mixtures with formic acid as the hydrogen source. Unfortunately, initial catalyst screening with benzaldehyde as substrate afforded low yields (< 20%) of benzyl alcohol (Table 1, entry 1). We considered that the presence of strongly bound I^- ligands might hinder reactivity at the Pd sites of **2-PdX** and sought to exchange the halide for a more weakly coordinating anion.

2.5 Postsynthetic ligand exchange at Pd



Scheme 8. Oxidative $\text{I}^- / \text{TFA}^-$ ligand exchange at Pd sites to generate **2-PdTFA**

The use of common halide abstraction reagents such as Ag^+ or Tl^+ salts is complicated by co-precipitation of the byproducts with the MOF. Based on soft/hard acid/base concepts, I^- ligands coordinate to Pd stronger than Cl^- ligands, and should lead to lower catalytic activity. In addition, both spectroscopic and elemental analysis data indicate that 1-PdI as the major metallolinker component in **2-PdX**. Therefore, we required a reagent that would facilitate I^- ligand exchange at Pd sites and generate fully soluble byproducts that can be removed by simple filtration. Consequently, when a suspension of **2-PdX** in CH_2Cl_2 was treated with PhI(TFA)_2 , the supernatant solution gradually turned red-purple over the course of 12 h, signaling the formation of I_2 and I^- ligand replacement with TFA^- (Scheme 8). After washing with CH_2Cl_2 , the PXRD pattern of the resulting solid **2-PdTFA** was largely unchanged from that of the starting material (Figure 12a). Elemental analysis of **2-PdTFA** showed the presence of I, Cl, and F. Based on the observed relative ratios of these halides, the ligand occupancy at the Pd sites is estimated to be 0.17 I^- , 0.39 Cl^- , and 0.44 CF_3COO^- , suggesting that $\text{I}^- / \text{TFA}^-$ ligand exchange proceeds in ~ 72 % yield and ligand substitution does not occur at the Pd–Cl sites. The solid-state ^{13}C NMR spectrum of **2-PdTFA** displays a partially resolved quartet at 116.6 ppm ($-\text{CF}_3$, $J_{\text{C-F}} \approx 280$ Hz) as well as a new resonance at 163 ppm assigned to the carbonyl group of TFA (Figure 13).

The solid-state ^{31}P NMR spectrum shows an upfield shift of the major resonance to 142 ppm, consistent with that observed upon I^-/TFA^- ligand exchange of the homogeneous complex (144.4 ppm) in CDCl_3 solution (Figure 12b & Figure 14b).

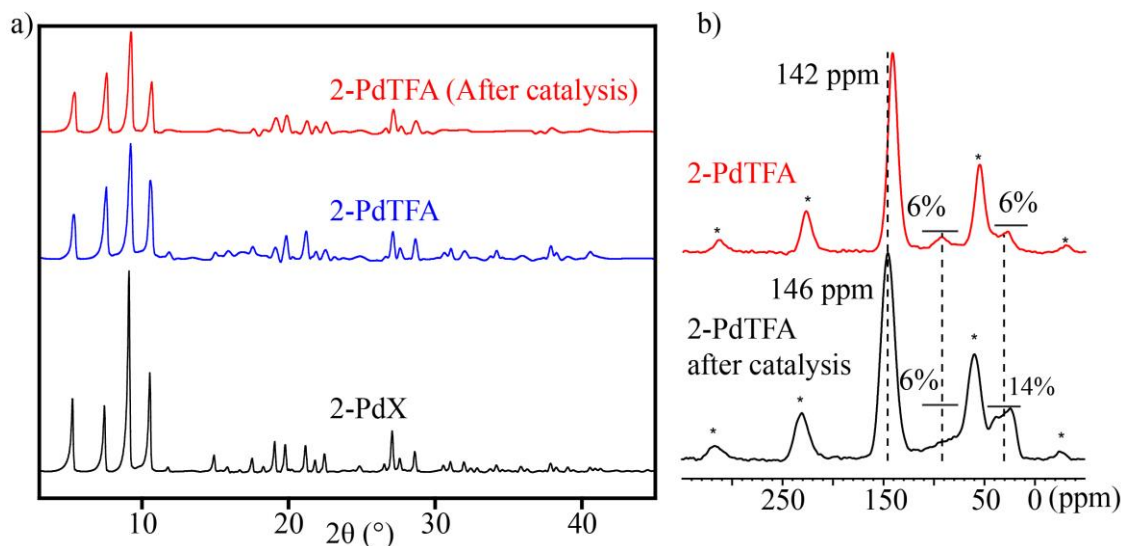


Figure 12. a) PXRD patterns (Cu-K α radiation, $\lambda = 1.5418 \text{ \AA}$) for samples of **2-PdX** and **2-PdTFA** before and after catalysis. b) Solid-state ^{31}P NMR spectra of **2-PdTFA** before and after catalysis. Asterisks (*) are used to denote spinning side bands.

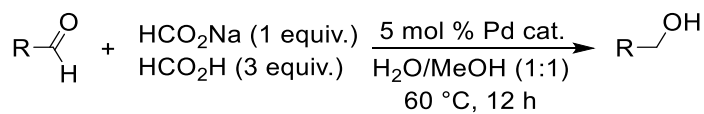
The spectrum also shows the appearance of a small signal around 30 ppm. This chemical shift is close to that observed for diaryl phosphinate esters ($\text{Ar}_2\text{P}(\text{O})\text{OR}$), suggesting a small amount of phosphine oxidation during the halide exchange reaction.^{156,157} A N_2 adsorption isotherm measured for **2-PdTFA** after activation (100 $^\circ\text{C}$, 10^{-4} torr, 12 h) provided a BET surface area of $594 \text{ m}^2 \text{ g}^{-1}$ (Figure 10b). The observed decrease in N_2 -accessible surface area is consistent with exchange of I^- for larger trifluoroacetate anions.

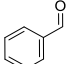
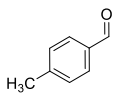
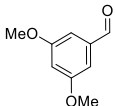
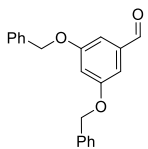
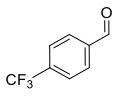
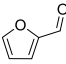
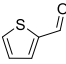
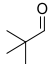
2.6 Catalytic study of 2-PdTFA

2-PdTFA proved to be a more active transfer hydrogenation catalyst than **2-PdX**.

Using catalyst loadings of 5 mol % based on Pd with benzaldehyde as the substrate and 3/1

HCO₂H/HCO₂Na as the hydrogen source, 19% and 100% conversion to benzyl alcohol was observed with **2-PdX** and **2-PdTFA**, respectively (Table 1, entries 1 and 2). UiO-67 was also tested as a catalyst (Table 1, entry 3), and no conversion of benzaldehyde to benzyl alcohol was observed under similar catalytic conditions. This result indicates that the Zr₆O₄(OH)₄(COO)₁₂ SBUs are not responsible for catalysis observed in **2-PdX** and **2-PdTFA**. **2-PdTFA** exhibits good catalytic activity for transfer hydrogenation of a range of aromatic and aliphatic aldehydes (Table 1, entries 8-14). However, decreased conversion was observed for substrates with strongly coordinating heteroatoms. The catalytic activity of **2-PdTFA** is not significantly inhibited by the presence of Hg⁰ (Table 1, entry 4), suggesting that catalysis is likely not due to the presence of Pd nanoparticles.¹⁵⁸ Similarly, a hot filtration test showed no indication of catalysis by leached homogeneous species. These observations, along with the increased catalytic activity of **2-PdTFA** versus **2-PdX**, support the immobilized pincer Pd centers as the active sites for catalysis. Moreover, when 3,5-dimethoxybenzaldehyde (Table 1, entry 9) and 3,5-dibenzyloxybenzaldehyde (Table 1, entry 10) were used as substrates with **2-PdTFA** as the catalyst, 100% and 27% conversion to the corresponding benzylic alcohols was observed respectively. The significant decrease in conversion for the large substrate is consistent with hindered access to active Pd sites within the MOF, indicating that catalysis does not occur exclusively at surface sites. PXRD analysis of the MOF recovered after catalysis did not show a significant loss of crystallinity (Figure 12a).

Table 1. Catalytic transfer hydrogenation of aldehydes

Entry	Substrate	Catalyst	% Conv. ^{b/c}	% Yield ^c
1		2-PdX	19	16
2		2-PdTFA	100	84
3		UiO-67	0	0
4		2-PdTFA + Hg ⁰	95	76
5		2-PdTFA (run 2)	96	78
6		2-PdTFA (run 3)	56	47
7		^t Bu ₄ (1-PdTFA)	6	< 5
8		2-PdTFA	100	86
9		2-PdTFA	100	89
10		2-PdTFA	27	22
11		2-PdTFA	100	73
12		2-PdTFA	100	75
13		2-PdTFA	71	48
14		2-PdTFA	97	64

^aReaction conditions: substrate (0.2 mmol), catalyst (0.01 mmol), sodium formate (0.2 mmol), formic acid (0.6 mmol) in 1:1 H₂O/MeOH (2 mL), 12 h, 60 °C. ^bBased on conversion to benzylic alcohol. ^cDetermined by ¹H NMR with internal standard (1,3,5-trimethoxybenzene) after work up.

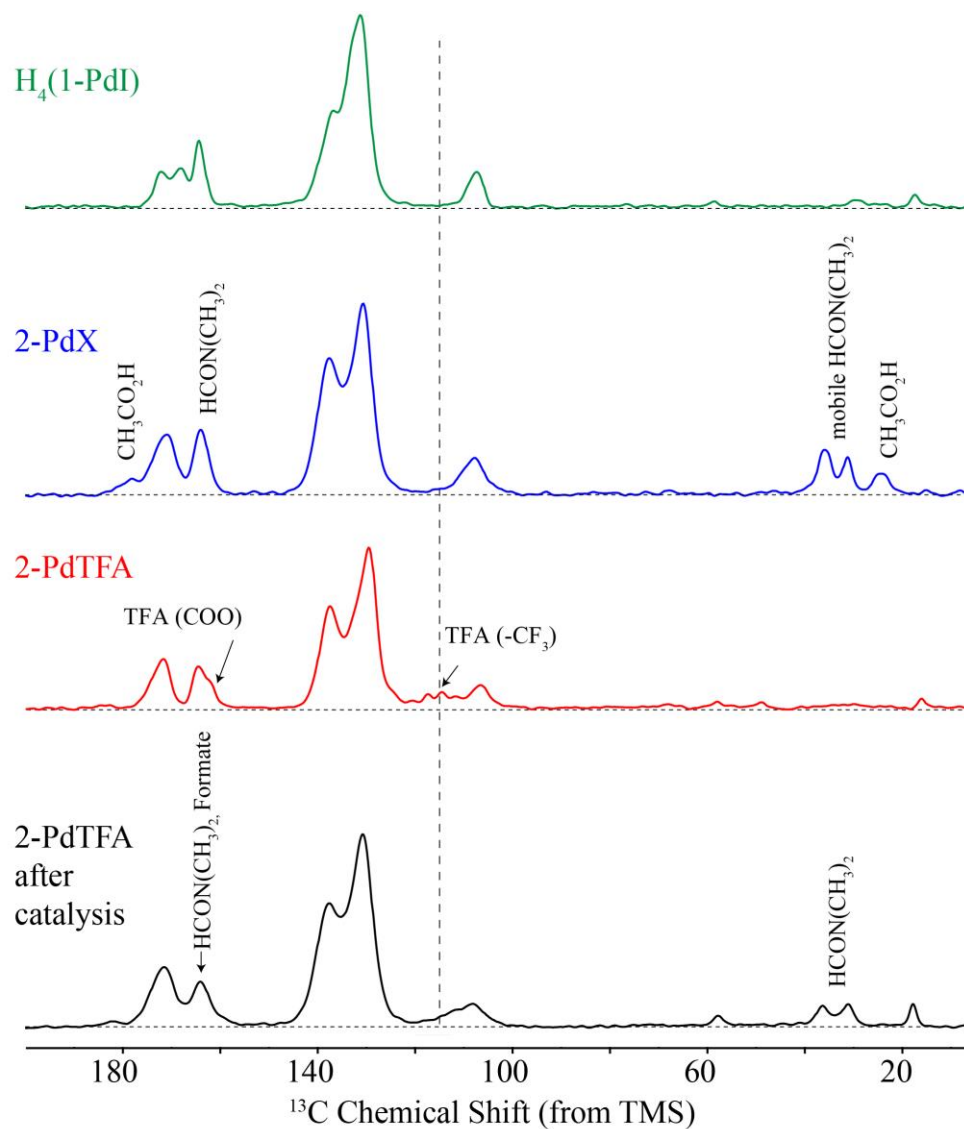
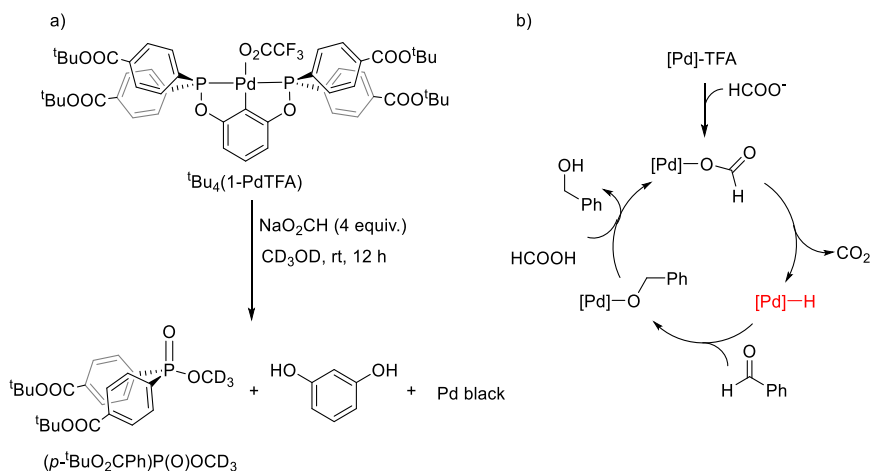


Figure 13. Solid-state ^{13}C NMR spectra of $\text{H}_4(1\text{-PdI})$, 2-PdX , and 2-PdTFA before and after catalysis.

The disappearance of the TFA resonances in the solid-state ^{13}C NMR spectrum support $\text{TFA}^-/\text{HCO}_2^-$ exchange during catalysis (Figure 13). The solid-state ^{31}P NMR spectrum also shows a slight downfield shift of the major resonance corresponding to the immobilized POCOP-Pd complex to 146 ppm (Figure 12b). However, an increase in the signal near 30 ppm indicates additional decomposition of the pincer complex during catalysis.

Consequently, the catalyst could only be recycled once without a drop in product yield (Table 1, entries 5 and 6).

To examine the effect of catalyst immobilization in a MOF on catalyst activity and stability, the catalytic activity of **2-PdTFA** was compared with a homogeneous analogue, ${}^t\text{Bu}_4(1\text{-PdTFA})$. Surprisingly, ${}^t\text{Bu}_4(1\text{-PdTFA})$ gave low conversion of benzaldehyde to benzyl alcohol (< 5 % yield) under the optimized conditions (Table 1, entry 7). Furthermore, a color change of the reaction mixture from pale yellow to dark brown was observed during the course of the reaction. In order to gain insight into the fate of the catalyst, the reaction of ${}^t\text{Bu}_4(1\text{-PdTFA})$ with 4 equiv. of HCO_2Na in CD_3OD was monitored by ${}^{31}\text{P}$ NMR spectroscopy (Scheme 9a)



Scheme 9. a) Reaction of ${}^t\text{Bu}_4(1\text{-PdTFA})$ with NaO_2CH resulting in decomposition of the pincer complex. b) Proposed mechanism for transfer hydrogenation of aldehydes with **2-PdTFA**.

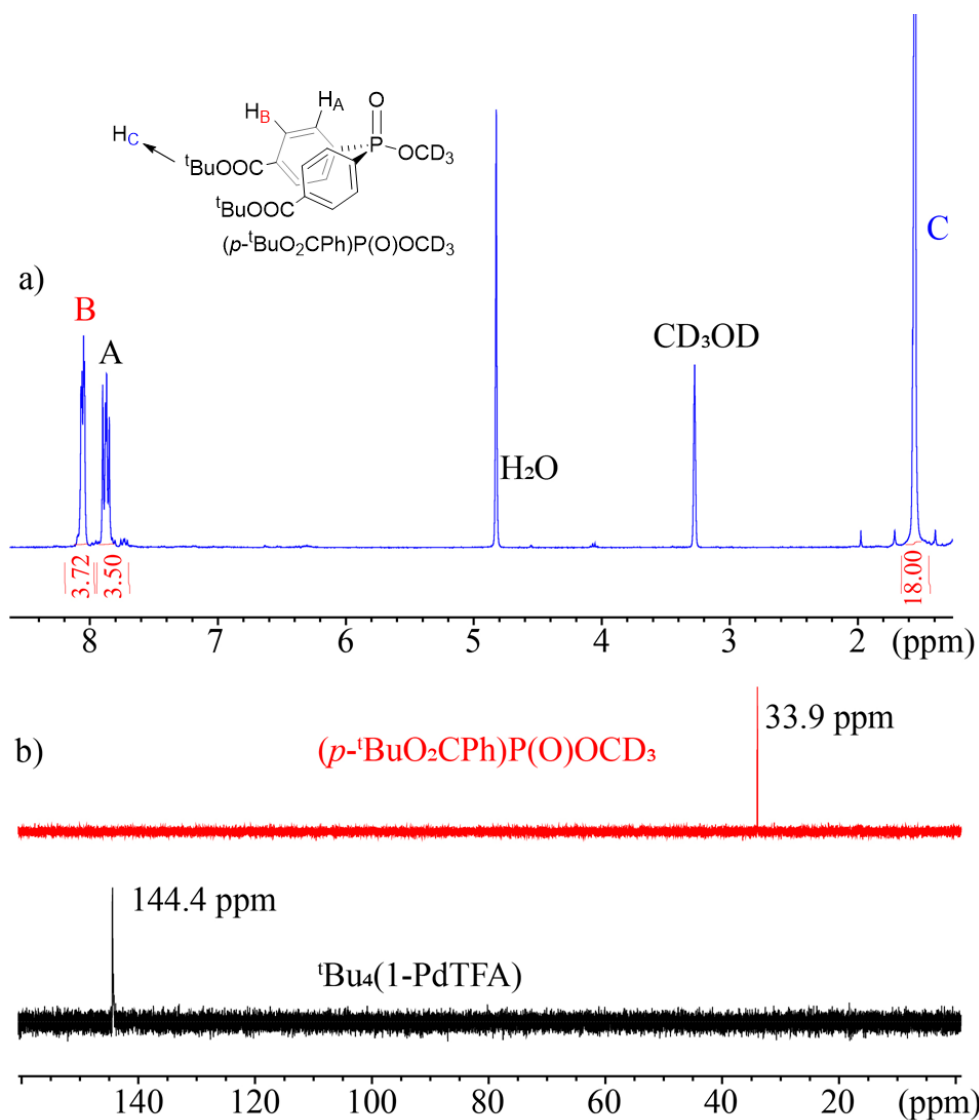


Figure 14. a) ^1H NMR spectrum (CD_3OD) of $(p\text{-}^t\text{BuO}_2\text{CPh})\text{P}(\text{O})\text{OCD}_3$. b) ^{31}P { ^1H } NMR spectra for $(p\text{-}^t\text{BuO}_2\text{CPh})\text{P}(\text{O})\text{OCD}_3$ (CD_3OD) and $^t\text{Bu}_4(1\text{-PdTFA})$ (CDCl_3)

Similar to the catalytic reaction, the solution darkened over time, and after 12 h, the ^{31}P NMR signal corresponding to $^t\text{Bu}_4(1\text{-PdTFA})$ (144 ppm) was completely replaced by a new resonance at 33.9 ppm (Figure 14b). ^1H NMR and ESI-MS analysis identified the major phosphorus-containing species as $(p\text{-}^t\text{BuO}_2\text{CPh})_2\text{P}(\text{O})\text{OCD}_3$ ($m/z= 436.19$) (Figure 14a). These results suggest that $^t\text{Bu}_4(1\text{-PdTFA})$ decomposes under the catalytic conditions to

generate catalytically inactive Pd species. The observed transfer hydrogenation of aldehydes by MOF-immobilized POCOP-PdTFA catalyst is proposed to involve formation of reactive Pd-H species, which could be susceptible to bimolecular deactivation processes under the catalytic conditions (Scheme 9b). Notably, others have reported difficulty isolating and characterizing monomeric diphosphine pincer complexes containing Pd-H species.^{148,159–162} Thus, it seems likely that the rigid immobilization of the POCOP-Pd complexes in **2-PdTFA** improves catalyst lifetime and activity by protecting reactive intermediates from deleterious deactivation pathways.

2.7 Conclusions

A crystalline, porous Zr MOF was synthesized from H₄(1-PdI) metallolinkers under solvothermal reactions. The structure and composition of **2-PdX** was elucidated using SPXRD, solution- and solid-state multinuclear NMR spectroscopy, elemental analysis and ICP-OES analytical methods. Encouraged by the porosity, thermal and chemical stability of **2-PdX**, we investigated its use for catalysis. However, **2-PdX** was found to be incompetent catalyst for transfer hydrogenation of benzaldehyde and its poor activity was postulated to be due to strongly coordinating I⁻ ligands at Pd sites. Indeed, **2-PdTFA** generated from a reaction of **2-PdX** with PhI(TFA)₂ via oxidative I⁻/TFA⁻ ligand exchange at Pd sites proved to be an effective and recyclable catalyst for both aromatic and aliphatic aldehydes. Experiments such as a mercury drop test, catalytic control reactions with UiO-67, and hot filtration test all support catalysis occurring at MOF-immobilized Pd sites. On the other hand, the homogeneous complex ^tBu₄(1-PdTFA) showed no catalytic activity under the optimized reaction conditions. The reaction of ^tBu₄(1-PdTFA) with

stoichiometric HCO_2Na revealed decomposition of the complex, highlighting the importance of catalyst immobilization in rigid MOF scaffold to increase catalyst stability and activity.

2.8 Experimental

Materials and General Considerations. *tert*-butyl-4-bromobenzoate,¹⁶³ $(\text{Et}_2\text{N})\text{PCl}_2$,¹⁶⁴ 2-iodoresorcinol,¹⁶⁵ $\text{Pd}(\text{PPh}_3)_4$,¹⁶⁶ $\text{PhI}(\text{TFA})_2$,¹⁶⁷ and UiO-67¹⁷ were synthesized following literature procedures. ZrCl_4 (Sigma Aldrich), *N,N*-dimethylformamide (DMF, 99.9%, EMD), and glacial acetic acid (Macron) used for synthetic preparations were used as received unless otherwise noted. All other solvents and reagents were purchased from commercial suppliers and used as received. Routine powder X-ray diffraction patterns for phase identification were collected on a Rigaku Miniflex 600 diffractometer using Nickel-filtered $\text{Cu-K}\alpha$ radiation ($\lambda = 1.5418 \text{ \AA}$). High-resolution synchrotron powder diffraction data (SPXRD) were collected at 295 K using beamline 11-BM at the Advanced Photon Source (APS, Argonne National Laboratory, Argonne, IL) using an average wavelength of 0.413959 \AA . ATR-IR spectra were measured using a Nicolet IR 200 with a diamond source. Inductively coupled plasma atomic emission spectroscopy (ICP-AES) measurements were performed using a Perkin Elmer (Optima 8000) instrument and were calibrated using atomic spectroscopy standards purchased from BDH. Elemental microanalyses were performed by Atlantic Microlab, Norcross, GA. ESI-MS experiments were performed at the University of Illinois Mass Spectrometry Laboratory.

Solution-state NMR spectra were measured using either a Varian Inova or MR 400 MHz spectrometer (101 MHz operating frequency for ^{13}C , 162 MHz operating frequency for ^{31}P ,

and 376 MHz operating frequency for ^{19}F). For ^1H and $^{13}\text{C}\{^1\text{H}\}$ NMR spectra, the solvent resonance was referenced as an internal standard. For $^{31}\text{P}\{^1\text{H}\}$ NMR spectra, 85% H_3PO_4 was used as an external standard (0 ppm). For ^{19}F NMR spectra, 1% CF_3COOH was used as an external standard (-76.55 ppm). Solid-State NMR experiments were performed on a Bruker (Billerica, MA) DSX-400 spectrometer at a resonance frequency of 400 MHz for ^1H and 162 MHz for ^{31}P and 100 MHz for ^{13}C , using magic-angle spinning (MAS) probe in double-resonance mode. Samples were packed into 4 mm rotors with Kel-F 22 μL inserts. Experiments were carried out at a spinning frequency of 14 kHz. Typical ^{31}P and ^1H 90° pulse-lengths were 4 μs and 6 μs , respectively. ^{13}C 90° pulse-lengths were 4.2 μs . ^{31}P [^1H] CP/ MAS spectra were obtained with a recycle delay of 2-4 s and two-pulse phase modulation (TPPM) decoupling. Background-free ^1H spectra were obtained using a subtraction scheme.¹⁶⁸ ^{13}C [^1H] composite-pulse multiCP/ MAS spectra had a recycle delay of 2s, 10 loops of CP, and a 200 ms ^1H magnetization recovery delay between CP periods. The first 9 CP contact-times were 1.1 ms and the last was 0.6 ms, with 83-100% linear-ramps on ^1H . ^{31}P and ^1H spectra were externally referenced to the upfield resonance of calcium hydroxyapatite (National Institute of Standards and Technology) at 2.73 ppm and 0.18 ppm, respectively; this corresponds to the 85% phosphoric acid scale for ^{31}P and to the neat TMS scale for ^1H . ^{13}C spectra were external referenced to the carbonyl of 1- ^{13}C Gly (β crystal form) at 176.49 ppm on the neat TMS scale.

Synthesis of diethylamino bis(tert-butyl 4-benzoyl)phosphine [$\text{Et}_2\text{NP}(\text{C}_6\text{H}_5\text{-CO}_2^t\text{Bu})_2$]. A 500 mL Schlenk flask was charged with tert-butyl-4-bromobenzoate (5.91 g, 23.0 mmol) under an N_2 atmosphere. The oil was dissolved in a mixture of THF (90 mL)

and pentane (30 mL). The reaction vessel was cooled to -110 °C in a liquid N₂ /ethanol bath. ⁿBuLi (10 mL, 2.2 M in hexane) was added dropwise over 20 minutes. The reaction solution changed from colorless to brown upon completion of the addition. The mixture was allowed to stir at -110 °C for 20 minutes. A solution of (NEt₂)PCl₂ (1.78 g, 10.2 mmol) in THF (10 mL) was added dropwise over 10 minutes, keeping the reaction mixture at -110 °C. The reaction solution changed from brown to yellow upon completion of the addition. The reaction was allowed to warm to room temperature and stirred overnight. The solvent was removed in vacuo, and the residue was extracted with pentane (~250 mL) and filtered through Celite. The solvent was removed from the filtrate in vacuo to yield a low-density pale yellow solid. The solid was dissolved in a minimum amount of pentane (~5-10 mL) and transferred to a 20 mL scintillation vial. Upon standing (~5 minutes), an off-white solid began to precipitate. The vial was placed in a freezer (-30 °C) for ~12 h to allow for maximum precipitation. The vial was centrifuged and the supernatant solution was decanted. The remaining solid was dried under vacuum to give Et₂NP(C₆H₅-CO₂^tBu)₂ (3.4 g, 72%). ¹H NMR (400 MHz, CDCl₃) δ 7.95 (d, ³J_{H-H} = 8.1 Hz, 4H, Ar), 7.43 (t, ³J_{H-H} = 7.3 Hz, 4H, Ar), 3.07 (dt, ³J_{C-P} = 16.4, ³J_{H-H} = 7.0 Hz, 4H, CH₂CH₃), 1.59 (s, 18H, ^tBu), 0.95 (t, ³J_{H-H} = 7.0 Hz, 6H, CH₂CH₃). ¹³C{¹H} NMR (101 MHz, CDCl₃) δ 165.70 (s, 2C, CO), 145.28 (d, ¹J_{C-P} = 16.9 Hz, 2C, ipso Ph 1), 131.91 (s, 2C, ipso Ph 4), 131.73 (d, ²J_{C-P} = 19.9 Hz, 4C, Ph), 129.11 (d, ³J_{C-P} = 5.8 Hz, 4C, Ph), 81.21 (s, 2C, C(CH₃)₃), 44.57 (d, ²J_{C-P} = 15.4 Hz, 2C, CH₂CH₃), 28.29 (s, 18C, C(CH₃)₃), 14.58 (d, ³J_{C-P} = 3.0 Hz, CH₂CH₃). ³¹P{¹H} NMR (162 MHz, CDCl₃) δ 60.93 (s, 1P).

Synthesis of chloro *bis*(*tert*-butyl 4-benzoyl)phosphine [CIP(C₆H₅-CO₂^tBu)₂]. HCl in Et₂O (1.0 M, 13.4 mL, 13.4 mmol) was added dropwise to a solution of Et₂NP(C₆H₅-CO₂^tBu)₂ (3.00 g, 6.56 mmol) in Et₂O (~30 mL) at 0 °C. Immediate formation of [Et₂NH₂]Cl was observed, and the reaction was allowed to stir at 0 °C for 1 h. The supernatant solution was separated using a filter cannula, and the solvent was removed in vacuo. The residue was extracted with pentane and filtered through a pad of Celite. The solvent was removed in vacuo to afford a white sticky, low density solid (2.56 g, 93%). ¹H NMR (400 MHz, CDCl₃) δ 7.98 (d, ³J_{H-H} = 8.1 Hz, 4H, Ar 3), 7.58 (t, ³J_{H-H} = 7.7 Hz, 4H, Ar 2), 1.56 (s, 18H, ^tBu). ¹³C{¹H} NMR (101 MHz, CDCl₃) δ 165.05 (s, 2C, CO), 143.29 (d, ¹J_{C-P} = 34.4 Hz, 2C, ipso Ph 1), 133.88 (s, 2C, ipso Ph 4), 131.50 (d, ²J_{C-P} = 24.3 Hz, 4C, Ph), 129.59 (d, ³J_{C-P} = 6.9 Hz, 4C, Ph), 81.68 (s, 2C, C(CH₃)₃), 28.24 (s, 18C, C(CH₃)₃). ³¹P{¹H} NMR (162 MHz, CDCl₃) δ 77.86 (s, 1P).

Synthesis of ^tBu₄(1-PdI). CIP(C₆H₅-CO₂^tBu)₂ (1.52 g, 3.61 mmol) was dissolved in Et₂O (~10 mL). NEt₃ (0.53 mL, 3.8 mmol) was added, and the solution was allowed to stir at room temperature for 10 minutes. A solution of 2-iodoresorcinol (0.405 g, 1.72 mmol) in Et₂O (~5 mL) was added dropwise resulting in precipitation of [HNEt₃]Cl. The reaction mixture was allowed to stir at room temperature for 2 h before filtering through a pad of Celite to remove [HNEt₃]Cl. The resulting solution of the ^tBu₄POCOP ligand was characterized in situ by ³¹P{¹H} NMR spectroscopy (δ = 110 ppm) and used without further purification. The Et₂O solution of ^tBu₄POCOP was added to a suspension of Pd(PPh₃)₄ (1.69 g, 1.46 mmol) in Et₂O (~ 25 mL), and the reaction mixture was stirred overnight at room temperature. The resulting yellow solution was filtered through Celite, and the filtrate

was concentrated on a rotary evaporator. The oily residue was dissolved in minimal CH_2Cl_2 , loaded onto a silica gel chromatography column packed with hexanes, and flash chromatographed using 9:1 hexanes:ethyl acetate as the eluent. The desired product was obtained as a bright yellow low-density solid (1.37 g, 72% yield). Product obtained from fractions that contain PPh_3 as a minor impurity can be recrystallized from MeCN. ^1H NMR (400 MHz, CDCl_3) δ 8.12 – 7.99 (m, 16H, benzoate Ar-H), 7.18 (t, $^3J_{\text{H-H}} = 7.8$ Hz, 1H, resorcinol Ar-H), 6.85 (d, $^3J_{\text{H-H}} = 7.9$ Hz, 2H, resorcinol Ar-H), 1.57 (s, 36H, ^tBu). $^{13}\text{C}\{^1\text{H}\}$ NMR (101 MHz, CDCl_3) δ 164.78 (s, 4C, CO), 163.99 (t, $J_{\text{C-P}} = 7.8$ Hz, Ar), 138.02 (s, Ar), 136.88 (t, $J_{\text{C-P}} = 25.7$ Hz, Ar), 135.47 (s, Ar), 132.19 (t, $J_{\text{C-P}} = 8.1$ Hz, Ar), 129.81 (t, $J_{\text{C-P}} = 5.6$ Hz, Ar), 129.59 (s, Ar), 107.61 (t, $J_{\text{C-P}} = 8.1$ Hz, Ar), 81.97 (s, 4C, $\text{C}(\text{CH}_3)_3$), 28.51 (s, 36C, $\text{C}(\text{CH}_3)_3$). $^{31}\text{P}\{^1\text{H}\}$ NMR (162 MHz, CDCl_3) δ 148.37 (s, 2P). Anal. Calcd. for $\text{C}_{50}\text{H}_{55}\text{IO}_{10}\text{P}_2\text{Pd}$: C, 54.04; H, 4.99. Found: C, 54.24; H, 5.08.

Synthesis of $\text{H}_4(1\text{-PdI})$. Trifluoroacetic acid (1 mL) was added to a solution of $^t\text{Bu}_4(1\text{-PdI})$ (1.03 g, 0.929 mmol) in CH_2Cl_2 (3 mL) resulting in a color change of the solution from yellow to dark purple. The solution was stirred for 12 h at room temperature before removing the solvent using a rotary evaporator. DI water was added resulting in precipitation of a dark yellow solid. The solid was collected by vacuum filtration and washed with DI water (3 x 5 mL) and CHCl_3 (~15 mL) until a bright yellow was obtained. The solid was dried under vacuum to afford $\text{H}_4(1\text{-PdI})$ (0.778 g, 94% yield). ^1H NMR (400 MHz, $\text{DMSO-}d_6$) δ 14.24 (s, 4H, COOH), 8.98 (d, $^3J_{\text{H-H}} = 7.9$ Hz, 8H, benzoate Ar-H), 8.92 – 8.83 (m, 8H, benzoate Ar-H), 8.10 (t, $^3J_{\text{H-H}} = 8.1$ Hz, 1H, resorcinol Ar-H), 7.79 (d, $^3J_{\text{H-H}} = 8.0$ Hz, 2H resorcinol Ar-H). $^{13}\text{C}\{^1\text{H}\}$ NMR (101 MHz, $\text{DMSO-}d_6$) δ 166.40 (s,

4C, CO), 163.30 (t, $J_{C-P} = 7.3$ Hz, Ar), 136.98 (s, Ar), 136.02 (t, $J_{C-P} = 25.3$ Hz, Ar), 134.64 (s, Ar), 132.13 (t, $J_{C-P} = 7.9$ Hz, Ar), 130.22 (s, Ar), 130.00 (t, $J_{C-P} = 5.3$ Hz, Ar), 107.77 (t, $J_{C-P} = 8.8$ Hz, Ar). $^{31}\text{P}\{^1\text{H}\}$ NMR (162 MHz, DMSO- d_6) δ 149.22 (s, 2P). Anal. Calcd. for $\text{C}_{34}\text{H}_{23}\text{IO}_{10}\text{P}_2\text{Pd}$: C, 45.13; H, 2.79. Found: C, 46.96; H, 2.94. One H_2O molecule is associated with the compound presumably via a hydrogen bonding interaction with the carboxylic acids.

Solvothermal synthesis of 2-PdX. Solutions of anhydrous ZrCl_4 (0.256 g, 1.10 mmol) in DMF (36 mL) and $\text{H}_4(1\text{-PdI})$ (0.360 g, 0.405 mmol) in DMF (36 mL) were sonicated for 5 minutes to ensure complete dissolution of the solids. 6 mL of each solution was added to each of six 20 mL screw-top scintillation vials. Glacial acetic acid (3 mL) was then added to each vial. The vials were sealed with Teflon-lined screw-top caps (Qorpak[®] CAP-00554), placed in a programmable oven at room temperature, and heated to 120 °C for 12 h. After cooling to room temperature, a light grey solid had settled on the bottom of the vials. The solvent was decanted and the solids were combined and washed with DMF (3 x ~ 18 mL) and acetone (1 x ~18 mL). The solid was dried in vacuo (0.01 torr) at room temperature for 2 h before activating under high vacuum (10^{-4} torr) at 150 °C for 12 h. The solid changes from a grey-white to light yellow color upon activation (0.482 g before activation, 0.382 g after activation). Anal. Calcd. for $\text{Zr}_6\text{O}_4(\text{OH})_4[\text{PdCl}_{0.4}\text{I}_{0.6}\text{C}_{34}\text{H}_{19}\text{O}_{10}\text{P}_2]_3(\text{C}_3\text{H}_7\text{NO})_{0.8}(\text{CH}_3\text{COOH})_{1.2}$; C, 38.74; H, 2.57; N, 0.93; I, 6.33; Cl, 1.18. Found: C, 35.85; H, 2.32; N, 0.53; I, 6.48; Cl, 1.0.

Repeated attempts at elemental analysis of **2-PdX** consistently showed residual N and a lower than expected C content. ^1H NMR analysis of a sample of activated **2-PdX** digested

with $\text{CF}_3\text{COOH}/\text{DMSO-d}_6$ confirmed that residual DMF is responsible for the observed N and also the presence of acetic acid. The amount of DMF and $\text{CH}_3\text{CO}_2\text{H}$ present in activated **2-PdX** could not be accurately determined using solution ^1H NMR due to incomplete dissolution of the MOF and decomposition of $\text{H}_4(1\text{-PdX})$ pincer complexes during acid digestion. However, integration of the quantitative solid-state MAS ^{13}C NMR spectrum indicates ~ 0.8 DMF and ~ 1.2 $\text{CH}_3\text{COOH}/\text{CH}_3\text{COO}^-$ molecules per $[\text{POCOP-PdX}]^{4-}$ linker. Missing-linker defects have been proposed to lower the C content of other Zr MOFs.^{17,47,169–171} While this may be the cause of the lower than expected C content for **2-PdX**, it may also be due to the phosphorus-containing impurity indicated by the signal at 93 ppm in the solid-state ^{31}P NMR spectrum. Furthermore, solid-state ^{31}P spectrum of **2-PdX** after activation shows a small signal at ~ 30 ppm, attributed to partial oxidation/decomposition of the phosphine pincer ligand. ICP-AES analysis of **2-PdX** revealed a higher than expected Zr/Pd ratio (2:0.93) consistent with either missing linker defects or partial ligand decomposition.

Synthesis of 2-PdTFA. A sample of **2-PdX** (0.182 g) was suspended in CH₂Cl₂ (5 mL) in a 20 mL scintillation vial. A solution of PhI(TFA)₂ (0.070 g, 0.16 mmol) in CH₂Cl₂ (5 mL) was added, and the vial was sealed and left gently stirring at room temperature. After 12 h, the reaction mixture was centrifuged and the pink-purple supernatant was decanted. A fresh solution of PhI(TFA)₂ (0.07 g, 0.16 mmol) in CH₂Cl₂ (5 mL) was added and the reaction was stirred for another 12 h. The mixture was centrifuged, and the clear colorless supernatant was decanted. The solid was washed with CH₂Cl₂ (3 x 10 mL) and soaked in methanol (15 mL) for 12 h. The solvent was decanted and the solid was washed with methanol (3 x 10 mL). Samples of **2-PdTFA** were dried under vacuum for 3 h prior to using for catalysis. For surface area measurements, a sample was activated under high vacuum (10⁻⁴ torr) at 100 °C for 12 h. The solid remained a silvery grey color upon activation. (0.217 g before activation, 0.204 g after activation). Selected CF₃COOH bands observed in the ATR-IR spectrum of **2-PdTFA**: 1655 cm⁻¹ [asymm. ν(COO)], 1199.8 cm⁻¹ [asymm. ν(C-F)], 1152 cm⁻¹ [asymm. ν(C-F)]. Anal. Calcd. for Zr₆O₄(OH)₄[C₃₄H₁₉O₁₀P₂Pd(CF₃COO)_{0.44}Cl_{0.39}I_{0.17}]₃; C, 39.25; H, 1.92; N, 0.0; I, 2.02; Cl, 1.30; F, 2.35. Found: C, 36.52; H, 1.76; N, 0.0; I, 2.71; Cl, 1.71; F, 3.13.

Similar to **2-PdX**, **2-PdTFA** exhibits a lower than expected C content. Halide analysis (combustion ion chromatography) of **2-PdTFA** shows the presence of I (2.71 wt. %), Cl (1.71 wt. %), and F (3.13 wt. %). Assuming the observed halide content is the result of charge balancing ligands at the Pd sites, I⁻, Cl⁻, and CF₃COO⁻ are present in a 1:2.26:2.57 mole ratio. Normalization gives 0.17 I⁻, 0.39 Cl⁻, and 0.44 CF₃COO⁻ per Pd. These results

suggest that reaction of **2-PdX** with $\text{PhI}(\text{TFA})_2$ facilitates I^-/TFA^- ligand exchange in ~ 72 % yield, but does not result in ligand substitution at the Pd–Cl sites.

Synthesis of $^t\text{Bu}_4(1\text{-PdTFA})$. $\text{Ag}(\text{O}_2\text{CCF}_3)$ (0.033 g, 0.15 mmol) in anhydrous acetone (~ 4 mL) was added dropwise to a solution of $^t\text{Bu}_4(1\text{-PdI})$ in anhydrous acetone (~ 6 mL). A white solid precipitate (AgI) was immediately observed upon addition of $\text{Ag}(\text{O}_2\text{CCF}_3)$. The reaction mixture was stirred at room temperature for 2 h before filtering through a frit containing Celite to remove AgI. The filtrate was evaporated to dryness in vacuo to obtain $^t\text{Bu}_4(1\text{-PdTFA})$ as a white solid (0.143 g, 97% yield). ^1H NMR (400 MHz, CDCl_3) δ 8.09 (d, $^3J_{\text{H-H}} = 7.9$ Hz, 8H, benzoate Ar-H), 7.89 (q, $^3J_{\text{H-H}} = 6.4$ Hz, 8H, benzoate Ar-H), 7.14 (t, $^3J_{\text{H-H}} = 8.1$ Hz, 1H, resorcinol Ar-H), 6.76 (d, $^3J_{\text{H-H}} = 8.1$ Hz, 2H, resorcinol Ar-H), 1.59 (s, 36H, ^tBu). $^{13}\text{C}\{^1\text{H}\}$ NMR (101 MHz, CDCl_3) δ 164.76 (s, 4C, CO), 161.47 (d, $J_{\text{C-P}} = 36.0$ Hz, Ar), 136.93 (t, $J_{\text{C-P}} = 25.4$ Hz, Ar), 135.60 (s, Ar), 131.71 (t, $J_{\text{C-P}} = 8.3$ Hz, Ar), 129.86 (t, $J_{\text{C-P}} = 5.6$ Hz, Ar), 117.85 (s, Ar), 114.95 (s, Ar), 107.93 (t, $J_{\text{C-P}} = 7.7$ Hz, Ar), 82.02 (s, 4C, $\text{C}(\text{CH}_3)_3$), 28.25 (s, 36C, $\text{C}(\text{CH}_3)_3$). $^{31}\text{P}\{^1\text{H}\}$ NMR (162 MHz, CDCl_3) δ 143.85 (2P). ^{19}F NMR (376 MHz, CDCl_3) δ -74.82.

Reaction of $^t\text{Bu}_4(1\text{-PdTFA})$ with HCO_2Na . Solid HCO_2Na (0.016 g, 0.23 mmol) was added to a solution of $^t\text{Bu}_4(1\text{-PdTFA})$ (0.060 g, 0.055 mmol) in CD_3OD (3 mL). The $^{31}\text{P}\{^1\text{H}\}$ NMR spectrum measured immediately after adding HCO_2Na showed a single resonance corresponding to $^t\text{Bu}_4(1\text{-PdTFA})$ at 144 ppm. After stirring for 12 h, the starting material resonance had completely disappeared and was replaced by a new signal at 33.8 ppm. The solvent was removed under vacuum and the phosphorus-containing product was isolated by flash chromatography on silica using hexanes:ethyl acetate (9/1, v/v) as the

eluent. The $^{31}\text{P}\{^1\text{H}\}$ NMR resonance of the isolated product matched that observed *in situ*, and the dominant resonances in the ^1H NMR spectrum could be assigned to *tert*-butyl benzoate groups (Figure 14a). The ESI mass spectrum of the isolated product showed a major peak at $m/z = 436.2$ which corresponds to $[(^t\text{BuO}_2\text{CPh})_2\text{P}(\text{O})\text{OCD}_3 + \text{H}]^+$. When the reaction was repeated using CH_3OH as the solvent, the ^1H NMR spectrum of the isolated product displayed a doublet at 3.79 ppm, confirming the presence of the phosphinate methyl ester. NMR data for product isolated from reaction with CH_3OH as the solvent: ^1H NMR (400 MHz, CDCl_3) δ 8.06 (dd, $^3J_{\text{H-H}} = 7.81$ Hz, $^4J_{\text{H-P}} = 3.13$ Hz, 4H, benzoate Ar-H), 7.85 (dd, $^3J_{\text{H-H}} = 7.81$ Hz, $^3J_{\text{H-P}} = 11.77$ Hz, 4H, benzoate Ar-H), 3.79 (d, $^3J_{\text{H-P}} = 10.93$ Hz, 3H, P-OCH₃), 1.59 (s, 18H, C(O)O-C(CH₃)₃). $^{31}\text{P}\{^1\text{H}\}$ NMR (162 MHz, CDCl_3) δ 31.03.

General procedure for catalytic hydrogenation of aldehydes. A 1 dram vial was charged with catalyst (0.01 mmol based on Pd), sodium formate (0.2 mmol), MeOH (1 mL), H₂O (1 mL), formic acid (0.6 mmol) and the desired aldehyde (0.2 mmol). The vial was sealed with a Teflon-lined screw cap and stirred gently (100 rpm) at 60 °C for 12 h. Upon cooling, the reaction mixture was extracted with CDCl_3 (1.2 mL) and 1, 3, 5-trimethoxybenzene (1 mmol) was added to the separated CDCl_3 solution as an internal standard. The alcohol products were identified and quantified by ^1H NMR spectroscopy. All runs were carried out in triplicate and the conversions and yields given in Table 1 are an average of 3 runs.

Hot filtration test. A 20 mL vial was charged with **2-PdTFA** (0.02 mmol based on Pd), sodium formate (0.4 mmol), MeOH (2 mL), H₂O (2 mL), formic acid (1.2 mmol), benzaldehyde (0.4 mmol) and 1, 3, 5-trimethoxybenzene (0.2 mmol). The vial was sealed with a Teflon lined screw cap and stirred gently at 60 °C. After 3 h, the catalyst was

removed by filtration, and half of the filtrate (aliquot A) was extracted with CDCl_3 (1.2 mL) and immediately analyzed by ^1H NMR spectroscopy. The remainder of the filtrate (aliquot B) was transferred to a 1 dram vial, sealed, and heated at 60 °C. After 13 h, the aliquot B was cooled to room temperature, extracted with CDCl_3 (1.2 mL), and analyzed by ^1H NMR. The ^1H NMR spectra showed 27% and 30 % yield (28 % and 20 % conversion) of benzaldehyde for aliquot A and B, respectively.

Synchrotron Powder Diffraction and Rietveld Refinement of 2-PdX.

Powder synchrotron X-ray diffraction data for **2-PdX** was collected on the 11-BM beamline at the Advanced Photon Source (APS, Argonne National Laboratory). Measurements were taken on a powder sample sealed in a 1.5 mm diameter kapton capillary at 298 K using a photon wavelength of $\lambda = 0.413959 \text{ \AA}$. An initial structure model was constructed from the positions of the heavy atoms (Zr, Pd) located using the charge flipping method within the PDXL 2 Structure Analysis Package (Rigaku Corporation).¹⁷² Subsequent Rietveld refinement was performed using GSAS as implemented in EXPGUI.^{173,174}

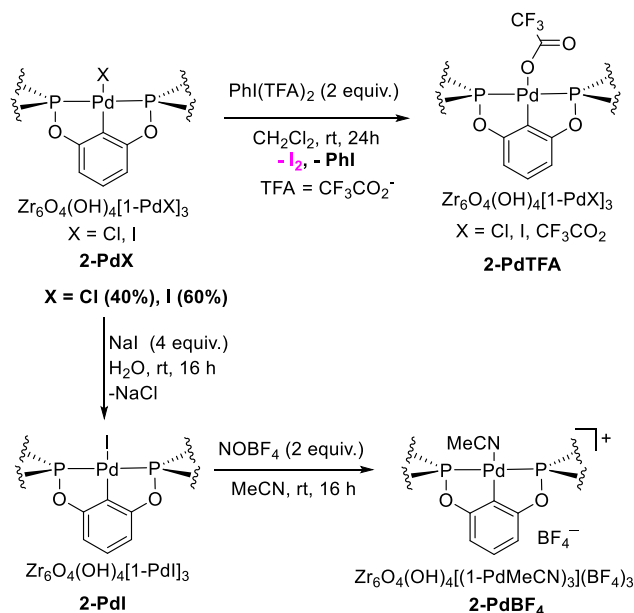
Chapter 3: Broad scope catalytic activity of POCOP-Pd pincer complexes immobilized in a Zr MOF

3.1 Introduction

As discussed in previous chapters, most industrial chemical processes use heterogeneous catalysts owing to their stability under harsh conditions, recyclability and easy catalyst-product separation although homogeneous catalysts generally provide greater selectivity and activity.^{5,175,176} However, catalytic reaction mechanisms in heterogeneous systems are often elusive owing to the ill-defined nature of the active sites. On the other hand, homogeneous catalysts offer better mechanistic understanding of structure-function relationship and control over factors that govern catalytic activity. Therefore, a hybrid approach to catalyst design that integrates the beneficial traits of heterogeneous and homogeneous catalysis could lead to more efficient catalytic processes. The well-defined structure of MOFs provides an ideal platform to design catalysts with uniform active sites mimicking that of homogeneous catalyst systems. Our group and others have been interested in utilizing rigid MOF scaffolds to protect key reactive intermediates of transition metal catalysts from undergoing bimolecular deactivation pathways.^{72,150,177,178} This chapter describes the use of NOBF_4 as a reagent for oxidative ligand exchange at POCOP-Pd sites immobilized in a Zr MOF. The remarkable improvement in catalytic activity for transfer hydrogenation of aldehydes with **2-PdTFA** compared to **2-PdX** can be linked to the presence of the more weakly coordinating TFA^- anionic ligand. Recently, we described a clean and complete oxidation of inner and outer sphere iodide species with NOBF_4 in a Zr MOF containing PNNNP-Pd pincer complexes.⁸⁵ The resulting MOF

showed superior catalytic activity for the intramolecular cyclization of *o*-alkynyl anilines compared to an analogous MOF prepared via I^-/TFA^- oxidative ligand exchange using $PhI(TFA)_2$.⁸⁵ Encouraged by the efficacy of $NOBF_4$ in the PNNNP-Pd system, we investigated I^-/BF_4^- oxidative ligand exchange at Pd centers in a Zr MOF assembled from POCOP-Pd linkers. Consequently, **2-PdBF₄** was generated by reaction of **2-PdI** with $NOBF_4$ as shown in Scheme 10, and exhibits superior catalytic activity for transfer hydrogenation of unsaturated organic substrates, alkyne hydration and intramolecular alkyne hydroarylation reactions compared to **2-PdX**, **2-PdI**, **2-PdTFA** and its homogeneous analogue $tBu_4(1-PdBF_4)$.

3.2 Synthesis and characterization of 2-PdBF₄



Scheme 10. Postsynthetic oxidative ligand exchange reactions at Pd using $PhI(TFA)_2$ and $NOBF_4$ as oxidants.

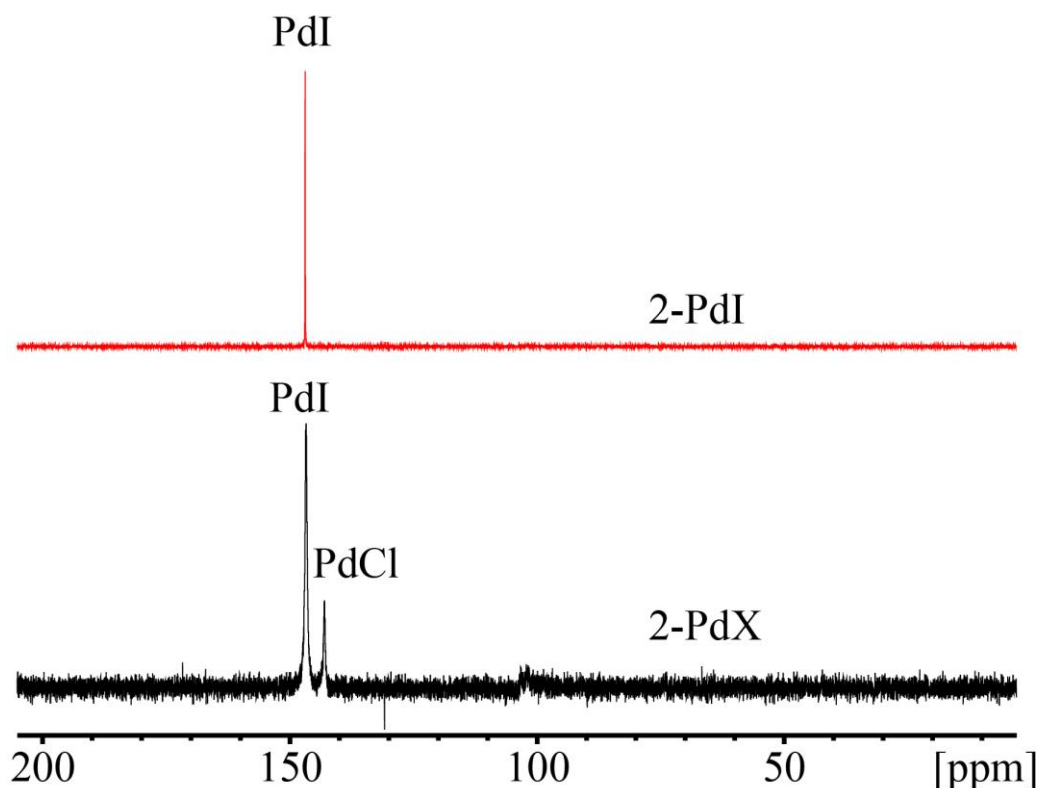


Figure 15. $^{31}\text{P}\{^1\text{H}\}$ NMR spectra ($\text{CF}_3\text{COOH}/\text{C}_6\text{D}_6$) of **2-PdX** and **2-PdI**.

A suspension of **2-PdX** in water was treated with an aqueous solution of NaI to afford **2-PdI** as a yellow microcrystalline powder (Scheme 10). The acid-digested ^{31}P NMR spectrum of **2-PdI** shows a single sharp resonance at 148 ppm, which is consistent with that observed for $\text{H}_4(1\text{-PdI})$ (148 ppm in DMSO-d_6) (Figure 15). The ^1H NMR spectrum of the acid-digested sample displays all resonances expected for a single $\text{H}_4(1\text{-PdI})$ pincer complex (Figure 16). Reaction of **2-PdI** with NOBF_4 (2 equiv. per Pd) in acetonitrile results in formation of **2-PdBF₄** as a white microcrystalline powder (Scheme 10). Upon addition of NOBF_4 , the reaction supernatant immediately becomes dark orange, indicating the generation of soluble iodine species. After a series of successive washes with MeCN, the

X-ray fluorescence (XRF) and X-ray photoelectron (XPS) spectra of **2-PdBF₄** showed complete disappearance of signals corresponding to iodine (Figure 17).

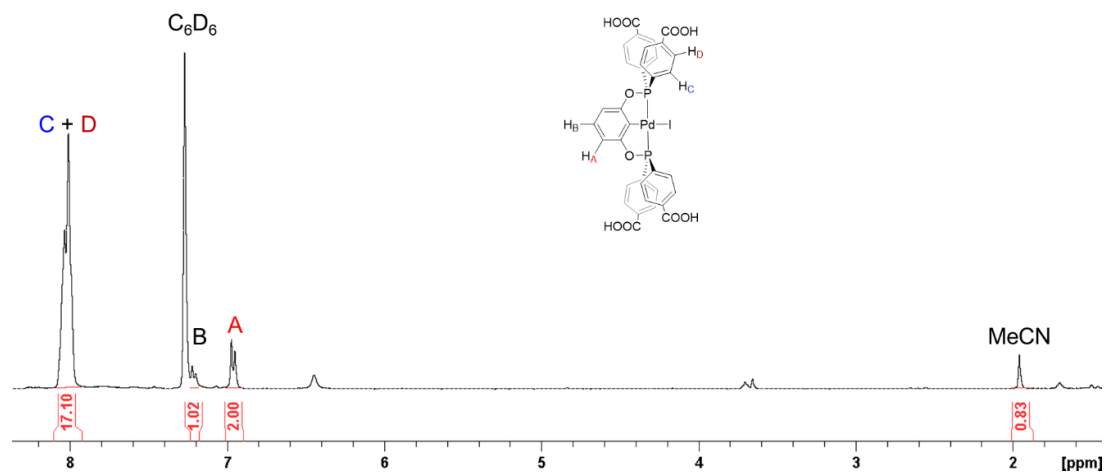


Figure 16. ¹H NMR spectrum (CF₃CO₂H/C₆D₆) of **2-PdI**.

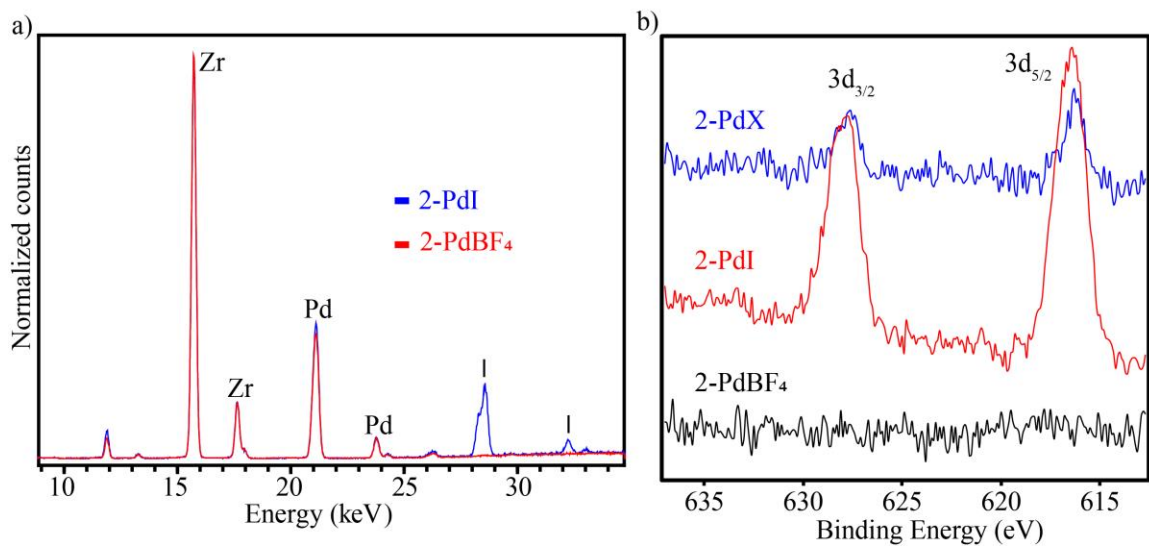
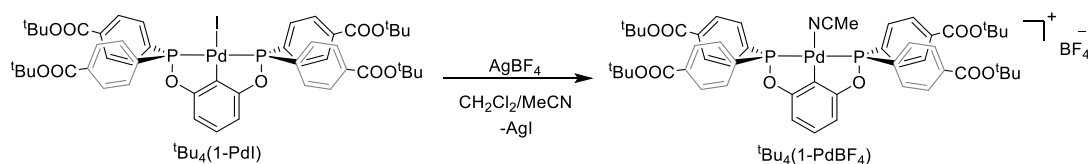


Figure 17. a) XRF spectra of **2-PdI** and **2-PdBF₄**. b) XPS spectra of **2-PdX**, **2-PdI** and **2-PdBF₄** showing the iodine 3d_{3/2} and 3d_{5/2} region.

The acid-digested ^{31}P NMR spectrum of **2-PdBF₄** contains two major resonances at 147 and 144 ppm along with an unidentified minor species at 91 ppm (Figure 18). The peak at 147 ppm appears at a similar chemical shift to that observed for $^t\text{Bu}_4(1\text{-PdBF}_4)$ (147.5 ppm in CDCl_3), which has been prepared via reaction of $^t\text{Bu}_4(1\text{-PdI})$ and AgBF_4 (Scheme 11). The resonance at 144 ppm is likely due to $\text{H}_4(1\text{-PdX})$ ($\text{X} = \text{TFA}^-$ or OH^-) species arising from ligand substitution under the digestion conditions ($\text{CF}_3\text{CO}_2\text{H}/\text{C}_6\text{D}_6$). This assignment is supported by the ^{31}P NMR spectrum of $^t\text{Bu}_4(1\text{-PdBF}_4)$ which shows similar speciation in the $\text{CF}_3\text{CO}_2\text{H}/\text{C}_6\text{D}_6$ solvent mixture (Figure 18).



Scheme 11. Synthesis of $^t\text{Bu}_4(1\text{-PdBF}_4)$

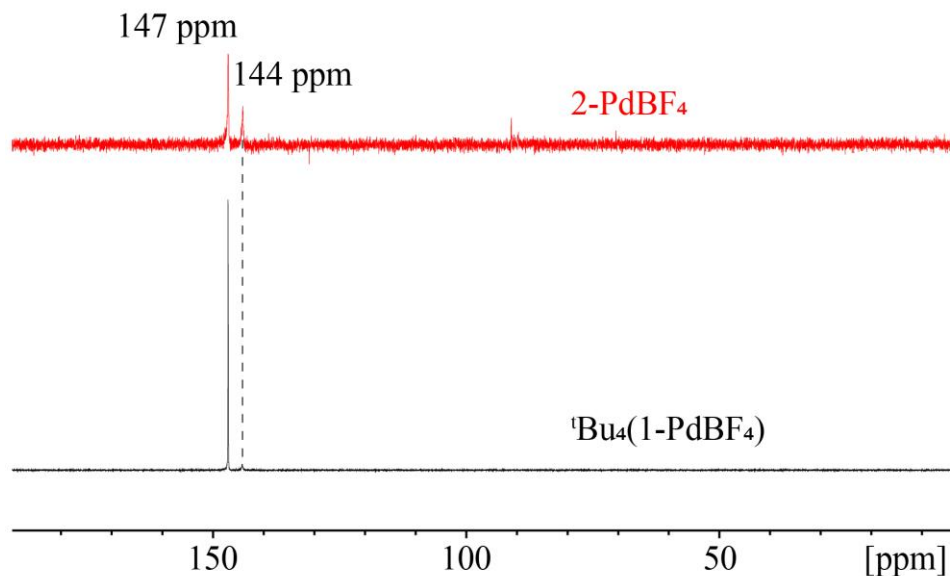


Figure 18. $^{31}\text{P}\{^1\text{H}\}$ NMR spectra ($\text{CF}_3\text{CO}_2\text{H}/\text{C}_6\text{D}_6$) of **2-PdBF₄** and $^t\text{Bu}_4(1\text{-PdBF}_4)$.

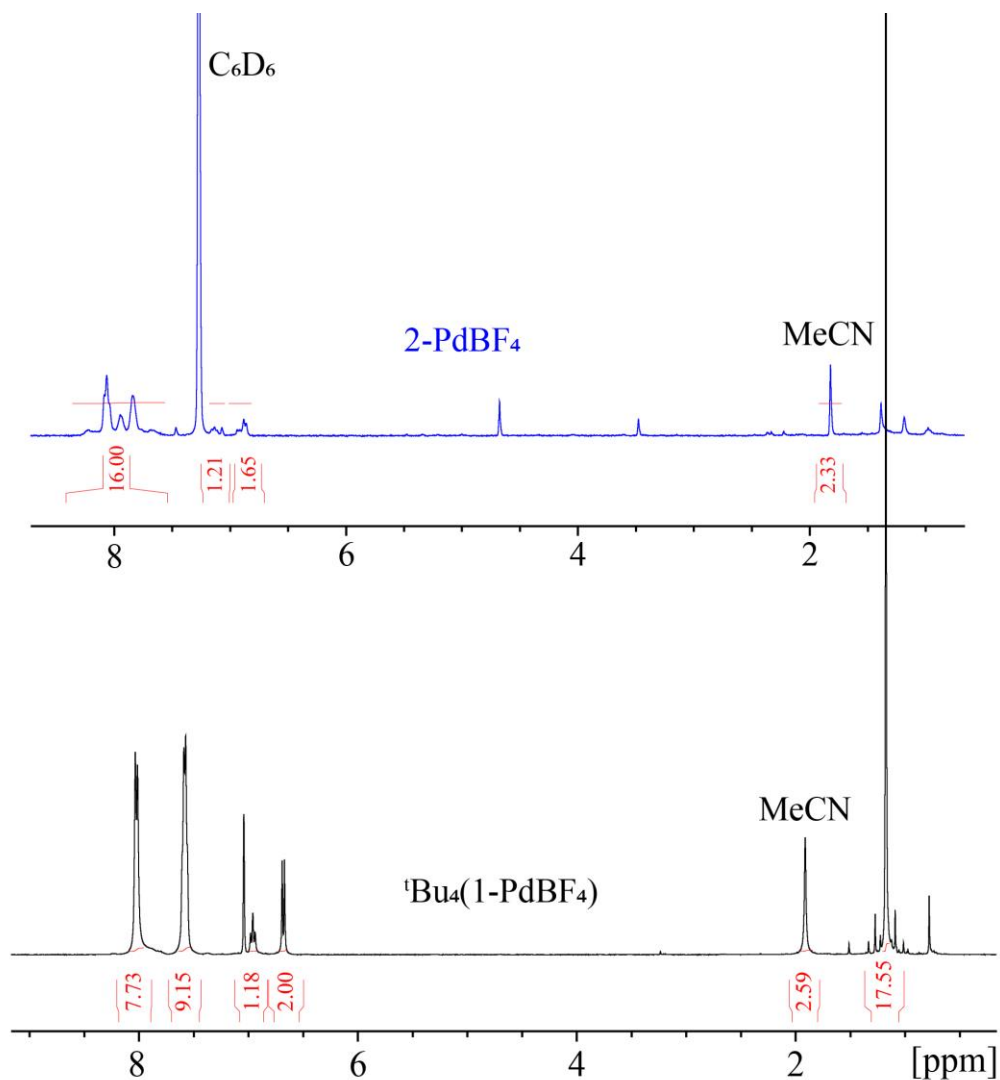


Figure 19. ^1H NMR spectra ($\text{CF}_3\text{CO}_2\text{H}/\text{C}_6\text{D}_6$) of **2-PdBF₄** and $^t\text{Bu}_4(1\text{-PdBF}_4)$.

Notably, POCOP-Pd^{IV} species have been proposed as intermediates in oxidative Heck reactions with iodonium salts.¹³⁴ In the present case, NOBF₄ is a potent oxidant and might be expected to effect Pd-based oxidation. Although a stoichiometric excess of NOBF₄ was used for the oxidative ligand exchange, we do not observe any clear spectroscopic evidence of oxidized Pd species in **2-PdBF₄**. The lack of any observed spectroscopic signature does not rule out the formation of Pd^{IV} intermediates during the

ligand exchange process. The acid-digested ^1H NMR spectrum of a dried sample of **2-PdBF₄** closely resembles that of $^t\text{Bu}_4(1\text{-PdBF}_4)$ in the same solvent mixture used for MOF digestion and shows the presence of ~ 1 equiv. of MeCN, suggesting that the solvent molecule serves as a ligand toward the cationic Pd center (Figure 19). In addition, elemental analysis of **2-PdBF₄** is in agreement with nearly complete exchange of the iodide ligand providing 0.23 % iodine content.

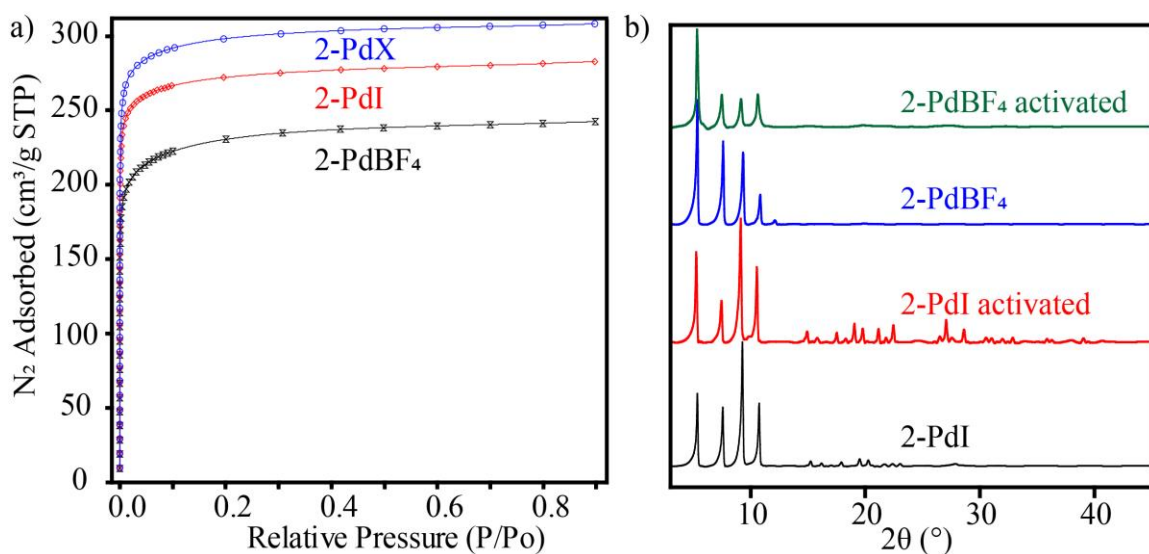


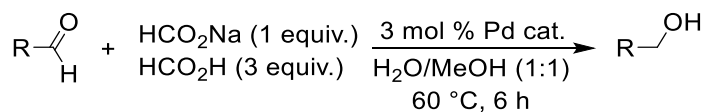
Figure 20. a) N_2 adsorption isotherms measured at 77 K for **2-PdX**, **2-PdI** and **2-PdBF₄** after desolvation at 100 $^\circ\text{C}$ and 10^{-4} torr for 16 h. b) PXRD patterns (Cu-K α radiation, $\lambda = 1.5418$ \AA) of **2-PdI** and **2-PdBF₄** before and after activation.

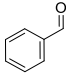
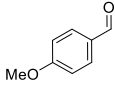
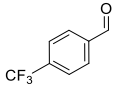
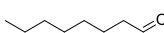
N_2 adsorption isotherms measured at 77 K for samples of **2-PdI** and **2-PdBF₄** activated at 100 $^\circ\text{C}$ and 10^{-4} torr for 20 h gave calculated BET surface areas of 1060 and 880 m^2g^{-1} , respectively (Figure 20a). The BET surface area of **2-PdI** is consistent with that previously reported for **2-PdX** (1164 m^2g^{-1}). The slight decrease in the BET surface area of **2-PdBF₄** is likely due to the presence of pore-occluding BF_4^- counterions. Subsequent, PXRD

measurements of activated samples of **2-PdI** and **2-PdBF₄** showed retention of bulk crystallinity (Figure 20b).

3.3 Transfer hydrogenation of aldehydes

With **2-PdBF₄** in hand, we set out to investigate its catalytic activity toward a series of reactions including transfer hydrogenation of unsaturated organic substrates, hydration of terminal alkynes, and intramolecular hydroarylation reactions. Initial catalytic screening with **2-PdBF₄** focused on transfer hydrogenation reactions similar to that previously reported with **2-PdTFA**. Transfer hydrogenation reactions with aldehyde substrates were carried out with 3 mol % catalyst loading (based on Pd) using formic acid as hydrogen source (Table 2). The reaction yields were determined by ¹H NMR using 1,3,5-trimethoxybenzene as internal standard. Under these conditions, **2-PdBF₄** catalyzes the transfer hydrogenation of benzaldehyde to benzyl alcohol in 98 % yield while **2-PdTFA** gives only 73 % yield (Table 2, entries 1-2). This comparison reveals that the more weakly coordinating BF₄⁻ counter anion offers a distinct improvement in catalytic activity. In line with our previous findings, the homogeneous complex, ^tBu₄(1-PdBF₄), displays poor catalytic activity (9 % yield) and shows complete decomposition under the reaction conditions (Figure 21b).¹⁵⁰ On the other hand, **2-PdBF₄** remains crystalline after the catalytic reaction, corroborating the beneficial effect of catalyst immobilization. **2-PdBF₄** also catalyzes transfer hydrogenation of both aryl and aliphatic aldehyde substrates in good yields (Table 2, entries 4-6).

Table 2. Transfer hydrogenation of aldehydes^a

Entry	Substrate	Catalyst	% Yield ^b
1		2-PdBF₄	98
2		2-PdTFA	73
3		^t Bu ₄ (1-PdBF ₄)	9
4		2-PdBF₄	98
5		2-PdBF₄	97
6 ^c		2-PdBF₄	92

^aReaction conditions: substrate (0.2 mmol), catalyst (0.006 mmol Pd), NaO₂CH (0.2 mmol), HCO₂H (0.6 mmol), H₂O/MeOH (1:1, v/v), 6 h, 60 °C. ^cReaction time was 12 h instead of 6 h. Yields were determined by ¹H NMR with respect to an internal standard (1, 3, 5-trimethoxybenzene).

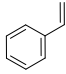
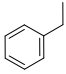
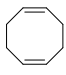
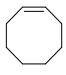
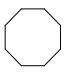
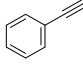
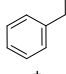
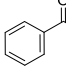
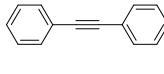
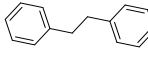
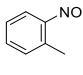
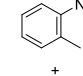
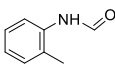
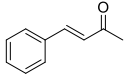
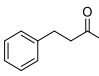
3.4 Transfer hydrogenation of alkene, alkyne and nitroarene substrates

The scope and generality of catalytic transfer hydrogenation with **2-PdBF₄** has been tested with alkene, alkyne and nitroarene substrates. Transfer hydrogenation of unsaturated organic substrates provides a mild alternative to direct hydrogenation, which often requires high pressure H₂ and complicated reaction setups.^{179,180} A multitude of homogenous catalysts have been developed for alkene transfer hydrogenation with reducing agents such as isopropanol, formic acid or ethanol.^{181–183} However, there have been relatively few

reports of heterogeneous systems that catalyze alkene transfer hydrogenation.^{184–186} Thus, there is significant interest in developing catalysts that are reusable and operate under mild conditions for hydrogenation of olefins. Furthermore, efficient and sustainable catalytic reduction of nitroarenes is used to prepare amines, which are useful intermediates for pharmaceuticals and agricultural chemicals.¹⁸⁷ Both homogeneous and heterogeneous catalysts have been developed for the reduction of nitro groups, but selective reduction to amines still presents challenges.^{187–190}

Under catalytic conditions similar to those used for aldehydes, styrene was fully converted to ethylbenzene in 6 h with **2-PdBF₄** as a catalyst (Table 3, entry 1). **2-PdBF₄** could be recycled twice with no loss of activity, but a slight decline was observed in the third run (72 % yield). This loss of activity is likely due to partial framework degradation resulting in catalyst deactivation. Two notable observations support this hypothesis: 1) The MOF changed color from white to dark brown after the third run; 2) PXRD analysis after the third run showed a significant loss of framework crystallinity and the appearance of new reflections attributable to zirconium oxide (Figure 21a). Nonetheless, **2-PdBF₄** outperforms analogues **2-PdX** and **2-PdI** as well as the homogeneous ^tBu₄(1-PdBF₄) complex for transfer hydrogenation of styrene (Table 3, entries 2-4). Further efforts to expand the substrate scope to terminal aliphatic olefins using 1-dodecene as a substrate gave a mixture of starting material, internal alkenes, and only a small amount of dodecane product. Alkene isomerization is not uncommon for Pd catalysts, and the low yield of hydrogenated product suggests that **2-PdBF₄** favors chain walking over hydrogenation and is less active toward internal alkenes.^{191–193}

Table 3. Transfer hydrogenation of alkene, alkyne and nitroarene substrates

Entry	Substrate	Product(s)	Catalyst	% Yield
1			2-PdBF₄	97
2			2-PdX	< 5
3			2-PdI	< 5
4			^t Bu ₄ (1-PdBF ₄)	20
5 ^c			2-PdBF₄	75
				22
6 ^d			2-PdBF₄	80
				17
7 ^c			2-PdBF₄	94
8 ^e			2-PdBF₄	92
				5
9			2-PdBF₄	94

^aReaction conditions: substrate (0.2 mmol), catalyst (0.006 mmol Pd), NaO₂CH (0.2 mmol), HCO₂H (0.6 mmol), H₂O/MeOH (1:1, v/v), 6 h, 60 °C. ^cLonger reaction time (12 h) was used. ^dReaction was carried out in MeOH without added H₂O. ^eIncreased amounts of HCO₂H (1.2 mmol) and catalyst (0.01 mmol) were used. Yields were determined by ¹H NMR with respect to an internal standard (1, 3, 5-trimethoxybenzene).

The decreased activity toward 1-dodecene and its internal isomers may also be a function of the size of the substrate since **2-PdBF₄** catalyzes the transfer hydrogenation of

1,5-cyclooctadiene to a mixture of cyclooctene and cyclooctane with 60 % overall conversion of the alkene groups (TABLE 3, entry 5).

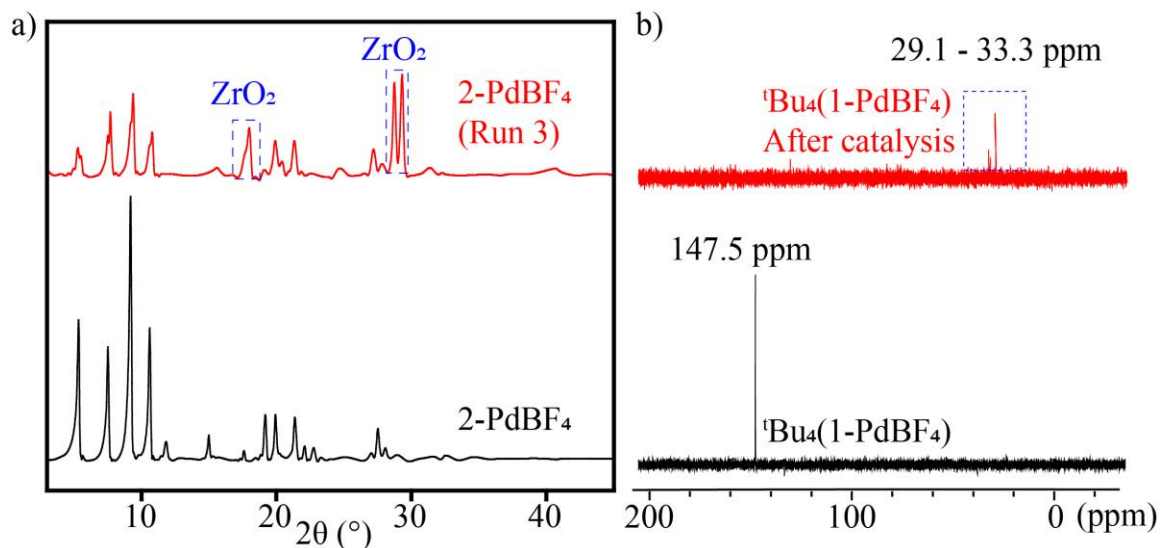


Figure 21. a) PXRD patterns (Cu-K α radiation, $\lambda = 1.5418 \text{ \AA}$) of **2-PdBF₄** before and after transfer hydrogenation of styrene. b) $^{31}\text{P}\{^1\text{H}\}$ NMR spectra of $^t\text{Bu}_4(1\text{-PdBF}_4)$ before and after transfer hydrogenation reactions.

Encouraged by the activity of **2-PdBF₄** for alkene transfer hydrogenation, we investigated the α,β -unsaturated carbonyl substrate benzylideneacetone. There has been considerable interest in chemoselective hydrogenation of this class of compounds.^{147,194–196} Gratifyingly, **2-PdBF₄** shows selectivity for transfer hydrogenation of the alkene over the ketone functional group after 6 h reaction time (Table 3, entry 9). Increasing the reaction time to 12 h gave 27 % of the fully hydrogenated product, 4-phenyl-2-butanol. This result indicates that **2-PdBF₄** is more active toward transfer hydrogenation of aldehydes and alkenes than ketones, advocating its use for chemoselective hydrogenation.

Initial screening of phenylacetylene as a substrate with **2-PdBF₄** under the optimized conditions provided a mixture of ethylbenzene (37 %) and acetophenone (60 %)

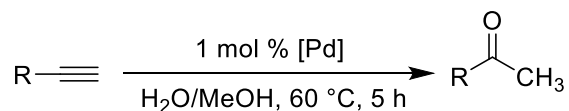
as hydrogenated and hydrated products, respectively. When water was excluded from the reaction, ethylbenzene and acetophenone were produced as major (80%) and minor (17 %) products, respectively (Table 3, entry 6). The hydration side reaction could not be completely inhibited owing to the presence of adventitious water in formic acid and methanol. The semi-hydrogenation product, styrene, was not observed. On the other hand, an internal alkyne, diphenylacetylene, afforded a ~ 3:1 mixture of 1, 2-diphenylethane and stilbene after 5 h, and extending the reaction time to 12 h provided full conversion to 1, 2-diphenylethane (Table 3, entry 7). Similar to 1-dodecene, 4-octyne provided mixtures of octene isomers under the optimized transfer hydrogenation condition. Furthermore, **2-PdBF₄** catalyzes the hydrogenation of 2-nitrotoluene to 2-aminotoluene in 92 % yield after 6 h with 5 mol % catalyst loading. However, full conversion of nitroarene substrates requires increased amounts of formic acid (6 equiv.), which also results in formation of N-o-tolylformamide (5 %) as minor side product (Table 3, entry 8).

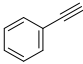
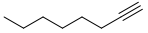

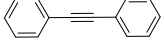
3.5 Terminal alkyne hydration

Catalytic hydration of alkynes is a useful organic transformation that has historically been facilitated by Hg(II) catalysts and strong Brønsted acids.^{196,197} Alternative catalyst systems have been sought due to environmental concerns related to toxicity of Hg(II), and some very efficient catalysts based on Au, Pt, Fe, Co have emerged that require only mild Brønsted acid or acid-free conditions.^{198–204} The stability and recyclability of **2-PdBF₄** makes it a potentially appealing catalyst for alkyne hydration. Indeed, 1 mol % of **2-PdBF₄** catalyzed the hydration of phenylacetylene to acetophenone in 95 % yield after 5 h at 60 °C using a 1/1 (v/v) mixture of MeOH and water as solvent (Table 4, entry 1). The

catalyst could be recycled up to five times with no loss of catalytic activity (Figure 22b), and PXRD analysis confirmed that the MOF remains crystalline after recycling experiments (FIGURE 22a).

Table 4. Catalytic hydration of alkynes



Entry	Substrate	Catalyst	% Yield
1		2-PdBF₄	95
2		2-PdX	< 5
3		2-PdI	< 5
4		^t Bu ₄ (1-PdBF ₄)	< 5
5		UiO-67	< 5
6		2-PdBF₄	94
7		2-PdBF₄	< 5
8		2-PdBF₄	< 5

^aReaction conditions: substrate (0.4 mmol), catalyst (0.004 mmol), H₂O/MeOH, 5 h, 60 °C. Yields were determined by ¹H NMR with respect to an internal standard (1, 3, 5-trimethoxybenzene).

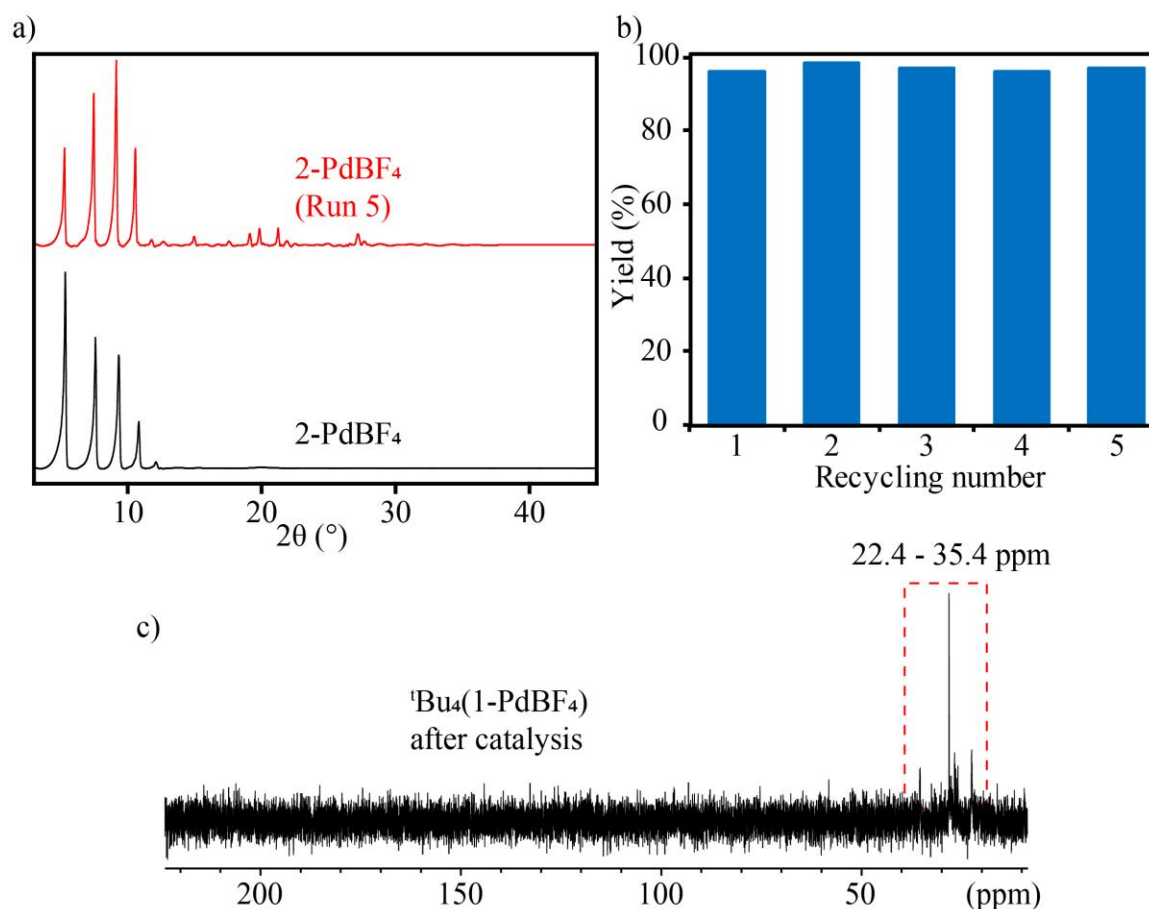


Figure 22. a) PXR D patterns (Cu-K α radiation, $\lambda = 1.5418 \text{ \AA}$) of **2-PdBF₄** before and after phenylacetylene hydration (Run 5). b) Recyclability plot for hydration of phenylacetylene with **2-PdBF₄**. c) $^{31}\text{P}\{^1\text{H}\}$ NMR spectrum of $^t\text{Bu}_4(1\text{-PdBF}_4)$ after phenylacetylene hydration attempt in THF/H₂O.

Under similar reaction conditions, **2-PdX**, **2-PdI**, and UiO-67 gave < 5 % yield of product (Table 4, entries 2, 3 and 5), again pointing to the importance of activation the Pd pincer sites. Furthermore, the inactivity of these MOFs indicates that the catalytic activity observed for **2-PdBF₄** is not likely due to coordinatively unsaturated Zr sites arising from framework defects. **2-PdBF₄** is also selective for hydration of terminal alkynes, and no substrate conversion was observed with diphenylacetylene and 4-octyne (Table 4, entries 7 and 8).

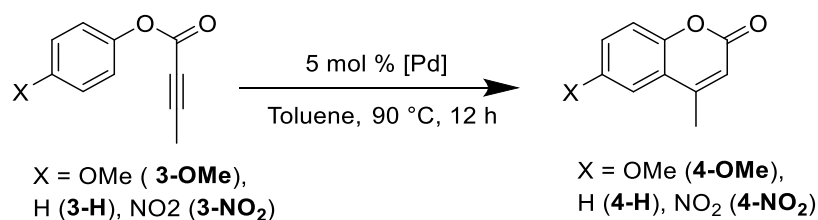
Catalytic alkyne hydration studies with the homogeneous complex, ${}^t\text{Bu}_4(1\text{-PdBF}_4)$, were complicated by its poor solubility in the MeOH/H₂O (1:1, v/v) solvent system. ³¹P NMR analysis of a catalytic reaction carried out in THF/H₂O (5/1, v/v) showed complete decomposition of the pincer complex and no substrate turnover (TABLE 4, entry 4, Figure 22c). The lack of catalytic activity of ${}^t\text{Bu}_4(1\text{-PdBF}_4)$ would seem to be due to catalyst deactivation processes and indicate that decomposed Pd species are unlikely to be involved in the MOF-catalyzed alkyne hydration reactions.

3.6 Intramolecular alkyne hydroarylation

The functionalization of arene C–H bonds to form new C–C bonds remains a synthetically challenging transformation. In this regard, catalytic hydroarylation represents as an atom-economic approach to couple unsaturated organic substrates (alkenes and alkynes) and arenes.^{205–210} The synthesis of biologically relevant coumarins via intramolecular hydroarylation of alkynes is one practical application of this synthetic transformation and can offer structural and functional group diversity. The Pechmann condensation has been one of the most widely used methods for preparation of coumarins, but requires stoichiometric amounts of Brønsted or Lewis acid, making it less attractive from an atom economy perspective.^{211,212} As a result, there has been interest in developing transition metal catalysts for intramolecular hydroarylation reactions, and Pd-based catalysts have received considerable attention.^{205,208,209,213} Consequently, we set out to explore the ability of the Lewis acidic Pd sites in **2-PdBF₄** to catalyze intramolecular hydroarylation of alkynes. Gratifyingly, the intramolecular hydroarylation of **3-OMe** with 5 mol % **2-PdBF₄** as catalyst proceeded smoothly to generate **4-OMe** in 81 % yield after

12 h in toluene at 90 °C (Table 5, entry 2). Moreover, **2-PdBF₄** could be recycled twice with no appreciable loss of activity, and a modest loss of activity observed in the fourth run is attributed to catalyst loss during the washing steps of the recycling process. PXRD analysis after the fourth run showed that the MOF retains its crystallinity. The heterogeneous nature of the catalyst was further supported by a hot filtration test which showed an abrupt halt in substrate conversion after removing the MOF from the reaction mixture.

Table 5. Synthesis of simple coumarins via intramolecular hydroarylation^a



Entry	X	Catalyst	% Yield
1	MeO	2-PdX	< 5
2	MeO	2-PdBF₄	81
3 ^c	MeO	^t Bu ₄ (1-PdBF ₄)	61
4	MeO	2-PdBF₄(Run 2)	81
5	MeO	2-PdBF₄(Run 4)	61
6	H	2-PdBF₄	73
7	NO ₂	2-PdBF₄	< 5

^aReaction conditions: substrate (0.1 mmol), catalyst (0.005 mmol), toluene-*d*₈, 12 h, 90 °C.

^c1,4-dioxane was used instead of toluene-*d*₈. Yields were determined by ¹H NMR with respect to an internal standard (hexamethylbenzene or hexaethylbenzene).

As expected, **2-PdX** was inactive (< 5 % yield of **4-OMe**) under identical reaction conditions (Table 5, entry 1). Pd-catalyzed hydroarylation reactions have been proposed to proceed via activation of the alkyne group by the Lewis acidic metal site followed by nucleophilic attack of the arene.²⁰⁸ This mechanism is akin to electrophilic aromatic substitution, and as a result, becomes unfavorable for electron deficient arenes. Indeed, while **2-PdBF₄** showed only a small decrease in activity with **3-H** as a substrate, no hydroarylation product was observed with the electron deficient substrate **3-NO₂** (Table 5, entries 6 and 7).

The homogeneous pincer complex ^tBu₄(1-PdBF₄) is poorly soluble under the catalytic reaction conditions optimized for **2-PdBF₄**. After solvent screening, 1, 4-dioxane was determined to be a suitable solvent, and ^tBu₄(1-PdBF₄) gave 61 % yield of **4-OMe** after 12 h at 90 °C. This result reveals that immobilization of the pincer complex in **2-PdBF₄** provides slight improvement in catalytic activity, but also highlights the advantages of using a porous heterogeneous support to obviate solubility limitations encountered in homogeneous systems.

3.7 Conclusions

2-PdBF₄ was successfully generated by reaction of **2-PdI** with NOBF₄ via I⁻/BF₄⁻ oxidative ligand exchange. Gratifyingly, **2-PdBF₄** demonstrated broad scope catalytic activity for transfer hydrogenation of unsaturated organic substrates, terminal alkyne hydration, and intramolecular hydroarylation of alkynes. The amplified catalytic activity of **2-PdBF₄** compared to **2-PdX**, **2-PdI** and **2-PdTFA** stresses the importance of developing suitable pre-catalyst activation procedures for solid catalysts. On the other hand, catalyst

deactivation processes observed in both transfer hydrogenation and hydration reactions with the homogeneous complex, $t\text{Bu}_4(1\text{-PdBF}_4)$, illustrate the benefit of catalyst immobilization in MOFs. Moreover, the MOF based heterogeneous catalysis avoids or minimizes solubility limitations encountered in the homogeneous system.

3.8 Experimental

General Considerations. Alkyne substrates for intramolecular hydroarylation reactions were prepared following literature procedures.²¹⁴ All hydroarylation reactions were carried out in nitrogen filled glovebox using solvents that were dried over CaH_2 and distilled or dried via passage through columns of drying agents using a solvent purification system from Pure Process Technologies. Other solvents and reagents were purchased from commercial suppliers and used as received. Routine X-ray powder diffraction (PXRD) patterns for phase identification were collected using a Rigaku Miniflex 600 diffractometer with Nickel-filtered $\text{Cu-K}\alpha$ radiation ($\lambda = 1.5418 \text{ \AA}$). ATR-IR spectra were measured using a Bruker Alpha II spectrometer with a diamond ATR accessory. N_2 adsorption isotherms (77 K, liquid nitrogen bath) were measured using a Micromeritics 3Flex Surface Characterization Analyzer. Prior to analysis, samples (100–200 mg) were heated under reduced pressure until the outgas rate was less than 2 mTorr/min. GC-MS analysis was performed using an Agilent 7890B GC system equipped with the HP-5 Ultra Inert column (30 m, 0.25 mm, 0.25 μm), and a FID detector. For MS detection an electron ionization system was used with an ionization energy of 70 eV. Elemental analyses (C, H, N) were performed by Robertson Microlit Laboratories (Ledgewood, NJ). XRF measurements for

I⁻/BF₄⁻ exchange reactions were monitored using Innov-X Systems X-500 spectrometer with Co-K α radiation sources. High resolution XPS analysis was performed at the Ohio State Surface Analysis lab using a Kratos Axis Ultra X-ray photoelectron spectrometer with a monochromatic Al K α X-ray source. The binding energy of all photoelectron spectra were referenced to adventitious carbon at 284.5 eV.

Solution-state NMR spectra were measured using Bruker 400 MHz spectrometer. For ¹H NMR spectra, the solvent resonance was referenced as an internal standard. For ³¹P NMR spectra, 85 % H₃PO₄ was used as an external standard (0 ppm). Solvent-suppressed ¹H NMR spectra were collected using 180° water selective excitation sculpting with default parameters and pulse shapes.

Synthesis of 2-PdI. A solution of NaI (0.070 g, 0.47 mmol) in H₂O (2 mL) was added to a suspension of **2-PdX** (0.126 g, 0.116 mmol) in H₂O (5 mL), and stirred gently at room temperature for 16 h. The solid was collected by centrifugation, washed with H₂O (5 × 10 mL) and MeCN (5 × 10 mL) and dried in vacuo to give a faint yellow microcrystalline powder (0.121 g). ³¹P{¹H} NMR (162 MHz, CF₃CO₂H/C₆D₆) δ 146.8 (s, 2P).

Synthesis of 2-PdBF₄. A solution of NOBF₄ (0.060 g, 0.50 mmol) in MeCN (1 mL) was added to a suspension of **2-PdI** (0.275 g, 0.25 mmol) in MeCN (5 mL), and stirred gently at room temperature for 16 h. The reaction supernatant turned orange upon NOBF₄ addition. The solid was collected by centrifugation, washed with MeCN (3 × 5 mL) and dried in vacuo to afford **2-PdBF₄** as a white microcrystalline powder (0.25 g). Anal calcd. for **2-PdBF₄**; Zr₆O₄(OH)₄ (OH)_{1.2} (1-Pd-MeCN)_{2.7}(BF₄)_{2.7}(H₂O)₂: C, 37.02; H, 2.19; N; 1.2. Found: C, 35.49; H, 2.45; N, 0.48. Similar to **2-PdX**, missing linker defects are

believed to contribute for the lower C content observed in **2-PdBF₄**. In addition, the acid-digested ³¹P NMR spectrum of **2-PdBF₄** shows unidentified signal at 91 ppm and this phosphorus-containing impurity might also be the cause for the lower C content.

Synthesis of ^tBu₄(1-PdBF₄). A solution of AgBF₄ (0.037 g, 0.19 mmol) in MeCN (1 mL) was added to a solution of ^tBu₄(1-PdI) (0.20 g, 0.18 mmol) in CH₂Cl₂ (5 mL). Upon addition of AgBF₄, formation of white AgI salt was observed. The silver salt was filtered using a 0.45 μm PTFE filter disk, volatiles were removed under reduced pressure, solid was dissolved in CH₂Cl₂, filtered again to ensure complete removal of AgI, and dried in vacuo to afford a white powder (0.19 g, 95 %). ¹H NMR (400 MHz, CDCl₃): δ 1.57 (s, 36H, ^tBu), 6.83 (d, 2H, ³J_{H-H} = 10.42 Hz, backbone Ar-H), 7.21 (t, 1H, ³J_{H-H} = 11.47 Hz, backbone Ar-H), 7.80 (m, 8H, benzoate Ar-H), 8.17 (d, 8H, ³J_{H-H} = 9.73 Hz, benzoate Ar-H). ³¹P{¹H} NMR (162 MHz, CDCl₃) δ 147.48 (s, 2P).

Transfer hydrogenation reactions: A 1 dram screw-top vial was charged with a catalyst (0.006 mmol of Pd), sodium formate (0.2 mmol), MeOH (0.5 mL), H₂O (0.5 mL), formic acid (0.6 mmol), substrate (0.2 mmol) and 1, 3, 5-trimethoxybenzene as internal standard. The vial was sealed with Teflon-lined cap and heated to 60 °C for 6 h for aldehyde and alkene substrates or 5 h for alkyne substrates. The reaction mixture was allowed to cool to room temperature, extracted with CDCl₃ and analyzed by ¹H NMR and GC-MS/FID. Reaction yields were determined by integration of the ¹H NMR spectra of the reaction mixtures with respect to the internal standard.

Alkyne hydration reactions: A 1 dram screw top vial was charged with a catalyst (0.004 mmol), MeOH (1 mL), H₂O (1 mL), substrate (0.4 mmol) and 1, 3, 5-trimethoxybenzene

as internal standard. The vial was sealed with Teflon-lined cap and heated to 60 °C for 5 h. The reaction mixture was allowed to cool to room temperature, extracted with CDCl_3 and analyzed by ^1H NMR and GC-MS/FID. Reaction yields were determined by integration of the ^1H NMR spectra of the reaction mixtures with respect to the internal standard.

Intramolecular hydroarylation reactions: In a nitrogen filled glovebox, a 1 dram screw-top vial was charged with a catalyst (0.005 mmol), toluene- d_8 (1 mL), substrate (0.1 mmol) and hexaethylbenzene as internal standard. The vial was sealed with Teflon-lined cap and heated to 90 °C for 12 h. The products of the reaction were characterized by ^1H NMR and GC-MS/FID. Yields of catalysis were determined by ^1H NMR. For recycling experiments, the catalyst was isolated from the reaction mixture *via* centrifugation, washed with toluene (3×2 mL), and resubjected to the catalytic conditions.

Chapter 4: Synthesis and reactivity of PNNNP-Co^{III} pincer complexes immobilized in a Zr MOF

Portions of this chapter have been described in *Inorg. Chem.* **2019**, 58, 3227–3236.

4.1 Introduction

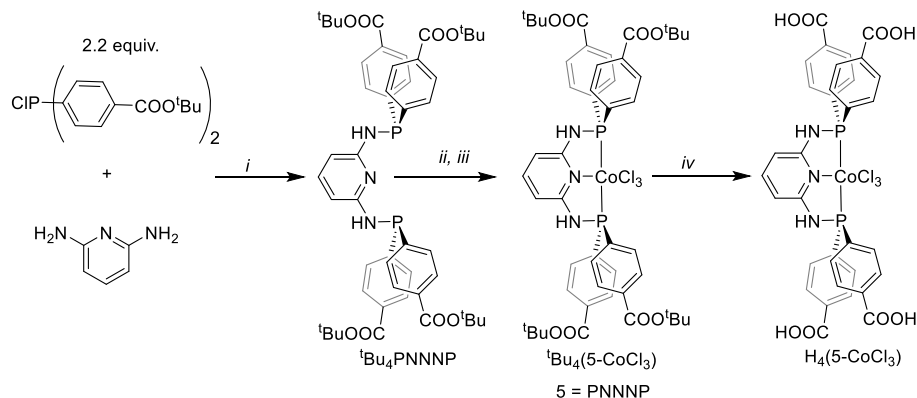
MOFs have emerged as a versatile class of porous materials with potential applications in areas such as gas storage and separation, heterogeneous catalysis, drug delivery, and electronic devices.^{215–218} Much of the interest in MOFs stems from their well-defined porous structures and ability to accommodate a wide range of chemical functionalities at both the inorganic and organic building units. However, reactive functional groups are often challenging to incorporate via *de novo* synthesis, prompting the development of a wide variety of postsynthetic modification strategies.^{219–221} Among these, postsynthetic metal exchange (PSME) at either the metal nodes or organic linkers has become a valuable strategy for accessing materials that cannot be obtained by direct solvothermal assembly.^{58,222–224} Significant progress towards understanding PSME at the metal nodes of MOFs^{225–233} has led to the development of new materials with enhanced performance in gas separation processes, heterogeneous catalysis, and other applications.^{234–250} However, PSME at organometallic linker groups has been explored to a lesser extent, and reported examples have generally been limited to MOFs containing metallosalen and metalloporphyrins struts.^{73,77,251–255} For example, Shultz et al. reported the demetallation of Mn from a metallosalen-based MOF using H₂O₂ as the demetalating reagent.²⁵¹ The resulting material could be remetallated with a variety of divalent transition metal cations, and its catalytic activity for enantioselective epoxidation restored. Ma and coworkers demonstrated that Cd²⁺ weakly bound at the porphyrin-based linkers of MMPF-5 could be readily exchanged for Co²⁺, yielding a material that performed well for catalytic epoxidation of trans-stilbene.⁷³ More recently, Jiang et al. have reported PSME of Cd for

first row transition metals at both the metal nodes and porphyrin linkers of a chiral porphyrin-salen MOF.²⁵⁴ The exchange could be carried out in a single crystal to single crystal transformation, and the Co²⁺-exchanged analogue catalyzed asymmetric cycloaddition of CO₂ with epoxides.

The combination of the chelating pincer framework and strong phosphine donor groups confers a high degree of stability that makes the pincer complexes resistant to demetallation and often allows them to withstand high temperatures and harsh catalytic conditions. Consequently, reported examples of metal exchange reactions with pincer ligand scaffolds are rare and have been limited to a few Zr and Ag complexes.^{256–259} To the best of our knowledge, there are no reported examples of transition metal exchange reactions with diphosphine pincer complexes. This chapter describes the synthesis, characterization and reactivity investigation of a Zr MOF, **6-CoCl₃**, constructed from PNNNP-Co^{III} pincer metallolinkers. Both the MOF and the homogeneous analogue of the linker undergo Co demetallation under reducing conditions and transmetallation with Rh^I and Pt^{II}. PSME was used to access MOFs containing PNNNP-M (M = Rh, Pt) pincer complexes that have been difficult to obtain by the direct solvothermal synthesis. Furthermore, a multimetallic MOF, containing both PNNNP-Rh and PNNNP-Pt pincer complexes, **6-RhPt**, has been generated through sequential substitution of Co with Pt followed by Rh.

4.2 Synthesis and characterization of PNNNP-CoCl₃ pincer complexes

Scheme 12. Synthesis of PNNNP-CoCl₃ pincer complexes



Reagents: *i*) Et₃N (2.5 equiv.), Toluene, 70 °C, 16 h. (*ii*) [CoCl₂(C₅H₅N)₄]Cl, CH₂Cl₂, rt, 1 h; (*iii*) [(*n*-C₄H₉)₄N]Cl, CH₂Cl₂, 35 °C, 16 h; (*iv*) CF₃CO₂H, HCl(aq.), CH₂Cl₂, rt, 16 h

The reaction between CIP(C₆H₅-COO^tBu)₂ and 2,6-diaminopyridine in the presence of Et₃N provides the ^tBu₄PNNNP pincer ligand as a white powder in 87 % yield (Scheme 12). Reaction of ^tBu₄PNNNP with [CoCl₂(C₅H₅N)₄]Cl followed by [(*n*-C₄H₉)₄N]Cl furnishes ^tBu₄(5-CoCl₃) (5 = PNNNP) as an orange powder in 84 % yield. The ³¹P{¹H} NMR spectrum of ^tBu₄(5-CoCl₃) shows a single resonance at 67.5 ppm, which is shifted downfield from that of the free ligand (25.4 ppm in CDCl₃) and consistent with metalation (Figure 23b). In addition, ¹H NMR spectrum shows all expected resonances for ^tBu₄(5-CoCl₃) (Figure 23a). Subsequent deprotection of the tert-butyl ester groups using CF₃CO₂H/CH₂Cl₂ generates the tetra-carboxylic acid metallolinker H₄(5-CoCl₃). H₄(5-CoCl₃) was characterized using ¹H and ³¹P NMR spectroscopy analysis as well as elemental analysis (Figure 23).

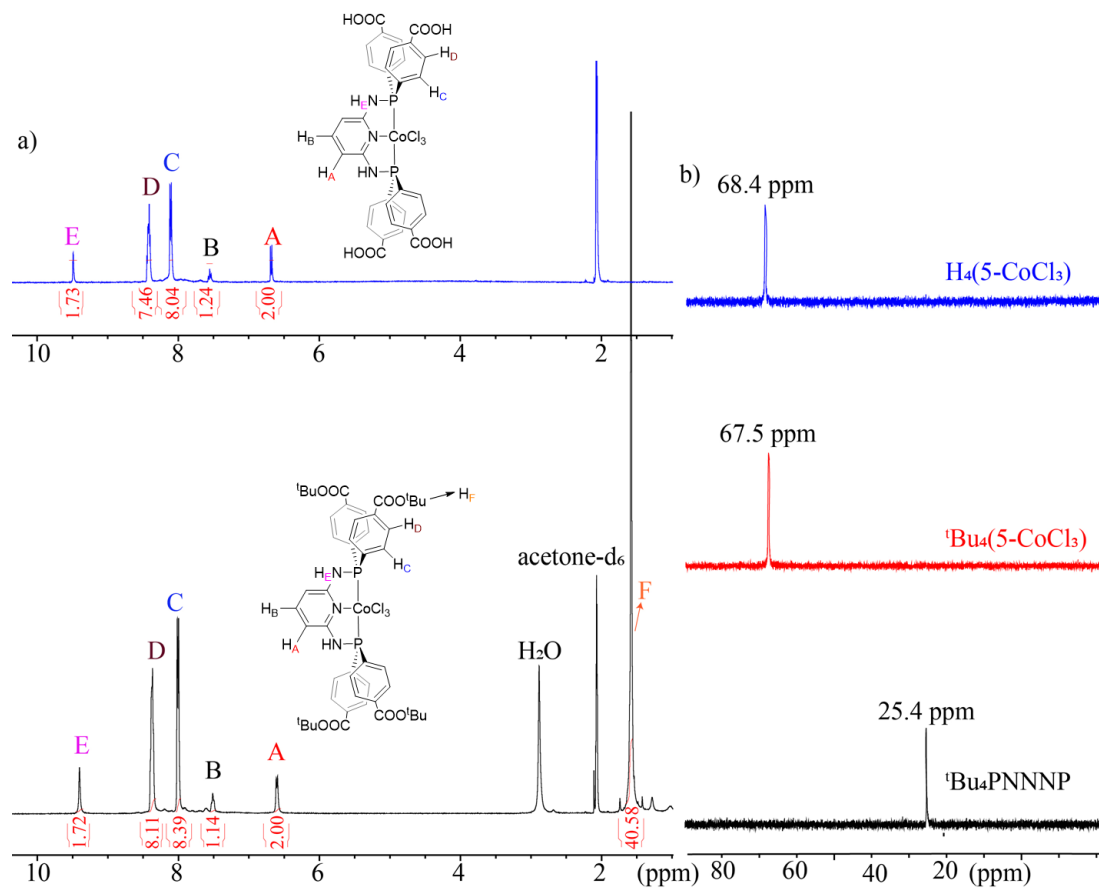
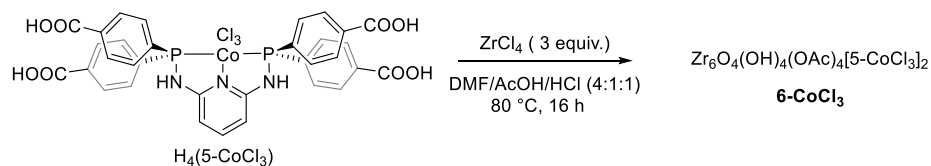


Figure 23. a) ^1H NMR spectra (acetone- d_6) of ${}^t\text{Bu}_4(5\text{-CoCl}_3)$ and $\text{H}_4(5\text{-CoCl}_3)$. b) $^{31}\text{P}\{^1\text{H}\}$ NMR spectra of ${}^t\text{Bu}_4\text{PNNNP}$, ${}^t\text{Bu}_4(5\text{-CoCl}_3)$ and $\text{H}_4(5\text{-CoCl}_3)$.

4.3 Synthesis and characterization of 6-CoCl_3



Scheme 13. Solvothermal synthesis of 6-CoCl_3

A solution of $\text{H}_4(5\text{-CoCl}_3)$ and ZrCl_4 in 4/1/1 (v/v/v) (DMF)/AcOH/HCl (conc. aq.) was sealed in a 20 mL vial and heated at 80 °C for 16 h, resulting in formation of 6-CoCl_3 as an orange microcrystalline powder (Scheme 13). The structure of 6-CoCl_3 has been

determined from SPXRD data (Figure 24a and b). Indexing provided a hexagonal unit cell ($a = 32.42 \text{ \AA}$, $c = 15.41 \text{ \AA}$) with no systematic absences that would indicate the presence of screw axes or glide planes. An initial structure model was constructed with $P6/mmm$ space group symmetry based on the positions of the heavy atoms located using a charge flipping algorithm.²⁶⁰

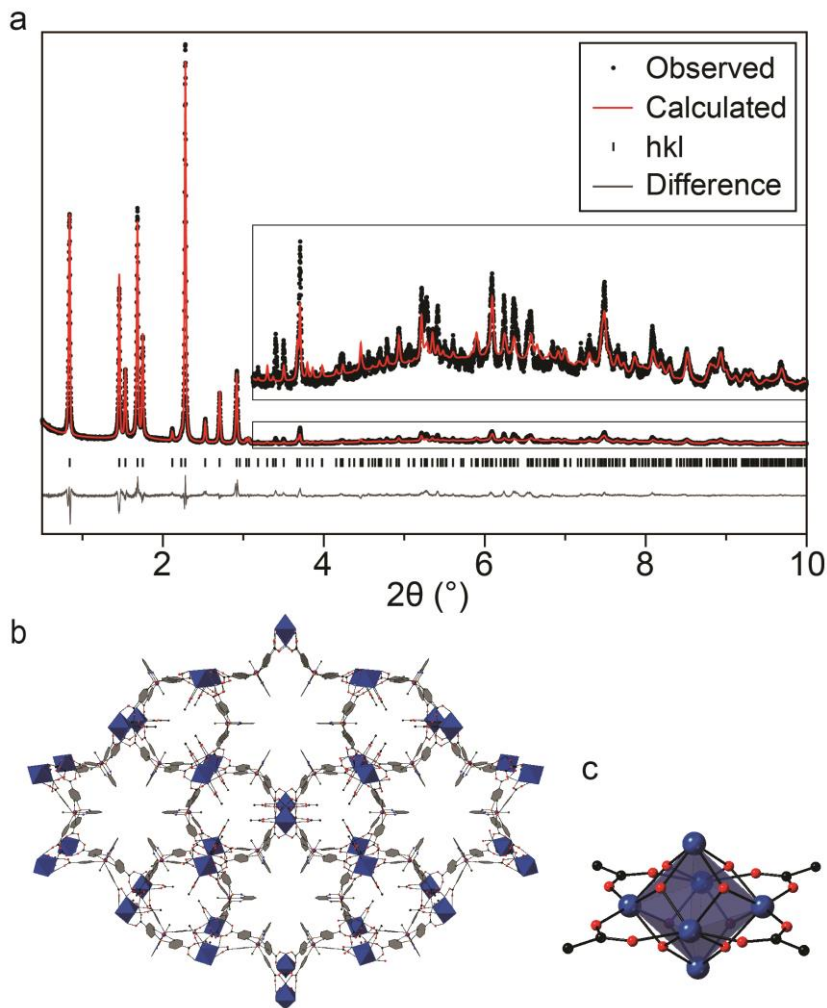


Figure 24. a) Final Rietveld refinement profile of **6-CoCl₃** from SPXRD data ($\lambda = 0.412697 \text{ \AA}$). b) Framework structure of **6-CoCl₃**. The blue octahedra represent $[\text{Zr}_6\text{O}_4(\text{OH})_4]^{12+}$ clusters. c) Structure of the D_{4h} $[\text{Zr}_6\text{O}_4(\text{OH})_4(\text{OAc})_4]^{8+}$ secondary building units.

The model indicated that the structure of **6-CoCl₃** is similar to that of csq-net Zr MOFs containing 8-connected Zr₆ clusters ($[(\text{Zr}_6\text{O}_4(\text{OH})_4(\text{OAc})_4)]^{8+}$, OAc = CH₃CO₂⁻, Figure 24c) and tetratopic metalloporphyrin- or pyrene-based linkers.^{261–263} Rietveld refinements using simulated annealing with the metal cluster and linker as rigid bodies were carried out in the *P6* space group for six structure permutations arising from three possible orientations of the Zr₆ clusters and two possible orientations of the [5-CoCl₃]⁴⁻ linkers (Figure 25). A structural arrangement with the C₄ axis of the Zr₆ clusters aligned perpendicular to the crystallographic c-axis and the central arene group of the [5-CoCl₃]⁴⁻ pincer complexes perpendicular to the ab plane provided the best fit to the data (Figure 24b). The space group symmetry was subsequently increased from *P6* to *P6/mmm* while maintaining the refinement residuals. When allowed to refine freely, the occupancy of the [5-CoCl₃]⁴⁻ rigid body converged to 47 % ($R_{\text{wp}} = 10.563$), which corresponds to a linker:Zr₆ cluster ratio of 0.94:1. The low refined occupancy of the [5-CoCl₃]⁴⁻ linker reflects a significant deviation from the anticipated framework formula of Zr₆O₄(OH)₄(OAc)₄(5-CoCl₃)₂ and points to missing-linker defects. The presence of these defects has been corroborated by spectroscopic characterization and elemental analysis (vide infra). The final structure of **6-CoCl₃** is best described by a xly net with the phosphine groups of [5-CoCl₃]⁴⁻ as 3-c branch points.²⁶⁴ It contains trigonal and hexagonal channels along the c-axis that have maximum diameters of ~ 10 Å and ~15 Å, respectively, with the CoCl₃ groups of the [5-CoCl₃]⁴⁻ pincers facing inward to the smaller trigonal channels.

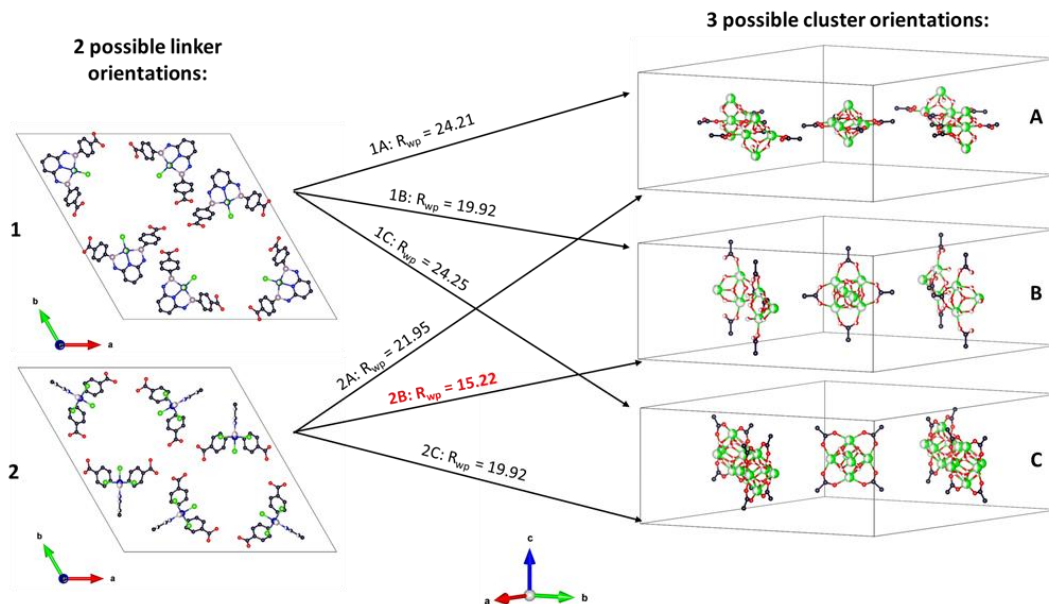


Figure 25. $[5\text{-CoCl}_3]^{4-}$ linker (left) and Zr_6 cluster (right) rigid bodies used for Rietveld refinement of **6-CoCl₃** in the $P6$ space group.

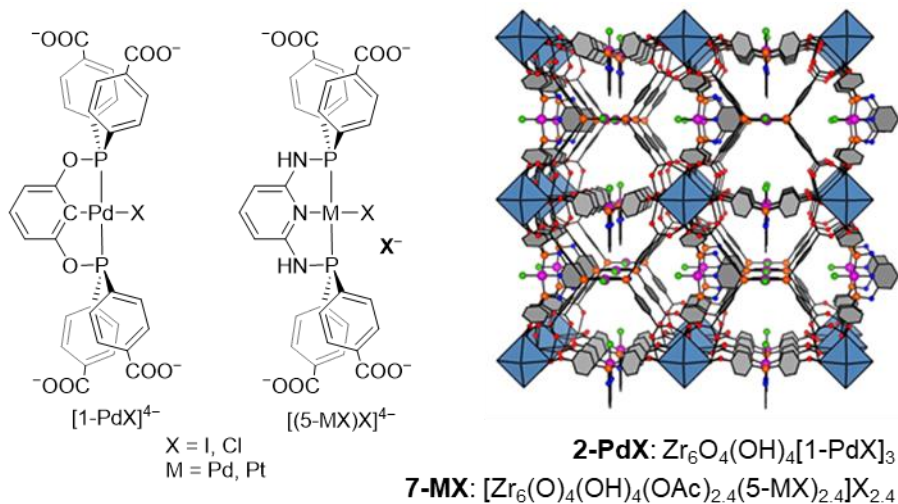


Figure 26. Square planar diphosphine pincer metallolinkers and framework structure adopted by the isostructural series of Zr pincer MOFs **2-PdX**, **7-PdX**, and **7-PtX**.

Notably, the structure of **6-CoCl₃** differs from that of an isostructural series of Zr MOFs assembled from Pd and Pt diphosphine pincer complexes.^{82,125} **2-PdX**, **7-PdX**, and **7-PtX** all adopt a cubic framework structure that can be described by a ftw net (Figure

26). The framework topology of Zr MOFs containing other tetratopic linkers has been shown to depend on the intramolecular torsion angles maintained between the linker core and benzoate arms.²⁶³ In the case of **6-CoCl₃**, the axial ligands of the pseudo-octahedral Co^{III} center are more likely to inhibit rotation of the benzoate groups than the square planar Pd and Pt centers in **2-PdX**, **7-PdX**, and **7-PtX**. Thus we attribute the difference in observed topologies of the Zr pincer MOFs to the coordination environment of the pincer-supported metal center and its impact on the freedom of rotation of the benzoate groups.

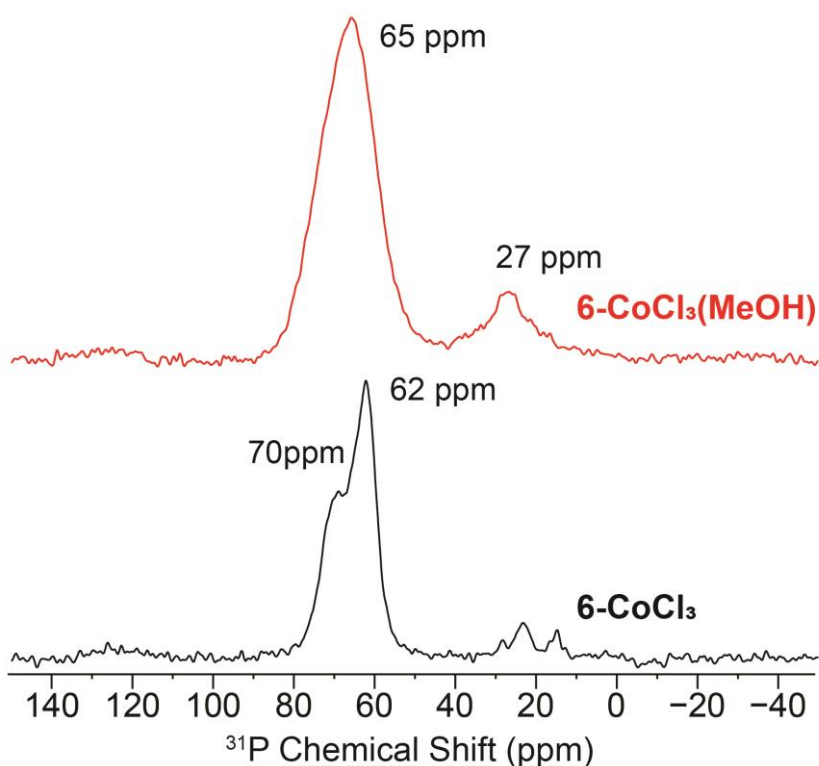


Figure 27. Solid-state ³¹P NMR spectra for as-synthesized **6-CoCl₃** and **6-CoCl₃(MeOH)** with magic-angle spinning (MAS) and total suppression of spinning sidebands (TOSS).

NMR spectroscopic characterization and elemental analysis of **6-CoCl₃** are consistent with the framework structure determined from the SPXRD data and provide further insight into the composition. The solid-state ³¹P NMR spectrum of **6-CoCl₃** reveals

two major resonances centered at 62 and 70 ppm (Figure 27). These signals appear at a similar chemical shift as the resonance observed for $\text{H}_4(5\text{-CoCl}_3)$ in solution (68.4 ppm, Figure 23b), supporting the presence of similar Co^{III} pincer species in the MOF.

Minor signals observed in the 15-30 ppm region are consistent with the presence of a small amount of oxidized phosphine species arising from decomposition of the PNNNP pincer linkers.^{82,125} However, quantitative analysis of the spectrum was hampered by fast T_2 relaxation that likely arises from a small amount of paramagnetic Co^{II} species present in the sample (vide infra). The solution-state ^{31}P NMR spectrum measured for an acid-digested ($\text{CF}_3\text{CO}_2\text{H}/\text{C}_6\text{D}_6$, 3/1, v/v) sample of **6-CoCl₃** exhibits a major signal at 67.6 ppm (~86 %) and minor one at 67.2 ppm (~14 %) (Figure 28). The ^{31}P NMR spectrum of $\text{H}_4(5\text{-CoCl}_3)$ shows similar speciation in the same solvent mixture, suggesting that the acid digestion conditions induce Co-Cl solvolysis. Consequently, the acid-digested ^{31}P NMR data do not provide direct insight into the speciation of the PNNNP- Co^{III} linkers present in the MOF. We surmise that the two distinct signals observed in the solid-state ^{31}P NMR spectrum of **6-CoCl₃** arise from a mixture of $\text{Co}^{\text{III}}\text{Cl}_3$ and $\text{Co}^{\text{III}}\text{Cl}_2(\text{X})$ pincer species, but the identity of the putative X ligand has not been firmly established.

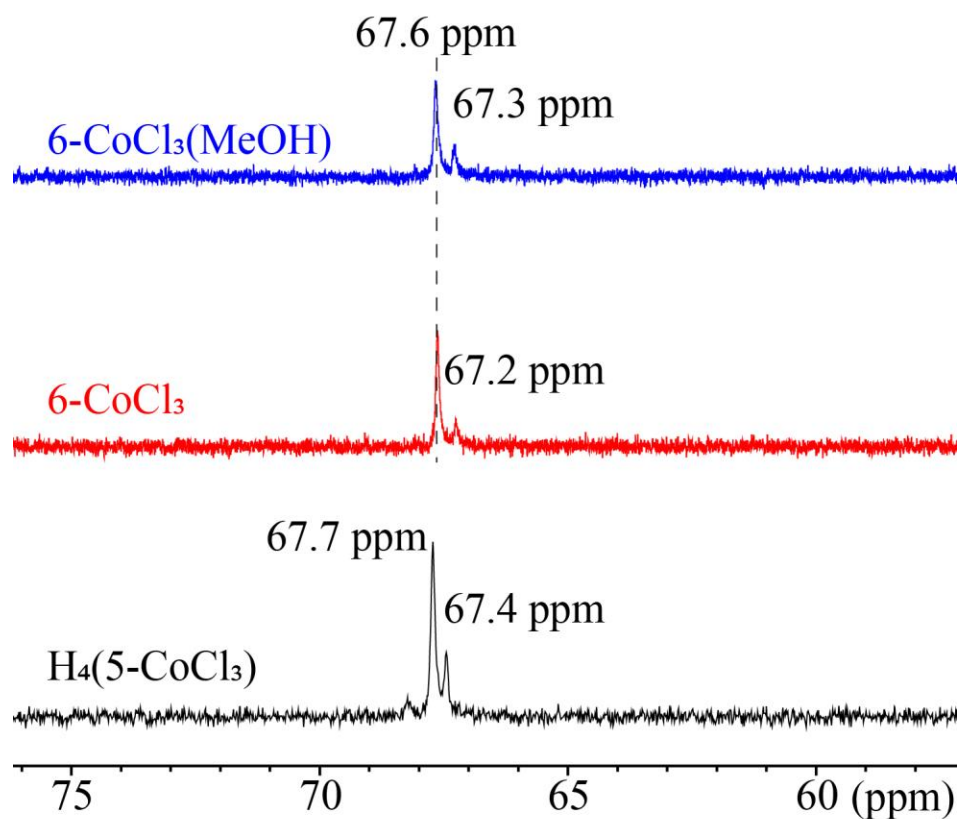


Figure 28. $^{31}\text{P}\{^1\text{H}\}$ NMR spectra ($\text{CF}_3\text{CO}_2\text{H}/\text{C}_6\text{D}_6$) of **6-CoCl₃**, **6-CoCl₃(MeOH)** and **H₄(5-CoCl₃)**.

The ^1H NMR spectrum of an acid-digested sample of as-synthesized **6-CoCl₃** displays all signals expected for **H₄(5-CoCl₃)** as well as resonances corresponding to AcOH, HCO₂H, and $[\text{Me}_2\text{NH}_2]^+$ (Figure 29). While the AcOH should result from digestion of $[\text{Zr}_6\text{O}_4(\text{OH})_4(\text{OAc})_4]^{8+}$ SBUs, the latter species seem to arise from pore-occluding guests. Indeed, the impurities responsible for the appearance of HCO₂H, and $[\text{Me}_2\text{NH}_2]^+$ could be removed by soaking the MOF in MeOH over a period of 24 h to generate **6-CoCl₃(MeOH)**. This washing procedure does not affect the bulk crystallinity of the MOF

but does exacerbate decomposition of the pincer complex as observed from the solid-state ^{31}P NMR spectrum (Figure 27). Moreover, the two distinct ^{31}P NMR resonances that were present in the solid-state spectrum of **6-CoCl₃** merge into a broad signal centered at 65 ppm in **6-CoCl₃(MeOH)** (Figure 27). Efforts to remove the impurities with other solvents such as acetone, DMF, or THF were unsuccessful.

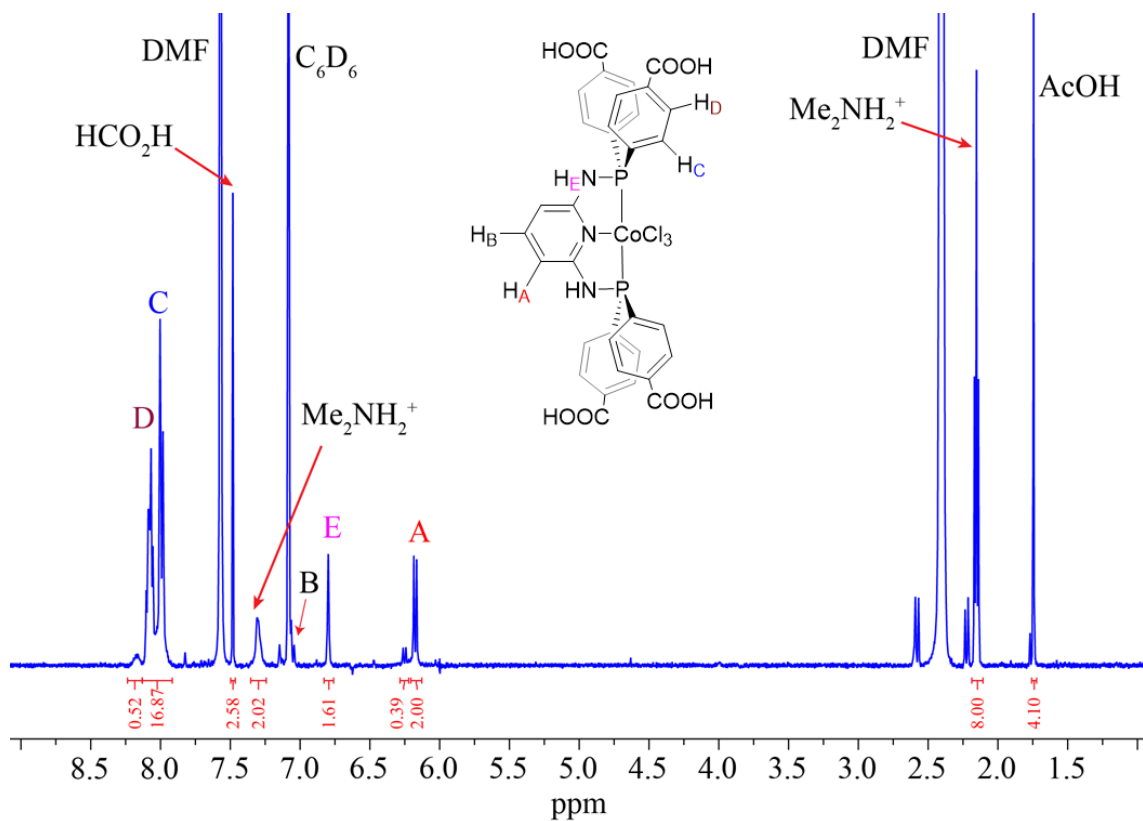


Figure 29. ^1H NMR spectrum ($\text{CF}_3\text{CO}_2\text{H}/\text{C}_6\text{D}_6$) of as synthesized **6-CoCl₃**.

TGA analysis of **6-CoCl₃** shows a ~53 % mass loss up to 200 °C, consistent with the loss of guest solvent molecules from the porous framework (Figure 30a). However, N_2 adsorption isotherms (77 K) measured for a sample of **6-CoCl₃(MeOH)** desolvated by heating under reduced pressure (10^{-4} Torr, 100 °C) showed low N_2 uptake and gave a

calculated BET surface area of $366 \text{ m}^2 \text{ g}^{-1}$ (Figure 30b). X-ray powder diffraction (PXRD) analysis of the desolvated samples revealed nearly complete loss of crystallinity and attempts to activate **6-CoCl₃** prior to solvent exchange or employ milder activation conditions to **6-CoCl₃(MeOH)** gave similar results. Despite its apparent structural collapse upon desolvation, **6-CoCl₃(MeOH)** retains guest accessible porosity when suspended in organic solvents as evidenced by its amenability to PSME (*vide infra*).

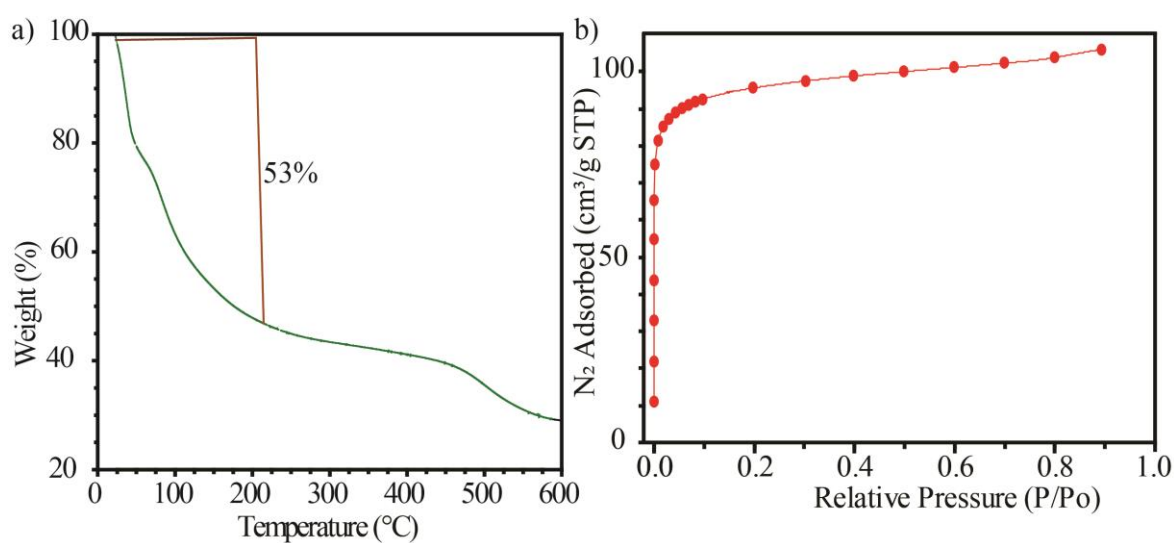


Figure 30. a) TGA data for a sample of **6-CoCl₃** measured at a ramp rate of $5 \text{ }^\circ\text{C}/\text{min}$ under flowing N_2 ($50 \text{ mL}/\text{min}$). b) N_2 adsorption isotherm measured at 77 K for **6-CoCl₃(MeOH)** after desolvation at $100 \text{ }^\circ\text{C}$ and 10^{-4} torr .

ICP-OES analysis of **6-CoCl₃(MeOH)** provided a Zr:Co ratio of 6:1.66, which is larger than expected for a defect-free structure (Zr:Co = 6:2), but in line with the presence of decomposed linker species observed in the solid-state ^{31}P NMR spectra. The Co deficiency is also consistent with the low occupancy of the $[\text{5-CoCl}_3]^{4-}$ linkers determined from the Rietveld refinement. The ^{31}P NMR spectrum of an acid-digested sample of activated **6-CoCl₃(MeOH)** exhibits a minor signal at 33.5 ppm , implicating the phosphinic

acid species ($\text{Ar}_2\text{PO}_2\text{H}$, $\text{Ar} = \text{p-C}_6\text{H}_4\text{CO}_2^-$) as the linker decomposition product (Figure 31b).⁸² Integration of the spectrum shows that $\text{Ar}_2\text{PO}_2\text{H}$ is present in a ~0.2:1 ratio with respect to $\text{H}_4(5\text{-CoCl}_3)$.

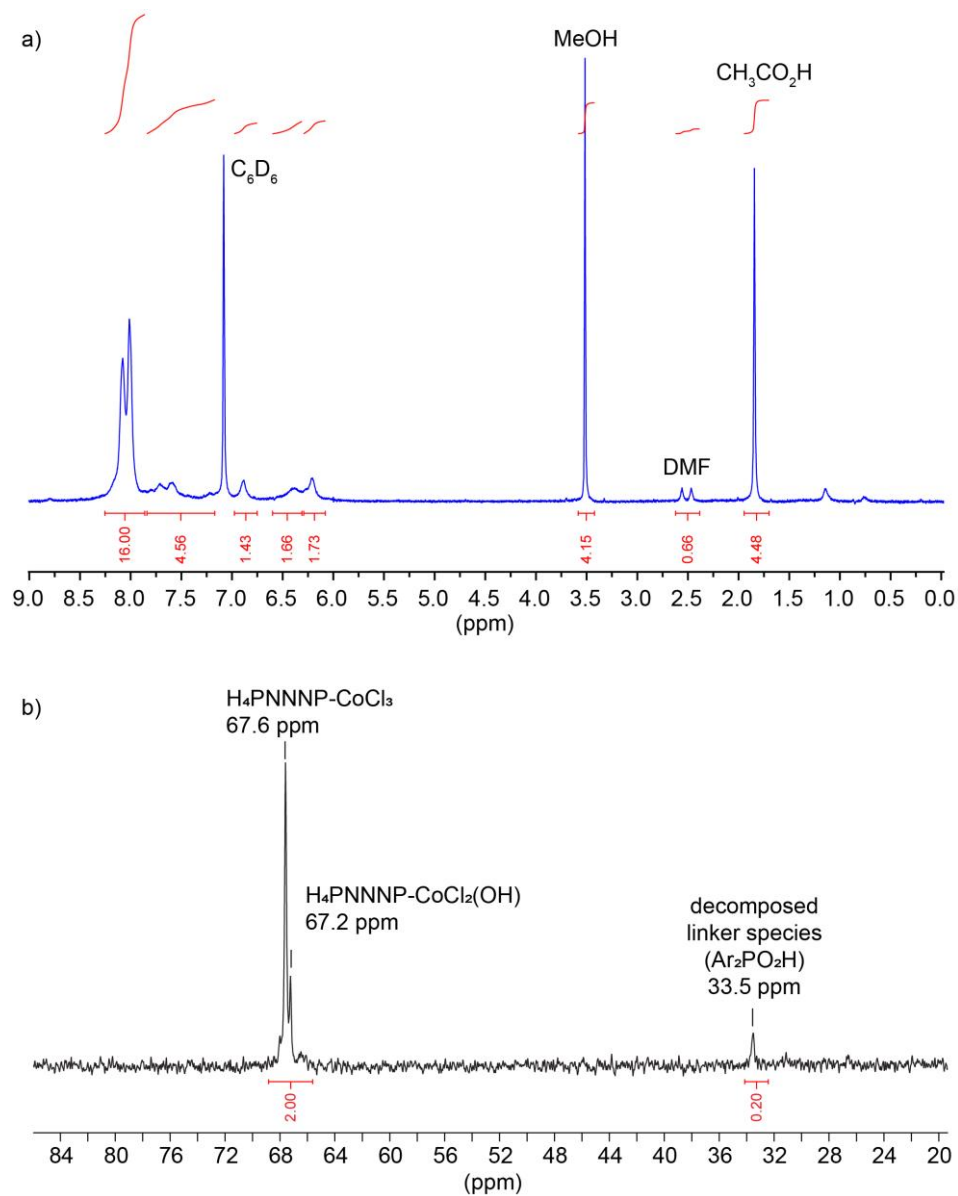


Figure 31. Acid-digested a) ^1H and b) $^{31}\text{P}\{^1\text{H}\}$ NMR spectra ($\text{CF}_3\text{CO}_2\text{H}/\text{C}_6\text{D}_6$) of **6-CoCl₃(MeOH)** after activation.

The corresponding ^1H NMR spectrum again shows the presence of $\text{CH}_3\text{CO}_2\text{H}$ as well as ~ 1.3 equiv. of MeOH per linker (Figure 31a). Based on the spectroscopic and analytical data, the empirical formula of desolvated **6-CoCl₃(MeOH)** is best provided as $[\text{Zr}_6\text{O}_4(\text{OH})_4](\text{OH})_{2.2}(\text{MeOH})_{2.2}(\text{OAc})_{2.5}(5\text{-CoCl}_3)_{1.66}(\text{Ar}_2\text{PO}_2\text{H})_{0.33}$.

4.4 Postsynthetic metal exchange (PSME)

In the course of our investigations, we observed that heating a suspension of **6-CoCl₃(MeOH)** in DMF at 85°C resulted in the formation of a green supernatant solution. Monitoring the thermolysis *via* XRF revealed a substantial loss of Co from the framework while PXRD analysis showed a decline in sample crystallinity (Figure 32).

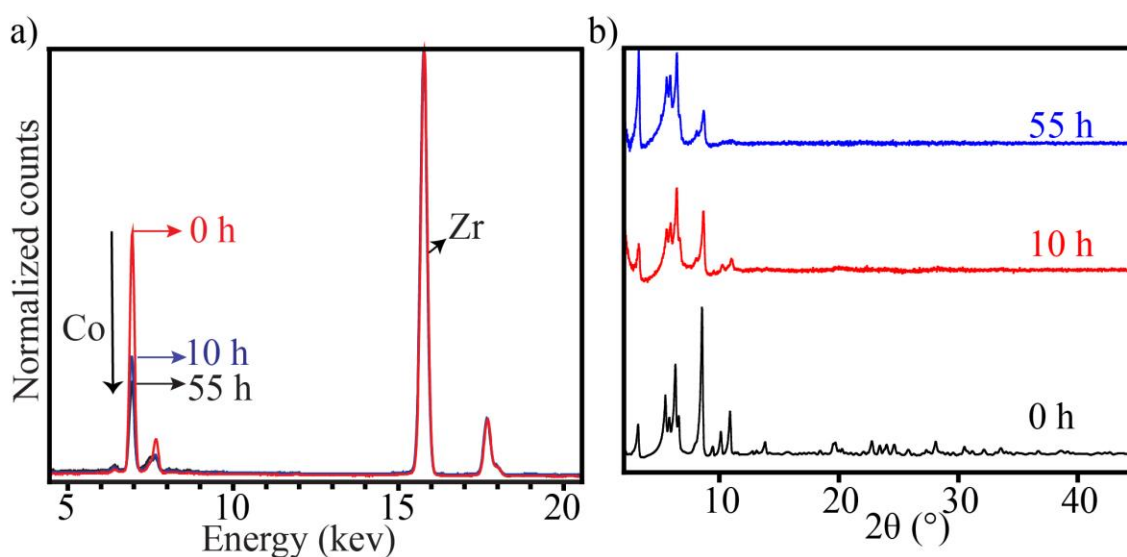


Figure 32. a) XRF spectra and b) PXRD patterns (Cu-K α radiation, $\lambda = 1.5418 \text{ \AA}$) of **6-CoCl₃** before and after heating at 85°C in DMF at different reaction time.

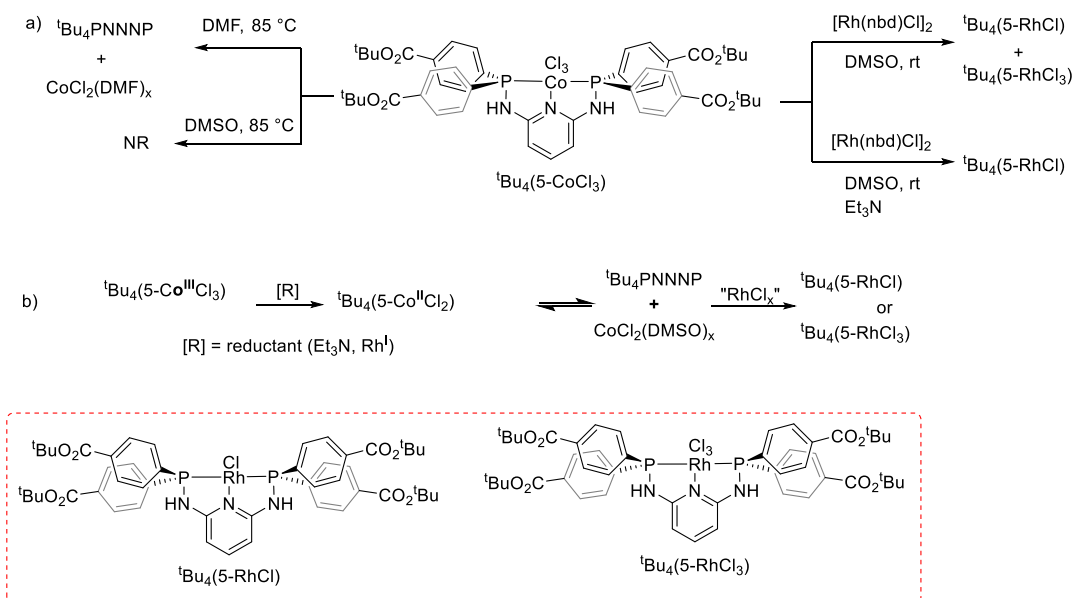
A similar experiment carried out with the homogeneous pincer complex $^t\text{Bu}_4(5\text{-CoCl}_3)$ also resulted in formation of a green solution and disappearance of the corresponding ^{31}P NMR signal at 67.2 ppm. Together these results pointed to surprisingly facile demetallation of the $[5\text{-CoCl}_3]^{4-}$ linkers, and we sought to leverage this behavior to access pincer MOFs

that have proven difficult or impossible to assemble under direct solvothermal conditions. For example, the Rh^I pincer complex ^tBu₄(5-RhCl) is highly susceptible to oxidation and has so far been incompatible with the deprotection conditions necessary for direct synthesis of a Zr MOF. In addition, linkers based on Pd^{II} and Pt^{II} diphosphine pincer complexes have been observed to form Zr MOFs with a ftw topology, but polymorphs with the csq topology have not been accessible by direct solvothermal synthesis. Consequently, we set out to elucidate the mechanism of demetallation of the PNNNP-Co^{III} pincer complexes and investigate Rh/Co and Pt/Co postsynthetic metal exchange in **6-CoCl₃(MeOH)**.

In order to establish the ability of the Co^{III} pincer species to undergo metal exchange, preliminary reactions were carried out with the homogeneous complex ^tBu₄(5-CoCl₃) (Scheme 14a). A solution of ^tBu₄(5-CoCl₃) and [Rh(nbd)Cl]₂ (0.5 equiv., nbd = 2,5-norbornadiene) in DMSO-*d*₆ was monitored by ³¹P NMR spectroscopy at room temperature. Within 4 h the spectrum showed complete disappearance of the signal corresponding to ^tBu₄(5-CoCl₃) concomitant with the appearance of two new doublet resonances centered at 80 ppm (¹J_{Rh-P} = 154.7 Hz) and 65 ppm (¹J_{Rh-P} = 93.7 Hz) in a 2:1 ratio, respectively (Figure 33a). The doublet at 80 ppm matches that observed for a sample of ^tBu₄(5-RhCl) synthesized by direct reaction of ^tBu₄PNNNP with [Rh(nbd)Cl]₂ while the upfield shift and smaller ¹J_{Rh-P} coupling for the signal at 65 ppm prompts its assignment as the Rh^{III} pincer complex ^tBu₄(5-RhCl₃).²⁶⁵ The presence of the Rh^{III} pincer complex reveals that a redox reaction occurs between Rh^I and Co^{III} during the metal exchange process and reduction of Co^{III} to a more labile Co^{II} species is likely a key factor in demetallation of the PNNNP pincer complexes. In support of this notion, ^tBu₄(5-CoCl₃)

showed no signs of demetallation upon heating at 85 °C in DMSO solution (Figure 33b). However, the corresponding ^{31}P NMR signal quickly disappeared upon addition of a stoichiometric amount of Et_3N at room temperature, indicating that Et_3N causes reduction to a paramagnetic PNNNP- Co^{II} species (Figure 33b).

Scheme 14. a) Demetallation and metal exchange reactions of ${}^t\text{Bu}_4(5\text{-CoCl}_3)$. b) Proposed mechanism for metal exchange of ${}^t\text{Bu}_4(5\text{-CoCl}_3)$.



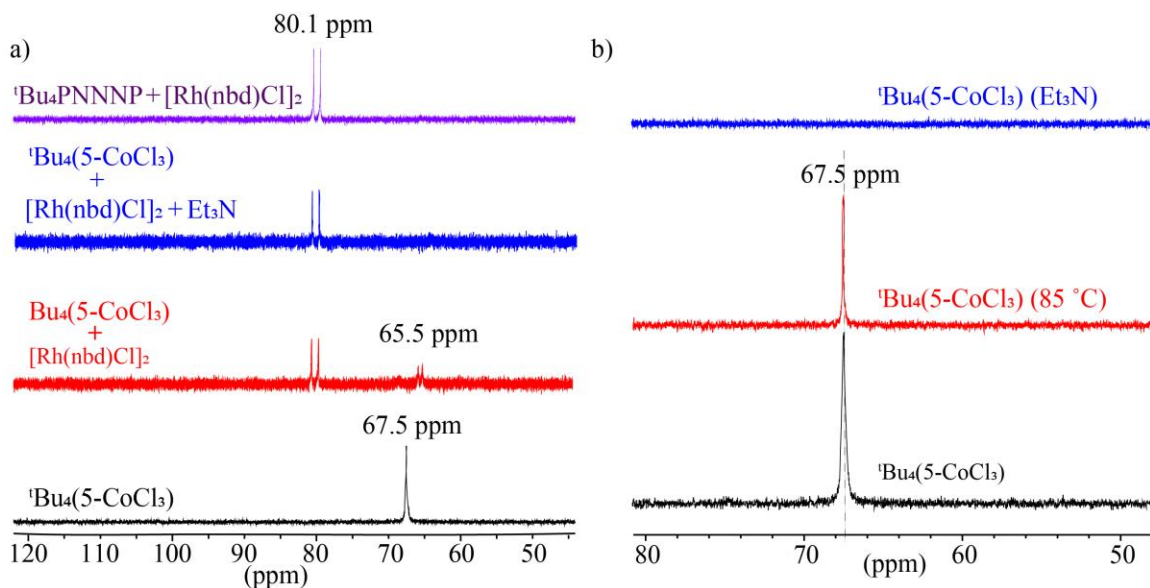


Figure 33. a) $^{31}\text{P}\{^1\text{H}\}$ NMR spectra for reactions between ${}^t\text{Bu}_4(5\text{-CoCl}_3)$ and $[\text{Rh}(\text{nbd})\text{Cl}]_2$ with and without Et_3N , and reaction of ${}^t\text{Bu}_4\text{PNNNP}$ with $[\text{Rh}(\text{nbd})\text{Cl}]_2$ in DMSO. b) $^{31}\text{P}\{^1\text{H}\}$ NMR spectra of ${}^t\text{Bu}_4(5\text{-CoCl}_3)$ before and after heating in DMSO at $85\text{ }^\circ\text{C}$, and after reaction with Et_3N at room temperature.

Moreover, when a THF suspension of **6-CoCl₃(MeOH)** was heated at $60\text{ }^\circ\text{C}$ in the presence of Et_3N (~ 2 equiv. per Co), the solid underwent a color change from orange to light pink. PXRD analysis showed that the MOF retains crystallinity and a large increase in the EPR signal compared to the spectrum measured for **6-CoCl₃(MeOH)** confirms the formation of paramagnetic Co^{II} species (Figure 34). Thus, it appears that the demetallation of the PNNNP- Co^{III} pincer complexes observed in DMF solution is facilitated by the ability of the solvent to reduce Co^{III} to Co^{II} and stabilize the expelled metal ion. When the metal exchange reaction between ${}^t\text{Bu}_4(5\text{-CoCl}_3)$ and $[\text{Rh}(\text{nbd})\text{Cl}]_2$ was carried out in DMSO solution containing NEt_3 as a sacrificial reductant, ${}^t\text{Bu}_4(5\text{-RhCl})$ was observed as the sole product (Figure 33a). Altogether these results support an exchange mechanism that involves initial reduction of Co^{III} to Co^{II} (Scheme 14b).

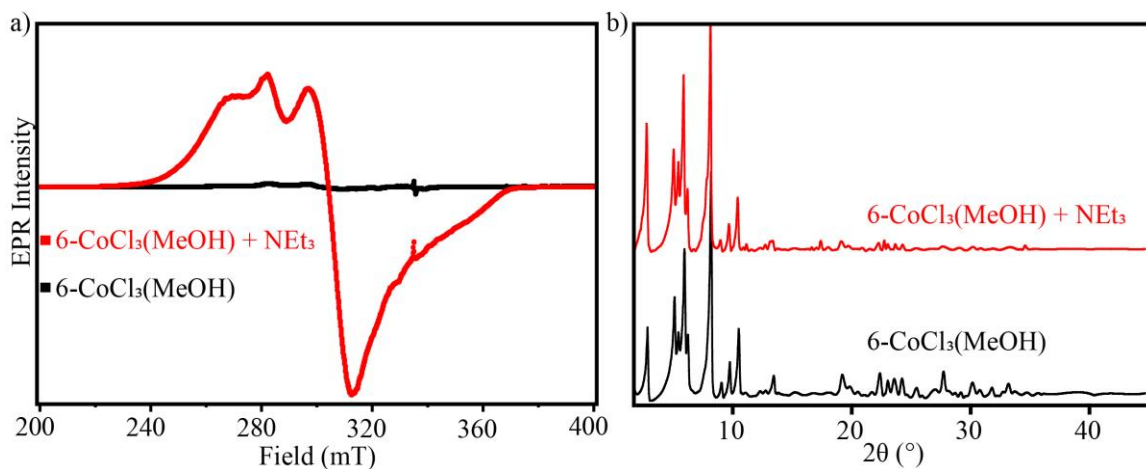
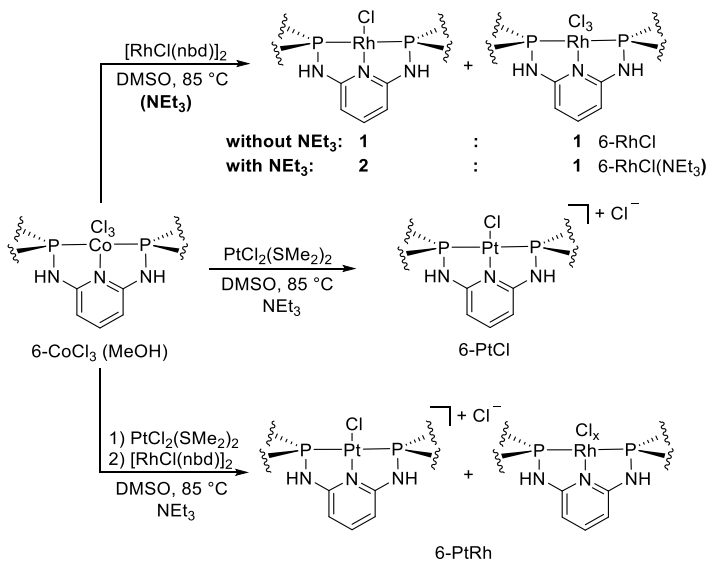


Figure 34. a) X-band EPR spectra of **6-CoCl₃(MeOH)** before and after reaction with Et₃N in THF. Spectra were recorded at 10 K. Microwave frequency = 9.385 GHz, power = 0.002 mW, modulation amplitude = 0.8 mT/100 kHz. b) PXRD patterns (Cu-K α radiation, λ = 1.5418 Å) of **6-CoCl₃(MeOH)** before and after reaction with Et₃N at 60 °C in THF.

Scheme 15. PSME reactions of **6-CoCl₃(MeOH)**



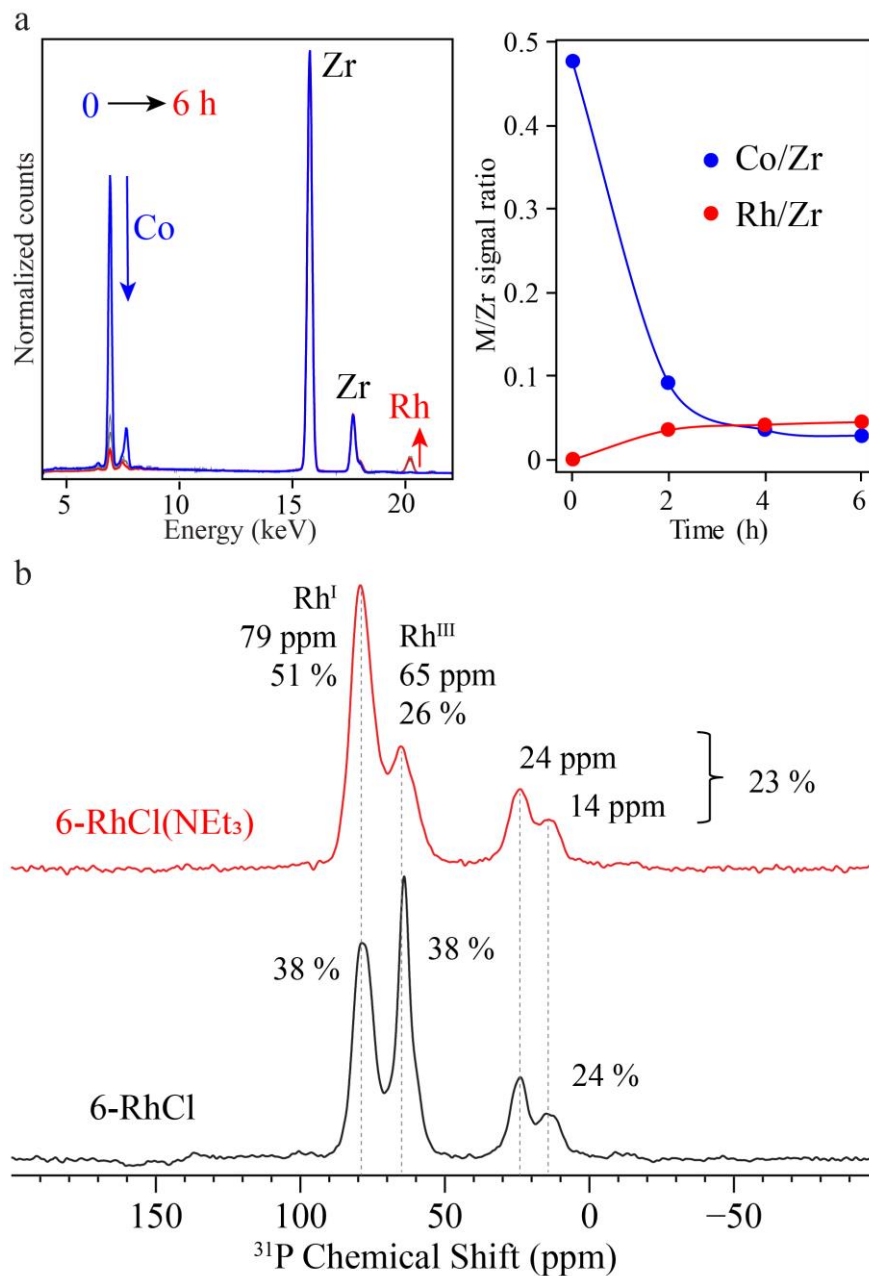


Figure 35. a) XRF spectra and kinetic plot showing the rate of Rh/Co PSME in **6-CoCl₃(MeOH)**. b) Solid-state ^{31}P NMR spectra of **6-RhCl** and **6-RhCl(NEt₃)** with MAS and TOSS.

Guided by the mechanistic information obtained from the homogeneous complex, Rh/Co PSME was investigated for **6-CoCl₃(MeOH)**. No metal exchange was observed when a

sample of **6-CoCl₃(MeOH)** was treated with a solution of [Rh(nbd)Cl]₂ in DMSO at room temperature for 12 h. However, heating the suspension at 85 °C resulted in the formation of **6-RhCl** as a bright yellow solid (Scheme 15). The progress of Rh/Co metal exchange was monitored by XRF (Figure 35a), and within 6 h, the Co-based emission signal had nearly disappeared, concomitant with the appearance of a new Rh signal. Similar results were obtained when the PSME reaction was carried out in the presence of a stoichiometric amount of NEt₃ to generate **6-RhCl(NEt₃)**. ICP-OES analysis of **6-RhCl** and **6-RhCl(NEt₃)** provided Zr:Rh:Co ratios of 6:1.64:0.03 and 6:1.33:0.15, respectively, confirming nearly complete Rh/Co exchange based on the empirical formula previously derived for **6-CoCl₃(MeOH)**. The solid-state ³¹P NMR spectra of **6-RhCl** and **6-RhCl(NEt₃)** both display two major resonances centered at 79 and 65 ppm that can be assigned as Rh^I and Rh^{III} pincer species, respectively (Figure 35b). Similar to the spectra measured for **6-CoCl₃(MeOH)**, minor signals (~23 %) attributed to decomposed linker species are observed in the 15-30 ppm region. Integration of the spectrum of **6-RhCl** shows a ~1:1 ratio of Rh^I:Rh^{III} pincer species, while the addition of Et₃N resulted in an increase to a ~2:1 Rh^I:Rh^{III} ratio for **6-RhCl(NEt₃)**. Thus, while Et₃N appears to maintain its role as a sacrificial reductant, it is less effective in the MOF than for the homogeneous complex. Attempts to prevent the oxidation of Rh^I by performing the exchange reaction in the presence of increased amounts of Et₃N resulted in little change in the Rh^I:Rh^{III} ratio observed by solid-state ³¹P NMR (Figure 36a).

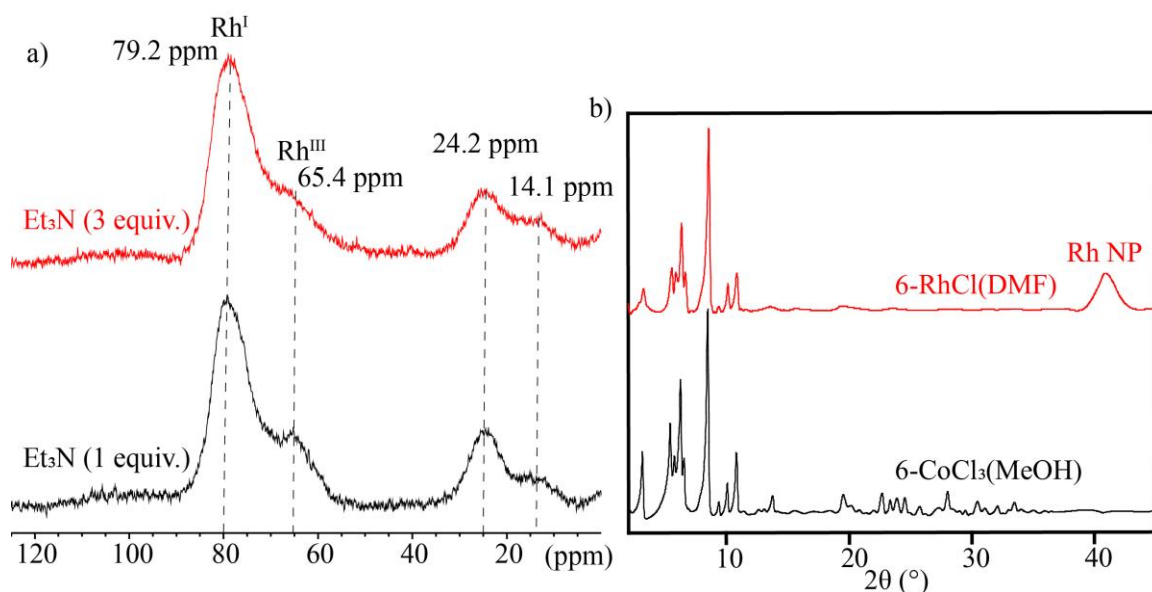


Figure 36. a) Solid-state ^{31}P NMR spectra for samples of **6-RhCl(Et₃N)** generated by Rh/Co PSME of **6-CoCl₃(MeOH)** with $[\text{Rh}(\text{nbd})\text{Cl}]_2$ and 1 or 3 equiv. of Et_3N per Co. b) PXRD patterns (Cu-K α radiation, $\lambda = 1.5418 \text{ \AA}$) of the product obtained upon reaction of **6-CoCl₃(MeOH)** with $[\text{Rh}(\text{nbd})\text{Cl}]_2$ in DMF. NP = nanoparticles.

Moreover, the use of DMF in place of DMSO resulted in Rh/Co metal exchange, but was accompanied by the formation of Rh nanoparticles (Figure 36b). The PXRD pattern of **6-RhCl** confirmed that the framework structure is retained after the PSME reaction (Figure 37a). Indexing and Pawley fitting of SPXRD data shows a slight increase in the unit cell parameters of **6-RhCl** ($a = 32.9152(9) \text{ \AA}$, $c = 15.5342(5) \text{ \AA}$) compared to **6-CoCl₃**. These changes are consistent with chelation of the larger Rh species by the PNNNP pincer ligands, but could also be influenced by differences in the identity of guest solvent molecules that occupy the framework channels – DMF for **6-CoCl₃** and DMSO for **6-RhCl**. Scanning electron microscopy (SEM) images of **6-CoCl₃(MeOH)** and **6-RhCl** show similar morphologies with small particles in the range of 100-300 nm (Figure 38a).

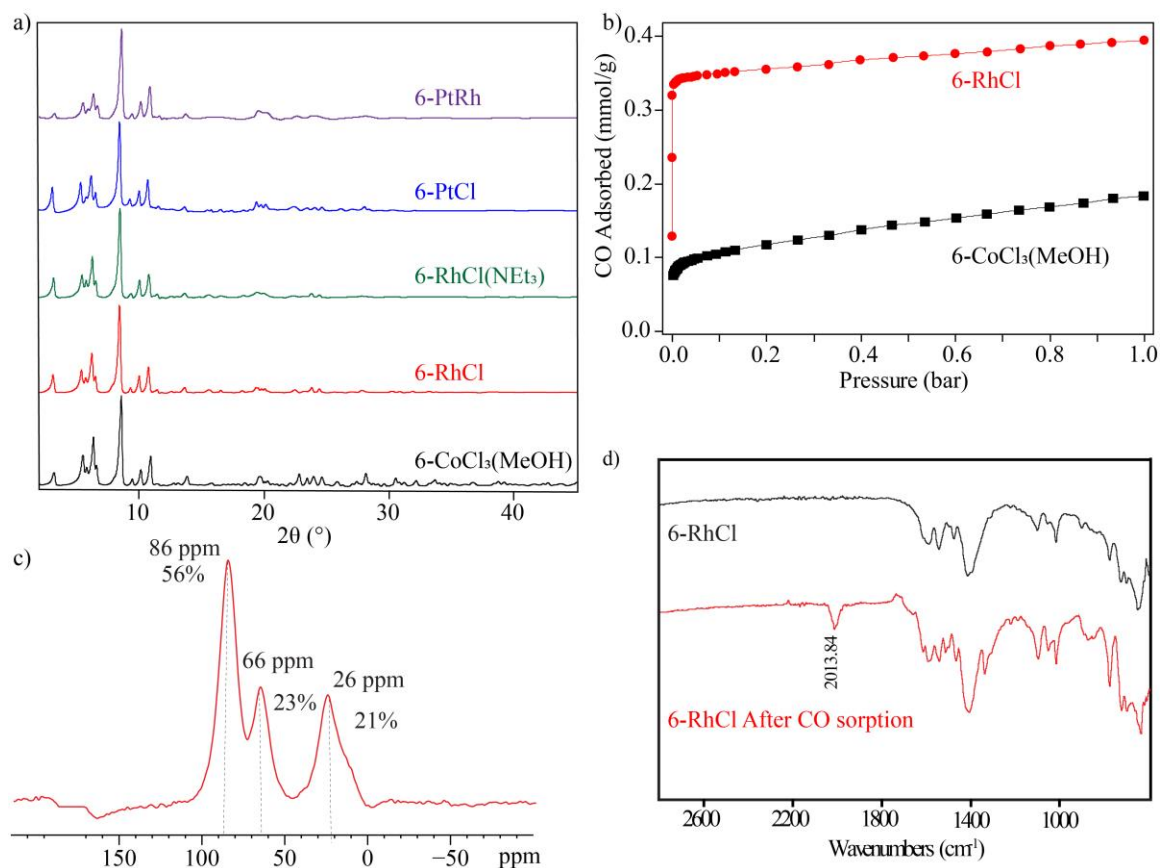


Figure 37. a) PXRD patterns (Cu-K α radiation, $\lambda = 1.5418 \text{ \AA}$) for **6-RhCl**, **6-RhCl(NEt₃)**, **6-PtCl**, and **6-PtRh**. b) CO adsorption isotherms measured for **6-CoCl₃(MeOH)** and **6-RhCl** at 303 K. c) Solid-state ^{31}P NMR spectrum of **6-RhCl** after CO adsorption measurement with MAS and TOSS. d) ATR-IR spectra of **6-RhCl** before and after CO adsorption measurement.

In addition, elemental mapping using energy dispersive X-ray spectroscopy (EDX) indicates a uniform distribution of Zr and Rh across the sample of **6-RhCl** (Figure 38b). Similar to **6-CoCl₃(MeOH)**, a desolvated sample of **6-RhCl** showed only modest N₂ uptake at 77 K, providing a calculated BET surface area of 316 m² g⁻¹. However, the CO adsorption isotherm (303 K) reveals a steep chemisorption step with an uptake of 0.35 mmol g⁻¹ at 0.1 bar (Figure 37b). The CO was not readily desorbed upon evacuation of the sample or heating under vacuum (10⁻⁴ torr, 373 K). The CO uptake by **6-RhCl** is

significantly larger than that observed for **6-CoCl₃(MeOH)** and corresponds to chemisorption at ~62 % of the Rh sites in the MOF, which is consistent with fraction of Rh^I sites determined by ³¹P NMR.

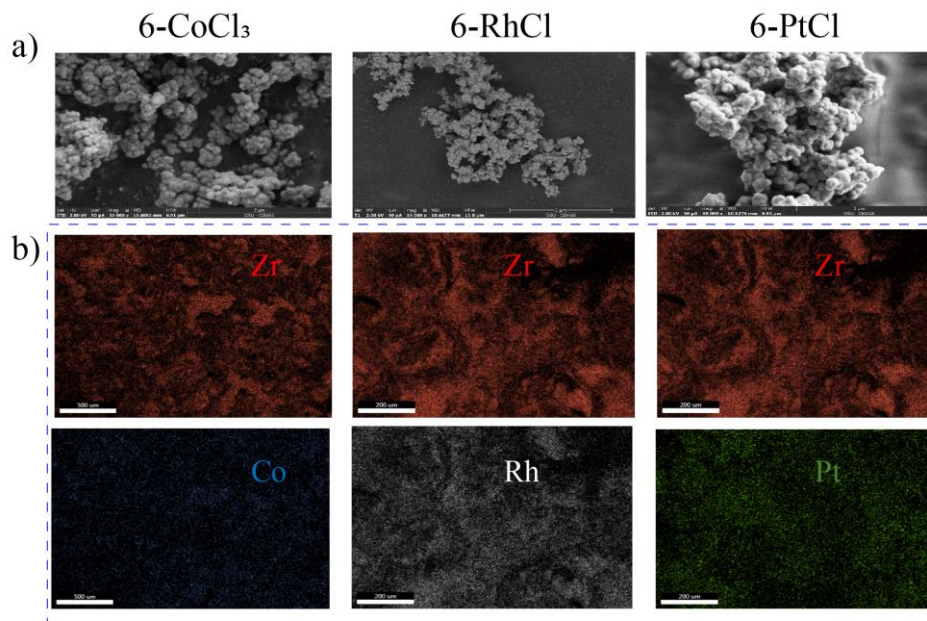


Figure 38. a) SEM images of **6-CoCl₃**, **6-RhCl** and **6-PtCl**. b) Elemental mapping of Zr and Co in **6-CoCl₃**, Zr and Rh in **6-RhCl**, and Zr and Pt in **6-PtCl** using EDX.

The ATR-IR spectrum of **6-RhCl** after the CO sorption experiment shows a strong CO stretch at 2013 cm⁻¹, in line with the formation of PNNNP-RhCl(CO) species (Figure 37d). Furthermore, the solid-state ³¹P NMR spectrum after CO sorption shows that the signal corresponding to the Rh^I pincer metallolinkers shifts slightly downfield to 86 ppm while that assigned to the Rh^{III} pincer species at ~65 ppm is not affected (Figure 37c).

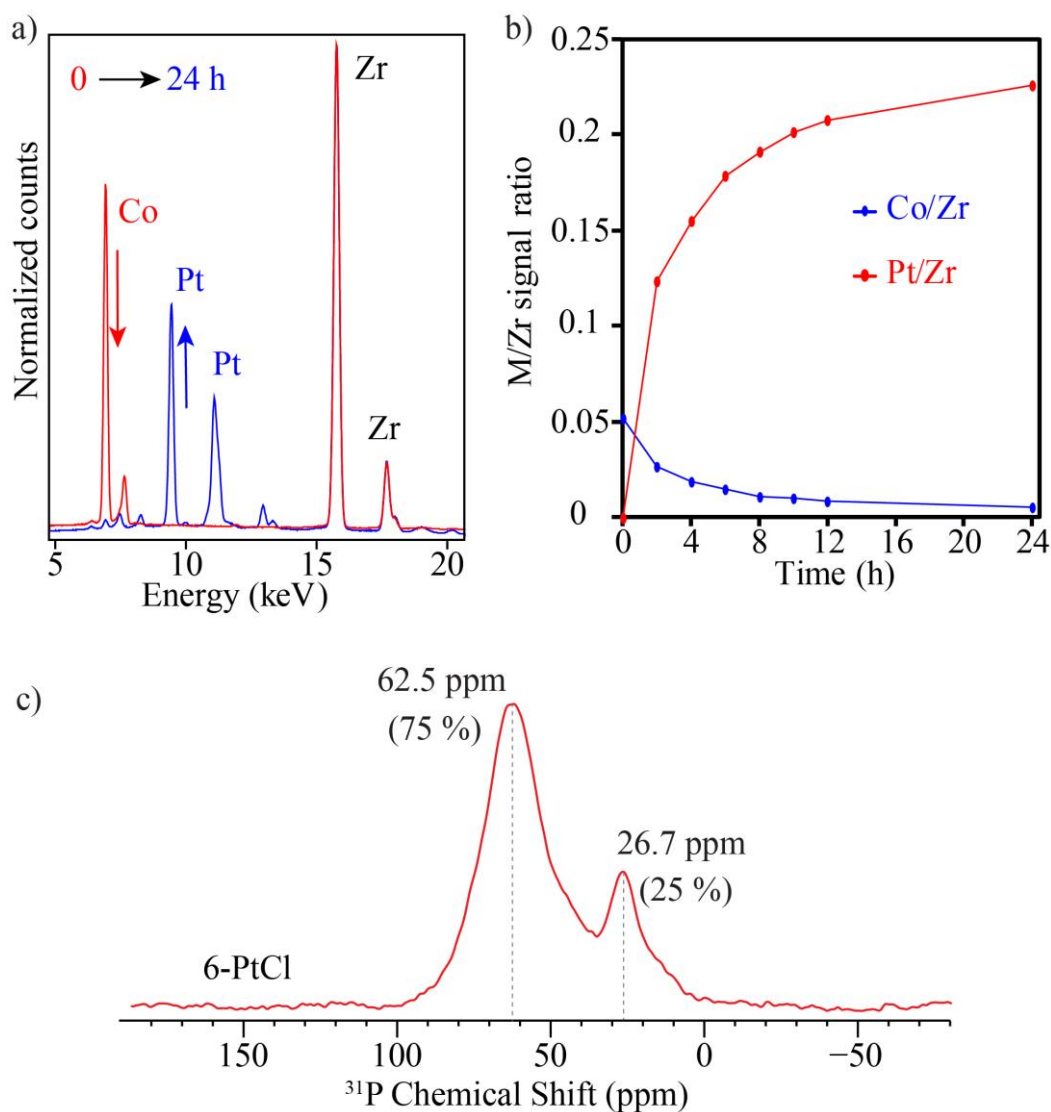


Figure 39. a) XRF spectra before and after the Pt/Co exchange reaction used to generate **6-PtCl**. b) Kinetic plot derived from XRF data measured for Pt/Co exchange reaction. c) Solid-state ^{31}P NMR spectrum of **6-PtCl** with MAS and TOSS.

Next, we sought to investigate the generation of **6-PtCl** via Pt/Co exchange. A suspension of **6-CoCl₃(MeOH)** in a DMSO solution containing $\text{PtCl}_2(\text{Me}_2\text{S})_2$ and NEt_3 was heated at 85 °C, resulting in the formation of **6-PtCl** as an off-white microcrystalline powder (Scheme 15). XRF analysis indicated nearly quantitative Pt/Co exchange after 24 h (Figure 39a) while PXRD confirmed that the framework retains crystallinity (Figure 37a).

Indexing and Pawley fitting of the SPXRD data provided unit cell parameters ($a = 33.0244(6) \text{ \AA}$, $c = 15.3783(4) \text{ \AA}$) of **6-PtCl** similar to those of **6-RhCl**. Monitoring of the reaction by XRF showed that the Pt/Co exchange approaches completion after ~12 h and is slower than the Rh/Co PSME reaction (Figure 39b). No metal exchange was observed in the absence of NEt_3 , which is consistent with the higher oxidation potential of Pt^{II} compared to Rh^{I} , and the inability of the former to reduce the PNNNP- Co^{III} complex. ICP-OES analysis provided a Zr:Pt:Co ratio of 6:1.96:0.05, indicating that the MOF contains slightly more Pt than expected based on the analyses of **6-CoCl₃** and **6-RhCl**. PXRD patterns of **6-PtCl** showed no indication of the presence of Pt nanoparticles, suggesting that despite extensive washing, a small amount of homogeneous Pt species likely remain trapped in the framework. The solid-state ^{31}P NMR spectrum of **6-PtCl** (Figure 39c) shows a broad resonance centered at 62.5 ppm that is consistent with the signal observed for the homogeneous complex $^t\text{Bu}_4(5\text{-PtCl})$ (62.6 ppm, $^1J_{^{195}\text{Pt}-^{31}\text{P}} = 2812 \text{ Hz}$) and the solid-state NMR data previously reported for **7-PtX**.¹²⁵ In addition, the solution-state ^{31}P NMR spectrum of an acid-digested sample of **6-PtCl** shows a single resonance at 63.2 ppm with characteristic ^{195}Pt - ^{31}P coupling (Figure 40a).

Lastly, we sought to take advantage of the slow Pt/Co exchange to generate a mixed-metal MOF containing both Pt and Rh pincer complexes. A suspension of **6-CoCl₃(MeOH)** in DMSO was treated with $\text{PtCl}_2(\text{SMe}_2)_2$ and NEt_3 at 85 °C for 10 h. After decanting the reaction supernatant, the solid was treated with a solution of $[\text{Rh}(\text{nbd})\text{Cl}]_2$ in DMSO for an additional 12 h to generate **6-PtRh** (Scheme 15).

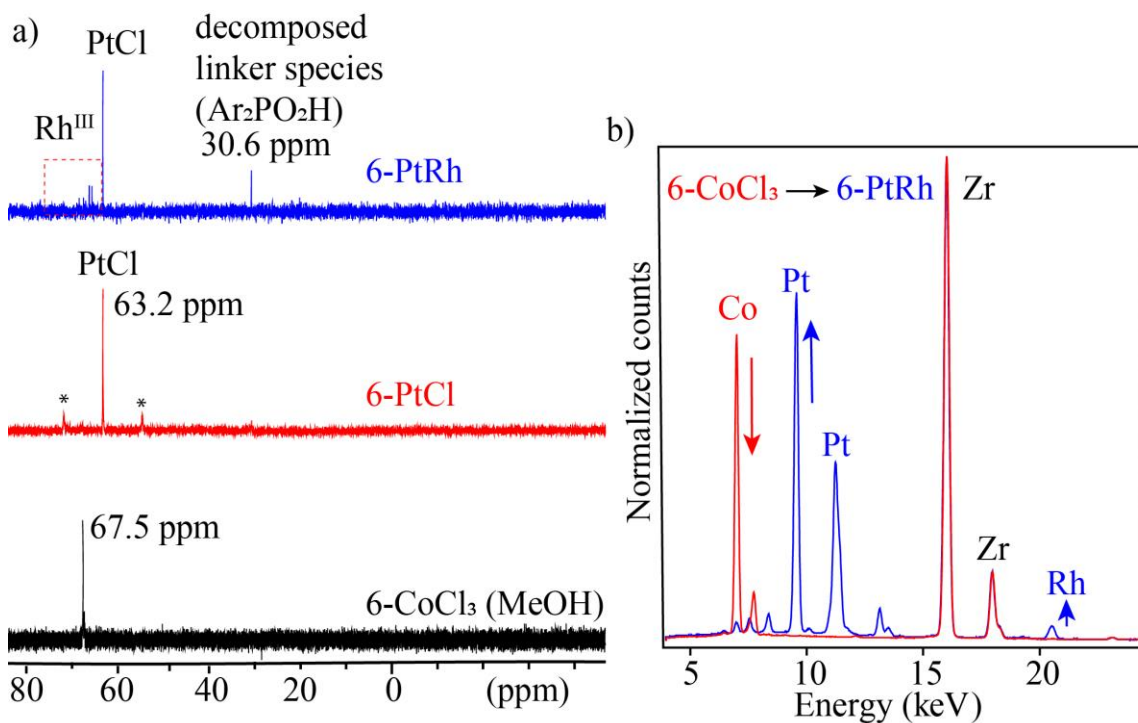


Figure 40. a) $^{31}\text{P}\{^1\text{H}\}$ NMR spectra ($\text{CF}_3\text{CO}_2\text{H}/\text{C}_6\text{D}_6$) of **6-CoCl₃(MeOH)**, **6-PtCl** and **6-PtRh**. Asterisks (*) are used to denote ^{195}Pt satellites. b) XRF spectra before and after the Pt/Co and Rh/Co exchange reactions used to generate **6-PtRh**.

XRF analysis confirmed the presence of both Pt and Rh in the solid product with nearly complete exchange of Co (Figure 40b). The presence of both Rh and Pt is further supported by ICP-OES analysis which provided a Zr:Pt:Rh:Co ratio of 6:1.38:0.5:0.05. ^{31}P NMR analysis of an acid-digested sample of **6-PtRh** showed a signal at 63 ppm that is consistent with the presence of $[\text{5-PtCl}]^{4-}$ linkers (Figure 40a). Resonances with characteristic $^{103}\text{Rh}-^{31}\text{P}$ coupling are also observed in the 64-70 ppm region. The observation of different PNNNP-Rh^{III} species is the result of oxidation induced by the acid digestion procedure, but nonetheless confirms Rh/Co exchange at the pincer sites.

4.5 Conclusions

Solvothermal reaction of $H_4(5-CoCl_3)$ pincer metallolinkers with $ZrCl_4$ generates a crystalline and porous **6- $CoCl_3$** MOF. **6- $CoCl_3$** adopts a structure with csq topology while Zr MOFs containing square planar PNNNP-MX (Pd and Pt) and POCOP-Pd pincer complexes form structures with ftw topology. The different structures indicate that the coordination geometry of the pincer-ligated metal fragment (i.e. pseudo-octahedral versus square planar) strongly influences MOF assembly. Based on trends observed for Zr MOFs containing other tetratopic linkers, the axial Cl^- ligands in $H_4(5-CoCl_3)$ metallolinkers are believed to inhibit rotation of the benzoate arms, enforcing a conformation that favors formation of the csq topology MOF.²⁶³ The PNNNP- Co^{III} pincer complex is sufficiently inert to allow for MOF assembly upon heating in a DMF/HOAc/HCl solvent mixture. However, heating a suspension of **6- $CoCl_3$** in DMF results in demetallation of the PNNNP ligands. The presence of mild reducing agents such as amines has been shown to result in reduction to a labile Co^{II} species that is responsible for the observed demetallation. This process has been exploited to carry out Rh/Co and Pt/Co PSME in **6- $CoCl_3$** . The metal substitutions are observed to be facile, providing access to **6- $RhCl$** and **6- $PtCl$** , which have not yet been obtained by direct solvothermal synthesis. Moreover, PSME reactions occur on timescales that allow for sequential metal exchange, as demonstrated by generation of the mixed metal pincer MOF **6- $PtRh$** . Linker-based metal exchange reactions have been relatively rare in MOFs and demetallation or metal exchange reactions with diphosphine pincer ligands are largely unprecedented. Consequently, the findings described herein offer a new pathway for the introduction of metal-based functionalities that are difficult to access

by direct synthesis and may have ramifications in both homogeneous and heterogeneous systems.

4.6 Experimental

General Considerations. $t\text{Bu}_4\text{PNNNP}$,¹²⁵ $[\text{CoCl}_2(\text{C}_5\text{H}_5\text{N})_4]\text{Cl}$,²⁶⁶ $[\text{Rh}(\text{CO})_2\text{Cl}]_2$,²⁶⁷ $\text{PtCl}_2(\text{SMe}_2)_2$,²⁶⁸ and $[\text{Rh}(\text{nbd})\text{Cl}]_2$ ²⁶⁹ were prepared following literature procedures. All metal exchange reactions were carried out in a nitrogen-filled glovebox using solvents that were dried over CaH_2 and distilled or dried via passage through columns of drying agents using a solvent purification system from Pure Process Technologies. Other solvents and reagents were purchased from commercial suppliers and used as received. Routine X-ray powder diffraction (PXRD) patterns for phase identification were collected using a Rigaku Miniflex 600 diffractometer with Nickel-filtered $\text{Cu-K}\alpha$ radiation ($\lambda = 1.5418 \text{ \AA}$). High-resolution synchrotron X-ray powder diffraction (SPXRD) data were collected at 295 K using beamline 11-BM at the Advanced Photon Source (APS, Argonne National Laboratory, Argonne, IL) with an average wavelength of 0.412697 \AA . Initial structural models for **6-CoCl₃** were constructed from the positions of the heavy atoms located using a charge flipping method within the PDXL2 Structure Analysis Package (Rigaku Corporation).²⁷⁰ Rietveld refinement was carried out with TOPAS-Academic.²⁷¹ A Bruker Tracer III-SD Handheld XRF Analyzer with a rhodium target and silicon drift detector at 40 keV voltage and $10 \mu\text{A}$ current was used to monitor metal exchange reactions. ATR-IR spectra were measured using a Nicolet IR 200 with a diamond ATR accessory. N_2 (77 K, liquid nitrogen bath) and CO (303 K) adsorption isotherms were measured using a Micromeritics 3Flex Surface Characterization Analyzer. Prior to analysis, samples

(100–200 mg) were heated under reduced pressure until the outgas rate was less than 2 mTorr/min. Inductively coupled plasma-optical emission spectroscopy (ICP-OES) measurements were performed by Robertson Microlit Laboratories (Ledgewood, NJ) or the Trace Element Research Laboratory at the Ohio State University. Other elemental analyses (C, H, N, Cl) were performed by Robertson Microlit Laboratories (Ledgewood, NJ) or Atlantic Microlab (Norcross, GA). Scanning electron microscopy (SEM) and elemental mapping of metals using energy-dispersive X-ray spectroscopy (EDX) were performed at the Center for Electron Microscopy and Analysis (CEMAS) at The Ohio State University using a Thermo Scientific Apreo LoVac Field Emission Scanning Electron Microscope. The samples were prepared by dispersing MOF powders onto double sided, conductive carbon tape that was attached to an aluminum sample holder. Electron paramagnetic resonance (EPR) spectra were collected at 10 K using a Bruker EMXPlus Electron Paramagnetic Resonance Spectrometer. Samples were prepared by suspending the MOFs in THF solvent in 4 mm quartz EPR tubes. Solution-state NMR spectra were measured using either a Varian Inova or Bruker 400 MHz spectrometer (162 MHz operating frequency for ^{31}P). For ^1H and $^{13}\text{C}\{^1\text{H}\}$ NMR spectra, the solvent resonance was referenced as an internal standard. For ^{31}P NMR spectra, 85 % H_3PO_4 was used as an external standard (0 ppm). Solid-state NMR experiments were performed using a Bruker DSX-400 spectrometer at a resonance frequency of 162 MHz for ^{31}P with a magic-angle spinning (MAS) probe in double-resonance mode. Samples were packed into 4 mm rotors with Kel-F 22 μL inserts. Experiments were carried out at spinning frequencies of 10–13.5 kHz. Typical ^{31}P and ^1H 90° pulse-lengths were 4 μs and 6 μs , respectively. ^{31}P NMR

spectra were obtained after composite-pulse multiple cross polarization from ^1H , with a recycle delay of 1 s and 10 blocks of 1.1-ms 90-100% ramp cross polarization separated by 0.5-s ^1H repolarization periods.²⁷² Four-pulse total suppression of sidebands (TOSS) was used to obtain spectra without spinning sidebands.²⁷³ Two-pulse phase modulation ^1H decoupling was applied during detection.²⁷⁴ ^{31}P spectra were externally referenced to the upfield resonance of calcium hydroxyapatite (National Institute of Standards and Technology) at 2.73 ppm; this corresponds to the 85 % H_3PO_4 scale.

Synthesis of $^t\text{Bu}_4(5\text{-CoCl}_3)$. A solution of $[\text{CoCl}_2(\text{C}_5\text{H}_5\text{N})_4]\text{Cl}$ (0.22 g, 0.44 mmol) in CH_2Cl_2 (5 mL) was added to a solution of $^t\text{Bu}_4\text{PNNNP}$ (0.40 g, 0.44 mmol) in CH_2Cl_2 (5 mL) under a N_2 atmosphere. An immediate color change to deep red was observed, and a solution of $[(n\text{-Bu})_4\text{N}]\text{Cl}$ (0.08 g, 0.22 mmol) in CH_2Cl_2 (3 mL) was added. The reaction was heated at 35 °C with vigorous stirring for 16 h before removing the volatiles under reduced pressure to afford a red solid. Residual pyridine was removed by dissolving the solid in toluene (10 mL) and evaporating to dryness using a rotatory evaporator at least three times. The crude material was then dissolved in minimal amount of CH_2Cl_2 and filtered through a plug of silica using ethyl acetate as eluent. Volatiles were removed under vacuum, and the product was obtained as a red powder (0.40 g, 84%). ^1H NMR (400 MHz, $(\text{CD}_3)_2\text{CO}$): δ 1.58 (s, 36H, ^tBu), 6.60 (d, 2H, $^3J_{\text{H-H}} = 8.78$ Hz, pyridine Ar-H), 7.52 (t, 1H, $^3J_{\text{H-H}} = 7.98$ Hz, pyridine Ar-H), 7.99 (d, 8H, $^3J_{\text{H-H}} = 7.42$ Hz, benzoate Ar-H), 8.36 (dt, 8H, $^3J_{\text{P-H}} = 13.09$ Hz, $^3J_{\text{H-H}} = 7.67$ Hz, benzoate Ar-H), 9.40 (br, 2H, N-H). $^{13}\text{C}\{^1\text{H}\}$ NMR (101 MHz, $(\text{CD}_3)_2\text{CO}$): δ 27.3 (s, 12C, $\text{C}(\text{CH}_3)_3$), 80.9 (s, 4C, $\text{C}(\text{CH}_3)_3$), 101.5 (br, 2C, Ar), 128.4 (t, $J = 5.54$ Hz, 8C, Ar), 132.5 (t, $J = 5.71$ Hz, 8C, Ar), 133.8 (s, 4C), 137.7 (t, $J =$

27.20 Hz, 4C, Ar), 141.1 (s, C, Ar), 160.9 (t, J = 9.64 Hz, 2C, Ar), 164.6 (s, 4C, CO₂). ³¹P{¹H} NMR (162 MHz, (CD₃)₂CO): δ 67.47 (s, 2P). Anal. Calcd for ^tBu₄(5-CoCl₃); C₄₉H₅₇Cl₃CoN₃O₈P₂: C, 56.41; H, 5.51; N, 4.03; Found: C, 55.23; H, 5.42; N, 4.05.

Synthesis of H₄(5-CoCl₃). A 20 mL scintillation vial was charged with ^tBu₄(5-CoCl₃) (0.40 g, 0.38 mmol), CH₂Cl₂ (3 mL), CF₃CO₂H (1 mL), and concentrated HCl (0.1 mL). The resulting solution was stirred at room temperature for 16 h. Deionized water (10 mL) was added to the reaction, resulting in formation of an orange precipitate. The mixture was sonicated briefly and stirred for 15 min. The solid was then collected by filtration, washed with deionized water (2 × 10 mL) and CHCl₃ (3 × 10 mL), and dried under reduced pressure to yield H₄(5-CoCl₃) as an orange powder (0.30 g, 88%). ¹H NMR (400 MHz, (CD₃)₂CO) δ 6.68 (d, 2H, ³J_{H-H} = 8.24 Hz, pyridine Ar-H), 7.55(t, 1H, ³J_{H-H} = 8.37 Hz, pyridine Ar-H), 8.11(d, 8H, ³J_{H-H} = 8.59 Hz, benzoate Ar-H), 8.42(m, 8H, benzoate Ar-H), 9.49(br, 2H, NH). ¹³C{¹H} NMR (101 MHz, (CD₃)₂CO) δ 101.3 (br, 2C, Ar), 128.7 (t, J = 5.47 Hz, 8C, Ar), 132.5 (t, J = 5.71 Hz, 8C, Ar), 138.0 (t, J = 27.8 Hz, 4C Ar), 141.1 (s, C), 160.9 (t, J = 9.40 Hz, 2C,Ar), 166.3 (s, 4C, CO₂). ³¹P{¹H} NMR (162 MHz, (CD₃)₂CO): δ 67.30 (s, 2P). Anal. Calcd for H₄(5-CoCl₃).2H₂O; C₃₃H₂₉Cl₃CoN₃O₁₀P₂: C, 46.37; H, 3.42; N, 4.92; Found: C, 45.73; H, 3.84; N, 4.82.

Synthesis of 6-CoCl₃ and 6-CoCl₃(MeOH) A 20 mL scintillation vial was charged with ZrCl₄ (0.05 g, 0.21 mmol), DMF (12 mL), and glacial acetic acid (3 mL) and sonicated for 20 min. Concentrated HCl (3 mL) followed by H₄(5-CoCl₃) (0.06 g, 0.07 mmol) were added to the vial, and the resulting orange solution was sonicated for 2 min to ensure complete dissolution. The reaction vial was sealed with a Teflon-lined screw-top cap

(Qorpak CAP-00554), placed in a room temperature oven, and heated to 80 °C for 16 h. After cooling to room temperature, the resulting solid was collected by centrifugation and washed with DMF (3 × 12 mL) to afford **6-CoCl₃**. The product was soaked in methanol (4 × 10 mL) over the course of 24 h to afford **6-CoCl₃(MeOH)** (0.07 g). Acid-digested ³¹P{¹H} NMR (162 MHz, CF₃CO₂H/C₆D₆): δ 67.6 (H₄(5-CoCl₃), 67.2 (H₄(5-CoCl₂(OH))), 33.5 (Ar₂PO₂H). Anal. Calcd. for **6-CoCl₃(MeOH);[Zr₆O₄OH₄](OH)_{2.2}(MeOH)_{2.2}(C₃₃H₂₁N₃O₈P₂CoCl₃)_{1.66}(CH₃CO₂)_{2.5}(C₁₄H₉O₆P)_{0.33}**: C, 33.50; H, 2.55; N, 2.92; Cl, 7.39. Found: C, 31.64; H, 2.96; N, 2.62; Cl, 7.04. ICP-OES: Zr, 23; Co, 3.35. Diaryl phosphinic acid linker fragments [(*p*-C₆H₄-CO₂)₂PO₂H] resulting from linker decomposition have been included in the empirical formula based on the minor resonances observed in the solid-state and acid-digested ³¹P NMR spectra.

Preparation of 6-RhCl. A solution of [Rh(nbd)Cl]₂ (0.06 g, 0.14 mmol) in DMSO (3 mL) was added to a suspension **6-CoCl₃(MeOH)** (0.18 g, 0.07 mmol) in DMSO (12 mL) in a 20 mL scintillation vial. The reaction vial was sealed with a Teflon-lined screw-top cap (Qorpak CAP-00554) and heated at 85 °C for 12 h. The reaction supernatant became dark green while the solid turned bright yellow within 2 h. After cooling, the solid was collected by centrifugation, and washed with DMSO (~5 × 10 mL) and methanol (3 × 10 mL over the course of 24 h). The solid was briefly dried in vacuo to give **6-RhCl** (0.32 g) as a yellow microcrystalline powder. TGA analysis of the sample showed a 38 wt % mass loss up to 200 °C, attributable to volatilization of DMSO solvent from the framework. Attempts to digest samples of **6-RhCl** with CF₃CO₂H and organic solvents resulted in oxidation of the

PNNNP-Rh linkers to a mixture of Rh^{III} species. For kinetic analyses of the reaction, the progress of metal exchange was monitored by XRF every two hours for a period of 12 hours. Solid samples were obtained by removing aliquots of the reaction mixture, collecting the solid by centrifugation, and washing with DMSO until the color disappeared from the supernatant (~5 × 10 mL). ICP-OES: Zr, 21.79; Rh, 5.86; Co, 0.06.

Preparation of 6-RhCl(NEt₃). A solution of [Rh(nbd)Cl]₂ (0.060 g, 0.14 mmol) in DMSO (3 mL) and NEt₃ (0.1 M in DMSO, 0.04 mmol) were added to a suspension of **6-CoCl₃(MeOH)** (0.18 g, 0.07 mmol) in DMSO (12 mL) in a 20 mL scintillation vial. The reaction mixture was heated at 85 °C for 12 h. The reaction supernatant became dark green while the solid turned bright yellow within 2 h. After allowing the reaction to cool to room temperature, the solid was collected by centrifugation, washed with DMSO (5 × 10 mL) and soaked in methanol for 24 h (3 × 10 mL). ICP-OES: Zr, 20.16; Rh, 5.04; Co, 0.32.

Preparation of 6-PtCl. A solution of PtCl₂(SMe₂)₂ (0.11 g, 0.28 mmol) in DMSO (3 mL) and NEt₃ (0.1 M in DMSO, 0.04 mmol) was added to a suspension of **6-CoCl₃(MeOH)** (0.18 g, 0.07 mmol) in DMSO (12 mL) in a 20 mL scintillation vial. The reaction vial was sealed with a Teflon-lined screw-top cap (Qorpak CAP-00554) and heated at 85 °C for 24 h. After allowing the reaction to cool to room temperature, the solid was collected by centrifugation and washed with DMSO (5 × 10 mL) or until the supernatant of the reaction became colorless. The solid was briefly dried in vacuo to give **6-PtCl** (0.30 g) as a yellow microcrystalline powder. TGA analysis of the sample showed a 34 wt % mass loss up to 200 °C, attributable to volatilization of DMSO solvent from the framework. Acid-digested

$^{31}\text{P}\{^1\text{H}\}$ NMR (162 MHz, $\text{CF}_3\text{CO}_2\text{H}/\text{C}_6\text{D}_6$): δ 63.2 ($J_{^{195}\text{Pt}-^{31}\text{P}} = 2814$ Hz). ICP-OES: Zr, 19.0; Pt, 13.3; Co, 0.07.

Preparation of 6-RhPt. $\text{PtCl}_2(\text{SMe}_2)_2$ (0.11 g, 0.28 mmol) in DMSO (3 mL) and NEt_3 (0.1 M in DMSO, 0.04 mmol) were added to a suspension of **6-CoCl₃(MeOH)** (0.18 g, 0.07 mmol) in DMSO (12 mL). The reaction vial was sealed with Teflon-lined screw-top cap (Qorpak CAP-00554) and heated at 85 °C for 10 h. After allowing the reaction to cool to room temperature, the supernatant was removed *via* centrifugation. The solid was re-suspended in fresh DMSO (12 mL), a solution of $[\text{RhCl}(\text{nbd})]_2$ (0.03 g, 0.07 mmol) in DMSO (3 mL) was added, and the mixture was heated at 85 °C for 12 h. After cooling the reaction to room temperature, the supernatant was decanted and the solid was washed with DMSO (5 x 10 mL). $^{31}\text{P}\{^1\text{H}\}$ NMR (162 MHz, $\text{CF}_3\text{CO}_2\text{H}/\text{C}_6\text{D}_6$): δ 68.3 (d, $^1J_{\text{P-Rh}} = 91$ Hz); 66.2 (d, $^1J_{\text{P-Rh}} = 88$ Hz, weak signal); 65.3 ((d, $^1J_{\text{P-Rh}} = 90$ Hz); 62.8 ($J_{^{195}\text{Pt}-^{31}\text{P}} = 2807$ Hz). ICP-OES: Zr:Pt:Rh:Co ratio of 6:1.38:0.5:0.05.

Reaction of $^t\text{Bu}_4(5\text{-CoCl}_3)$ with $[\text{Rh}(\text{nbd})\text{Cl}]_2$. A solution of $[\text{Rh}(\text{nbd})\text{Cl}]_2$ (3.3 mg, 0.007 mmol) in DMSO (0.2 mL) was added to a solution of $^t\text{Bu}_4(5\text{-CoCl}_3)$ (15 mg, 0.014 mmol) in DMSO (0.4 mL) in a 1-dram vial. The reaction mixture was transferred to an NMR tube and monitored by ^{31}P NMR spectroscopy. $^{31}\text{P}\{^1\text{H}\}$ NMR (162 MHz, DMSO-d_6): δ 80 ($^1J_{^{103}\text{Rh}-\text{P}} = 154.7$ Hz); 65 ($^1J_{^{103}\text{Rh}-\text{P}} = 93.7$ Hz).

Reaction of $^t\text{Bu}_4(5\text{-CoCl}_3)$ and $[\text{Rh}(\text{nbd})\text{Cl}]_2$ with NEt_3 . A 1-dram vial was charged with $^t\text{Bu}_4(5\text{-CoCl}_3)$ (10 mg, 0.01 mmol), DMSO (0.3 mL), NEt_3 (0.1 M in DMSO, 0.02 mmol), and $[\text{Rh}(\text{nbd})\text{Cl}]_2$ (3 mg, 0.006 mmol) in DMSO (0.2 mL). The reaction mixture was

transferred to an NMR tube and monitored by ^{31}P NMR spectroscopy. $^{31}\text{P}\{^1\text{H}\}$ NMR (162 MHz, DMSO- d_6): δ 80.3 (d, $^1J_{\text{P-Rh}} = 153.7$ Hz).

Reaction of $^t\text{Bu}_4\text{PNNNP}$ with $[\text{Rh}(\text{nbdc})\text{Cl}]_2$. A solution of $[\text{Rh}(\text{nbdc})\text{Cl}]_2$ (2.7 mg, 0.006 mmol) in DMSO (0.2 mL) was added to a solution of $^t\text{Bu}_4\text{PNNNP}$ (10 mg, 0.011 mmol) in DMSO (0.4 mL). An immediate color change to bright yellow was observed and $^{31}\text{P}\{^1\text{H}\}$ NMR showed the formation of a single species giving rise to a major resonance at 79.8 ppm (d, 2P, $^1J_{\text{P-Rh}} = 154.3$ Hz) within 2 h.

Chapter 5: Synthesis, characterization and reactivity of isostructural Zr MOFs assembled from PNNNP-Ru pincer complexes

Portions of this chapter have been described in *Organometallics* **2019**, 38, 3419-3428.

5.1 Introduction

Diphosphine pincer complexes have been employed for a wide range of homogeneous catalytic transformations due to their electronic and steric diversity as well as chemical and thermal stability.^{90,111,130,275–281} In particular, homogeneous Ru diphosphine pincer complexes have been widely studied as catalysts for dehydrogenation, transfer and direct hydrogenation of organic transformations.^{91,111} However, the catalytic activity of these Ru pincer complexes may suffer from deactivation bimolecular pathways in the homogeneous catalysis.^{121,122} Hence, their immobilization in MOFs may offer a platform to explore single site isolation or secondary environment effects on their stability, activity and selectivity. A diverse range of strategies including encapsulation, activation of metal nodes, postsynthetic grafting and direct assembly have been used to functionalize MOFs with catalytically active transition metal species.^{282–295} However, further postsynthetic steps are still often necessary to activate MOF-supported precatalysts. In some cases, desolvation carried out by heating a MOF in vacuo can remove bound solvent molecules, generating coordinatively unsaturated metal sites for Lewis acid-catalyzed transformations.^{35,45,296–298} In other cases, one or more reagents may be required to facilitate precatalyst activation via X-type ligand exchange or abstraction, similar to procedures commonly employed for homogeneous organometallic complexes.^{299–303} For example, reagents such as silver salts of weakly coordinating anions have been used to exchange metal-coordinated halide ligands in MOFs and organoaluminum or organolithium reagents have been employed to activate metal nodes for olefin oligomerization catalysis.^{304–308} Careful consideration of precatalyst activation procedures is perhaps more important for

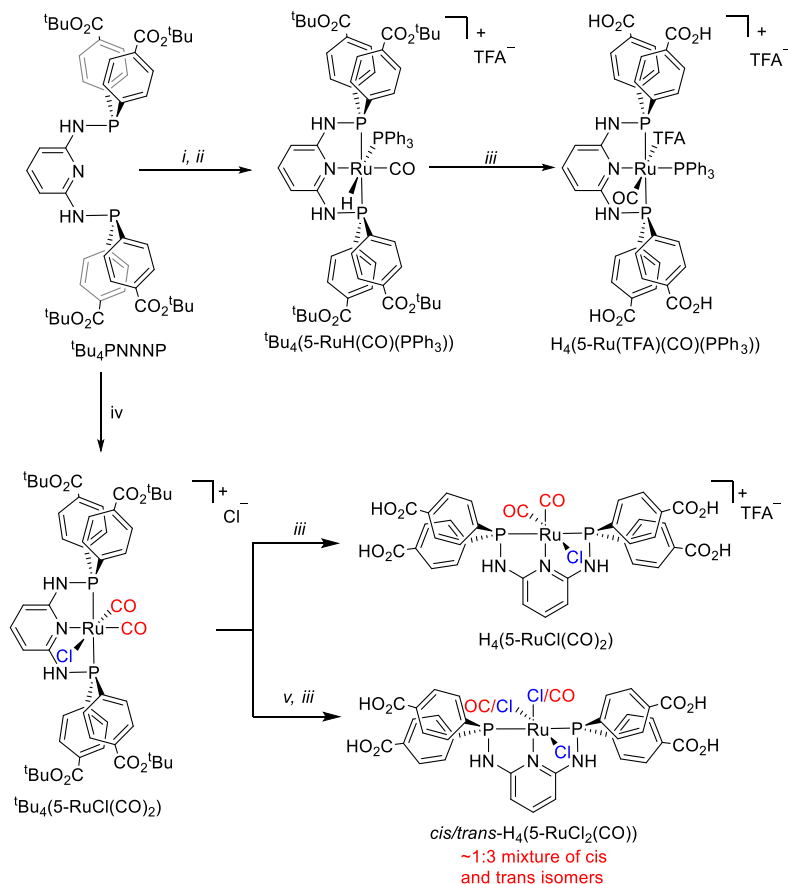
MOF-based catalysts than for homogeneous systems. First of all, the strategies used to introduce catalytic functionality may rely on transition metal species with muted reactivity to prevent decomposition or undesirable side reactions during incorporation. Secondly, MOFs and other heterogeneous supports may give rise to reagent compatibility issues that are not encountered with homogeneous systems. For example, strong acids or bases may lead to framework degradation.^{309,310} In our own experience, halide ligand abstraction with silver salts has not proven to be particularly effective with MOFs, in part due to the precipitation of insoluble silver halide byproducts that are inseparable from the heterogeneous catalyst.¹²⁵

This chapter describes the synthesis, characterization, reactivity and catalytic activity investigation of an isostructural series of Zr MOFs (**8-RuCl₂(CO)**, **9-RuCl(CO)₂** and **10-RuCl₂(CO)**) constructed from PNNNP-Ru pincer complexes containing different ancillary ligands (chloride, CO, or phosphines). Despite the differences in ancillary ligands coordinated to the Ru centers, solvothermal reactions of the PNNNP-Ru metallolinkers with ZrCl₄ converge to MOFs with a csq-type net that are similar to **6-CoCl₃** discussed in Chapter 4. For many catalytic transformations carried out with Ru diphosphine pincer complexes, metal-ligand cooperativity resulting from ligand-based deprotonation/dearomatization has been proposed to facilitate key steps in catalytic cycles.^{281,311,312} Similarly, deprotonation/dearomatization with KO^tBu followed by CO ligand removal with Me₃NO activates **9-RuCl(CO)₂** for catalytic hydrosilylation of aldehydes with Et₃SiH. However, **8-RuCl₂(CO)**, **9-RuCl(CO)₂** and **10-RuCl₂(CO)** as well as homogeneous PNNNP-Ru analogues of the immobilized pincer complexes show low

activity for the hydrosilylation reaction when subjected to similar precatalyst activation conditions.

5.2 Synthesis and characterization of PNNNP-Ru metallolinkers

Scheme 16. Synthesis of PNNNP-Ru metallolinkers



Reagents: (i) $\text{RuCl(H)(CO)(PPh}_3)_3$, THF, 70°C , 16 h; (ii) NaO_2CCF_3 , THF/ CHCl_3 , rt, 2 h; (iii) $\text{CF}_3\text{CO}_2\text{H}$, CH_2Cl_2 , rt, 16 h; (iv) $\text{RuCl}_2(\text{CO})_3$ (THF), 1,4-dioxane, 100°C , 16 h; (v) Me_3NO , CH_2Cl_2 , rt, 1 h.

Reaction of $t\text{Bu}_4\text{PNNNP}$ with $\text{RuCl(H)(CO)(PPh}_3)_3$ followed by outer sphere Cl^- exchange with NaTFA furnished $t\text{Bu}_4(5\text{-RuH(CO)(PPh}_3))$ as a grey powder in 93 % yield (Scheme 16). The ^{31}P NMR spectrum of $t\text{Bu}_4(5\text{-RuH(CO)(PPh}_3))$ in DMSO-d_6 shows a

doublet at 99.8 ppm assigned to the pincer phosphine groups and a triplet at 39.8 ppm for PPh₃ in 2:1 ratio respectively (Figure 42).

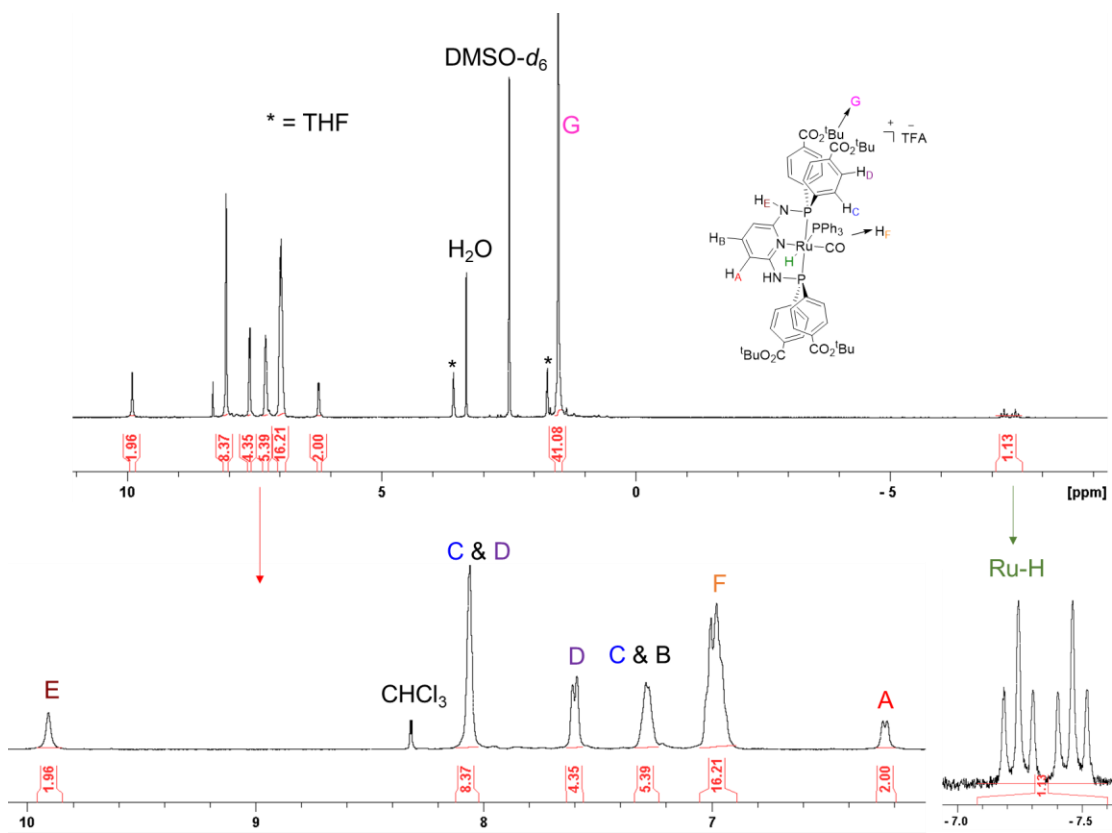


Figure 41. ¹H NMR spectrum of ^tBu₄(5-RuH(CO)(PPh₃)) in DMSO-*d*₆

Consistent with the structure, the ¹H NMR spectrum of ^tBu₄(5-RuH(CO)(PPh₃)) displayed all expected resonances including a doublet of triplets at -7.2 ppm for the Ru-H group (Figure 41). The stereochemistry of ^tBu₄(5-RuH(CO)(PPh₃)) was also established from the ¹H NMR spectrum. The large *J*_{H-P} coupling constant (²*J*_{H-P} = 86.9 Hz) within the doublet of triplet splitting pattern for Ru-H is consistent with that observed for analogous Ru-H pincer complexes containing a hydride ligand *trans* to PPh₃ (Figure 41).³¹³ On the other hand, ²*J*_{H-P} coupling constants for diphosphine Ru-H pincer complexes with the hydride ligand *cis* to

PPh_3 are typically observed within the 20-25 Hz range, resulting in pseudo-quartet splitting patterns.³¹³

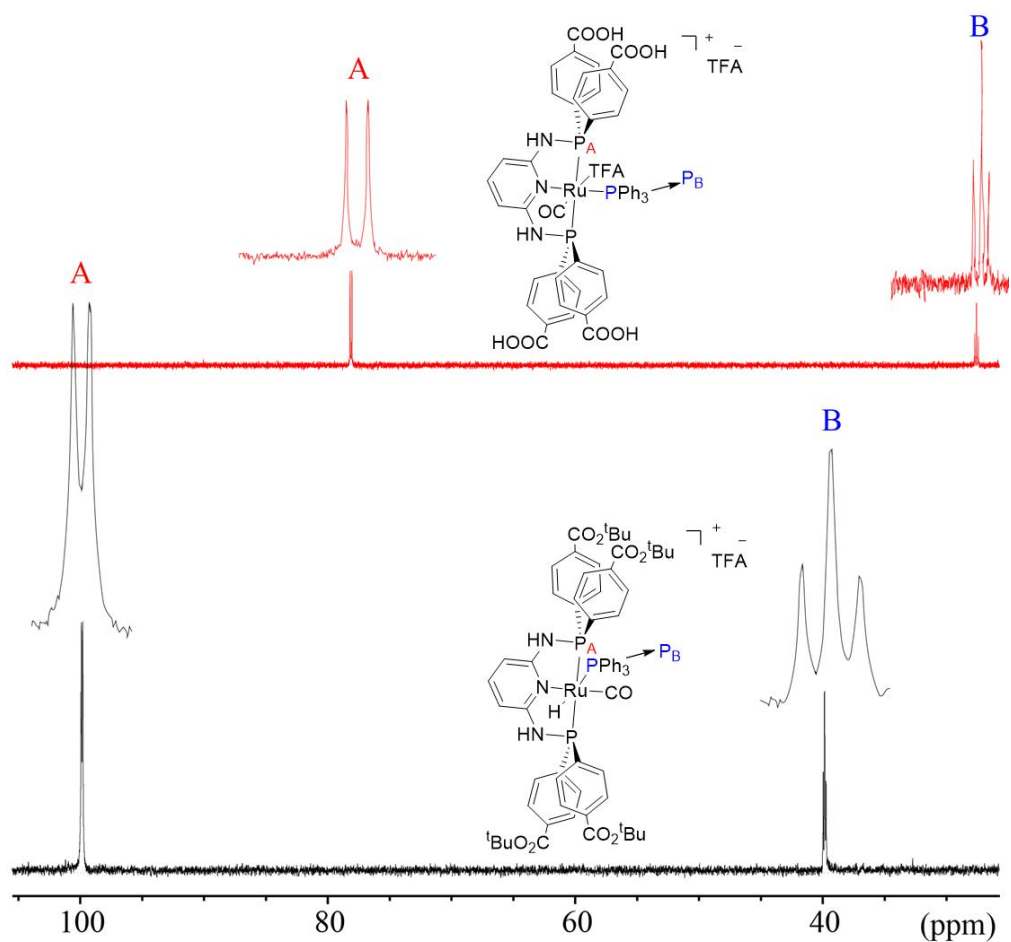


Figure 42. $^{31}\text{P}\{^1\text{H}\}$ NMR spectra of ${}^t\text{Bu}_4(5\text{-RuH}(\text{CO})(\text{PPh}_3))$ and $\text{H}_4(5\text{-Ru}(\text{TFA})(\text{CO})(\text{PPh}_3))$ in DMSO-d_6 .

The tert-butyl ester groups of ${}^t\text{Bu}_4(5\text{-RuH}(\text{CO})(\text{PPh}_3))$ were deprotected with $\text{CF}_3\text{CO}_2\text{H}/\text{CH}_2\text{Cl}_2$ to generate $\text{H}_4(5\text{-Ru}(\text{TFA})(\text{CO})(\text{PPh}_3))$ as a white powder in 87 % yield. $\text{H}_4(5\text{-Ru}(\text{TFA})(\text{CO})(\text{PPh}_3))$ was characterized by ^1H and ^{31}P NMR spectroscopy (Figure 42 and Figure 43) and its purity was confirmed by elemental analysis.

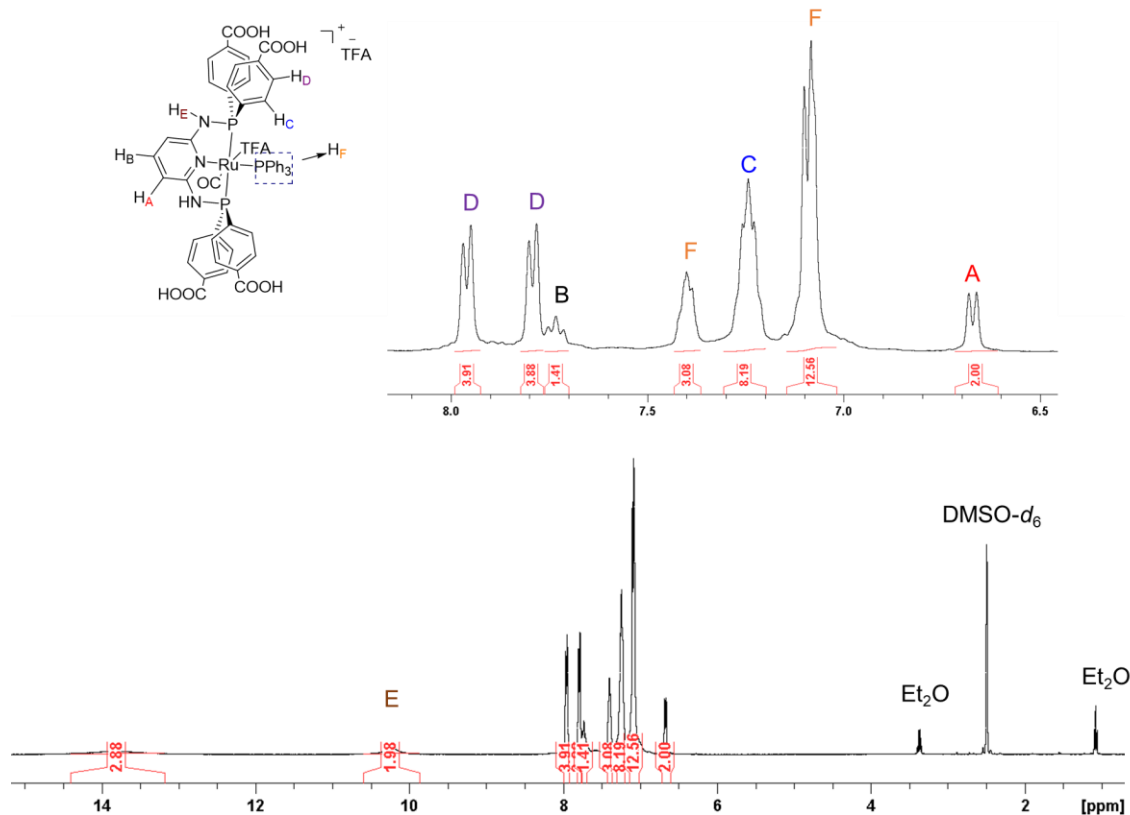


Figure 43. ^1H NMR spectrum of $\text{H}_4(5\text{-Ru}(\text{TFA})(\text{CO})(\text{PPh}_3))$ in $\text{DMSO-}d_6$.

$\text{H}_4(5\text{-RuCl}(\text{CO})_2)$ was prepared from the reaction of ${}^t\text{Bu}_4\text{PNNNP}$ and $\text{RuCl}_2(\text{CO})_3(\text{THF})$ followed by deprotection of the tert-butyl ester groups using $\text{CF}_3\text{CO}_2\text{H}/\text{CH}_2\text{Cl}_2$ as shown in Scheme 16. ${}^t\text{Bu}_4(5\text{-RuCl}(\text{CO})_2)$ and $\text{H}_4(5\text{-RuCl}(\text{CO})_2)$ were characterized using multinuclear NMR spectroscopy (Figure 44 and Figure 45), IR spectroscopy and elemental analysis. The *cis* stereochemistry of ${}^t\text{Bu}_4(5\text{-RuCl}(\text{CO})_2)$ and $\text{H}_4(5\text{-RuCl}(\text{CO})_2)$ are established by the presence of two distinct sets of aromatic ^1H NMR resonances corresponding to inequivalent benzoate groups as well as two carbonyl stretching bands of equal intensity appearing at 2064 and 2010 cm^{-1} in the ATR-IR spectrum (Figure 44 and Figure 55d). These spectroscopic features are in line with an analogous PNP-Ru pincer complex reported by Mashuta and coworkers.³¹⁴

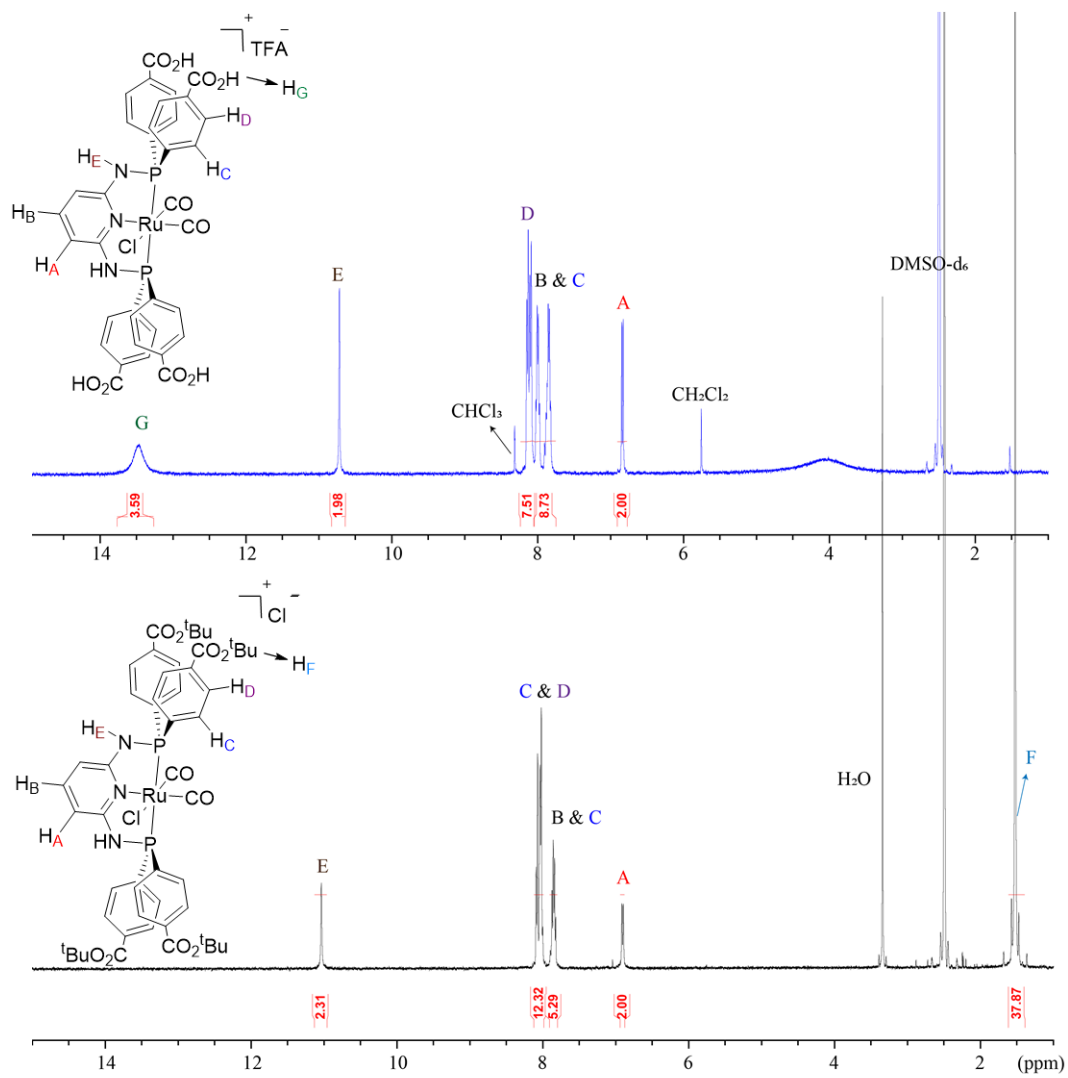


Figure 44. ^1H NMR spectra of ${}^t\text{Bu}_4(5\text{-RuCl(CO)}_2)$ and $\text{H}_4(5\text{-RuCl(CO)}_2)$ in DMSO-d_6 .

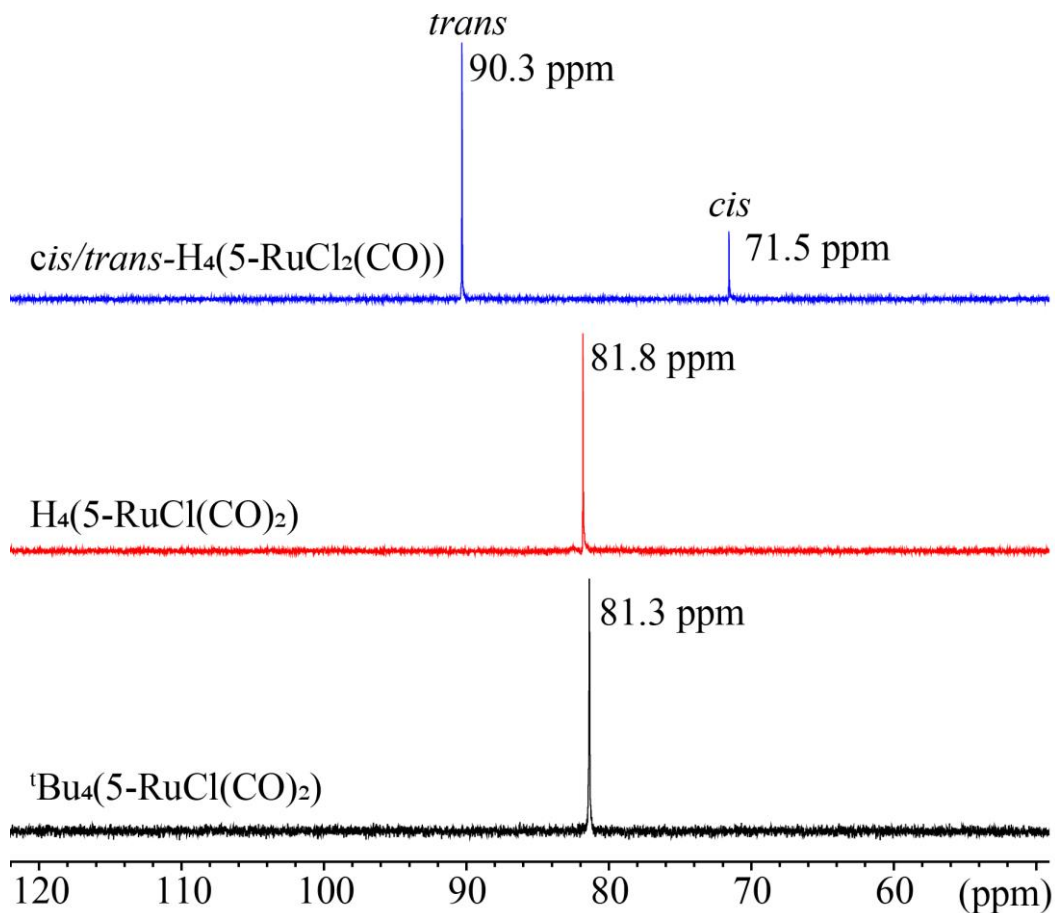


Figure 45. $^{31}\text{P}\{^1\text{H}\}$ NMR spectra of ${}^t\text{Bu}_4(5\text{-RuCl}(\text{CO})_2)$, $\text{H}_4(5\text{-RuCl}(\text{CO})_2)$ and $\text{cis/trans-H}_4(5\text{-RuCl}_2(\text{CO}))$ in DMSO- d_6 .

Treatment of ${}^t\text{Bu}_4(5\text{-RuCl}(\text{CO})_2)$ with a mild oxidative decarbonylating agent, Me_3NO , facilitates loss of a CO ligand and subsequent deprotection gives $\text{cis/trans-H}_4(5\text{-RuCl}_2(\text{CO}))$.³¹⁵ The ^1H and ^{31}P NMR spectra of the product indicate a $\sim 1:3$ mixture of cis and trans isomers (Figure 45 and Figure 46).

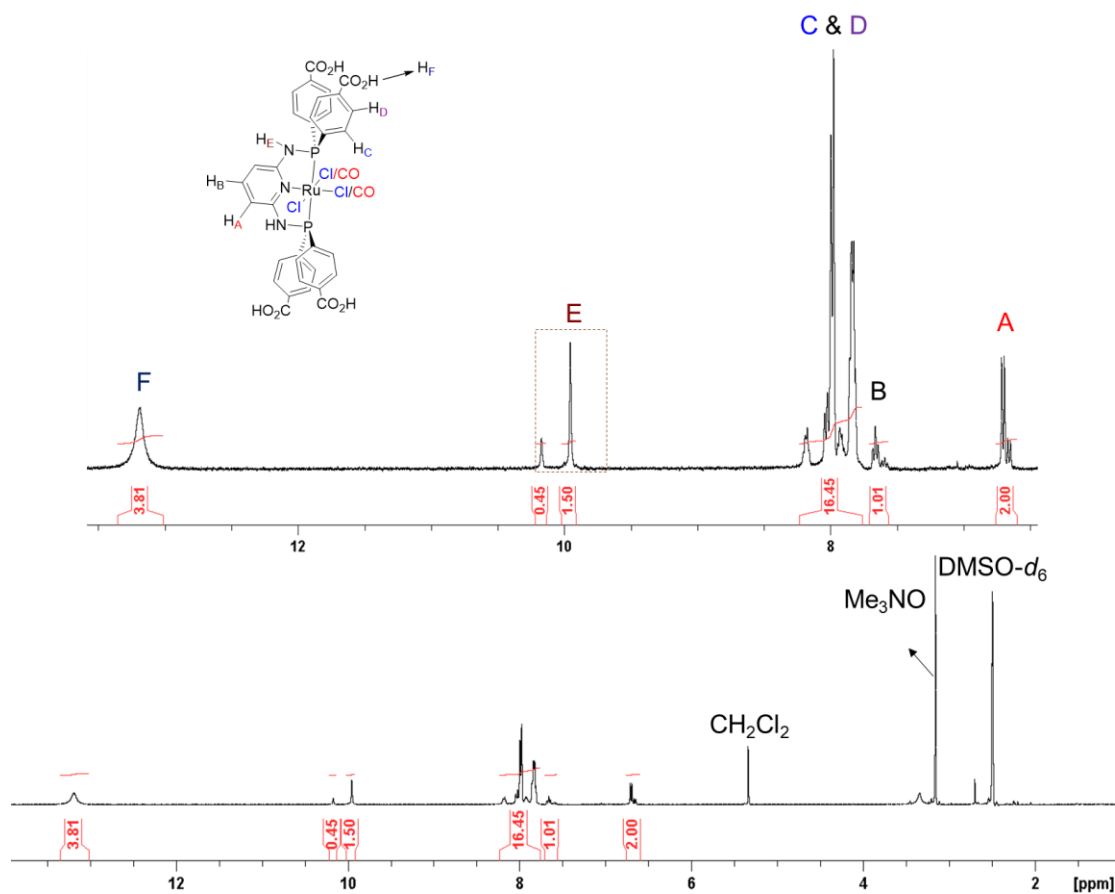


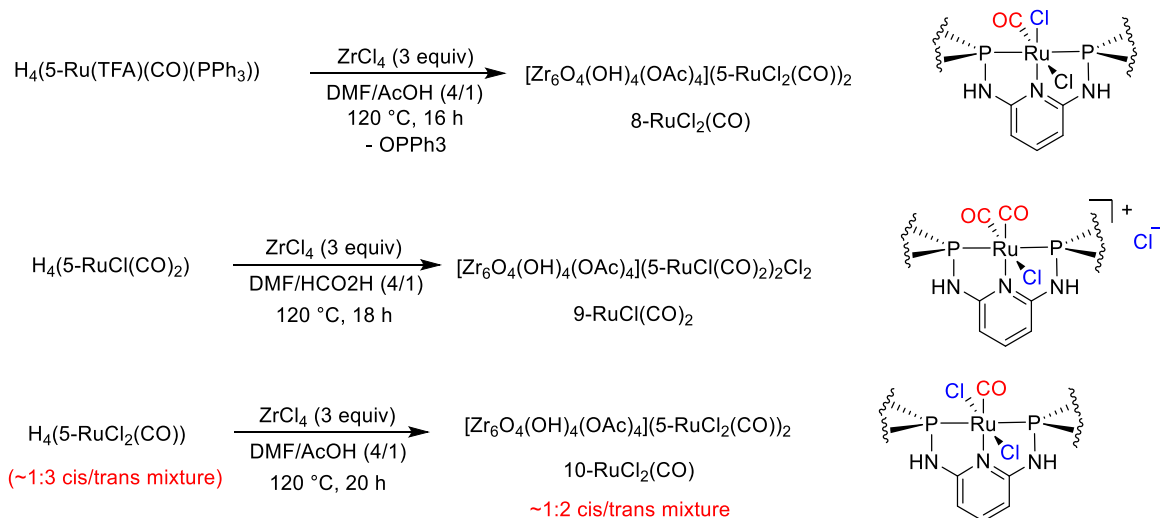
Figure 46. ^1H NMR spectrum of $cis/trans\text{-H}_4(5\text{-RuCl}_2(\text{CO}))$ in $\text{DMSO-}d_6$.

5.3 Synthesis and characterization of Zr MOFs containing PNNNP-Ru metallolinkers

Solvothermal reactions of $\text{H}_4(5\text{-Ru}(\text{TFA})(\text{CO})(\text{PPh}_3))$, $\text{H}_4(5\text{-RuCl}(\text{CO})_2)$, and $cis/trans\text{-H}_4(5\text{-RuCl}_2(\text{CO}))$ with ZrCl_4 in DMF using $\text{CH}_3\text{CO}_2\text{H}$ or HCO_2H as modulators yields an isostructural series of MOFs, **8-RuCl₂(CO)**, **9-RuCl(CO)₂** and **10-RuCl₂(CO)**, as off-white microcrystalline powders (Scheme 17). Although **9-RuCl(CO)₂** could be synthesized using $\text{CH}_3\text{CO}_2\text{H}$ as a modulator, we found that HCO_2H provides a more

crystalline product. PXRD analysis indicates that **8-RuCl₂(CO)**, **9-RuCl(CO)₂** and **10-RuCl₂(CO)** adopt csq-type frameworks that are analogous to **6-CoCl₃** (Figure 47c).³¹⁶

Scheme 17. Solvothermal syntheses and structural formulas of **8-RuCl₂(CO)**, **9-RuCl(CO)₂** and **10-RuCl₂(CO)**



The framework structure of **8-RuCl₂(CO)** was interrogated by Rietveld refinement of SPXRD data. Initial indexing provided a hexagonal unit cell ($a = 31.937(7)$ Å, $c = 15.798(4)$ Å) and a structure model was constructed with $P6/mmm$ space group symmetry based on the structure of **6-CoCl₃**.³¹⁶ Rietveld refinement was carried out using simulated annealing with a [Zr₆O₄(OH)₄(OAc)₄]⁸⁺ metal cluster and an idealized [5-RuCl₃]⁴⁻ linker as rigid bodies. Although the metallolinker in **8-RuCl₂(CO)** was identified as *cis*-[5-RuCl₂(CO)]⁴⁻ based on NMR and IR spectroscopic data (vide infra), the CO ligand was approximated by a nearly isoelectronic chloride group in the rigid body to maintain space group symmetry and simplify the Rietveld refinement. The refinement converged to $R_{wp} = 14.03$ with final lattice parameters of $a = 31.9437(6)$ Å, $c = 15.8051(3)$ Å.

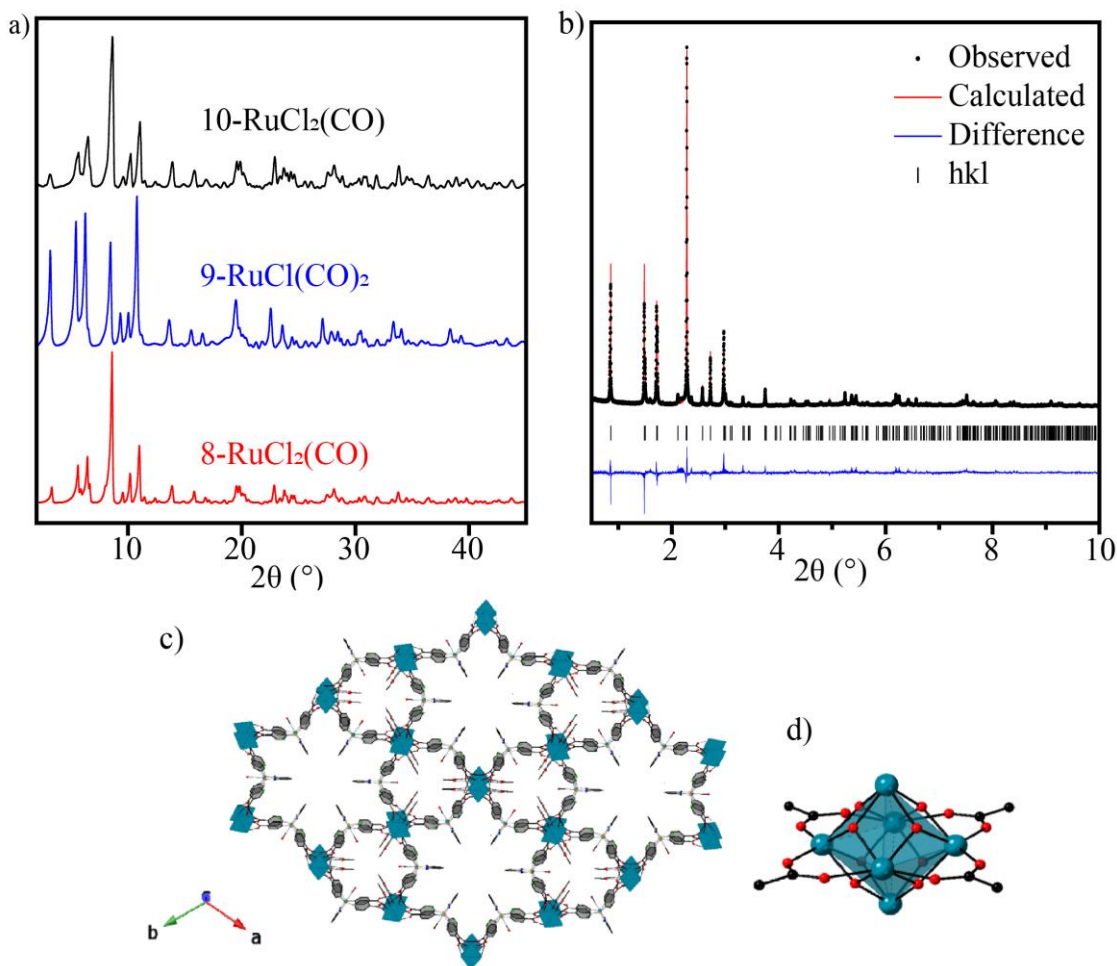


Figure 47. a) PXR patterns (Cu-K α radiation, $\lambda = 1.5418 \text{ \AA}$) for **8-RuCl₂(CO)**, **9-RuCl(CO)₂** and **10-RuCl₂(CO)**. b) Rietveld refinement profile of **8-RuCl₂(CO)** from SPXR data ($\lambda = 0.414536 \text{ \AA}$). c) Framework structure of **8-RuCl₂(CO)**. d) Structure of the D_{4h} [Zr₆O₄(OH)₄(OAc)₄]⁸⁺ secondary building units.

The refined structure of **8-RuCl₂(CO)** shows small trigonal and larger hexagonal channels along the *c*-axis (Figure 47c). The large channels have maximum diameter of $\sim 15 \text{ \AA}$, but are constricted to a minimum diameter of $\sim 6 \text{ \AA}$ by the inward facing arene groups of the pincer complexes. The mean plane of the pincer arene groups is oriented perpendicular to the crystallographic *ab* plane. The *cis*-[5-RuCl₂(CO)]⁴⁻ linkers and OAc groups of the

$[\text{Zr}_6\text{O}_4(\text{OH})_4(\text{OAc})_4]^{8+}$ metal clusters face inward to the smaller trigonal channels, restricting their diameter to $\sim 6 \text{ \AA}$.

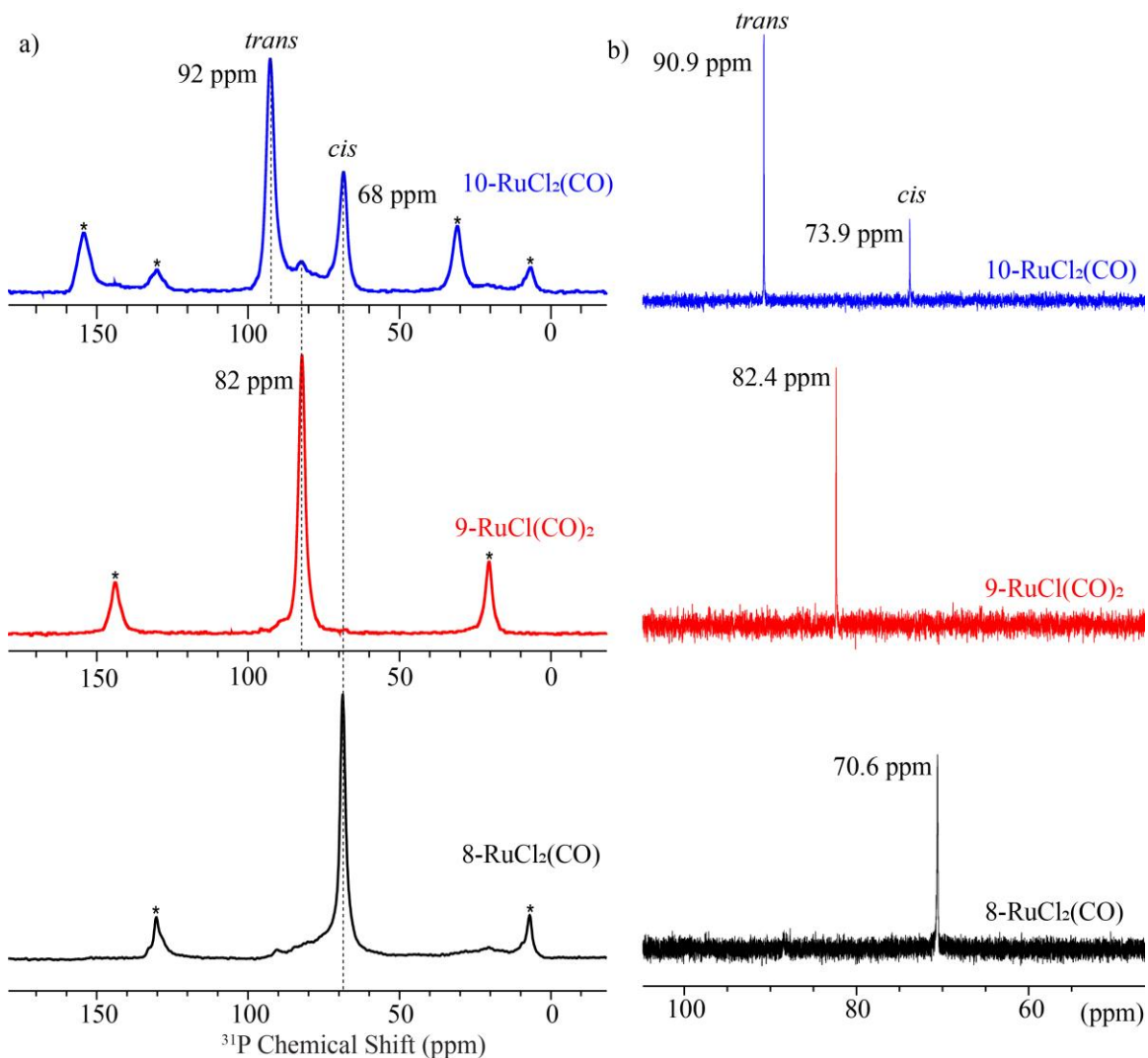


Figure 48. a) Solid-state ^{31}P NMR spectra of **8-RuCl₂(CO)**, **9-RuCl(CO)₂** and **10-RuCl₂(CO)**. Asterisks (*) mark spinning side bands. b) CsF- and acid-digested ^{31}P $\{^1\text{H}\}$ NMR spectra of **8-RuCl₂(CO)**, **9-RuCl(CO)₂** and **10-RuCl₂(CO)**. **8-RuCl₂(CO)** was digested with CsF/DMSO- d_6 /D₂O while **9-RuCl(CO)₂** and **10-RuCl₂(CO)** were digested with CF₃CO₂H/DMSO- d_6 .

Solution- and solid-state NMR spectroscopy have been used to determine the composition of **8-RuCl₂(CO)**, **9-RuCl(CO)₂** and **10-RuCl₂(CO)**. The solid-state ^{31}P NMR spectrum of

8-RuCl₂(CO) shows a single major resonance centered at 68 ppm, and no signal attributable to the PPh₃ ligand was observed (Figure 48a). This finding is corroborated by solution-state NMR analysis of a CsF-digested sample which shows one major singlet resonance at 70.6 ppm in the ³¹P NMR spectrum and a set of signals in the ¹H NMR spectrum that are consistent with a single PNNNP-Ru complex exhibiting C_s symmetry (Figure 48b and Figure 49).

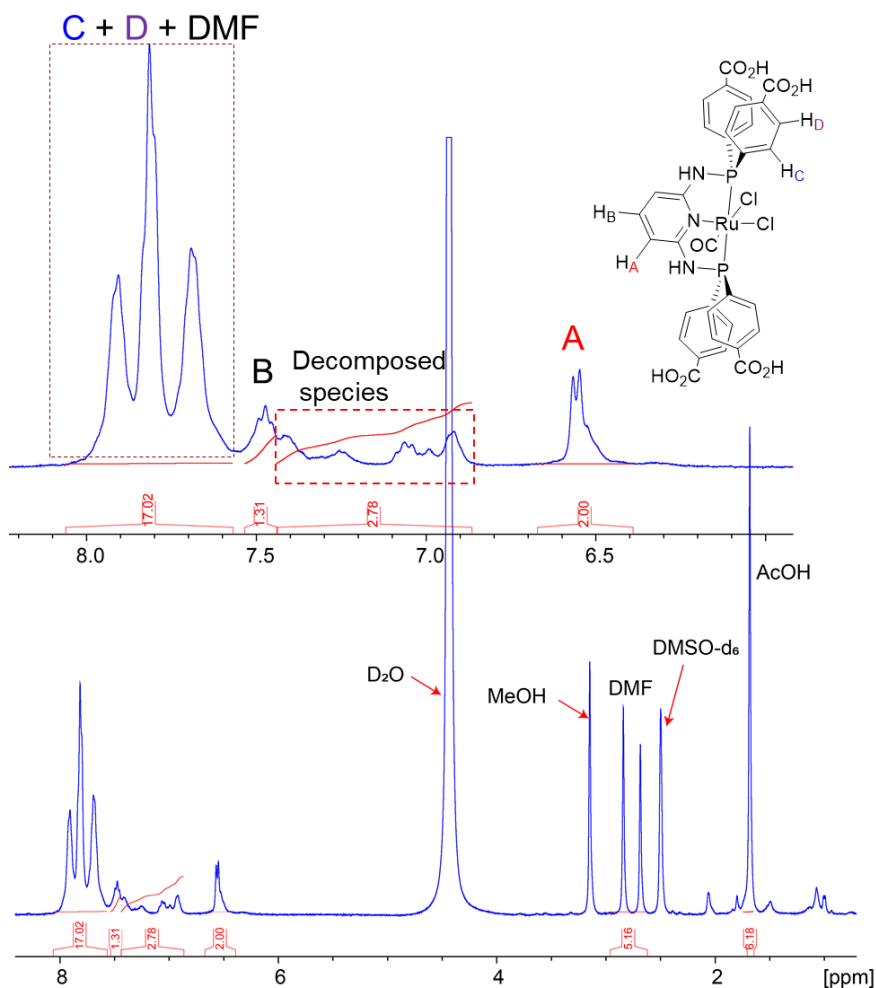


Figure 49. CsF-digested ¹H NMR spectrum (DMSO-d₆/D₂O) of **8-RuCl₂(CO)** after MeOH solvent exchange.

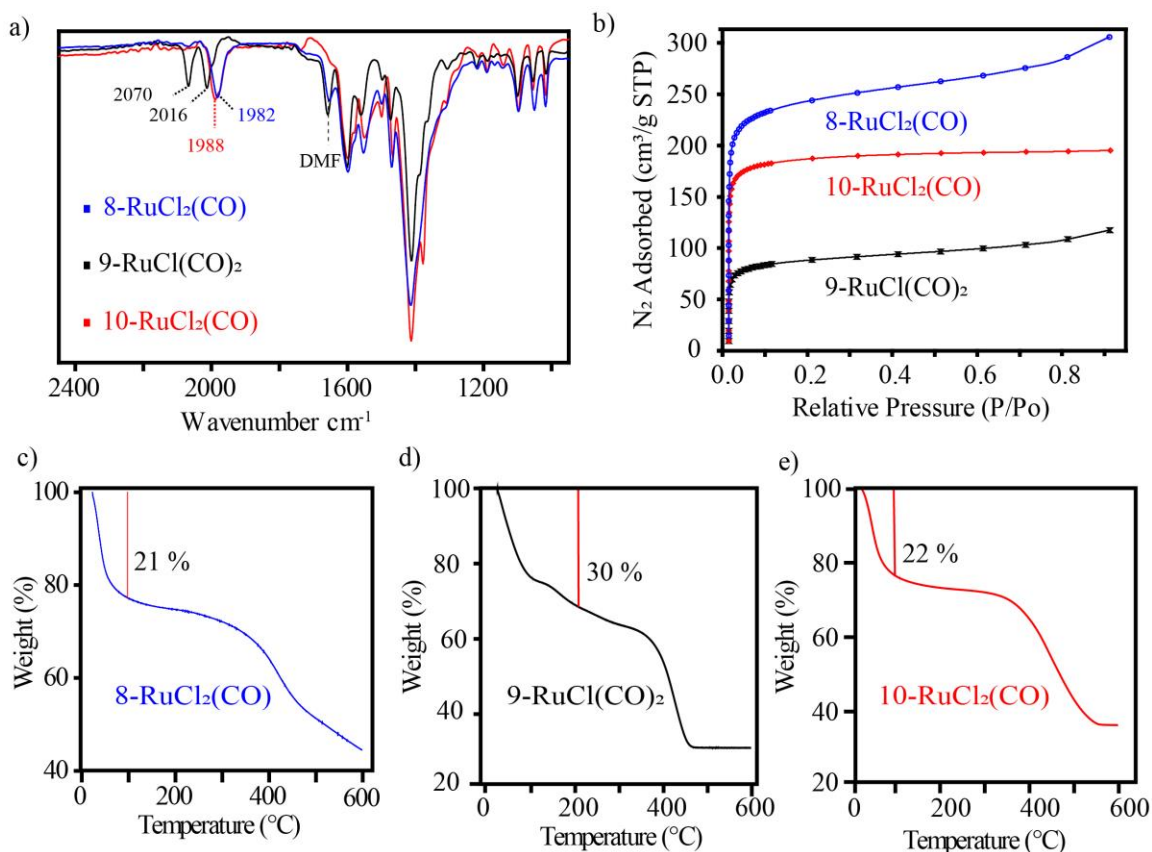


Figure 50. a) ATR-IR spectra of **8-RuCl₂(CO)**, **9-RuCl(CO)₂** and **10-RuCl₂(CO)**. b) N₂ adsorption isotherms at 77 K for samples of **8-RuCl₂(CO)**, **10-RuCl₂(CO)** and **9-RuCl(CO)₂** after desolvation at 100 °C and 10⁻⁴ torr. TGA for samples of **8-RuCl₂(CO)** (c), **9-RuCl(CO)₂** (d), and **10-RuCl₂(CO)** (e) measured at a ramp rate of 5 °C/min under flowing N₂ (50 mL/min).

The ATR-IR spectrum of **8-RuCl₂(CO)** shows a broad Ru-CO stretching band at 1982 cm⁻¹ (Figure 50a). Overall, the spectroscopic data are consistent with *cis*-[5-RuCl₂(CO)]⁴⁻ linkers resulting from substitution of the Ph₃P and TFA ancillary ligands in H₄(5-Ru(TFA)(CO)(PPh₃)) with Cl⁻ during the solvothermal assembly. Accordingly, ³¹P NMR analysis of the supernatant solution from the solvothermal synthesis shows the presence of Ph₃PO (Figure 51f). The ¹H NMR spectrum of a CsF-digested sample of **8-RuCl₂(CO)** also shows that CH₃CO₂H is present in a ~2:1 ratio with respect to the [5-RuCl₂(CO)]

metallo-linkers, supporting the presence of $[\text{Zr}_6\text{O}_4(\text{OH})_4(\text{OAc})_4]^{8+}$ SBUs in the MOF (Figure 49); the bound acetate is also detected in ^{13}C NMR spectrum of the MOF (Figure 51a).

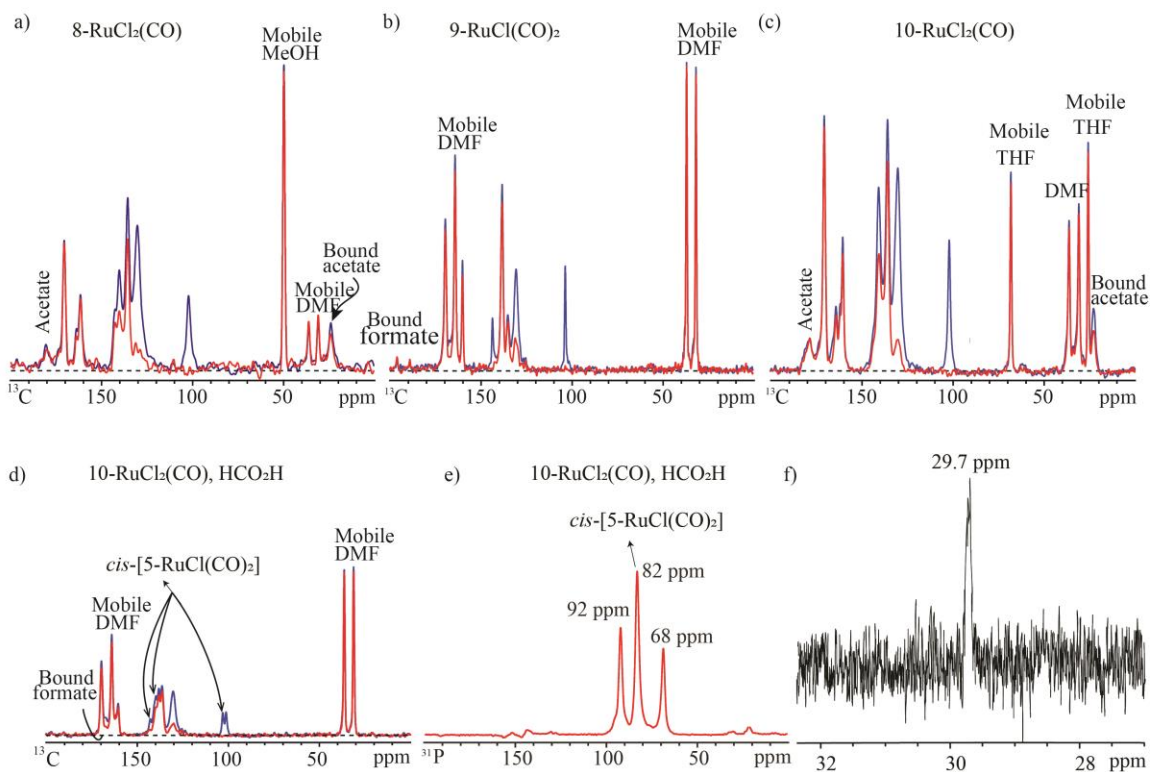


Figure 51. Solid-state ^{13}C NMR spectra of **8-RuCl₂(CO)** (a), **9-RuCl(CO)₂** (b), **10-RuCl₂(CO)** (c), and **10-RuCl₂(CO)** (d) synthesized using HCO_2H as a modulator. Quantitative multiCP ^{13}C NMR spectra of without (blue line) and with (red line) recoupled ^1H dipolar dephasing, recorded at 14 kHz MAS. The spectrum in red shows nonprotonated carbons and highly mobile segments. (e) Solid-state ^{31}P NMR spectrum for **10-RuCl₂(CO)** synthesized using HCO_2H as a modulator with MAS and TOSS. (f) $^{31}\text{P}\{^1\text{H}\}$ NMR spectrum for reaction supernatant of **8-RuCl₂(CO)**.

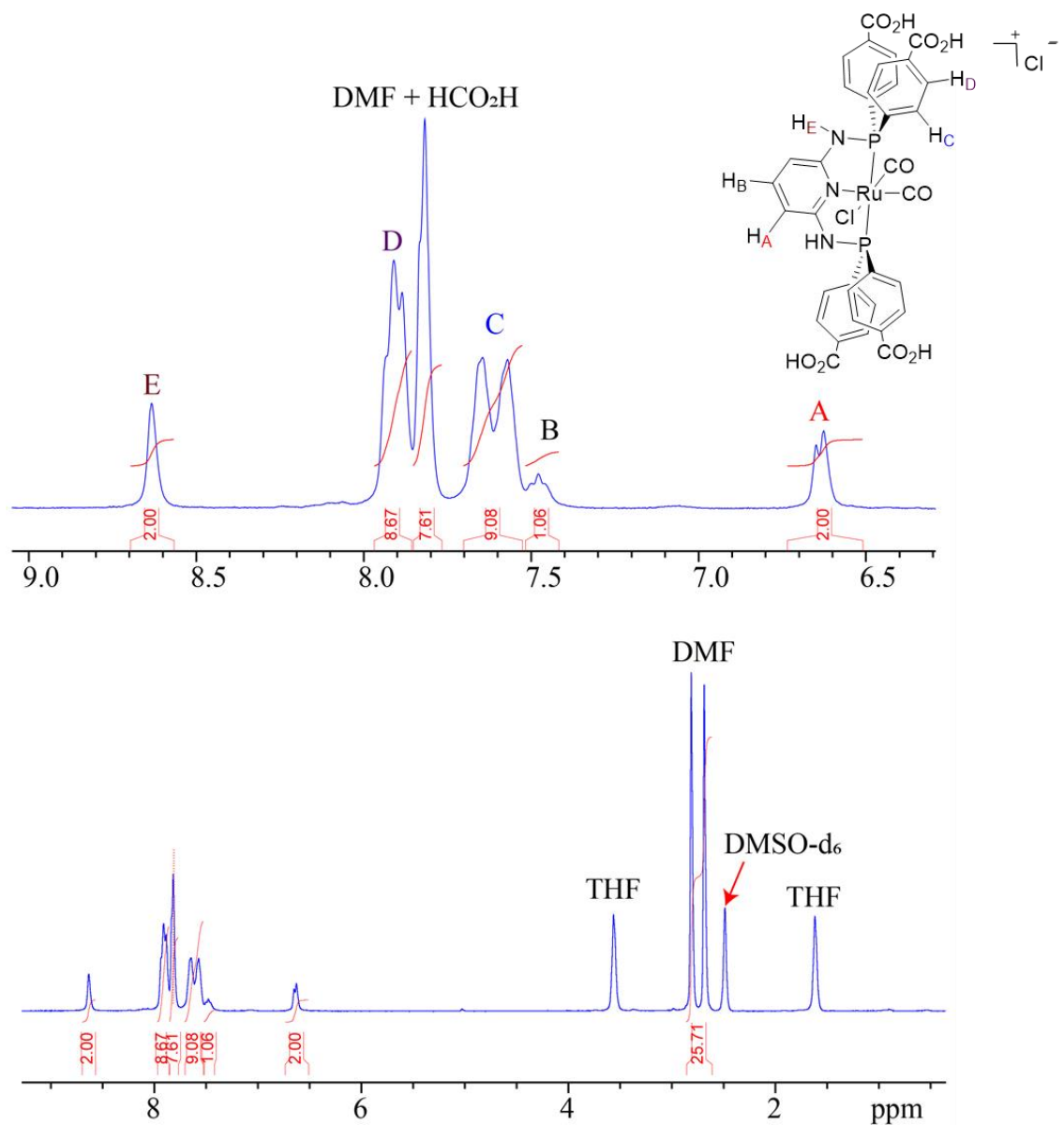


Figure 52. Acid-digested ^1H NMR spectrum ($\text{CF}_3\text{CO}_2\text{H}/\text{DMSO-d}_6$) of $9\text{-RuCl}(\text{CO})_2$ after THF washing.

The solid-state and acid-digested ^{31}P NMR spectra of $9\text{-RuCl}(\text{CO})_2$ both exhibit a major resonance at 82 ppm, which is consistent with the presence of $\text{H}_4(5\text{-RuCl}(\text{CO})_2)$ pincer complexes (81.8 ppm in DMSO-d_6). The solid-state ^{13}C NMR spectrum of the MOF and the ^1H NMR spectrum after acid digestion show all expected resonances for $\text{H}_4(5\text{-$

RuCl(CO)₂) as well as HCO₂H arising from [Zr₆O₄(OH)₄(O₂CH)₄]⁸⁺ SBUs (Figure 51b and Figure 52). The ATR-IR spectrum of **9-RuCl(CO)₂** contains two strong $\nu(\text{CO})$ bands of similar intensity at 2070 and 2016 cm⁻¹, indicating the two carbonyl ligands remain in a *cis* arrangement (Figure 50a).

The solid-state ³¹P NMR spectrum of **10-RuCl₂(CO)** shows two major resonances at 68 and 92 ppm, corresponding to a ~1:2 mixture of *cis*- and *trans*-[5-RuCl₂(CO)]⁴⁺ linkers in the MOF (Figure 48a). The minor resonance at 82 ppm matches that observed for **9-RuCl(CO)₂**, indicating that **10-RuCl₂(CO)** contains a small amount (< 10 %) of *cis*-[5-RuCl(CO)₂] metallolinkers. This species is likely generated from CO produced as a result of DMF decomposition. Greater amounts of *cis*-[5-RuCl(CO)₂] were observed when the solvothermal synthesis of **10-RuCl₂(CO)** was carried out with longer reaction times or with HCO₂H instead of CH₃CO₂H as the modulator (Figure 51d, e), but its formation could be almost completely inhibited by limiting solvothermal reaction times to 20 h. Under these conditions, the acid-digested ³¹P NMR spectrum of **10-RuCl₂(CO)** shows only resonances attributable to *cis*- and *trans*-[5-RuCl₂(CO)]⁴⁺ complexes at 73.9 and 90.9 ppm, respectively, and a single $\nu(\text{CO})$ band at 1988 cm⁻¹ in the ATR-IR spectrum (Figure 48b and Figure 50a).

Thermogravimetric analyses (TGA) of MeOH-exchanged samples of **8-RuCl₂(CO)** and **10-RuCl₂(CO)** show the loss of guest solvent molecules (~20 wt %) up to 100 °C and the onset of framework decomposition at 300-350 °C (Figure 50c, e). PXRD analysis revealed that **9-RuCl(CO)₂** was unstable to drying after MeOH solvent exchange (Figure 53b).

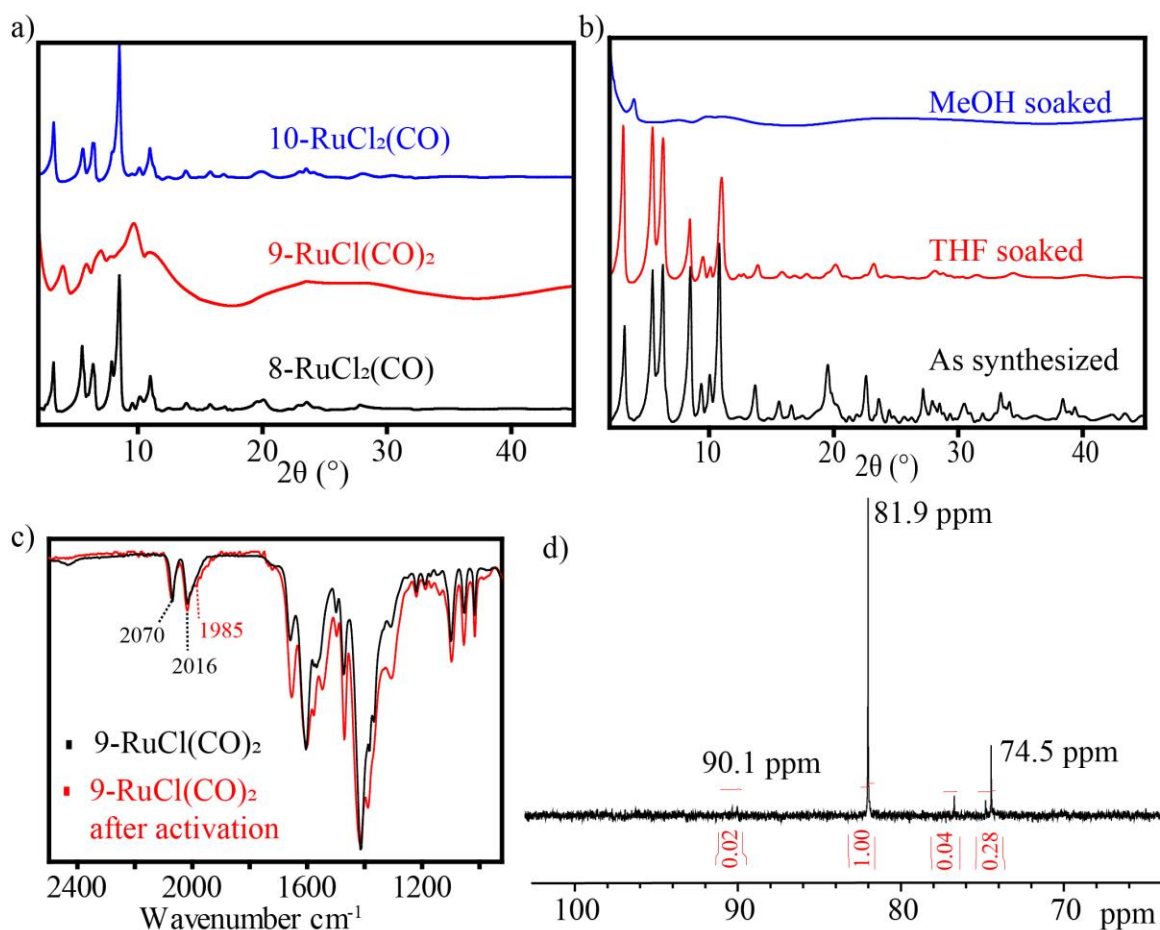


Figure 53. a) PXRD patterns (Cu-K α radiation, $\lambda = 1.5418 \text{ \AA}$) for activated samples of **8-RuCl₂(CO)**, **9-RuCl(CO)₂** and **10-RuCl₂(CO)**. b) PXRD patterns for as synthesized, THF and MeOH solvent exchanged samples of **9-RuCl(CO)₂**. c) ATR-IR spectra for **9-RuCl(CO)₂** before and after activation. d) Acid-digested $^{31}\text{P}\{^1\text{H}\}$ NMR spectrum ($\text{CF}_3\text{CO}_2\text{H}/\text{DMSO-d}_6$) of **9-RuCl(CO)₂** after activation.

As a result, THF was used for solvent-exchange although ^1H NMR analysis showed that it could not completely remove DMF guest solvent molecules. Subsequent TGA analysis of THF-exchanged **9-RuCl(CO)₂** shows the loss of guest solvent molecules ($\sim 30 \text{ wt } \%$) up to $200 \text{ }^\circ\text{C}$ and framework decomposition above $350 \text{ }^\circ\text{C}$ (Figure 50d). N_2 adsorption isotherms (77 K) measured for samples of **8-RuCl₂(CO)**, **9-RuCl(CO)₂**, and **10-RuCl₂(CO)** after solvent exchange and desolvation by heating at $100 \text{ }^\circ\text{C}$ and 10^{-4} torr for

16 h gave calculated BET surface areas of 928, 334, and 728 m^2g^{-1} , respectively (Figure 50b). Notably, the BET surface area of **8-RuCl₂(CO)** is only slightly lower than the theoretical accessible surface area (1019 m^2g^{-1}) calculated using the structure model obtained from Rietveld refinement.³¹⁷

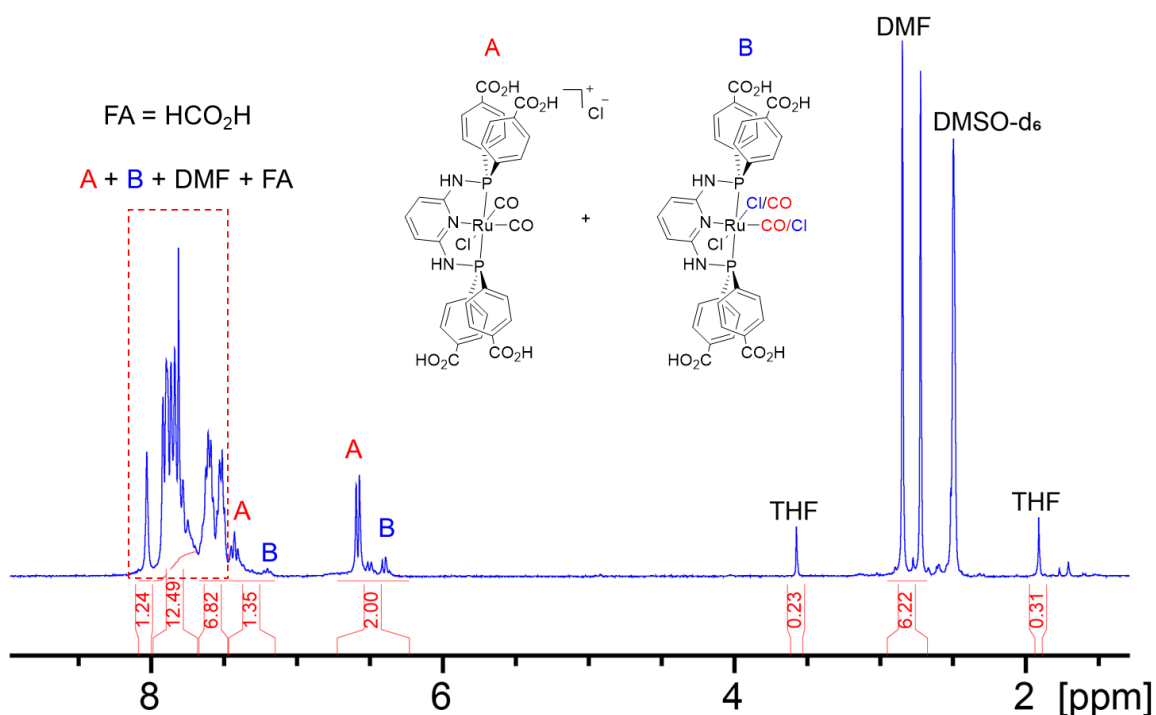


Figure 54. Acid-digested ¹H NMR spectrum (CF₃CO₂H/DMSO-d₆) of **9-RuCl(CO)₂** after activation.

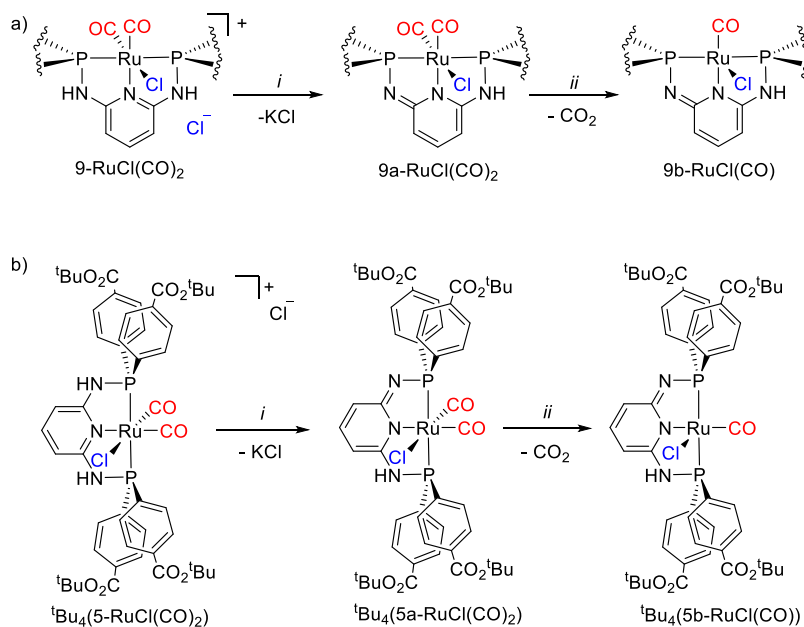
9-RuCl(CO)₂ showed a modest increase in N₂ uptake and BET surface area (451 m^2g^{-1}) when the MOF was activated by lyophilization with benzene. However, PXRD analysis shows that while **8-RuCl₂(CO)** and **10-RuCl₂(CO)** remain crystalline after activation, **9-RuCl(CO)₂** experiences a loss of crystallinity (Figure 53a). The poor structural stability of **9-RuCl(CO)₂** may be due to a greater number of defects resulting from the use of HCO₂H as modulator.³¹⁸ The ATR-IR spectra of activated samples of **9-RuCl(CO)₂** still show the

presence of two $\nu(\text{CO})$ bands, indicating that desolvation does not lead to significant loss of Ru-coordinated CO ligands (Figure 53c). ^1H and ^{31}P NMR analyses of acid-digested samples of desolvated **9-RuCl(CO)₂** confirm that $\text{H}_4(5\text{-RuCl(CO)}_2)$ is the major linker component with only a small amount of *cis/trans*- $\text{H}_4(5\text{-RuCl}_2(\text{CO}))$ species resulting from CO ligand loss (Figure 53d and Figure 54).

5.4 Postsynthetic activation of **9-RuCl(CO)₂**

Deprotonation of the methylene or amide linker groups of Ru diphosphine pincer complexes has proven to be a valuable strategy for precatalyst activation.^{91,311,312,319} The deprotonation step often eliminates coordinated halide ligands, increases the ligand donor strength of the central pyridine, and can switch on metal-ligand cooperativity in subsequent steps of a catalytic cycle. With this precedent in mind, we investigated a sequence of postsynthetic deprotonation and CO ligand removal steps as a means of activating **8-RuCl₂(CO)**, **9-RuCl(CO)₂** and **10-RuCl₂(CO)** for further reactivity and catalytic studies. The MOFs were treated with KO^tBu (2 equiv. per Ru) in THF to induce deprotonation of the NH linker groups (Scheme 18a). Subsequent PXRD analysis revealed reflections attributable to crystalline KCl in **9a-RuCl(CO)₂**, but not in the base-treated samples of **8-RuCl₂(CO)** and **10-RuCl₂(CO)** (Figure 55b). The difference in reactivity observed for **9-RuCl(CO)₂** is presumably due to the presence of outer sphere Cl⁻ ions that are more easily released than the inner sphere halides found in **8-RuCl₂(CO)** and **10-RuCl₂(CO)** MOFs.

Scheme 18. Deprotonation and CO removal reactions



Reagents: (i) KO^tBu , THF, rt, 16 h; (ii) Me_3NO , THF/ CH_2Cl_2 , rt, 16 h.

The ATR-IR spectrum of **9a-RuCl(CO)₂** shows that the CO stretching bands are shifted to lower energy by $\sim 20\text{ cm}^{-1}$ compared to those observed for **9-RuCl(CO)₂** (Figure 55a). This redshift is consistent with weakening of $\text{C}\equiv\text{O}$ bonds due to an increase in electron density at the Ru center.³²⁰ The homogeneous complex analogue, ${}^t\text{Bu}_4(5\text{a-RuCl}(\text{CO})_2)$, prepared via reaction of ${}^t\text{Bu}_4(5\text{-RuCl}(\text{CO})_2)$ with KO^tBu exhibits a similar shift in the CO stretching bands (Scheme 18b, Figure 55d). The Ru sites in the product **9a-RuCl(CO)₂** remain coordinatively saturated owing to the presence of the two strongly bound CO ligands. Consequently, the MOF was treated with Me_3NO to generate **9b-RuCl(CO)**. The loss of a CO ligand was confirmed by the appearance of a single broad CO stretching band at 1955 cm^{-1} (Figure 55a).

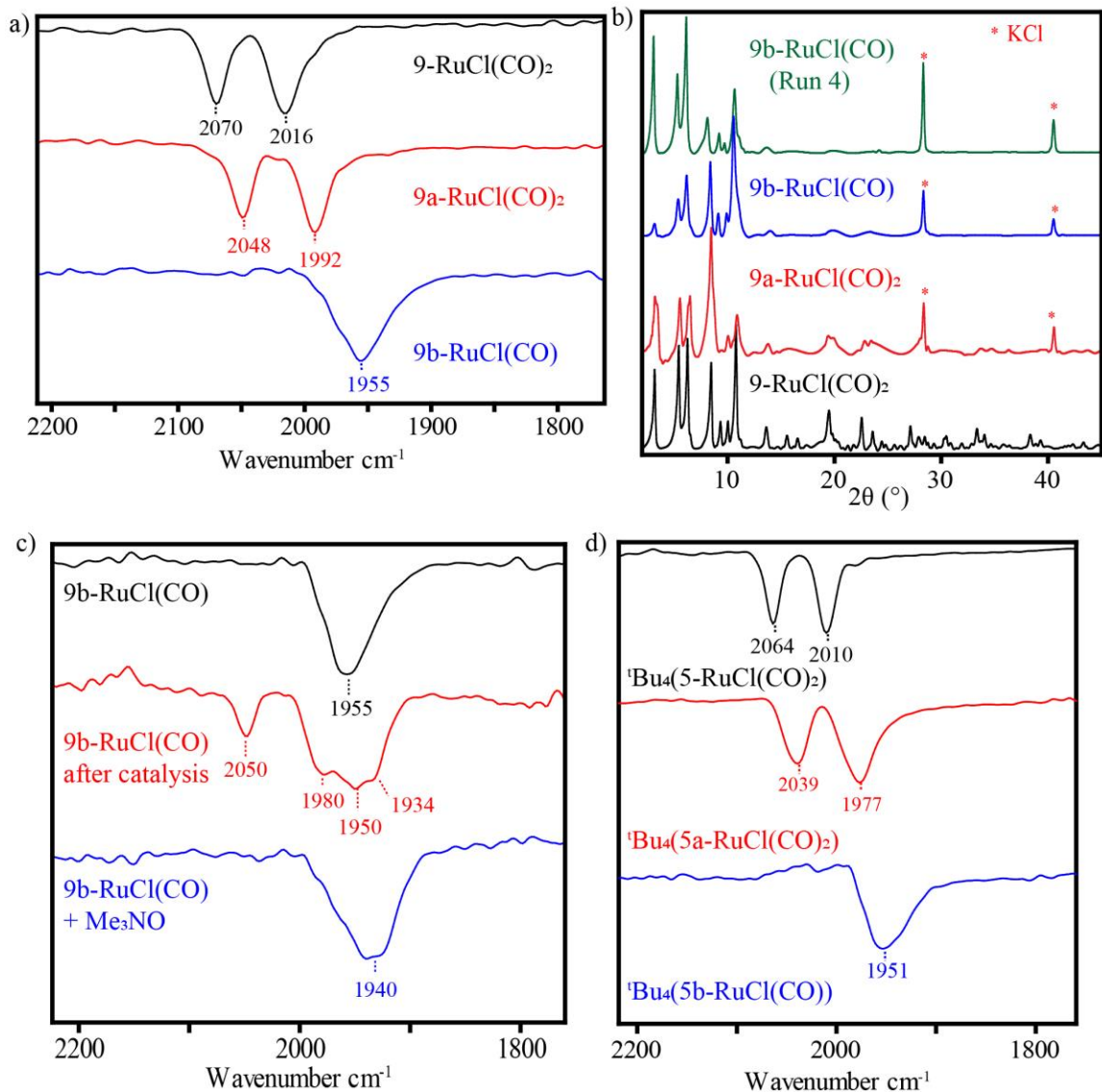
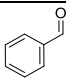
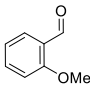
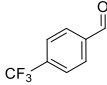
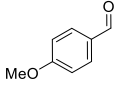
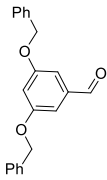


Figure 55. a) ATR-IR spectra for $9\text{-RuCl}(\text{CO})_2$, $9a\text{-RuCl}(\text{CO})_2$, and $9b\text{-RuCl}(\text{CO})$. b) PXRD patterns (Cu-K α radiation, $\lambda = 1.5418 \text{ \AA}$) for $9\text{-RuCl}(\text{CO})_2$, $9a\text{-RuCl}(\text{CO})_2$, and $9b\text{-RuCl}(\text{CO})$ before catalysis and after catalytic run 4. c) ATR-IR spectra for $9b\text{-RuCl}(\text{CO})$ before and after catalysis, and after catalyst regeneration with Me_3NO . d) ATR-IR spectra for homogeneous complexes of $t\text{Bu}_4(5\text{-RuCl}(\text{CO})_2)$, $t\text{Bu}_4(5a\text{-RuCl}(\text{CO})_2)$, and $t\text{Bu}_4(5b\text{-RuCl}(\text{CO}))$.

5.5 Catalytic hydrosilylation studies

Table 6. Catalytic Hydrosilylation of aryl aldehydes^a

$$\text{R}-\text{CHO} + \text{Et}_3\text{SiH} \text{ (2 equiv.)} \xrightarrow[1,4\text{-dioxane, } 100\text{ }^\circ\text{C, } 12\text{ h}]{5\text{ mol \% [Ru]}} \text{R}-\text{CH}_2\text{OSiEt}_3$$

Entry	Substrate	Catalyst	% Yield ^b
1		8-RuCl₂(CO)	< 5
2		8-RuCl₂(CO)-KO^tBu	< 5
3		9-RuCl(CO)₂	< 5
4		9a-RuCl(CO)₂	10
5		9b-RuCl(CO)	94
6		10-RuCl₂(CO)	6
7		10-RuCl₂(CO)-KO^tBu	< 5
8		^t Bu ₄ (5-RuCl(CO) ₂)	< 5
9		^t Bu ₄ (5b-RuCl(CO))	10
10		9b-RuCl(CO) (Run 2)	33
11 ^c		9b-RuCl(CO) (Run 3)	95
12		9b-RuCl(CO) (Run 4)	72
13		9b-RuCl(CO)	91
14		9b-RuCl(CO)	92
15		9b-RuCl(CO)	69
16		9b-RuCl(CO)	9

^aReaction conditions: substrate (0.2 mmol), catalyst (0.01 mmol), silane (0.4 mmol), dioxane (1 mL), 12 h, 100 °C. ^bYields were determined by ¹H NMR with respect to an internal standard (hexamethylbenzene). ^cThe catalyst was regenerated by treatment with Me₃NO.

Catalytic hydrosilylation of carbonyls provides a mild and economical route for generating silane protected alcohols. Homogeneous organometallic complexes, including those supported by diphosphine pincer ligands, have been reported to efficiently catalyze hydrosilylation of carbonyl groups.^{321–325} However, relatively few MOFs have been reported to catalyze hydrosilylation reactions.^{326–329} Hydrosilylation of carbonyls with a well-defined and recyclable catalyst presents an attractive approach to hydrogenation of carbonyl substrates. Consequently, we set out to examine the PNNNP-Ru MOFs as catalysts for hydrosilylation of aldehydes and ketones.

Initial catalytic reactions were carried out at 100 °C in 1,4-dioxane with benzaldehyde and Et₃SiH as substrates and 5 mol % catalyst loading (based on Ru). Product yields were determined by ¹H NMR and/or GC-MS/FID analysis with hexamethylbenzene as an internal standard. The unactivated MOFs **8-RuCl₂(CO)**, **9-RuCl(CO)₂** and **10-RuCl₂(CO)** afforded less than 6 % yield of benzyloxytriethylsilane under these conditions (Table 6, entries 1, 3 and 6). In contrast, **9b-RuCl(CO)** proved to be an effective catalyst, providing the silyl ether product in 94 % yield after 12 h (Table 6, entry 5). The deprotonated MOF **9a-RuCl(CO)₂** (10 % yield) and a sample of **9-RuCl(CO)₂** treated with Me₃NO (6 % yield) showed little activity for the reaction. These results support catalysis occurring at the activated Ru sites rather than Lewis acidic Zr sites and highlight the importance of the deprotonation and CO ligand removal steps for precatalyst activation. Recent work by Huang and co-workers suggests that a deprotonated PNNNP-NiH complex may act as a basic “organocatalyst” in hydrosilylation reactions without direct involvement of the Ni center.^{330,331} While we cannot rule the possibility of a related mechanism for **9b-**

RuCl(CO), the need for CO ligand removal implies the requirement of a coordinatively unsaturated Ru center. The catalytic efficiency of **9b-RuCl(CO)** dropped considerably (33 % yield) upon attempted recycling of the catalyst. The ATR-IR spectrum of the MOF after the second run showed the appearance of new CO stretching bands at 2050 and 1980 cm^{-1} , consistent with the formation of *cis*-[5-RuCl(CO)₂]³⁻ pincer species (Figure 55c). However, the identity of species for the additional new broad stretching frequencies around 1950 and 1934 cm^{-1} have not been established. The appearance of *cis*-[5-RuCl(CO)₂]³⁻ can be attributed to off-cycle decarbonylation of benzaldehyde, and based on the poor catalytic activity of **9-RuCl(CO)₂** and **9a-RuCl(CO)₂**, should lead to catalyst deactivation. Notably, **9b-RuCl(CO)** was not observed to catalyze decarbonylation of benzaldehyde at elevated temperatures nor in the presence of Me₃NO as a CO scavenger. Nevertheless, we found that the recovered MOF catalyst could be reactivated for subsequent hydrosilylation reactions upon treatment with Me₃NO. The ensuing catalytic run (Table 6, entry 11) showed nearly complete recovery of the catalytic activity, although a modest drop in activity was observed in subsequent recycling steps. Notably, **9b-RuCl(CO)** remains crystalline after regenerating and recycling the catalyst (Figure 55b). Moreover, no additional substrate conversion was observed in the reaction supernatant after hot filtration, supporting the heterogeneous nature of the catalysis. **9b-RuCl(CO)** demonstrates good catalytic activity for hydrosilylation of a range of benzaldehyde derivatives (Table 6, entries 13-16). However, < 10 % yield of hydrosilylated product was obtained with a large substrate, 3, 5-dibenzyloxybenzaldehyde, indicating substrate transport limitations within

the MOF (Table 6, entry 17). **9b-RuCl(CO)** also shows unexpectedly low catalytic activity with acetophenone as a substrate.

The homogeneous complexes ${}^t\text{Bu}_4(5\text{-RuCl}(\text{CO})_2)$ and *cis/trans* ${}^t\text{Bu}_4(5\text{-RuCl}_2(\text{CO}))$ were found to be inactive for the catalytic hydrosilylation reaction (Table 6, entry 8). In addition, a homogeneous analogue of **9b-RuCl(CO)** prepared by treating ${}^t\text{Bu}_4(5\text{-RuCl}(\text{CO})_2)$ with KO^tBu followed by Me_3NO showed only a slight increase in catalytic activity (Table 6, entry 9). Interestingly, NMR analysis of ${}^t\text{Bu}_4(5\text{b-RuCl}(\text{CO})_2)$ showed a mixture of species that could not be clearly identified, but give rise to signals characteristic of PNNNP-Ru complexes. The ATR-IR spectrum of ${}^t\text{Bu}_4(5\text{b-RuCl}(\text{CO})_2)$ also shows a single broad CO stretching band at 1951 cm^{-1} , confirming formation of monocarbonyl species resembling that observed in **9b-RuCl(CO)** (Figure 55d). Attempts to isolate and further characterize these species were unsuccessful. ${}^{31}\text{P}$ NMR analysis of the homogeneous reaction mixture after catalysis shows a similarly complex mixture of species, but no signals indicative of pincer decomposition were observed. Although it is not presently clear why the homogeneous PNNNP-Ru complexes are inactive for catalytic hydrosilylation, their immobilization as linkers in **9b-RuCl(CO)** proves to be beneficial for stabilizing catalytically active species.

5.5 Conclusions

A series of three isostructural, **8-RuCl₂(CO)**, **9-RuCl(CO)₂**, **10-RuCl₂(CO)**, Zr MOFs have been assembled from PNNNP-Ru metallolinkers containing different combination of ancillary ligands at the Ru centers. The structure and composition of these MOFs have been determined using PXRD, solid- and solution-state NMR spectroscopy, IR spectroscopy and

elemental analysis. Among them, only **9-RuCl(CO)₂** could be readily activated to generate a heterogeneous catalyst for the hydrosilylation of aryl aldehydes with Et₃SiH. The difference in reactivity among the series is rationalized by the presence of outer sphere Cl⁻ ions in **9-RuCl(CO)₂** that are more readily eliminated than the inner sphere Cl ligands in **8-RuCl₂(CO)** and **10-RuCl₂(CO)**. Subsequent CO-ligand removal from **9a-RuCl(CO)₂** generates a coordinatively unsaturated PNNNP-Ru species capable of catalyzing hydrosilylation reactions. These results demonstrate the importance of rational and diligent activation of MOF precatalysts. Moreover, the disparate reactivity of **9b-RuCl(CO)₂** and its homogeneous analogue point to a beneficial site isolation effect.

5.6 Experimental

General Considerations. RuHCl(CO)(PPh₃)₃³³² was prepared following a literature procedure. THF and 1,4-dioxane were degassed by sparging with ultra-high purity argon and dried via passage through columns of drying agents using a solvent purification system from Pure Process Technologies. All other solvents and reagents were purchased from commercial suppliers and used as received. Routine X-ray powder diffraction (PXRD) patterns for phase identification were collected using a Rigaku Miniflex 600 diffractometer with Nickel-filtered Cu-K α radiation ($\lambda = 1.5418 \text{ \AA}$). High-resolution synchrotron X-ray powder diffraction (SPXRD) data were collected at 295 K using beamline 11-BM at the Advanced Photon Source (APS, Argonne National Laboratory, Argonne, IL) with an average wavelength of 0.414536 \AA . Rietveld refinement was carried out with TOPAS-Academic.²⁷¹ ATR-IR spectra were measured using a Bruker Alpha II spectrometer with a diamond ATR accessory. N₂ adsorption isotherms (77 K, liquid nitrogen bath) were

measured using a Micromeritics 3Flex Surface Characterization Analyzer. Prior to analysis, samples (100–200 mg) were heated under reduced pressure until the outgas rate was less than 2 mTorr/min. GC-MS analysis was performed using an Agilent 7890B GC system equipped with the HP-5 Ultra Inert column (30 m, 0.25 mm, 0.25 μ m), and a FID detector. For MS detection an electron ionization system was used with an ionization energy of 70 eV. Elemental analyses (C, H, N) were performed by Robertson Microlit Laboratories (Ledgewood, NJ).

Solution-state NMR spectra were measured using either a Varian Inova or Bruker 400 MHz spectrometer. For ^1H and $^{13}\text{C}\{^1\text{H}\}$ NMR spectra, the solvent resonance was referenced as an internal standard. For ^{31}P NMR spectra, 85 % H_3PO_4 was used as an external standard (0 ppm). Solvent-suppressed ^1H NMR spectra were collected using 180° water selective excitation sculpting with default parameters and pulse shapes.³³³ Solid-state NMR experiments were performed using a Bruker DSX-400 spectrometer at a resonance frequency of 162 MHz for ^{31}P with a magic-angle spinning (MAS) probe in double-resonance mode. Samples were packed into 4 mm rotors with Kel-F 22 μL HRMAS inserts. Experiments were carried out at spinning frequencies of 10–13.5 kHz. Typical ^{31}P and ^1H 90° pulse-lengths were 4 μs and 6 μs , respectively. ^{31}P NMR spectra were obtained after composite-pulse multiple cross polarization from ^1H , with a recycle delay of 1 s and 10 blocks of 1.1-ms 90-100% ramp cross polarization separated by 0.5-s ^1H repolarization periods.²⁷² Four-pulse total suppression of sidebands (TOSS) was used to obtain spectra almost without spinning sidebands.²⁷³ Two-pulse phase modulation ^1H decoupling was applied during detection.²⁷⁴ ^{31}P spectra were externally referenced to the upfield resonance

of calcium hydroxyapatite (National Institute of Standards and Technology) at 2.73 ppm; this corresponds to the 85 % H₃PO₄ scale.

Synthesis of ¹Bu₄(5-RuH(CO)(PPh₃)). A solution of ¹Bu₄PNNNP (0.77 g, 0.88 mmol) in THF (3 mL) was added dropwise to a suspension of RuCl(H)(CO)(PPh₃)₃ (0.84 g, 0.88 mmol) in THF (20 mL). The reaction was heated at 60 °C overnight with vigorous stirring, resulting in formation of a white precipitate. After cooling to room temperature, the solid was collected by filtration, washed with Et₂O (3 × 10 mL), and dried in vacuo to afford [¹Bu₄(5-RuH(CO)(PPh₃))]Cl as a white powder (0.84 g, 73 %). ¹H NMR (400 MHz, DMSO-*d*₆) δ -7.24 (dt, 1H, ²J_{P-H} = 86.88 Hz, 26.23 Hz, Ru-H), 1.53 (s, 36H, ¹Bu), 6.26 (d, 2H, ³J_{H-H} = 8.26 Hz, pyridine Ar-H), 6.98 (m, 15H, PPh₃ Ar-H), 7.28 (m, 5H, pyridine and benzoate Ar-H), 7.60 (d, 4H, ³J_{H-H} = 8.15 Hz, benzoate Ar-H), 8.06 (m, 8H, benzoate Ar-H), 9.94 (br, 2H, NH). ³¹P{¹H} NMR (162 MHz, DMSO-*d*₆) δ 39.8 (t, 1P, ²J_{P-P} = 18.69 Hz), 99.9 (d, 2P, ²J_{P-P} = 19.31 Hz). ATR-IR: ν(CO) 1940 cm⁻¹. [¹Bu₄(5-RuH(CO)(PPh₃))]Cl·H₂O; C₆₈H₇₅ClN₃O₁₀P₃Ru: C, 61.70; H, 5.71; N, 3.17. Found: C, 61.30; H, 5.47; N, 3.13. A solution of NaTFA (0.14 g, 0.96 mmol) in THF (5 mL) was added to a solution of [¹Bu₄(5-RuH(CO)(PPh₃))]Cl (0.92 g, 0.70 mmol) in CHCl₃ (5 mL) and stirred at room temperature for 2 h. The volatiles were removed under reduced pressure, and the solid was extracted into CHCl₃ (5 mL) with sonication. The resulting suspension was filtered through a pad of celite to ensure complete removal of NaCl. After removing the solvent in vacuo, ¹Bu₄(5-RuH(CO)(PPh₃)) was obtained as a grey powder (0.90 g, 93%). ¹H NMR (400 MHz, DMSO-*d*₆) δ -7.35 (dt, 1H, ²J_{P-H} = 86.57 Hz, 23.35 Hz, Ru-H), 1.52 (s, 36H, ¹Bu), 6.23 (d, 2H, ³J_{H-H} = 7.24 Hz, pyridine Ar-H), 6.99 (m, 15H, PPh₃ Ar-H), 7.28 (br, 5H, pyridine and

benzoate Ar-H), 7.60 (d, 4H, $^3J_{\text{H-H}} = 7.63$ Hz, benzoate Ar-H), 8.06 (br, 8H, benzoate Ar-H), 9.90 (br, 2H, NH). $^{31}\text{P}\{^1\text{H}\}$ NMR (162 MHz, DMSO- d_6) δ 39.8 (t, 1P, $^2J_{\text{P-P}} = 19.75$ Hz), 99.8 (d, 2P, $^2J_{\text{P-P}} = 19.26$ Hz). ATR-IR: $\nu(\text{CO})$ 1945 cm^{-1}

Synthesis of $\text{H}_4(5\text{-Ru}(\text{TFA})(\text{CO})(\text{PPh}_3))$. A 20 mL scintillation vial was charged with $^t\text{Bu}_4(5\text{-RuH}(\text{CO})(\text{PPh}_3))$ (0.90 g, 0.60 mmol), CH_2Cl_2 (3 mL), and $\text{CF}_3\text{CO}_2\text{H}$ (1 mL) and stirred at room temperature for 16 h. The solvent was then removed using a rotary evaporator, and the resulting brown solid was dissolved in a minimal amount of methanol (~ 2 mL). The product was precipitated with Et_2O (~ 15 mL), collected by filtration, and washed with Et_2O (3×10 mL). The product was obtained as a white powder (0.66 g, 87%) after drying in vacuo. ^1H NMR (400 MHz, DMSO- d_6) δ 6.67 (d, 2H, $^3J_{\text{H-H}} = 7.76$ Hz, pyridine Ar-H), 7.08 (m, 12H, PPh_3 Ar-H), 7.24 (t, 8H, $^3J_{\text{H-H}} = 6.00$ Hz, benzoate Ar-H), 7.39 (br, 3H, PPh_3 Ar-H), 7.73 (t, 1H, $^3J_{\text{H-H}} = 8.23$ Hz, pyridine Ar-H), 7.79 (d, 4H, $^3J_{\text{H-H}} = 7.86$ Hz, benzoate Ar-H), 7.95 (d, 4H, $^3J_{\text{H-H}} = 7.86$ Hz, benzoate Ar-H). $^{31}\text{P}\{^1\text{H}\}$ NMR (162 MHz, DMSO- d_6) δ 27.6 (t, 1P, $^2J_{\text{P-P}} = 24.3$ Hz), 78.1 (d, 2P, $^2J_{\text{P-P}} = 22.68$ Hz). ATR-IR: $\nu(\text{CO})$ 1982 cm^{-1} . Anal. Calcd for $\text{H}_4(5\text{-Ru}(\text{TFA})(\text{CO})(\text{PPh}_3))$; $\text{C}_{56}\text{H}_{40}\text{F}_6\text{N}_3\text{O}_{13}\text{P}_3\text{Ru}$: C, 52.92; H, 3.17; N, 3.31. Found: C, 53.44; H, 3.47; N, 3.42.

Synthesis of $8\text{-RuCl}_2(\text{CO})$. A 20 mL scintillation vial was charged with ZrCl_4 (16 mg, 0.070 mmol), DMF (4 mL), and glacial acetic acid (1.5 mL). The mixture was sonicated for 20 min until it gave a clear colorless solution. The solution was then added to a vial containing a solution of $\text{H}_4(5\text{-Ru}(\text{TFA})(\text{CO})(\text{PPh}_3))$ (30 mg, 0.024 mmol) in DMF (2 mL). The vial was sealed with a Teflon-lined screw-top cap (Qorpak CAP-00554) and heated to 120 $^\circ\text{C}$ in a programmable oven for 16 h. After allowing the reaction to cool to room

temperature, the solid was collected by centrifugation, washed with DMF (3×10 mL), and soaked in MeOH (4×10 mL) for a total of 24 h. **8-RuCl₂(CO)** was obtained as a nearly colorless microcrystalline powder (40 mg) after drying in vacuo. $^{31}\text{P}\{^1\text{H}\}$ NMR (162 MHz, CsF/DMSO-*d*₆/D₂O) δ 70.8 (s, 2P), 28.5 (broad, minor impurity). Based on elemental analysis and NMR spectroscopic data obtained for **8-RuCl₂(CO)** after MeOH solvent exchange and activation, the empirical formula is best given as: $\text{Zr}_6\text{O}_4(\text{OH})_4(\text{CH}_3\text{CO}_2)_{2.8}(\text{OH})_{0.4}(5\text{-RuCl}_2(\text{CO}))_2(\text{Ar}_2\text{PO}_2\text{Me})_{0.4}(\text{MeOH})_{0.15}(\text{DMF})_{0.5}$, (Ar = *p*-C₆H₄-CO₂). The presence of Ar₂PO₂Me in **8-RuCl₂(CO)** is supported by the minor resonance observed in solid- and solution-state ^{31}P NMR spectra around 20 ppm. In addition, the CsF-digested ^1H NMR spectrum of **8-RuCl₂(CO)** after activation shows set of resonances in the aromatic region attributed to the decomposed species. Anal. Calcd. for **8-RuCl₂(CO)**;

$\text{Zr}_6\text{O}_4(\text{OH})_4(\text{CH}_3\text{CO}_2)_{2.8}(\text{OH})_{0.4}(\text{C}_{33}\text{H}_{21}\text{N}_3\text{O}_8\text{P}_2\text{RuCl}_2(\text{CO}))_2(\text{C}_{14}\text{H}_9\text{O}_6\text{P})_{0.4}(\text{MeOH})_{0.15}(\text{DMF})_{0.5}$: C, 35.88; H, 2.38; N, 3.35. Found: C, 36.09; H, 2.88; N, 3.23

Synthesis of RuCl₂(CO)₃(THF). RuCl₂(CO)₃(THF) was prepared by modification of a procedure reported for the synthesis of [RuCl₂(CO)₂]_n.³³⁴ A 200 mL Schlenk flask was charged with RuCl₃·3H₂O (2 g, 0.76 mmol) and formic acid (67 mL). The flask was fitted with a reflux condenser and heated in an oil bath at 107 °C for 14 h under a nitrogen atmosphere. It is critical that the reaction be carried out at the specified temperature to obtain the desired product as higher or lower temperatures lead to mixtures of unidentified products. After cooling to room temperature, the excess formic acid was evaporated from the faint yellow solution under reduced pressure, and the resulting solid was washed with

CH₂Cl₂ (3 × 10 mL) to afford a white powder (1.75 g). The white solid was identified as the formic acid adduct RuCl₂(CO)₃(HCO₂H) based on the ATR-IR spectrum ($\nu(\text{CO})$ 2146 and 2066 cm⁻¹, $\nu(\text{CO}_2)$ 1735 and 1141 cm⁻¹, $\nu(\text{OH})$ 3164 cm⁻¹). Recrystallization from hot THF (5 mL) gave the THF adduct RuCl₂(CO)₃(THF) as a white low dense solid (1.5 g). ATR-IR: $\nu(\text{CO})$ 2137 and 2054 cm⁻¹, $\nu(\text{THF})$ 1023 and 874 cm⁻¹.

Synthesis of ^tBu₄(5-RuCl(CO)₂). A solution of RuCl₂(CO)₃(THF) (0.15 g, 0.46 mmol) in 1,4-dioxane (5 mL) was added to a solution of ^tBu₄PNNNP (0.41 g, 0.47 mmol) in 1,4-dioxane (5 mL) and stirred at 100 °C for 16 h. The reaction was allowed to cool to room temperature, and solid was collected by filtration and washed with 1, 4-dioxane (2 × 10 mL) and pentane (3 × 10 mL). The solid was dried in vacuo to afford a colorless powder (0.33 g, 65 %). ¹H NMR (400 MHz, DMSO-*d*₆) δ 1.52 (s, 36H, ^tBu), 6.90 (d, 2H, ³J_{H-H} = 8.87 Hz, pyridine Ar-H), 7.86 (m, 5H, pyridine and benzoate Ar-H), 8.06 (m, 12H, benzoate Ar-H), 11.04 (s, 2H, NH). ³¹P{¹H} NMR (162 MHz, DMSO-*d*₆): δ 81.3 (s, 2P). ATR-IR: $\nu(\text{CO})$ 2062 and 2009 cm⁻¹. Anal. Calcd for ^tBu₄(5-RuCl(CO)₂); C₅₁H₅₇Cl₂RuN₃O₁₀P₂: C, 55.39; H, 5.20; N, 3.80. Found: C, 55.28; H, 5.17; N, 3.76.

Synthesis of H₄(5-RuCl(CO)₂). A 20 ml scintillation vial was charged with ^tBu₄(5-RuCl(CO)₂) (0.25 g, 0.23 mmol), CH₂Cl₂ (3 mL), and CF₃CO₂H (1 mL). The vial was sealed and the solution was stirred at room temperature for 16 h. Deionized water (5 mL) was added to the reaction, resulting in formation of a white precipitate. The product was collected by filtration, washed with deionized water (2 × 10 mL) and CHCl₃ (3 × 10 mL), and dried under reduced pressure to yield a white powder (0.21 g, 97 %). ¹H NMR (400 MHz, DMSO-*d*₆) δ 6.83 (d, 2H, ³J_{H-H} = 8.25 Hz, pyridine Ar-H), 7.84 (m, 5H, pyridine and

benzoate Ar-H), 7.99 (m, 4H, benzoate Ar-H), 8.09 (d, 4H, $^3J_{\text{H-H}} = 8.00$ Hz, benzoate Ar-H), 8.14 (d, 4H, $^3J_{\text{H-H}} = 7.87$, benzoate Ar-H), 10.72 (s, 2H, NH), 13.47 (br, 4H, CO₂H). $^{31}\text{P}\{^1\text{H}\}$ NMR (162 MHz, DMSO-*d*₆): δ 81.8 (s, 2P). ^{19}F NMR (376 MHz, DMSO-*d*₆): δ -74.0 (s, 3F). ATR-IR: $\nu(\text{CO})$ 2077 and 2022 cm^{-1} . Anal. Calcd for H₄(5-RuCl(CO)₂)·H₂O; C₃₇H₂₇ClF₃N₃O₁₃P₂Ru: C, 45.48; H, 2.79; N, 4.30. Found: C, 45.28; H, 2.84; N, 4.32.

Synthesis of 9-RuCl(CO)₂. A 20 mL scintillation vial was charged with ZrCl₄ (44 mg, 0.19 mmol), DMF (8 mL), formic acid (3 mL). The mixture was sonicated for 20 min to afford a colorless solution. The solution was then added to a solution of H₄(5-RuCl(CO)₂) (60 mg, 0.062 mmol) in DMF (4 mL) in a 20 mL scintillation vial. The vial was sealed with a Teflon-lined screw-top cap (Qorpak CAP-00554) and heated to 120 °C in a programmable oven for 18 h. After cooling to room temperature, the solid was collected by centrifugation, washed with DMF (3 × 10 mL), and soaked in THF (4 × 10 mL) for a total of 24 h. **9-RuCl(CO)₂** was obtained as a nearly colorless microcrystalline powder (77 mg) after drying in vacuo. $^{31}\text{P}\{^1\text{H}\}$ NMR (162 MHz, CF₃CO₂H/DMSO-*d*₆) δ 82.4 (s, 2P). ATR-IR: $\nu(\text{CO})$ 2067 and 2013 cm^{-1} . Based on elemental analysis and NMR spectroscopic data obtained for **9-RuCl(CO)₂** after THF solvent exchange and activation, the empirical formula is best given as: Zr₆O₄(OH₄)(HCO₂)₄(5-RuCl(CO)₂)₂Cl₂(DMF)₂(H₂O)₂. Anal. Calcd. for **9-RuCl(CO)₂**; Zr₆O₄OH₄(HCO₂)₄(C₃₃H₂₁N₃O₈P₂RuCl(CO)₂)₂Cl₂(H₂O)₂(DMF)₂: C, 34.36; H, 2.45; N; 4.01. Found: C, 32.90; H, 2.85; N, 4.01.

Synthesis of *cis/trans*-^tBu₄(5-RuCl₂(CO)). A solution of Me₃NO in CH₂Cl₂ (0.10 M, 3.8 mL, 0.38 mmol) was added to a solution of ^tBu₄(5-RuCl(CO)₂) (0.42 g, 0.38 mmol) in

CH₂Cl₂ (5 mL) in 20 mL scintillation vial, and the resulting mixture was stirred at room temperature for 1 h. The solution turned yellow immediately upon addition of Me₃NO. The volatiles were removed under reduced pressure to yield a yellow powder (0.39 g, 96 %). ¹Bu₄(5-RuCl₂(CO)) was obtained as a mixture of *cis* and *trans* isomers (*cis/trans* ratio ~ 1:2). ¹H NMR (400 MHz, DMSO-*d*₆) δ 1.51 (s, 36H, ¹Bu), 6.72 (d, 2H, ³J_{H-H} = 8.29 Hz, pyridine Ar-H, *cis*-isomer), 6.75 (d, 2H, ³J_{H-H} = 8.10 Hz, pyridine Ar-H, *trans*-isomer), 7.59 (t, 1H, ³J_{H-H} = 8.14 Hz, pyridine Ar-H, *cis*-isomer), 7.66 (t, 1H, ³J_{H-H} = 8.15 Hz, pyridine Ar-H, *trans*-isomer), 7.85 (dd, 8H, ³J_{H-H} = 11.79 Hz, ³J_{P-H} = 6.30 Hz, benzoate Ar-H, *trans*-isomer), 7.93 (d, 8H, ³J_{H-H} = 8.73 Hz, benzoate Ar-H, *trans*-isomer), 7.97 (br, 8H, benzoate Ar-H, *cis*-isomer), 8.03-8.22 (8H, benzoate Ar-H, *cis*-isomer), 10.14 (s, 2H, NH, *trans*-isomer), 10.42 (s, 2H, NH, *cis*-isomer). ³¹P{¹H} NMR (162 MHz, DMSO-*d*₆): δ 71.3 (s, 2P, *cis*-isomer), 90.2 (s, 2P, *trans*-isomer). ATR-IR: ν(CO) 1964 cm⁻¹.

Synthesis of *cis/trans*-H₄(5-RuCl₂(CO)). A 20 mL scintillation vial was charged with *cis/trans* mixture of ¹Bu₄(5-RuCl₂(CO)) (0.35 g, 0.32 mmol), CH₂Cl₂ (3 mL), CF₃CO₂H (1 mL), and HCl_{conc} (0.1 mL). The vial was sealed and stirred at room temperature for 16 h. Et₂O (10 mL) was added to the reaction solution resulting in white precipitate. The solid was collected by filtration, washed with Et₂O (3 × 10 mL) and dried in vacuo to afford the product as light yellow powder (0.25 g, 91 %). ¹H NMR (400 MHz, DMSO-*d*₆) δ 6.65 (d, 2H, ³J_{H-H} = 8.02 Hz, pyridine Ar-H, *cis*-isomer), 6.70 (d, 2H, ³J_{H-H} = 8.01 Hz, pyridine Ar-H, *trans*-isomer), 7.59 (t, 1H, ³J_{H-H} = 7.84 Hz, pyridine Ar-H, *cis*-isomer), 7.66 (t, 1H, ³J_{H-H} = 8.19 Hz, pyridine Ar-H, *trans*-isomer), 7.83 (dd, 8H, ³J_{H-H} = 12.63 Hz, ³J_{P-H} = 6.68 Hz, benzoate Ar-H, *trans*-isomer), 7.93 (dd, 4H, ³J_{H-H} = 13.56 Hz, ³J_{P-H} = 6.67 Hz, benzoate Ar-

H, *cis*-isomer), 7.98 (d, 8H, $^3J_{\text{H-H}} = 8.23$ Hz, benzoate Ar-H, *trans*), 8.03 (d, 4H, $^3J_{\text{H-H}} = 8.01$ Hz, benzoate Ar-H, *cis*-isomer), 8.18 (dd, 4H, $^3J_{\text{H-H}} = 12.51$ Hz, $^3J_{\text{P-H}} = 6.93$ Hz, benzoate Ar-H, *cis*-isomer), 9.95 (s, 2H, NH, *trans*-isomer), 10.17 (s, 2H, NH, *cis*-isomer), 13.18 (br, 4H, CO₂H). $^{31}\text{P}\{^1\text{H}\}$ NMR (162 MHz, DMSO-*d*₆): δ 71.5 (s, 2P, *cis*-isomer), 90.3 (s, 2P, *trans*-isomer). ATR-IR: $\nu(\text{CO})$ 1974 cm⁻¹.

Synthesis of 10-RuCl₂(CO). A 20 mL scintillation vial was charged with ZrCl₄ (49 mg, 0.21 mmol), DMF (8 mL), and glacial acetic acid (3 mL). The mixture was sonicated for 20 min to afford a colorless solution. The solution was then added to a solution of *cis/trans* H₄(5-RuCl₂(CO)) (60 mg, 0.070 mmol) in DMF (4 mL) in a 20 mL scintillation vial. The vial was sealed with a Teflon-lined screw-top cap (Qorpak CAP-00554) and heated to 120 °C in a programmable oven for 20 h. After cooling the reaction to room temperature, the solid was collected by centrifugation, washed with DMF (3 × 10 mL), and soaked in MeOH (4 × 10 mL) for a total of 24 h. **10-RuCl₂(CO)** was obtained as a colorless microcrystalline powder (61 mg) after drying in vacuo. $^{31}\text{P}\{^1\text{H}\}$ NMR (162 MHz, CF₃CO₂H/DMSO-*d*₆) δ 90.9 (s, 2P, *trans*-isomer), 73.9 (s, 2p, *cis*-isomer). ATR-IR: $\nu(\text{CO})$ 1988 cm⁻¹. Based on elemental analysis and NMR spectroscopic data obtained for **10-RuCl₂(CO)** after MeOH solvent exchange and activation, the empirical formula is best given as: Zr₆O₄(OH)₄(CH₃CO₂)₄(5-RuCl₂(CO))₂(H₂O)₂(MeOH). Anal. Calcd. for **10-RuCl₂(CO)**; Zr₆O₄(OH)₄(CH₃CO₂)₄(C₃₃H₂₁N₃O₈P₂RuCl₂(CO))₂(H₂O)₂(MeOH)₂: C, 34.51; H, 2.60; N, 3.10. Found: C, 33.64; H, 2.87; N, 3.22.

Synthesis of 9a-RuCl(CO)₂ and 9b-RuCl(CO). A 20 mL scintillation was charged with **9-RuCl(CO)₂** (0.154 g, 0.11 mmol per Ru) and solution of KO^tBu in THF was added (0.1

M, 2.2 mL, 0.22 mmol). An immediate color change to yellow was observed upon KO^tBu addition and the resulting mixture was gently stirred at room temperature for 16 h. The solid was collected via centrifugation, and washed with THF (3 × 10 mL) to afford **9a-RuCl(CO)₂**. **9a-RuCl(CO)₂** was then treated with a solution of Me₃NO in CH₂Cl₂ (0.1 M, 2.2 mL, 0.22 mmol) at room temperature for 16 h to generate **9b-RuCl(CO)**. The solid was collected via centrifugation, washed with THF (4 × 10 mL) and dried in vacuo to afford a yellow microcrystalline powder (128 mg).

General Procedure for Hydrosilylation Reactions. In a N₂-filled glovebox, a 1 dram screw-top vial was charged with catalyst (5 mol % based on Ru), 1, 4-dioxane (1 mL), Et₃SiH (0.4 mmol), substrate (0.2 mmol), and hexamethylbenzene as internal standard (0.025 mmol). The vial was sealed with a Teflon-lined screw-top cap and the reaction mixture was heated at 100 °C for 12 h. The products of the reaction were characterized by ¹H NMR and GC-MS/FID. Yields of catalysis were determined by ¹H NMR. For recycling experiments without regeneration, the catalyst was isolated from the reaction mixture via centrifugation, washed with 1, 4-dioxane (3 × 2 mL), and resubjected to the catalytic conditions. Regeneration and recycling was carried out by washing the solid catalyst with 1, 4-dioxane (3 × 2 mL) and then treating the solid with a solution of Me₃NO in CH₂Cl₂ as described above.

Bibliography

- (1) Kakaei, K.; Esrafil, M. D.; Ehsani, A. Introduction to Catalysis. *Interface Sci. Technol.* **2019**, *27*, 1–21.
- (2) Spivey, J. J. Catalysis in the Development of Clean Energy Technologies. *Catal. Today* **2005**, *100*, 171–180.
- (3) Farrauto, R. J.; Heck, R. M. Environmental Catalysis into the 21st Century. *Catal. Today* **2000**, *55*, 179–187.
- (4) Hagen, J. *Industrial Catalysis*; Wiley: New Jersey, 2015.
- (5) Schlögl, R. Heterogeneous Catalysis. *Angew. Chem. Int. Ed.* **2015**, *54*, 3465–3520.
- (6) Franke, R.; Selent, D.; Börner, A. Applied Hydroformylation. *Chem. Rev.* **2012**, *112*, 5675–5732.
- (7) Müller, C.; Nijkamp, M. G.; Vogt, D. Continuous Homogeneous Catalysis. *Eur. J. Inorg. Chem.* **2005**, *2005*, 4011–4021.
- (8) Kuil, L. A.; Grove, D. M.; Zwiiker, J. W.; Jennekens, L. W.; Drenth, W.; Koten, G. New Soluble Polysiloxane Polymers Containing a Pendant Terdentate Aryldiamine Ligand Substituent Holding a Highly Catalytically Active Organometallic Nickel(II) Center. *Chem. Mater.* **1994**, *6*, 1675–1683.
- (9) Wljkens, P.; Grove, D. M.; Koten, B. G. Van. Homogeneous Catalysts Based on Silane Dendrimers Functionalized with Arylnickel(n) Complexes. *Nature* **1994**, *372*, 659–663.
- (10) Lu, W.; Wei, Z.; Gu, Z. Y.; Liu, T. F.; Park, J.; Park, J.; Tian, J.; Zhang, M.; Zhang, Q.; Gentle, T.; Bosch, M.; Zhou, H. C. Tuning the Structure and Function of Metal-Organic Frameworks via Linker Design. *Chem. Soc. Rev.* **2014**, *43*, 5561–5593.
- (11) Zhou, H. C.; Long, J. R.; Yaghi, O. M. Introduction to Metal-Organic Frameworks. *Chem. Rev.* **2012**, *112*, 673–674.
- (12) Furukawa, H.; Cordova, K. E.; O’Keeffe, M.; Yaghi, O. M. The Chemistry and Applications of Metal-Organic Frameworks. *Science* **2013**, *341*, 1230444.
- (13) Kalmutzki, M. J.; Hanikel, N.; Yaghi, O. M. Secondary Building Units as the Turning Point in the Development of the Reticular Chemistry of MOFs. *Sci. Adv.* **2018**, *4*, eaat9180.
- (14) Stock, N.; Biswas, S. Synthesis of Metal-Organic Frameworks (MOFs): Routes to Various MOF Topologies, Morphologies, and Composites. *Chem. Rev.* **2012**, *112*, 933–969.
- (15) Webber, T. E.; Liu, W. G.; Desai, S. P.; Lu, C. C.; Truhlar, D. G.; Penn, R. L. Role of a Modulator in the Synthesis of Phase-Pure NU-1000. *ACS Appl. Mater. Interfaces* **2017**, *9*, 39342–39346.
- (16) Islamoglu, T.; Otake, K. I.; Li, P.; Buru, C. T.; Peters, A. W.; Akpınar, I.; Garibay,

- S. J.; Farha, O. K. Revisiting the Structural Homogeneity of NU-1000, a Zr-Based Metal-Organic Framework. *CrystEngComm* **2018**, *20*, 5913–5918.
- (17) Katz, M. J.; Brown, Z. J.; Colón, Y. J.; Siu, P. W.; Scheidt, K. A.; Snurr, R. Q.; Hupp, J. T.; Farha, O. K. A Facile Synthesis of UiO-66, UiO-67 and Their Derivatives. *Chem. Commun.* **2013**, *49*, 9449–9451.
- (18) Yuan, S.; Feng, L.; Wang, K.; Pang, J.; Bosch, M.; Lollar, C.; Sun, Y.; Qin, J.; Yang, X.; Zhang, P.; Wang, Q.; Zou, L.; Zhang, Y.; Zhang, L.; Fang, Y.; Li, J.; Zhou, H. C. Stable Metal–Organic Frameworks: Design, Synthesis, and Applications. *Adv. Mater.* **2018**, *30*, 1–35.
- (19) Bai, Y.; Dou, Y.; Xie, L. H.; Rutledge, W.; Li, J. R.; Zhou, H. C. Zr-Based Metal–Organic Frameworks: Design, Synthesis, Structure, and Applications. *Chem. Soc. Rev.* **2016**, *45*, 2327–2367.
- (20) Li, H.; Wang, K.; Sun, Y.; Lollar, C. T.; Li, J.; Zhou, H. C. Recent Advances in Gas Storage and Separation Using Metal–Organic Frameworks. *Mater. Today* **2018**, *21*, 108–121.
- (21) Lin, R. B.; Xiang, S.; Xing, H.; Zhou, W.; Chen, B. Exploration of Porous Metal–Organic Frameworks for Gas Separation and Purification. *Coord. Chem. Rev.* **2019**, *378*, 87–103.
- (22) Huxford, R. C.; Della Rocca, J.; Lin, W. Metal-Organic Frameworks as Potential Drug Carriers. *Curr. Opin. Chem. Biol.* **2010**, *14*, 262–268.
- (23) Kreno, L. E.; Leong, K.; Farha, O. K.; Allendorf, M.; Van Duyne, R. P.; Hupp, J. T. Metal-Organic Framework Materials as Chemical Sensors. *Chem. Rev.* **2012**, *112*, 1105–1125.
- (24) Lee, J.; Farha, O. K.; Roberts, J.; Scheidt, K. A.; Nguyen, S. T.; Hupp, J. T. Metal-Organic Framework Materials as Catalysts. *Chem. Soc. Rev.* **2009**, *38*, 1450–1459.
- (25) Davis, M. E. New Vistas in Zeolite and Molecular Sieve Catalysis. *Acc. Chem. Res.* **1993**, *26*, 111–115.
- (26) Liang, J.; Liang, Z.; Zou, R.; Zhao, Y. Heterogeneous Catalysis in Zeolites, Mesoporous Silica, and Metal–Organic Frameworks. *Adv. Mater.* **2017**, *29*, 1–21.
- (27) Valtchev, V.; Mintova, S. *1. Zeolites and MOFs? Dare to Know Them!*; Amsterdam University Press, 2018.
- (28) H. Deng, S.; Grunder, K. E. Cordova; C. Valente, H. . F.; M.; Hmadeh, F. ;Gándara, A. C.; Whalley, Z. Liu; S. Asahina;Yaghi, O. M. Large-Pore Apertures in a Series of Metal-Organic Frameworks. *Science* **2012**, *336*, 1018.
- (29) Farha, O. K.; Eryazici, I.; Jeong, N. C.; Hauser, B. G.; Wilmer, C. E.; Sarjeant, A. A.; Snurr, R. Q.; Nguyen, S. T.; Yazaydin, A. Ö.; Hupp, J. T. Metal-Organic Framework Materials with Ultrahigh Surface Areas: Is the Sky the Limit? *J. Am. Chem. Soc.* **2012**, *134*, 15016–15021.
- (30) Howarth, A. J.; Peters, A. W.; Vermeulen, N. A.; Wang, T. C.; Hupp, J. T.; Farha, O. K. Best Practices for the Synthesis, Activation, and Characterization of Metal–organic Frameworks. *Chem. Mater.* **2017**, *29*, 26–39.
- (31) Butova, V. V.; Soldatov, M. A.; Guda, A. A.; Lomachenko, K. A.; Lamberti, C. Metal-Organic Frameworks: Structure, Properties, Methods of Synthesis and Characterization. *Russ. Chem. Rev.* **2016**, *85*, 280–307.

- (32) Carboni, M.; Abney, C. W.; Liu, S.; Lin, W. Highly Porous and Stable Metal-Organic Frameworks for Uranium Extraction. *Chem. Sci.* **2013**, *4*, 2396–2402.
- (33) Falkowski, J. M.; Sawano, T.; Zhang, T.; Tsun, G.; Chen, Y.; Lockard, J. V.; Lin, W. B. Privileged Phosphine-Based Metal-Organic Frameworks for Broad-Scope Asymmetric Catalysis. *J. Am. Chem. Soc.* **2014**, *136*, 5213–5216.
- (34) Vermoortele, F.; Valvekens, P.; de Vos, D. CHAPTER 8. Catalysis at the Metallic Nodes of MOFs; 2013; pp 268–288.
- (35) Schlichte, K.; Kratzke, T.; Kaskel, S. Improved Synthesis, Thermal Stability and Catalytic Properties of the Metal-Organic Framework Compound Cu₃(BTC)₂. *Microporous Mesoporous Mater.* **2004**, *73*, 81–88.
- (36) Vimont, A.; Goupil, J. M.; Lavalley, J. C.; Daturi, M.; Surblé, S.; Serre, C.; Millange, F.; Férey, G.; Audebrand, N. Investigation of Acid Sites in a Zeotypic Giant Pores Chromium(III) Carboxylate. *J. Am. Chem. Soc.* **2006**, *128*, 3218–3227.
- (37) Hu, Z.; Zhao, D. Metal-Organic Frameworks with Lewis Acidity: Synthesis, Characterization, and Catalytic Applications. *CrystEngComm* **2017**, *19*, 4066–4081.
- (38) Hall, J. N.; Bollini, P. Structure, Characterization, and Catalytic Properties of Open-Metal Sites in Metal Organic Frameworks. *React. Chem. Eng.* **2019**, *4*, 207–222.
- (39) Zheng, X.; Zhang, L.; Fan, Z.; Cao, Y.; Shen, L.; Au, C.; Jiang, L. Enhanced Catalytic Activity over MIL-100(Fe) with Coordinatively Unsaturated Fe²⁺/Fe³⁺ Sites for Selective Oxidation of H₂S to Sulfur. *Chem. Eng. J.* **2019**, *374*, 793–801.
- (40) Chui, S. S. Y.; Lo, S. M. F.; Charmant, J. P. H.; Orpen, A. G.; Williams, I. D. A Chemically Functionalizable Nanoporous Material [Cu₃(TMA)₂ (H₂O)₃](N). *Science* **1999**, *283*, 1148–1150.
- (41) Ye, G.; Zhang, D.; Li, X.; Leng, K.; Zhang, W.; Ma, J.; Sun, Y.; Xu, W.; Ma, S. Boosting Catalytic Performance of Metal-Organic Framework by Increasing the Defects via a Facile and Green Approach. *ACS Appl. Mater. Interfaces* **2017**, *9*, 34937–34943.
- (42) Gutov, O. V.; Hevia, M. G.; Escudero-Adán, E. C.; Shafir, A. Metal-Organic Framework (MOF) Defects under Control: Insights into the Missing Linker Sites and Their Implication in the Reactivity of Zirconium-Based Frameworks. *Inorg. Chem.* **2015**, *54*, 8396–8400.
- (43) Fang, Z.; Bueken, B.; De Vos, D. E.; Fischer, R. A. Defect-Engineered Metal-Organic Frameworks. *Angew. Chem. Int. Ed.* **2015**, *54*, 7234–7254.
- (44) Dissegna, S.; Epp, K.; Heinz, W. R.; Kieslich, G.; Fischer, R. A. Defective Metal-Organic Frameworks. *Adv. Mater.* **2018**, *30*, 1–23.
- (45) Vermoortele, F.; Bueken, B.; Le Bars, G.; Van De Voorde, B.; Vandichel, M.; Houthoofd, K.; Vimont, A.; Daturi, M.; Waroquier, M.; Van Speybroeck, V.; Kirschhock, C.; De Vos, D. E. Synthesis Modulation as a Tool to Increase the Catalytic Activity of Metal-Organic Frameworks: The Unique Case of UiO-66(Zr). *J. Am. Chem. Soc.* **2013**, *135*, 11465–11468.
- (46) Liu, Y.; Klet, R. C.; Hupp, J. T.; Farha, O. Probing the Correlations between the Defects in Metal-Organic Frameworks and Their Catalytic Activity by an Epoxide Ring-Opening Reaction. *Chem. Commun.* **2016**, *52*, 7806–7809.
- (47) Wu, H.; Chua, Y. S.; Krungleviciute, V.; Tyagi, M.; Chen, P.; Yildirim, T.; Zhou,

- W. Unusual and Highly Tunable Missing-Linker Defects in Zirconium Metal-Organic Framework UiO-66 and Their Important Effects on Gas Adsorption. *J. Am. Chem. Soc.* **2013**, *135*, 10525–10532.
- (48) Zhao, M.; Deng, K.; He, L.; Liu, Y.; Li, G.; Zhao, H.; Tang, Z. Core-Shell Palladium Nanoparticle@metal-Organic Frameworks as Multifunctional Catalysts for Cascade Reactions. *J. Am. Chem. Soc.* **2014**, *136*, 1738–1741.
- (49) Zhang, W.; Lu, G.; Cui, C.; Liu, Y.; Li, S.; Yan, W.; Xing, C.; Chi, Y. R.; Yang, Y.; Huo, F. A Family of Metal-Organic Frameworks Exhibiting Size-Selective Catalysis with Encapsulated Noble-Metal Nanoparticles. *Adv. Mater.* **2014**, *26*, 4056–4060.
- (50) Liu, H.; Liu, Y.; Li, Y.; Tang, Z.; Jiang, H. Metal-Organic Framework Supported Gold Nanoparticles as a Highly Active Heterogeneous Catalyst for Aerobic Oxidation of Alcohols. *J. Phys. Chem. C* **2010**, *114*, 13362–13369.
- (51) Ling, P.; Lei, J.; Zhang, L.; Ju, H. Porphyrin-Encapsulated Metal-Organic Frameworks as Mimetic Catalysts for Electrochemical DNA Sensing via Allosteric Switch of Hairpin DNA. *Anal. Chem.* **2015**, *87*, 3957–3963.
- (52) Drout, R. J.; Robison, L.; Farha, O. K. Catalytic Applications of Enzymes Encapsulated in Metal–Organic Frameworks. *Coord. Chem. Rev.* **2019**, *381*, 151–160.
- (53) Song, J.; Luo, Z.; Britt, D. K.; Furukawa, H.; Yaghi, O. M.; Hardcastle, K. I.; Hill, C. L. A Multiunit Catalyst with Synergistic Stability and Reactivity: A Polyoxometalate-Metal Organic Framework for Aerobic Decontamination. *J. Am. Chem. Soc.* **2011**, *133*, 16839–16846.
- (54) Shah, W. A.; Waseem, A.; Nadeem, M. A.; Kögerler, P. Leaching-Free Encapsulation of Cobalt-Polyoxotungstates in MIL-100 (Fe) for Highly Reproducible Photocatalytic Water Oxidation. *Appl. Catal. A Gen.* **2018**, *567*, 132–138.
- (55) Li, Z.; Rayder, T. M.; Luo, L.; Byers, J. A.; Tsung, C. K. Aperture-Opening Encapsulation of a Transition Metal Catalyst in a Metal-Organic Framework for CO₂ Hydrogenation. *J. Am. Chem. Soc.* **2018**, *140*, 8082–8085.
- (56) Brozek, C. K.; Dincă, M. Cation Exchange at the Secondary Building Units of Metal-Organic Frameworks. *Chem. Soc. Rev.* **2014**, *43*, 5456–5467.
- (57) Cohen, S. M. The Postsynthetic Renaissance in Porous Solids. *J. Am. Chem. Soc.* **2017**, *139*, 2855–2863.
- (58) Deria, P.; Mondloch, J. E.; Karagiari, O.; Bury, W.; Hupp, J. T.; Farha, O. K. Beyond Post-Synthesis Modification: Evolution of Metal-Organic Frameworks via Building Block Replacement. *Chem. Soc. Rev.* **2014**, *43*, 5896–5912.
- (59) Evans, J. D.; Sumby, C. J.; Doonan, C. J. Post-Synthetic Metalation of Metal-Organic Frameworks. *Chem. Soc. Rev.* **2014**, *43*, 5933–5951.
- (60) Lalonde, M.; Bury, W.; Karagiari, O.; Brown, Z.; Hupp, J. T.; Farha, O. K. Transmetalation: Routes to Metal Exchange within Metal-Organic Frameworks. *J. Mater. Chem. A* **2013**, *1*, 5453–5468.
- (61) Yin, Z.; Wan, S.; Yang, J.; Kurmoo, M.; Zeng, M. H. Recent Advances in Post-Synthetic Modification of Metal–Organic Frameworks: New Types and Tandem

- Reactions. *Coord. Chem. Rev.* **2019**, *378*, 500–512.
- (62) Manna, K.; Ji, P.; Greene, F. X.; Lin, W. Metal-Organic Framework Nodes Support Single-Site Magnesium-Alkyl Catalysts for Hydroboration and Hydroamination Reactions. *J. Am. Chem. Soc.* **2016**, *138*, 7488–7491.
- (63) Feng, X.; Ji, P.; Li, Z.; Drake, T.; Oliveres, P.; Chen, E. Y.; Song, Y.; Wang, C.; Lin, W. Aluminum Hydroxide Secondary Building Units in a Metal-Organic Framework Support Earth-Abundant Metal Catalysts for Broad-Scope Organic Transformations. *ACS Catal.* **2019**, *9*, 3327–3337.
- (64) Hwang, Y. K.; Hong, D. Y.; Chang, J. S.; Jung, S. H.; Seo, Y. K.; Kim, J.; Vimont, A.; Daturi, M.; Serre, C.; Ferey, G. Amine Grafting on Coordinatively Unsaturated Metal Centers of MOFs: Consequences for Catalysis and Metal Encapsulation. *Angew. Chem. Int. Ed.* **2008**, *47*, 4144–4148.
- (65) Canivet, J.; Aguado, S.; Schuurman, Y.; Farrusseng, D. MOF-Supported Selective Ethylene Dimerization Single-Site Catalysts through One-Pot Postsynthetic Modification. *J. Am. Chem. Soc.* **2013**, *135*, 4195–4198.
- (66) Li, J.; Ren, Y.; Qi, C.; Jiang, H. The First Porphyrin-Salen Based Chiral Metal-Organic Framework for Asymmetric Cyanosilylation of Aldehydes. *Chem. Commun.* **2017**, *53*, 8223–8226.
- (67) Zhang, Z. J.; Zhang, L. P.; Wojtas, L.; Nugent, P.; Eddaoudi, M.; Zaworotko, M. J. Templated Synthesis, Postsynthetic Metal Exchange, and Properties of a Porphyrin-Encapsulating Metal-Organic Material. *J. Am. Chem. Soc.* **2012**, *134*, 924–927.
- (68) Li, J.; Ren, Y.; Yue, C.; Fan, Y.; Qi, C.; Jiang, H. Highly Stable Chiral Zirconium-Metallosalen Frameworks for CO₂ Conversion and Asymmetric C-H Azidation. *ACS Appl. Mater. Interfaces* **2018**, *10*, 36047–36057.
- (69) Roy, S.; Huang, Z.; Bhunia, A.; Castner, A.; Gupta, A. K.; Zou, X.; Ott, S. Electrocatalytic Hydrogen Evolution from a Cobaloxime-Based Metal-Organic Framework Thin Film. *J. Am. Chem. Soc.* **2019**, *141*, 15942–15950.
- (70) Sharma, N.; Dhankhar, S. S.; Nagaraja, C. M. A Mn(II)-Porphyrin Based Metal-Organic Framework (MOF) for Visible-Light-Assisted Cycloaddition of Carbon Dioxide with Epoxides. *Microporous Mesoporous Mater.* **2019**, *280*, 372–378.
- (71) Shultz, A. M.; Sarjeant, A. A.; Farha, O. K.; Hupp, J. T.; Nguyen, S. T. Post-Synthesis Modification of a Metal-Organic Framework to Form Metallosalen-Containing MOF Materials. *J. Am. Chem. Soc.* **2011**, *133*, 13252–13255.
- (72) Sun, C.; Skorupskii, G.; Dou, J. H.; Wright, A. M.; Dinca, M. Reversible Metalation and Catalysis with a Scorpionate-like Metallo-Ligand in a Metal-Organic Framework. *J. Am. Chem. Soc.* **2018**, *140*, 17394–17398.
- (73) Wang, X. Sen; Chrzanowski, M.; Wojtas, L.; Chen, Y. S.; Ma, S. Formation of a Metalloporphyrin-Based Nanoreactor by Postsynthetic Metal-Ion Exchange of a Polyhedral-Cage Containing a Metal-Metalloporphyrin Framework. *Chem. Eur. J.* **2013**, *19*, 3297–3301.
- (74) Xia, Q.; Li, Z.; Tan, C.; Liu, Y.; Gong, W.; Cui, Y. Multivariate Metal-Organic Frameworks as Multifunctional Heterogeneous Asymmetric Catalysts for Sequential Reactions. *J. Am. Chem. Soc.* **2017**, *139*, 8259–8266.
- (75) Yuan, G.; Jiang, H.; Zhang, L.; Liu, Y.; Cui, Y. Metallosalen-Based Crystalline

- Porous Materials: Synthesis and Property. *Coord. Chem. Rev.* **2019**, *378*, 483–499.
- (76) Chen, Y. Z.; Jiang, H. L. Porphyrinic Metal-Organic Framework Catalyzed Heck-Reaction: Fluorescence “Turn-On” Sensing of Cu(II) Ion. *Chem. Mater.* **2016**, *28*, 6698–6704.
- (77) Guo, X. G.; Qiu, S.; Chen, X.; Gong, Y.; Sun, X. Postsynthesis Modification of a Metallosalen-Containing Metal-Organic Framework for Selective Th(IV)/Ln(III) Separation. *Inorg. Chem.* **2017**, *56*, 12357–12361.
- (78) Bhattacharjee, S.; Khan, M. I.; Li, X.; Zhu, Q. L.; Wu, X. T. Recent Progress in Asymmetric Catalysis and Chromatographic Separation by Chiral Metal–Organic Frameworks. *Catalysts* **2018**, *8*, 120.
- (79) Xia, Q.; Liu, Y.; Li, Z.; Gong, W.; Cui, Y. A Cr(Salen)-Based Metal-Organic Framework as a Versatile Catalyst for Efficient Asymmetric Transformations. *Chem. Commun.* **2016**, *52*, 13167–13170.
- (80) Zhu, C.; Yuan, G.; Chen, X.; Yang, Z.; Cui, Y. Chiral Nanoporous Metal-Metallosalen Frameworks for Hydrolytic Kinetic Resolution of Epoxides. *J. Am. Chem. Soc.* **2012**, *134*, 8058–8061.
- (81) Feng, D.; Gu, Z. Y.; Li, J. R.; Jiang, H. L.; Wei, Z.; Zhou, H. C. Zirconium-Metalloporphyrin PCN-222: Mesoporous Metal-Organic Frameworks with Ultrahigh Stability as Biomimetic Catalysts. *Angew. Chem. Int. Ed.* **2012**, *51*, 10307–10310.
- (82) Burgess, S. A.; Kassie, A.; Baranowski, S. A.; Fritzsche, K. J.; Schmidt-Rohr, K.; Brown, C. M.; Wade, C. R. Improved Catalytic Activity and Stability of a Palladium Pincer Complex by Incorporation into a Metal-Organic Framework. *J. Am. Chem. Soc.* **2016**, *138*, 1780–1783.
- (83) Kassie, A. A.; Duan, P.; Gray, M. B.; Schmidt-Rohr, K.; Woodward, P. M.; Wade, C. R. Synthesis and Reactivity of Zr MOFs Assembled from PNNNP-Ru Pincer Complexes. *Organometallics* **2019**, *38*, 3419–3428.
- (84) Rimoldi, M.; Nakamura, A.; Vermeulen, N. A.; Henkelis, J. J.; Blackburn, A. K.; Hupp, J. T.; Stoddart, J. F.; Farha, O. K. A Metal-Organic Framework Immobilised Iridium Pincer Complex. *Chem. Sci.* **2016**, *7*, 4980–4984.
- (85) Reiner, B. R.; Kassie, A. A.; Wade, C. R. Unveiling Reactive Metal Sites in a Pd Pincer MOF: Insights into Lewis Acid and Pore Selective Catalysis. *Dalton Trans.* **2019**, *48*, 9588–9595.
- (86) Zhang, Y.; Li, J.; Yang, X.; Zhang, P.; Pang, J.; Li, B.; Zhou, H. C. A Mesoporous NNN-Pincer-Based Metal-Organic Framework Scaffold for the Preparation of Noble-Metal-Free Catalysts. *Chem. Commun.* **2019**, *55*, 2023–2026.
- (87) Sun, C. Y.; To, W. P.; Hung, F. F.; Wang, X. L.; Su, Z. M.; Che, C. M. Metal-Organic Framework Composites with Luminescent Pincer Platinum(II) Complexes: 3MMLCT Emission and Photoinduced Dehydrogenation Catalysis. *Chem. Sci.* **2018**, *9*, 2357–2364.
- (88) van Koten, G.; Milstein, D. *Organometallic Pincer Chemistry*; Springer, 2013.
- (89) Albrecht, M.; Van Koten, G. Platinum Group Organometallics Based on “Pincer” Complexes: Sensors, Switches, and Catalysts. *Angew. Chem. Int. Ed.* **2001**, *40*, 3750.

- (90) Van Der Boom, M. E.; Milstein, D. Cyclometalated Phosphine-Based Pincer Complexes: Mechanistic Insight in Catalysis, Coordination, and Bond Activation. *Chem. Rev.* **2003**, *103*, 1759–1792.
- (91) Li, H.; Gonçalves, T. P.; Lupp, D.; Huang, K. W. PN₃(P)-Pincer Complexes: Cooperative Catalysis and Beyond. *ACS Catal.* **2019**, *9*, 1619–1629.
- (92) Choi, J.; MacArthur, A. H. R.; Brookhart, M.; Goldman, A. S. Dehydrogenation and Related Reactions Catalyzed by Iridium Pincer Complexes. *Chem. Rev.* **2011**, *111*, 1761–1779.
- (93) Selander, N.; Szabó, K. J. Catalysis by Palladium Pincer Complexes. *Chem. Rev.* **2011**, *111*, 2048–2076.
- (94) Morales-Morales, D. Pincer Complexes. Applications in Catalysis. *Rev. la Soc. Química México* **2004**, *48*, 338–346.
- (95) Milstein, D. Discovery of Environmentally Benign Catalytic Reactions of Alcohols Catalyzed by Pyridine-Based Pincer Ru Complexes, Based on Metal-Ligand Cooperation. *Top. Catal.* **2010**, *53*, 915–923.
- (96) Oulie, P.; Nebra, N.; Saffon, N.; Maron, L.; Martin-Vaca, B.; Bourissou, D. 2-Indenylidene Pincer Complexes of Zirconium and Palladium. *J. Am. Chem. Soc.* **2009**, *131*, 3493–3498.
- (97) Espinosa-Jalapa, N. Á.; Ke, D.; Nebra, N.; Le Goanvic, L.; Mallet-Ladeira, S.; Monot, J.; Martin-Vaca, B.; Bourissou, D. Enhanced Catalytic Performance of Indenediide Palladium Pincer Complexes for Cycloisomerization: Efficient Synthesis of Alkylidene Lactams. *ACS Catal.* **2014**, *4*, 3605–3611.
- (98) Zhou, J.; Lee, C. I.; Ozerov, O. V. Computational Study of the Mechanism of Dehydrogenative Borylation of Terminal Alkynes by SiNN Iridium Complexes. *ACS Catal.* **2018**, *8*, 536–545.
- (99) Agapie, T.; Bercaw, J. E. Cyclometalated Tantalum Diphenolate Pincer Complexes: Intramolecular C-H/M-CH₃ σ -Bond Metathesis May Be Faster than O-H/M-CH₃ Protonolysis. *Organometallics* **2007**, *26*, 2957–2959.
- (100) Adhikari, D.; Mossin, S.; Basuli, F.; Huffman, J. C.; Szilagyi, R. K.; Meyer, K.; Mindiola, D. J. Structural, Spectroscopic, and Theoretical Elucidation of a Redox-Active Pincer-Type Ancillary Applied in Catalysis. *J. Am. Chem. Soc.* **2008**, *130*, 3676–3682.
- (101) Renkema, K. B.; Kissin, Y. V.; Goldman, A. S. Mechanism of Alkane Transfer-Dehydrogenation Catalyzed by a Pincer-Ligated Iridium Complex. *J. Am. Chem. Soc.* **2003**, *125*, 7770–7771.
- (102) Morgan, E.; MacLean, D. F.; McDonald, R.; Turculet, L. Rhodium and Iridium Amido Complexes Supported by Silyl Pincer Ligation: Ammonia N-H Bond Activation by a [PSiP]Lr Complex. *J. Am. Chem. Soc.* **2009**, *131*, 14234–14236.
- (103) Martin, C.; Mallet-Ladeira, S.; Miqueu, K.; Bouhadir, G.; Bourissou, D. Combined Experimental/Computational Study of Iridium and Palladium Hydride PP(O)P Pincer Complexes. *Organometallics* **2014**, *33*, 571–577.
- (104) Shih, W. C.; Ozerov, O. V. Selective Ortho C-H Activation of Pyridines Directed by Lewis Acidic Boron of PBP Pincer Iridium Complexes. *J. Am. Chem. Soc.* **2017**, *139*, 17297–17300.

- (105) Hara, N.; Saito, T.; Semba, K.; Kuriakose, N.; Zheng, H.; Sakaki, S.; Nakao, Y. Rhodium Complexes Bearing PALP Pincer Ligands. *J. Am. Chem. Soc.* **2018**, *140*, 7070–7073.
- (106) You, D.; Yang, H.; Sen, S.; Gabbai, F. P. Modulating the σ -Accepting Properties of an Antimony Z-Type Ligand via Anion Abstraction: Remote-Controlled Reactivity of the Coordinated Platinum Atom. *J. Am. Chem. Soc.* **2018**, *140*, 9644–9651.
- (107) Press, L. P.; Kosanovich, A. J.; McCulloch, B. J.; Ozerov, O. V. High-Turnover Aromatic C-H Borylation Catalyzed by POCOP-Type Pincer Complexes of Iridium. *J. Am. Chem. Soc.* **2016**, *138*, 9487–9497.
- (108) Nebra, N.; Monot, J.; Shaw, R.; Martin-Vaca, B.; Bourissou, D. Metal-Ligand Cooperation in the Cycloisomerization of Alkynoic Acids with Indenediide Palladium Pincer Complexes. *ACS Catal.* **2013**, *3*, 2930–2934.
- (109) O'Reilly, M. E.; Veige, A. S. Trianionic Pincer and Pincer-Type Metal Complexes and Catalysts. *Chem. Soc. Rev.* **2014**, *43*, 6325–6369.
- (110) Younus, H. A.; Su, W.; Ahmad, N.; Chen, S.; Verpoort, F. Ruthenium Pincer Complexes: Synthesis and Catalytic Applications. *Adv. Synth. Catal.* **2015**, *357*, 283–330.
- (111) Gunanathan, C.; Milstein, D. Bond Activation and Catalysis by Ruthenium Pincer Complexes. *Chem. Rev.* **2014**, *114*, 12024–12087.
- (112) Tanaka, R.; Yamashita, M.; Nozaki, K. Catalytic Hydrogenation of Carbon Dioxide Using Ir(III)-Pincer Complexes. *J. Am. Chem. Soc.* **2009**, *131*, 14168–14169.
- (113) Bruneau-Voisine, A.; Wang, D.; Roisnel, T.; Darcel, C.; Sortais, J. B. Hydrogenation of Ketones with a Manganese PN3P Pincer Pre-Catalyst. *Catal. Commun.* **2017**, *92*, 1–4.
- (114) Zhou, C.; Hu, J.; Wang, Y.; Yao, C.; Chakraborty, P.; Li, H.; Guan, C.; Huang, M. H.; Huang, K. W. Selective Carbonylation of Benzene to Benzaldehyde Using a Phosphorus-Nitrogen PN3P-Rhodium(i) Complex. *Org. Chem. Front.* **2019**, *6*, 721–724.
- (115) Pan, Y.; Pan, C. L.; Zhang, Y.; Li, H.; Min, S.; Guo, X.; Zheng, B.; Chen, H.; Anders, A.; Lai, Z.; Zheng, J.; Huang, K. W. Selective Hydrogen Generation from Formic Acid with Well-Defined Complexes of Ruthenium and Phosphorus-Nitrogen PN3-Pincer Ligand. *Chem. Asian J.* **2016**, *11*, 1357–1360.
- (116) Leveson-Gower, R. B.; Webb, P. B.; Cordes, D. B.; Slawin, A. M. Z.; Smith, D. M.; Tooze, R. P.; Liu, J. Synthesis, Characterization, and Catalytic Properties of Iridium Pincer Complexes Containing NH Linkers. *Organometallics* **2018**, *37*, 30–39.
- (117) Glatz, M.; Stöger, B.; Bichler, B.; Bauer, G.; Veiros, L. F.; Pignitter, M.; Kirchner, K. Base-Initiated Formation of FeI–PNP Pincer Complexes. *Eur. J. Inorg. Chem.* **2020**, *2020*, 1101–1105.
- (118) Göttker-Schnetmann, I.; White, P.; Brookhart, M. Iridium Bis(Phosphinite) p-XPCP Pincer Complexes: Highly Active Catalysts for the Transfer Dehydrogenation of Alkanes. *J. Am. Chem. Soc.* **2004**, *126*, 1804–1811.
- (119) Gupta, M.; Hagen, C.; Flesher, R. J.; Kaska, W. C.; Jensen, C. M. A Highly Active Alkane Dehydrogenation Catalyst: Stabilization of Dihydrido Rhodium and Iridium Complexes by a P-C-P Pincer-Ligand. *Chem. Commun.* **1996**, 2083–2084.

- (120) Jensen, C. M. Iridium PCP Pincer Complexes: Highly Active and Robust Catalysts for Novel Homogeneous Aliphatic Dehydrogenations. *Chem. Commun.* **1999**, 2443–2449.
- (121) Gruver, B. C.; Adams, J. J.; Arulsamy, N.; Roddick, D. M. Acceptor Pincer Chemistry of Osmium: Catalytic Alkane Dehydrogenation by (CF₃PCP)Os(Cod)(H). *Organometallics* **2013**, *32*, 6468–6475.
- (122) Gruver, B. C.; Adams, J. J.; Warner, S. J.; Arulsamy, N.; Roddick, D. M. Acceptor Pincer Chemistry of Ruthenium: Catalytic Alkane Dehydrogenation by (CF₃PCP)Ru(Cod)(H). *Organometallics* **2011**, *30*, 5133–5140.
- (123) Huang, Z.; Brookhart, M.; Goldman, A. S.; Kundu, S.; Ray, A.; Scott, S. L.; Vicente, B. C. Highly Active and Recyclable Heterogeneous Iridium Pincer Catalysts for Transfer Dehydrogenation of Alkanes. *Adv. Synth. Catal.* **2009**, *351*, 188–206.
- (124) Wang, X.; Ling, E. A. P.; Guan, C.; Zhang, Q.; Wu, W.; Liu, P.; Zheng, N.; Zhang, D.; Lopatin, S.; Lai, Z.; Huang, K. W. Single-Site Ruthenium Pincer Complex Knitted into Porous Organic Polymers for Dehydrogenation of Formic Acid. *ChemSusChem* **2018**, *11*, 3591–3598.
- (125) Reiner, B. R.; Mucha, N. T.; Rothstein, A.; Temme, J. S.; Duan, P.; Schmidt-Rohr, K.; Foxman, B. M.; Wade, C. R. Zirconium Metal-Organic Frameworks Assembled from Pd and Pt PNNNP Pincer Complexes: Synthesis, Postsynthetic Modification, and Lewis Acid Catalysis. *Inorg. Chem.* **2018**, *57*, 2663–2672.
- (126) He, J.; Bohnsack, A. M.; Waggoner, N. W.; Dunning, S. G.; Lynch, V. M.; Kaska, W. C.; Humphrey, S. M. 1-D and 2-D Phosphine Coordination Materials Based on a Palladium(II) PCP Pincer Metalloligand. *Polyhedron* **2018**, *143*, 149–156.
- (127) He, J.; Waggoner, N. W.; Dunning, S. G.; Steiner, A.; Lynch, V. M.; Humphrey, S. M. A PCP Pincer Ligand for Coordination Polymers with Versatile Chemical Reactivity: Selective Activation of CO₂ Gas over CO Gas in the Solid State. *Angew. Chem. Int. Ed.* **2016**, *55*, 12351–12355.
- (128) He, S.; Allemond, L. L.; Dunning, S. G.; Iii, J. E. R.; Lynch, V. M.; Humphrey, S. M. In Situ Formation and Solid-State Oxidation of a Triselenane NSeN- Pincer MOF. *Chem. Commun.* **2020**, *56*, 1286–1289.
- (129) Albrecht, M.; Lindner, M. M. Cleavage of Unreactive Bonds with Pincer Metal Complexes. *Dalton Trans.* **2011**, *40*, 8733–8744.
- (130) Benito-Garagorri, D.; Kirchner, K. Modularly Designed Transition Metal PNP and PCP Pincer Complexes Based on Aminophosphines: Synthesis and Catalytic Applications. *Acc. Chem. Res.* **2008**, *41*, 201–213.
- (131) Gunanathan, C.; Milstein, D. Metal-Ligand Cooperation by Aromatization-De aromatization: A New Paradigm in Bond Activation and “Green” Catalysis. *Acc. Chem. Res.* **2011**, *44*, 588–602.
- (132) Valdés, H.; García-Eleno, M. A.; Canseco-Gonzalez, D.; Morales-Morales, D. Recent Advances in Catalysis with Transition-Metal Pincer Compounds. *ChemCatChem* **2018**, *10*, 3136–3172.
- (133) Liu, J. K.; Gong, J. F.; Song, M. P. Chiral Palladium Pincer Complexes for Asymmetric Catalytic. *Org. Biomol. Chem.* **2019**, *17*, 6069–6098.
- (134) Aydin, J.; Larsson, J. M.; Selander, N.; Szabó, K. J. Pincer Complex-Catalyzed

- Redox Coupling of Alkenes with Iodonium Salts via Presumed Palladium(IV) Intermediates. *Org. Lett.* **2009**, *11*, 2852–2854.
- (135) Bedford, R. B.; Draper, S. M.; Scullyb, P. N.; Welcha, S. L. Palladium Bis(Phosphinite) 'PCP'-Pincer Complexes and Their Application as Catalysts in the Suzuki Reaction. *New J. Chem* **2000**, *24*, 745–747.
- (136) Sommer, W. J.; Yu, K.; Sears, J. S.; Ji, Y.; Zheng, X.; Davis, R. J.; Sherrill, C. D.; Jones, C. W.; Week, M. Investigations into the Stability of Tethered Palladium(II) Pincer Complexes during Heck Catalysis. *Organometallics* **2005**, *24*, 4351–4361.
- (137) Olsson, D.; Nilsson, P.; El Masnaouy, M.; Wendt, O. F. A Catalytic and Mechanistic Investigation of a PCP Pincer Palladium Complex in the Stille Reaction. *Dalton Trans.* **2005**, *2*, 1924–1929.
- (138) Aydin, J.; Kumar, K. S.; Eriksson, L.; Szabó, K. J. Palladium Pincer Complex-Catalyzed Condensation of Sulfonimines and Isocynoacetate to Imidazoline Derivatives. Dependence of the Stereoselectivity on the Ligand Effects. *Adv. Synth. Catal.* **2007**, *349*, 2585–2594.
- (139) Feng, J. J.; Chen, X. F.; Shi, M.; Duan, W. L. Palladium-Catalyzed Asymmetric Addition of Diarylphosphines to Enones toward the Synthesis of Chiral Phosphines. *J. Am. Chem. Soc.* **2010**, *132*, 5562–5563.
- (140) Longmire, J. M.; Zhang, X.; Shang, M. Synthesis and X-Ray Crystal Structures of Palladium(II) and Platinum(II) Complexes of the PCP-Type Chiral Tridentate Ligand (1R,1'R)-1,3-Bis[1-(Diphenylphosphino)Ethyl]Benzene. Use in the Asymmetric Aldol Reaction of Methyl Isocynoacetate and Aldehydes. *Organometallics* **1998**, *17*, 4374–4379.
- (141) Shi, M.; Nicholas, K. M. Palladium-Catalyzed Carboxylation of Allyl Stannanes. *J. Am. Chem. Soc.* **1997**, *119*, 5057–5058.
- (142) Franks, R. J.; Nicholas, K. M. Palladium-Catalyzed Carboxylative Coupling of Allylstannanes and Allyl Halides. *Organometallics* **2000**, *19*, 1458–1460.
- (143) Solin, N.; Kjellgren, J.; Szabó, K. J. Pincer Complex-Catalyzed Allylation of Aldehyde and Imine Substrates via Nucleophilic H1-Allyl Palladium Intermediates. *J. Am. Chem. Soc.* **2004**, *126*, 7026–7033.
- (144) Solin, N.; Kjellgren, J.; Szabó, K. J. Palladium-Catalyzed Electrophilic Substitution via Monoallylpalladium Intermediates. *Angew. Chem. Int. Ed.* **2003**, *42*, 3656–3658.
- (145) Johansson, R.; Wendt, O. F. Insertion of CO₂ into a Palladium Allyl Bond and a Pd(II) Catalysed Carboxylation of Allyl Stannanes. *Dalton Trans.* **2007**, 488–492.
- (146) Li, J.; Lutz, M.; Spek, A. L.; Van Klink, G. P. M.; Van Koten, G.; Klein Gebbink, R. J. M. Chiral Amino Alcohol Derived Bis-Phosphoramidite Pincer Palladium Complexes and Their Applications in Asymmetric Allylation of Aldimines. *Organometallics* **2010**, *29*, 1379–1387.
- (147) Ding, B.; Zhang, Z.; Liu, Y.; Sugiya, M.; Imamoto, T.; Zhang, W. Chemoselective Transfer Hydrogenation of α,β -Unsaturated Ketones Catalyzed by Pincer-Pd Complexes Using Alcohol as a Hydrogen Source. *Org. Lett.* **2013**, *15*, 3690–3693.
- (148) Adhikary, A.; Schwartz, J. R.; Meadows, L. M.; Krause, J. A.; Guan, H. Interaction of Alkynes with Palladium POCOP-Pincer Hydride Complexes and Its Unexpected Relation to Palladium-Catal

- alyzed Hydrogenation of Alkynes. *Inorg. Chem. Front.* **2014**, *1*, 71–82.
- (149) Fujimoto, K.; Yoneda, T.; Yorimitsu, H.; Osuka, A. Synthesis and Catalytic Activities of Porphyrin-Based PCP Pincer Complexes. *Angew. Chem. Int. Ed.* **2014**, *53*, 1127–1130.
- (150) Burgess, S. A.; Kassie, A.; Baranowski, S. A.; Fritzsching, K. J.; Schmidt-Rohr, K.; Brown, C. M.; Wade, C. R. Improved Catalytic Activity and Stability of a Palladium Pincer Complex by Incorporation into a Metal-Organic Framework. *J. Am. Chem. Soc.* **2016**, *138*, 1780–1783.
- (151) Reiner, B. R.; Mucha, N. T.; Rothstein, A.; Temme, J. S.; Duan, P.; Schmidt-Rohr, K.; Foxman, B. M.; Wade, C. R. Zirconium Metal–Organic Frameworks Assembled from Pd and Pt PNNNP Pincer Complexes: Synthesis, Postsynthetic Modification, and Lewis Acid Catalysis. *Inorg. Chem.* **2018**, *57*, 2663–2672.
- (152) Cavka, J. H.; Jakobsen, S.; Olsbye, U.; Guillou, N.; Lamberti, C.; Bordiga, S.; Lillerud, K. P. A New Zirconium Inorganic Building Brick Forming Metal Organic Frameworks with Exceptional Stability. *J. Am. Chem. Soc.* **2008**, *130*, 13850–13851.
- (153) Kalidindi, S. B.; Nayak, S.; Briggs, M. E.; Jansat, S.; Katsoulidis, A. P.; Miller, G. J.; Warren, J. E.; Antypov, D.; Corà, F.; Slater, B.; Prestly, M. R.; Mart-Gastaldo, C.; Rosseinsky, M. J. Chemical and Structural Stability of Zirconium-Based Metal-Organic Frameworks with Large Three-Dimensional Pores by Linker Engineering. *Angew. Chem. Int. Ed.* **2015**, *54*, 221–226.
- (154) Jiang, H. L.; Feng, D.; Wang, K.; Gu, Z. Y.; Wei, Z.; Chen, Y. P.; Zhou, H. C. An Exceptionally Stable, Porphyrinic Zr Metal-Organic Framework Exhibiting PH-Dependent Fluorescence. *J. Am. Chem. Soc.* **2013**, *135*, 13934–13938.
- (155) Wang, D.; Astruc, D. The Golden Age of Transfer Hydrogenation. *Chem. Rev.* **2015**, *115*, 6621–6686.
- (156) Albanese, D.; Landini, D.; Maia, A. Dramatic Effect of the Metal Cation in Dealkylation Reactions of Phosphinic Esters Promoted by Complexes of Polyether Ligands with Metal Iodides. *J. Org. Chem.* **2001**, *66*, 3249–3252.
- (157) Goldman, W.; Olszewski, T. K.; Boduszek, B.; Sawka-Dobrowolska, W. Aminophosphine Oxides in a Pyridine Series. Studies on the Cleavage of Pyridine-2- and Pyridine-4-Yl-(N-Benzylamino)-Methyldiphenylphosphine Oxides in Acidic Solutions. *Tetrahedron* **2006**, *62*, 4506–4518.
- (158) Widegren, J. A.; Finke, R. G. A Review of the Problem of Distinguishing True Homogeneous Catalysis from Soluble or Other Metal-Particle Heterogeneous Catalysis under Reducing Conditions. *J. Mol. Catal. A Chem.* **2003**, *198*, 317–341.
- (159) Yeoul, S.; Kim, H.; Sik, H.; Park, S. Preparation of the Palladium (II) Dimethylamide Exchange with the Dicyclohexylamide. *J. Organomet. Chem.* **1999**, *592*, 194–197.
- (160) Rimml, H.; Venanzi, L. M. A STABLE BINUCLEAR COMPLEX CONTAINING Pd-H-Pd BONDS. *J. Organomet. Chem.* **1984**, *260*, C52–C54.
- (161) Johansson, R.; Wendt, O. F. Synthesis and Reactivity of (PCP) Palladium Hydroxy Carbonyl and Related Complexes toward CO₂ and Phenylacetylene.

- Organometallics* **2007**, *26*, 2426–2430.
- (162) Boro, B. J.; Duesler, E. N.; Goldberg, K. I.; Kemp, R. A. An Unprecedented Bonding Mode for Potassium within a PCP-Pincer Palladium Hydride-K-Selectride® Complex. *Inorg. Chem. Commun.* **2008**, *11*, 1426–1429.
- (163) Weideler, M.; Mishra, A.; Nattestad, A.; Powar, S.; Mozer, A. J.; Mena-Osteritz, E.; Cheng, Y. B.; Bach, U.; Bäuerle, P. Synthesis and Characterization of Perylene-Bithiophene-Triphenylamine Triads: Studies on the Effect of Alkyl-Substitution in p-Type NiO Based Photocathodes. *J. Mater. Chem.* **2012**, *22*, 7366–7379.
- (164) Zeini Jahromi, E.; Gailer, J. Probing Bioinorganic Chemistry Processes in the Bloodstream to Gain New Insights into the Origin of Human Diseases. *Dalton Trans.* **2010**, *39*, 329–336.
- (165) Suzuki, K.; Tsujiyama, S. Preparation of Benzocyclobutenone Derivatives Based on an Efficient Generation of Benzynes. *Org. Synth.* **2007**, *84*, 272.
- (166) Cotton, A.; Smith, D. TETRAKIS (TRIPHENYLPHOSPHINE)PALLADIUM (0). *Inorg. Synth.* **1972**, *XIII*, 121–124.
- (167) Zagulyaeva, A. A.; Yusubov, M. S.; Zhdankin, V. V. A General and Convenient Preparation of [Bis(Trifluoroacetoxy)Iodo] Perfluoroalkanes and [Bis(Trifluoroacetoxy)Iodo] Arenes by Oxidation of Organic Iodides Using Oxone and Trifluoroacetic Acid. *J. Org. Chem.* **2010**, *75*, 2119–2122.
- (168) Chen, Q.; Hou, S. S.; Schmidt-Rohr, K. A Simple Scheme for Probehead Background Suppression in One-Pulse 1H NMR. *Solid State Nucl. Magn. Reson.* **2004**, *26*, 11–15.
- (169) Øien, S.; Wragg, D.; Reinsch, H.; Svelle, S.; Bordiga, S.; Lamberti, C.; Lillerud, K. P. Detailed Structure Analysis of Atomic Positions and Defects in Zirconium Metal-Organic Frameworks. *Cryst. Growth Des.* **2014**, *14*, 5370–5372.
- (170) Shearer, G. C.; Chavan, S.; Ethiraj, J.; Vitillo, J. G.; Svelle, S.; Olsbye, U.; Lamberti, C.; Bordiga, S.; Lillerud, K. P. Tuned to Perfection: Ironing out the Defects in Metal-Organic Framework UiO-66. *Chem. Mater.* **2014**, *26*, 4068–4071.
- (171) Trickett, C. A.; Gagnon, K. J.; Lee, S.; Gándara, F.; Bürgi, H. B.; Yaghi, O. M. Definitive Molecular Level Characterization of Defects in UiO-66 Crystals. *Angew. Chem. Int. Ed.* **2015**, *54*, 11162–11167.
- (172) Schucka, G.; Iwataa, A.; Sasakib, A.; Himedab, A.; Konakab, H.; Muroyamab, N. Crystal Structure Analysis Using Integrated X-Ray Powder Diffraction Software Suite PDXL. *Acta Cryst.* **2010**, *A66*, s311.
- (173) Toby, B. H. EXPGUI, a Graphical User Interface for GSAS. *J. Appl. Crystallogr.* **2001**, *34*, 210–213.
- (174) Larson, A.C.; Dreele, R. B. V. GENERAL STRUCTURE ANALYSIS SYSTEM. *LAUR*, **2004**, 86.
- (175) Corma, A.; García, H. Lewis Acids: From Conventional Homogeneous to Green Homogeneous and Heterogeneous Catalysis. *Chem. Rev.* **2003**, *103*, 4307–4365.
- (176) Herrmann, W. A.; Cornils, B. Organometallic Homogeneous Catalysis—Quo Vadis? *Angew. Chem. Int. Ed.* **1997**, *36*, 1048–1067.
- (177) Sawano, T.; Lin, Z.; Boures, D.; An, B.; Wang, C.; Lin, W. Metal-Organic Frameworks Stabilize Mono(Phosphine)-Metal Complexes for Broad-Scope

- Catalytic Reactions. *J. Am. Chem. Soc.* **2016**, *138*, 9783–9786.
- (178) Kassie, A. A.; Duan, P.; Gray, M. B.; Schmidt-Rohr, K.; Woodward, P. M.; Wade, C. R. Synthesis and Reactivity of Zr MOFs Assembled from PNNNP-Ru Pincer Complexes. *Organometallics* **2019**, *38*, 3419–3428.
- (179) Wang, D.; Astruc, D. The Golden Age of Transfer Hydrogenation. *Chem. Rev.* **2015**, *115*, 6621–6686.
- (180) Brieger, G.; Nestruck, T. J. Catalytic Transfer Hydrogenation. *Chem. Rev.* **1974**, *74*, 567–580.
- (181) Verendel, J. J.; Pàmies, O.; Diéguez, M.; Andersson, P. G. Asymmetric Hydrogenation of Olefins Using Chiral Crabtree-Type Catalysts: Scope and Limitations. *Chem. Rev.* **2014**, *114*, 2130–2169.
- (182) Ager, D. J.; De Vries, A. H. M.; De Vries, J. G. Asymmetric Homogeneous Hydrogenations at Scale. *Chem. Soc. Rev.* **2012**, *41*, 3340–3380.
- (183) Zhang, G.; Yin, Z.; Tan, J. Cobalt(II)-Catalysed Transfer Hydrogenation of Olefins. *RSC Adv.* **2016**, *6*, 22419–22423.
- (184) Guo, S.; Yang, P.; Zhou, J. Nickel-Catalyzed Asymmetric Transfer Hydrogenation of Conjugated Olefins. *Chem. Commun.* **2015**, *51*, 12115–12117.
- (185) Wang, Y.; Huang, Z.; Leng, X.; Zhu, H.; Liu, G.; Huang, Z. Transfer Hydrogenation of Alkenes Using Ethanol Catalyzed by a NCP Pincer Iridium Complex: Scope and Mechanism. *J. Am. Chem. Soc.* **2018**, *140*, 4417–4429.
- (186) Ito, Y.; Ohta, H.; Yamada, Y. M. A.; Enoki, T.; Uozumi, Y. Transfer Hydrogenation of Alkenes Using Ni/Ru/Pt/Au Heteroquatermetallic Nanoparticle Catalysts: Sequential Cooperation of Multiple Nano-Metal Species. *Chem. Commun.* **2014**, *50*, 12123–12126.
- (187) Imamura, K.; Okubo, Y.; Ito, T.; Tanaka, A.; Hashimoto, K.; Kominami, H. Photocatalytic Hydrogenation of Alkenes to Alkanes in Alcoholic Suspensions of Palladium-Loaded Titanium(IV) Oxide without the Use of Hydrogen Gas. *RSC Adv.* **2014**, *4*, 19883–19886.
- (188) Long, J.; Zhou, Y.; Li, Y. Transfer Hydrogenation of Unsaturated Bonds in the Absence of Base Additives Catalyzed by a Cobalt-Based Heterogeneous Catalyst. *Chem. Commun.* **2015**, *51*, 2331–2334.
- (189) Kadam, H. K.; Tilve, S. G. Advancement in Methodologies for Reduction of Nitroarenes. *RSC Adv.* **2015**, *5*, 83391–83407.
- (190) Jiang, C.; Shang, Z.; Liang, X. Chemoselective Transfer Hydrogenation of Nitroarenes Catalyzed by Highly Dispersed, Supported Nickel Nanoparticles. *ACS Catal.* **2015**, *5*, 4814–4818.
- (191) Jagadeesh, R. V.; Surkus, A.-E.; Junge, H.; Pohl, M.-M.; Radnik, J.; Rabeah, J.; Huan, H.; Schünemann, V.; Brückner, A.; Beller, M. B. Nanoscale Fe₂O₃-Based Catalysts for Selective Hydrogenation of Nitroarenes to Anilines. *Science* **2013**, *342*, 1583–1587.
- (192) Cheong, W. C.; Yang, W.; Zhang, J.; Li, Y.; Zhao, D.; Liu, S.; Wu, K.; Liu, Q.; Zhang, C.; Wang, D.; Peng, Q.; Chen, C.; Li, Y. Isolated Iron Single-Atomic Site-Catalyzed Chemoselective Transfer Hydrogenation of Nitroarenes to Arylamines. *ACS Appl. Mater. Interfaces* **2019**, *11*, 33819–33824.

- (193) Pelšs, A.; Kumpulainen, E. T. T.; Koskinen, A. M. P. Highly Chemoselective Copper-Catalyzed Conjugate Reduction of Stereochemically Labile α,β -Unsaturated Amino Ketones. *J. Org. Chem.* **2009**, *74*, 7598–7601.
- (194) Mebi, C. A.; Nair, R. P.; Frost, B. J. PH-Dependent Selective Transfer Hydrogenation of α,β -Unsaturated Carbonyls in Aqueous Media Utilizing Half-Sandwich Ruthenium(II) Complexes. *Organometallics* **2007**, *26*, 429–438.
- (195) Castellanos-Blanco, N.; Flores-Alamo, M.; García, J. J. Nickel-Catalyzed Alkylation and Transfer Hydrogenation of α,β -Unsaturated Enones with Methanol. *Organometallics* **2012**, *31*, 680–686.
- (196) Thomas, R. J.; Campbell, K. N.; Hennion, G. F. Catalytic Hydration of Alkylacetylenes. *J. Am. Chem. Soc.* **1938**, *60*, 718–720.
- (197) Mello, R.; Alcalde-Aragonés, A.; González-Núñez, M. E. Silica-Supported HgSO₄/H₂SO₄: A Convenient Reagent for the Hydration of Alkynes under Mild Conditions. *Tetrahedron Lett.* **2010**, *51*, 4281–4283.
- (198) Antenucci, A.; Flamini, P.; Fornaiolo, M. V.; Di Silvio, S.; Mazzetti, S.; Mencarelli, P.; Salvio, R.; Bassetti, M. Iron(III)-Catalyzed Hydration of Unactivated Internal Alkynes in Weak Acidic Medium, under Lewis Acid-Assisted Brønsted Acid Catalysis. *Adv. Synth. Catal.* **2019**, *361*, 4517–4526.
- (199) Tachinami, T.; Nishimura, T.; Ushimaru, R.; Noyori, R.; Naka, H. Hydration of Terminal Alkynes Catalyzed by Water-Soluble Cobalt Porphyrin Complexes. *J. Am. Chem. Soc.* **2013**, *135*, 50–53.
- (200) Heidrich, M.; Bergmann, M.; Müller-Borges, D.; Plenio, H. Bis(pentipicyenyl)-N-Heterocyclic Carbene (NHC) Gold Complexes: Highly Active Catalysts for the Room Temperature Hydration of Alkynes. *Adv. Synth. Catal.* **2018**, *360*, 3572–3578.
- (201) Marion, N.; Ramo'n, R. S.; Nolan, S. P. [(NHC)AuI]-Catalyzed Acid-Free Alkyne Hydration at Part-per-Million Catalyst Loadings. *J. Am. Chem. Soc.* **2009**, *131*, 448–449.
- (202) Gatto, M.; Del Zotto, A.; Segato, J.; Zuccaccia, D. Hydration of Alkynes Catalyzed by L-Au-X under Solvent- and Acid-Free Conditions: New Insights into an Efficient, General, and Green Methodology. *Organometallics* **2018**, *37*, 4685–4691.
- (203) Trentin, F.; Chapman, A. M.; Scarso, A.; Sgarbossa, P.; Michelin, R. A.; Strukul, G.; Wass, D. F. Platinum(II) Diphosphinamine Complexes for the Efficient Hydration of Alkynes in Micellar Media. *Adv. Synth. Catal.* **2012**, *354*, 1095–1104.
- (204) Lin, Z.; Zhang, Z. M.; Chen, Y. S.; Lin, W. Highly Efficient Cooperative Catalysis by CoIII(Porphyrin) Pairs in Interpenetrating Metal–Organic Frameworks. *Angew. Chem. Int. Ed.* **2016**, *55*, 13739–13743.
- (205) Jia, C.; Piao, D.; Oyamada, J.; Lu, W.; Kitamura, T.; Fujiwara, Y. Efficient Activation of Aromatic C-H Bonds for Addition to C-C Multiple Bonds. *Science* **2000**, *287*, 1992–1995.
- (206) Jia, C.; Lu, W.; Oyamada, J.; Kitamura, T.; Matsuda, K.; Irie, M.; Fujiwara, Y. Novel Pd(II)- and Pt(II)-Catalyzed Regio- and Stereoselective Trans-Hydroarylation of Alkynes by Simple Arenes. *J. Am. Chem. Soc.* **2000**, *122*, 7252–7263.

- (207) Saravanakumar, R.; Ramkumar, V.; Sankararaman, S. Synthesis and Structure of 1,4-Diphenyl-3-Methyl-1,2,3-Triazol-5-Ylidene Palladium Complexes and Application in Catalytic Hydroarylation of Alkynes. *Organometallics* **2011**, *30*, 1689–1694.
- (208) Tunge, J. A.; Foresee, L. N. Mechanistic Studies of Fujiwara Hydroarylation. C-H Activation versus Electrophilic Aromatic Substitution. *Organometallics* **2005**, *24*, 6440–6444.
- (209) Jia, C.; Piao, D.; Kitamura, T.; Fujiwara, Y. New Method for Preparation of Coumarins and Quinolinones via Pd-Catalyzed Intramolecular Hydroarylation of C-C Triple Bonds. *J. Org. Chem.* **2000**, *65*, 7516–7522.
- (210) Hahn, C.; Miranda, M.; Chittineni, N. P. B.; Pinion, T. A.; Perez, R. Mechanistic Studies on Platinum(II) Catalyzed Hydroarylation of Alkynes. *Organometallics* **2014**, *33*, 3040–3050.
- (211) Senthna, S.; Phadke, R. The Pechmann Reaction. *Org. React.* **1953**, *7*, 1–58.
- (212) Kaufman, K. D.; Kelly, R. C. A New Synthesis of Coumarins. *J. Heterocycl. Chem.* **1965**, *2*, 91–92.
- (213) Trost, B. M.; Toste, F. D. A New Palladium-Catalyzed Addition: A Mild Method for the Synthesis of Coumarins. *J. Am. Chem. Soc.* **1996**, *118*, 6305–6306.
- (214) Bernhard, N.; Wolfgang, S. Simple Method for the Esterification of Carboxylic Acids. *Angew. Chem. Int. Ed.* **1978**, *17*, 522–524.
- (215) Furukawa, H.; Cordova, K. E.; O’Keeffe, M.; Yaghi, O. M. The Chemistry and Applications of Metal-Organic Frameworks. *Science* **2013**, *341*, 1230444.
- (216) Cui, Y.; Li, B.; He, H.; Zhou, W.; Chen, B.; Qian, G. Metal–Organic Frameworks as Platforms for Functional Materials. *Acc. Chem. Res.* **2016**, *49*, 483–493.
- (217) Maurin, G.; Serre, C.; Cooper, A.; Férey, G. The New Age of MOFs and of Their Porous-Related Solids. *Chem. Soc. Rev.* **2017**, *46*, 3104–3107.
- (218) Stassen, I.; Burtch, N.; Talin, A.; Falcaro, P.; Allendorf, M.; Ameloot, R. An Updated Roadmap for the Integration of Metal–Organic Frameworks with Electronic Devices and Chemical Sensors. *Chem. Soc. Rev.* **2017**, *46*, 3185–3241.
- (219) Cohen, S. M. Postsynthetic Methods for the Functionalization of Metal-Organic Frameworks. *Chem. Rev.* **2012**, *112*, 970–1000.
- (220) Evans, J. D.; Sumby, C. J.; Doonan, C. J. Post-Synthetic Metalation of Metal–Organic Frameworks. *Chem. Soc. Rev.* **2014**, *43*, 5933–5951.
- (221) Islamoglu, T.; Goswami, S.; Li, Z.; Howarth, A. J.; Farha, O. K.; Hupp, J. T. Postsynthetic Tuning of Metal–Organic Frameworks for Targeted Applications. *Acc. Chem. Res.* **2017**, *50*, 805–813.
- (222) Lalonde, M.; Bury, W.; Karagiari, O.; Brown, Z.; Hupp, J. T.; Farha, O. K. Transmetalation: Routes to Metal Exchange within Metal–Organic Frameworks. *J. Mater. Chem. A* **2013**, *1*, 5453–5468.
- (223) Brozek, C. K.; Dincă, M. Cation Exchange at the Secondary Building Units of Metal–Organic Frameworks. *Chem. Soc. Rev.* **2014**, *43*, 5456–5467.
- (224) Morris, R. E.; Brammer, L. Coordination Change, Lability and Hemilability in Metal–Organic Frameworks. *Chem. Soc. Rev.* **2017**, *46*, 5444–5462.
- (225) Das, S.; Kim, H.; Kim, K. Metathesis in Single Crystal: Complete and Reversible

- Exchange of Metal Ions Constituting the Frameworks of Metal–Organic Frameworks. *J. Am. Chem. Soc.* **2009**, *131*, 3814–3815.
- (226) Brozek, C. K.; Dincă, M. Lattice-Imposed Geometry in Metal–Organic Frameworks: Lacunary Zn₄O Clusters in MOF-5 Serve as Tripodal Chelating Ligands for Ni²⁺. *Chem. Sci.* **2012**, *3*, 2110–2113.
- (227) Brozek, C. K.; Bellarosa, L.; Soejima, T.; Clark, T. V.; López, N.; Dincă, M. Solvent-Dependent Cation Exchange in Metal–Organic Frameworks. *Chem. Eur. J.* **2014**, *20*, 6871–6874.
- (228) Bellarosa, L.; Brozek, C. K.; García-Melchor, M.; Dincă, M.; López, N. When the Solvent Locks the Cage: Theoretical Insight into the Transmetalation of MOF-5 Lattices and Its Kinetic Limitations. *Chem. Mater.* **2015**, *27*, 3422–3429.
- (229) Park, J.; Feng, D.; Zhou, H. Dual Exchange in PCN-333: A Facile Strategy to Chemically Robust Mesoporous Chromium Metal–Organic Framework with Functional Groups. *J. Am. Chem. Soc.* **2015**, *137*, 11801–11809.
- (230) Papazoi, E.; Douvali, A.; Rapti, S.; Skliri, E.; Armatas, G. S.; Papaefstathiou, G. S.; Wang, X.; Huang, Z.-F.; Kaziannis, S.; Kosmidis, C.; Hatzidimitriou, A. G.; Lazarides, T.; Manos, M. J. A Microporous Mg²⁺ MOF with Cation Exchange Properties in a Single-Crystal-to-Single-Crystal Fashion. *Inorg. Chem. Front.* **2017**, *4*, 530–536.
- (231) Wang, J.-H.; Zhang, Y.; Li, M.; Yan, S.; Li, D.; Zhang, X.-M. Solvent-Assisted Metal Metathesis: A Highly Efficient and Versatile Route towards Synthetically Demanding Chromium Metal–Organic Frameworks. *Angew. Chem. Int. Ed.* **2017**, *56*, 6478–6482.
- (232) Dolgoplova, E. A.; Ejegbavwo, O. A.; Martin, C. R.; Smith, M. D.; Setyawan, W.; Karakalos, S. G.; Henager, C. H.; Loye, H. Z.; Shustova, N. B. Multifaceted Modularity: A Key for Stepwise Building of Hierarchical Complexity in Actinide Metal–Organic Frameworks. *J. Am. Chem. Soc.* **2017**, *139*, 16852–16861.
- (233) Denny, M. S.; Parent, L. R.; Patterson, J. P.; Meena, S. K.; Pham, H.; Abellan, P.; Ramasse, Q. M.; Paesani, F.; Gianneschi, N. C.; Cohen, S. M. Transmission Electron Microscopy Reveals Deposition of Metal Oxide Coatings onto Metal–Organic Frameworks. *J. Am. Chem. Soc.* **2018**, *140*, 1348–1357.
- (234) Wang, X. J.; Li, P. Z.; Liu, L.; Zhang, Q.; Borah, P.; Wong, J. D.; Chan, X. X.; Rakesh, G.; Li, Y.; Zhao, Y. Significant Gas Uptake Enhancement by Post-Exchange of Zinc(II) with Copper(II) within a Metal–Organic Framework. *Chem. Commun.* **2012**, *48*, 10286–10288.
- (235) Denysenko, D.; Jelic, J.; Reuter, K.; Volkmer, D. Postsynthetic Metal and Ligand Exchange in MFU-4l: A Screening Approach toward Functional Metal–Organic Frameworks Comprising Single-Site Active Centers. *Chem. Eur. J.* **2015**, *21*, 8188–8199.
- (236) Xiao, Z.; Wang, Y.; Zhang, S.; Fan, W.; Xin, X.; Pan, X.; Zhang, L.; Sun, D. Stepwise Synthesis of Diverse Isomer MOFs via Metal-Ion Metathesis in a Controlled Single-Crystal-to-Single-Crystal Transformation. *Cryst. Growth Des.* **2017**, *17*, 4084–4089.
- (237) Cui, P.-P.; Zhang, X.-D.; Wang, P.; Zhao, Y.; Azam, M.; Al-Resayes, S. I.; Sun,

- W.-Y. Zinc(II) and Copper(II) Hybrid Frameworks via Metal-Ion Metathesis with Enhanced Gas Uptake and Photoluminescence Properties. *Inorg. Chem.* **2017**, *56*, 14157–14163.
- (238) Stubbs, A. W.; Braglia, L.; Borfecchia, E.; Meyer, R. J.; Román- Leshkov, Y.; Lamberti, C.; Dincă, M. Selective Catalytic Olefin Epoxidation with MnII-Exchanged MOF-5. *ACS Catal.* **2018**, *8*, 596–601.
- (239) Towsif Abtab, S. M.; Alezi, D.; Bhatt, P. M.; Shkurenko, A.; Belmabkhout, Y.; Aggarwal, H.; Weseliński, Ł. J.; Alsadun, N.; Samin, U.; Hedhili, M. N.; Eddaoudi, M. Reticular Chemistry in Action: A Hydrolytically Stable MOF Capturing Twice Its Weight in Adsorbed Water. *Chem* **2018**, *4*, 94–105.
- (240) Wright, A. M.; Rieth, A. J.; Yang, S.; Wang, E. N.; Dincă, M. Precise Control of Pore Hydrophilicity Enabled by Post-Synthetic Cation Exchange in Metal–Organic Frameworks. *Chem. Sci.* **2018**, *9*, 3856–3859.
- (241) Cui, P.; Li, J.-J.; Dong, J.; Zhao, B. Modulating CO₂ Adsorption in Metal–Organic Frameworks via Metal-Ion Doping. *Inorg. Chem.* **2018**, *57*, 6135–6141.
- (242) Comito, R. J.; Wu, Z.; Zhang, G.; Lawrence, J. A.; Korzyński, M. D.; Kehl, J. A.; Miller, J. T.; Dincă, M. Stabilized Vanadium Catalyst for Olefin Polymerization by Site Isolation in a Metal-Organic Framework. *Angew. Chem. Int. Ed.* **2018**, *57*, 8135–8139.
- (243) Grancha, T.; Ferrando-Soria, J.; Zhou, H.-C.; Gascon, J.; Seoane, B.; Pasán, J.; Fabelo, O.; Julve, M.; Pardo, E. Postsynthetic Improvement of the Physical Properties in a Metal-Organic Framework through a Single Crystal to Single Crystal Transmetalation. *Angew. Chem. Int. Ed.* **2015**, *54*, 6521–6525.
- (244) Sava Gallis, D. F.; Parkes, M. V.; Greathouse, J. A.; Zhang, X.; Nenoff, T. M. Enhanced O₂ Selectivity versus N₂ by Partial Metal Substitution in Cu-BTC. *Chem. Mater.* **2015**, *27*, 2018–2025.
- (245) Kobalz, K.; Kobalz, M.; Möllmer, J.; Junghans, U.; Lange, M.; Bergmann, J.; Dietrich, S.; Wecks, M.; Gläser, R.; Krautscheid, H. Bis(Carboxyphenyl)-1,2,4-Triazole Based Metal–Organic Frameworks: Impact of Metal Ion Substitution on Adsorption Performance. *Inorg. Chem.* **2016**, *55*, 6938–6948.
- (246) Comito, R. J.; Fritzsche, K. J.; Sundell, B. J.; Schmidt-Rohr, K.; Dincă, M. Single-Site Heterogeneous Catalysts for Olefin Polymerization Enabled by Cation Exchange in a Metal-Organic Framework. *J. Am. Chem. Soc.* **2016**, *138*, 10232–10237.
- (247) Asha, K. S.; Bhattacharjee, R.; Mandal, S. Complete Transmetalation in a Metal-Organic Framework by Metal Ion Metathesis in a Single Crystal for Selective Sensing of Phosphate Ions in Aqueous Media. *Angew. Chem. Int. Ed.* **2016**, *55*, 11528–11532.
- (248) Jayasinghe, A. S.; Salzman, S.; Forbes, T. Z. Metal Substitution into Metal Organic Nanotubes: Impacts on Solvent Uptake and Stability. *Cryst. Growth Des.* **2016**, *16*, 7058–7066.
- (249) Dolgoplova, E. A.; Brandt, A. J.; Ejegbavwo, O. A.; Duke, A. S.; Maddumapatabandi, T. D.; Gallenage, R. P.; Larson, B. W.; Reid, O. G.; Ammal, S. C.; Heyden, A.; Chandrashekar, M.; Stavila, V.; Chen, D. A.; Shustova, N. B.

- Electronic Properties of Bimetallic Metal–Organic Frameworks (MOFs): Tailoring the Density of Electronic States through MOF Modularity. *J. Am. Chem. Soc.* **2017**, *139*, 5201–5209.
- (250) Chandrasekhar, P.; Savitha, G.; Moorthy, J. N. Robust MOFs of “Tsg” Topology Based on Trigonal Prismatic Organic and Metal Cluster SBUs: Single Crystal to Single Crystal Postsynthetic Metal Exchange and Selective CO₂ Capture. *Chem. Eur. J.* **2017**, *23*, 7297–7305.
- (251) Shultz, A. M.; Sarjeant, A. A.; Farha, O. K.; Hupp, J. T.; Nguyen, S. T. Post-Synthesis Modification of a Metal–Organic Framework To Form Metallosalen-Containing MOF Materials. *J. Am. Chem. Soc.* **2011**, *133*, 13252–13255.
- (252) Zhang, Z.; Zhang, L.; Wojtas, L.; Nugent, P.; Eddaoudi, M.; Zaworotko, M. J. Templated Synthesis, Postsynthetic Metal Exchange, and Properties of a Porphyrin-Encapsulating Metal–Organic Material. *J. Am. Chem. Soc.* **2012**, *134*, 924–927.
- (253) Chen, Y.-Z.; Jiang, H.-L. Porphyrinic Metal–Organic Framework Catalyzed Heck-Reaction: Fluorescence “Turn-On” Sensing of Cu(II) Ion. *Chem. Mater.* **2016**, *28*, 6698–6704.
- (254) Li, J.; Fan, Y.; Ren, Y.; Liao, J.; Qi, C.; Jiang, H. Development of Isostructural Porphyrin–Salen Chiral Metal–Organic Frameworks through Postsynthetic Metalation Based on Single-Crystal to Single-Crystal Transformation. *Inorg. Chem.* **2018**, *57*, 1203–1212.
- (255) Li, J.; Ren, Y.; Yue, C.; Fan, Y.; Qi, C.; Jiang, H. Highly Stable Chiral Zirconium–Metallosalen Frameworks for CO₂ Conversion and Asymmetric C–H Azidation. *ACS Appl. Mater. Interfaces* **2018**, *10*, 36047–36057.
- (256) Asay, M.; Quezada-Miriel, M.; Ochoa-Sanfelize, J. R.; Martinez-Otero, D. 2,6-Lutidine-Linked Bis-Saturated NHC Pincer Ligands, Silver Complexes and Transmetalation. *J. Organomet. Chem.* **2018**, *859*, 10–17.
- (257) Monot, J.; Merceron-Saffon, N.; Martin-Vaca, B.; Bourissou, D. SCS Indenediide Pincer Complexes: Zr to Pd and Pt Transmetalation. *J. Organomet. Chem.* **2017**, *829*, 37–41.
- (258) Reilly, S. W.; Webster, C. E.; Hollis, T. K.; Valle, H. U. Transmetalation from CCC-NHC Pincer Zr Complexes in the Synthesis of Air-Stable CCC-NHC Pincer Co(III) Complexes and Initial Hydroboration Trials. *Dalton Trans.* **2016**, *45*, 2823–2828.
- (259) Rubio, R. J.; Andavan, G. T. S.; Bauer, E. B.; Hollis, T. K.; Cho, J.; Tham, F. S.; Donnadieu, B. Toward a General Method for CCC N-Heterocyclic Carbene Pincer Synthesis: Metallation and Transmetalation Strategies for Concurrent Activation of Three C–H Bonds. *J. Organomet. Chem.* **2005**, *690*, 5353–5364.
- (260) Gándara, F.; Bennett, T. D. Crystallography of Metal–Organic Frameworks. *IUCrJ* **2014**, *1*, 563–570.
- (261) Feng, D.; Gu, Z.-Y.; Li, J.-R.; Jiang, H.-L.; Wei, Z.; Zhou, H.-C. Zirconium-Metalloporphyrin PCN-222: Mesoporous Metal–Organic Frameworks with Ultrahigh Stability as Biomimetic Catalysts. *Angew. Chem. Int. Ed.* **2012**, *51*, 10307–10310.
- (262) Mondloch, J. E.; Bury, W.; Fairen-Jimenez, D.; Kwon, S.; DeMarco, E. J.; Weston,

- M. H.; Sarjeant, A. A.; Nguyen, S. T.; Stair, P. C.; Snurr, R. Q.; Farha, O. K.; Hupp, J. T. Vapor-Phase Metalation by Atomic Layer Deposition in a Metal–Organic Framework. *J. Am. Chem. Soc.* **2013**, *135*, 10294–10297.
- (263) Li, P.; Chen, Q.; Wang, T. C.; Vermeulen, N. A.; Mehdi, B. L.; Dohnalkova, A.; Browning, N. D.; Shen, D.; Anderson, R.; Gómez-Gualdrón, D. A.; Cetin, F. M.; Jagiello, J.; Asiri, A. M.; Stoddart, J. F.; Farha, O. K. Hierarchically Engineered Mesoporous Metal–Organic Frameworks toward Cell-Free Immobilized Enzyme Systems. *Chem* **2018**, *4*, 1022–1034.
- (264) Li, M.; Li, D.; O’Keeffe, M.; Yaghi, O. M. Topological Analysis of Metal–Organic Frameworks with Polytopic Linkers and/or Multiple Building Units and the Minimal Transitivity Principle. *Chem. Rev.* **2014**, *114*, 1343–1370.
- (265) Wang, Y.; Zheng, B.; Pan, Y.; Pan, C.; He, L.; Huang, K.-W. C–H and H–H Bond Activation via Ligand Dearomatization/Rearomatization of a PN3P–Rhodium (I) Complex. *Dalton Trans.* **2015**, *44*, 15111–15115.
- (266) Pazderski, L.; Surdykowski, A.; Pazderska-Szabłowicz, M.; Sitkowski, J.; Kozerski, L.; Kamiński, B.; Szłyk, E. ¹H, ¹³C, ¹⁵N NMR and ¹³C, ¹⁵N CPMAS Studies of Cobalt(III)-Chloride-Pyridine Complexes, Spontaneous Py→Cl Substitution in Trans-[Co(Py)₄Cl₂]Cl, and a New Synthesis of Mer-[Co(Py)₃Cl₃]. *Cent. Eur. J. Chem* **2008**, *6*, 55–64.
- (267) Walz, L.; Scheer, P. Structure of Di- μ -Chloro-Bis[Dicarbonylrhodium(I)]. *Acta Crystallogr. Sect. C Cryst. Struct. Commun.* **1991**, *47*, 640–641.
- (268) Otto, S.; Roodt, A. Reactivity Studies of Trans-[PtClMe(SMe₂)₂] towards Anionic and Neutral Ligand Substitution Processes. *J. Organomet. Chem.* **2006**, *691*, 4626–4632.
- (269) Abel, E. W.; Bennett, M. A.; Wilkinson, G. 646. Norbornadiene–Metal Complexes and Some Related Compounds. *J. Chem. Soc.* **1959**, 3178–3182.
- (270) Schuck, G.; Iwata, A.; Sasaki, A.; Himeda, A.; Konaka, H.; Muroyama, N. Crystal Structure Analysis Using Integrated X-Ray Powder Diffraction Software Suite PDXL. *Acta Crystallogr. Sect. A Found. Crystallogr.* **2010**, *66*, s311.
- (271) Coelho, A. A. TOPAS and TOPAS-Academic: An Optimization Program Integrating Computer Algebra and Crystallographic Objects Written in C++. *J. Appl. Crystallogr.* **2018**, *51*, 210–218.
- (272) Duan, P.; Schmidt-Rohr, K. Composite-Pulse and Partially Dipolar Dephased MultiCP for Improved Quantitative Solid-State ¹³C NMR. *J. Magn. Reson.* **2017**, *285*, 68–78.
- (273) Dixon, W. T.; Schaefer, J.; Sefcik, M. D.; Stejskal, E. O.; McKay, R. A. Total Suppression of Sidebands in CPMAS C-13 NMR. *J. Magn. Reson.* **1982**, *49*, 341–345.
- (274) Bennett, A. E.; Rienstra, C. M.; Auger, M.; Lakshmi, K. V.; Griffin, R. G. Heteronuclear Decoupling in Rotating Solids. *J. Chem. Phys.* **1995**, *103*, 6951–6958.
- (275) Selander, N.; J. Szabó, K. Catalysis by Palladium Pincer Complexes. *Chem. Rev.* **2011**, *111*, 2048–2076.
- (276) Werkmeister, S.; Neumann, J.; Junge, K.; Beller, M. Pincer-Type Complexes for

- Catalytic (De)Hydrogenation and Transfer (De)Hydrogenation Reactions: Recent Progress. *Chem. Eur. J.* **2015**, *21*, 12226–12250.
- (277) Kumar, A.; Bhatti, T. M.; Goldman, A. S. Dehydrogenation of Alkanes and Aliphatic Groups by Pincer-Ligated Metal Complexes. *Chem. Rev.* **2017**, *117*, 12357–12384.
- (278) Bauer, G.; Hu, X. Recent Developments of Iron Pincer Complexes for Catalytic Applications. *Inorg. Chem. Front.* **2016**, *3*, 741–765.
- (279) Junge, K.; Papa, V.; Beller, M. Cobalt–Pincer Complexes in Catalysis. *Chem. Eur. J.* **2019**, *25*, 122–143.
- (280) Peris, E.; Crabtree, R. H. Key Factors in Pincer Ligand Design. *Chem. Soc. Rev.* **2018**, *47*, 1959–1968.
- (281) Li, H.; Zheng, B.; Huang, K.-W. A New Class of PN₃-Pincer Ligands for Metal–Ligand Cooperative Catalysis. *Coord. Chem. Rev.* **2015**, *293–294*, 116–138.
- (282) Henschel, A.; Gedrich, K.; Kraehnert, R.; Kaskel, S. Catalytic Properties of MIL-101. *Chem. Commun.* **2008**, 4192–4194.
- (283) Horike, S.; Dincă, M.; Tamaki, K.; Long, J. R. Size-Selective Lewis Acid Catalysis in a Microporous Metal–Organic Framework with Exposed Mn²⁺ Coordination Sites. *J. Am. Chem. Soc.* **2008**, *130*, 5854–5855.
- (284) Trickett, C. A.; Osborn Popp, T. M.; Su, J.; Yan, C.; Weisberg, J.; Huq, A.; Urban, P.; Jiang, J.; Kalmutzki, M. J.; Liu, Q.; Baek, J.; Head-Gordon, M. P.; Somorjai, G. A.; Reimer, J. A.; Yaghi, O. M. Identification of the Strong Brønsted Acid Site in a Metal–Organic Framework Solid Acid Catalyst. *Nat. Chem.* **2019**, *11*, 170–176.
- (285) Abdel-Mageed, A. M.; Rungtaweivoranit, B.; Parlinska-Wojtan, M.; Pei, X.; Yaghi, O. M.; Behm, R. J. Highly Active and Stable Single-Atom Cu Catalysts Supported by a Metal–Organic Framework. *J. Am. Chem. Soc.* **2019**, *141*, 5201–5210.
- (286) Otake, K.; Ye, J.; Mandal, M.; Islamoglu, T.; Buru, C. T.; Hupp, J. T.; Delferro, M.; Truhlar, D. G.; Cramer, C. J.; Farha, O. K. Enhanced Activity of Heterogeneous Pd(II) Catalysts on Acid-Functionalized Metal–Organic Frameworks. *ACS Catal.* **2019**, *9*, 5383–5390.
- (287) Berijani, K.; Morsali, A.; Hupp, J. T. An Effective Strategy for Creating Asymmetric MOFs for Chirality Induction: A Chiral Zr-Based MOF for Enantioselective Epoxidation. *Catal. Sci. Technol.* **2019**, *9*, 3388–3397.
- (288) Alkordi, M. H.; Liu, Y.; Larsen, R. W.; Eubank, J. F.; Eddaoudi, M. Zeolite-like Metal–Organic Frameworks as Platforms for Applications: On Metalloporphyrin-Based Catalysts. *J. Am. Chem. Soc.* **2008**, *130*, 12639–12641.
- (289) Juan-Alcañiz, J.; Ramos-Fernandez, E. V.; Lafont, U.; Gascon, J.; Kapteijn, F. Building MOF Bottles around Phosphotungstic Acid Ships: One-Pot Synthesis of Bi-Functional Polyoxometalate-MIL-101 Catalysts. *J. Catal.* **2010**, *269*, 229–241.
- (290) Cohen, S. M.; Zhang, Z.; Boissonnault, J. A. Toward “MetalloMOFzymes”: Metal–Organic Frameworks with Single-Site Metal Catalysts for Small-Molecule Transformations. *Inorg. Chem.* **2016**, *55*, 7281–7290.
- (291) Noh, H.; Cui, Y.; Peters, A. W.; Pahls, D. R.; Ortuño, M. A.; Vermeulen, N. A.; Cramer, C. J.; Gagliardi, L.; Hupp, J. T.; Farha, O. K. An Exceptionally Stable Metal–Organic Framework Supported Molybdenum(VI) Oxide Catalyst for



- Cyclohexene Epoxidation. *J. Am. Chem. Soc.* **2016**, *138*, 14720–14726.
- (292) Wang, L.; Agnew, D. W.; Yu, X.; Figueroa, J. S.; Cohen, S. M. A Metal–Organic Framework with Exceptional Activity for C–H Bond Amination. *Angew. Chem. Int. Ed.* **2018**, *57*, 511–515.
- (293) Yang, D.; Ortuño, M. A.; Bernales, V.; Cramer, C. J.; Gagliardi, L.; Gates, B. C. Structure and Dynamics of Zr₆O₈ Metal–Organic Framework Node Surfaces Probed with Ethanol Dehydration as a Catalytic Test Reaction. *J. Am. Chem. Soc.* **2018**, *140*, 3751–3759.
- (294) Rimoldi, M.; Howarth, A. J.; DeStefano, M. R.; Lin, L.; Goswami, S.; Li, P.; Hupp, J. T.; Farha, O. K. Catalytic Zirconium/Hafnium-Based Metal–Organic Frameworks. *ACS Catal.* **2017**, *7*, 997–1014.
- (295) Li, Z.; Peters, A. W.; Bernales, V.; Ortuño, M. A.; Schweitzer, N. M.; DeStefano, M. R.; Gallington, L. C.; Platero-Prats, A. E.; Chapman, K. W.; Cramer, C. J.; Gagliardi, L.; Hupp, J. T.; Farha, O. K. Metal–Organic Framework Supported Cobalt Catalysts for the Oxidative Dehydrogenation of Propane at Low Temperature. *ACS Cent. Sci.* **2017**, *3*, 31–38.
- (296) Vimont, A.; Goupil, J. M.; Lavalley, J. C.; Daturi, M.; Surble, S.; Serre, C.; Millange, F.; Ferey, G.; Audebrand, N. Investigation of Acid Sites in a Zeotypic Giant Pores Chromium(III) Carboxylate. *J. Am. Chem. Soc.* **2006**, *128*, 3218–3227.
- (297) Hu, Z.; Zhao, D. Metal–Organic Frameworks with Lewis Acidity: Synthesis, Characterization, and Catalytic Applications. *CrystEngComm* **2017**, *19*, 4066–4081.
- (298) Hall, J. N.; Bollini, P. Structure, Characterization, and Catalytic Properties of Open-Metal Sites in Metal Organic Frameworks. *React. Chem. Eng.* **2019**, *4*, 207–222.
- (299) Sawano, T.; Thacker, N. C.; Lin, Z.; McIsaac, A. R.; Lin, W. Robust, Chiral, and Porous BINAP-Based Metal–Organic Frameworks for Highly Enantioselective Cyclization Reactions. *J. Am. Chem. Soc.* **2015**, *137*, 12241–12248.
- (300) Ji, P.; Manna, K.; Lin, Z.; Urban, A.; Greene, F. X.; Lan, G.; Lin, W. Single-Site Cobalt Catalysts at New Zr₈(M₂-O)₈(M₂-OH)₄ Metal–Organic Framework Nodes for Highly Active Hydrogenation of Alkenes, Imines, Carbonyls, and Heterocycles. *J. Am. Chem. Soc.* **2016**, *138*, 12234–12242.
- (301) Manna, K.; Ji, P.; Greene, F. X.; Lin, W. Metal–Organic Framework Nodes Support Single-Site Magnesium–Alkyl Catalysts for Hydroboration and Hydroamination Reactions. *J. Am. Chem. Soc.* **2016**, *138*, 7488–7491.
- (302) Zhang, T.; Manna, K.; Lin, W. Metal–Organic Frameworks Stabilize Solution-Inaccessible Cobalt Catalysts for Highly Efficient Broad-Scope Organic Transformations. *J. Am. Chem. Soc.* **2016**, *138*, 3241–3249.
- (303) Song, Y.; Li, Z.; Ji, P.; Kaufmann, M.; Feng, X.; Chen, J. S.; Wang, C.; Lin, W. Metal–Organic Framework Nodes Support Single-Site Nickel(II) Hydride Catalysts for the Hydrogenolysis of Aryl Ethers. *ACS Catal.* **2019**, *9*, 1578–1583.
- (304) Canivet, J.; Aguado, S.; Schuurman, Y.; Farrusseng, D. MOF-Supported Selective Ethylene Dimerization Single-Site Catalysts through One-Pot Postsynthetic Modification. *J. Am. Chem. Soc.* **2013**, *135*, 4195–4198.
- (305) Feng, D.; Gu, Z.-Y.; Chen, Y.-P.; Park, J.; Wei, Z.; Sun, Y.; Bosch, M.; Yuan, S.; Zhou, H.-C. A Highly Stable Porphyrinic Zirconium Metal–Organic Framework

- with Shp-a Topology. *J. Am. Chem. Soc.* **2014**, *136*, 17714–17717.
- (306) Metzger, E. D.; Brozek, C. K.; Comito, R. J.; Dincă, M. Selective Dimerization of Ethylene to 1-Butene with a Porous Catalyst. *ACS Cent. Sci.* **2016**, *2*, 148–153.
- (307) Metzger, E. D.; Comito, R. J.; Hendon, C. H.; Dincă, M. Mechanism of Single-Site Molecule-Like Catalytic Ethylene Dimerization in Ni-MFU-4l. *J. Am. Chem. Soc.* **2017**, *139*, 757–762.
- (308) Ji, P.; Solomon, J. B.; Lin, Z.; Johnson, A.; Jordan, R. F.; Lin, W. Transformation of Metal–Organic Framework Secondary Building Units into Hexanuclear Zr-Alkyl Catalysts for Ethylene Polymerization. *J. Am. Chem. Soc.* **2017**, *139*, 11325–11328.
- (309) Bosch, M.; Zhang, M.; Zhou, H.-C. Increasing the Stability of Metal-Organic Frameworks. *Adv. Chem.* **2014**, *2014*, 1–8.
- (310) Howarth, A. J.; Liu, Y.; Li, P.; Li, Z.; Wang, T. C.; Hupp, J. T.; Farha, O. K. Chemical, Thermal and Mechanical Stabilities of Metal–Organic Frameworks. *Nat. Rev. Mater.* **2016**, *1*, 15018.
- (311) Gunanathan, C.; Milstein, D. Metal–Ligand Cooperation by Aromatization–Dearomatization: A New Paradigm in Bond Activation and “Green” Catalysis. *Acc. Chem. Res.* **2011**, *44*, 588–602.
- (312) Khusnutdinova, J. R.; Milstein, D. Metal-Ligand Cooperation. *Angew. Chem. Int. Ed.* **2015**, *54*, 12236–12273.
- (313) Jia, G.; Lee, H. M.; Williams, I. D. Synthesis, Characterization, and Acidity Properties of [MCl(H₂)(L)(PMP)]BF₄ (M) Ru, L) PPh₃, CO; M) Os, L) PPh₃; PMP) 2,6-(Ph₂PCH₂)₂C₅H₃N). *Organometallics* **1997**, *16*, 3941–3949.
- (314) Gibson, D. H.; Pariya, C.; Mashuta, M. S. Synthesis and Characterization of Ruthenium(II) Hydrido and Hydroxo Complexes Bearing the 2,6-Bis(Di-Tert-Butylphosphinomethyl)Pyridine Ligand. *Organometallics* **2004**, *23*, 2510–2513.
- (315) Luh, T.-Y. Trimethylamine N-Oxide—a Versatile Reagent for Organometallic Chemistry. *Coord. Chem. Rev.* **1984**, *60*, 255–276.
- (316) Kassie, A. A.; Duan, P.; McClure, E. T.; Schmidt-Rohr, K.; Woodward, P. M.; Wade, C. R. Postsynthetic Metal Exchange in a Metal-Organic Framework Assembled from Co(III) Diphosphine Pincer Complexes. *Inorg. Chem.* **2019**, *58*, 3227–3236.
- (317) Duren, T.; Millange, F.; Ferey, G.; Walton, K. S.; Snurr, R. Q. Calculating Geometric Surface Areas as a Characterization Tool for Metal-Organic Frameworks. *J. Phys. Chem. C* **2007**, *111*, 15350–15356.
- (318) Shearer, G. C.; Chavan, S.; Bordiga, S.; Svelle, S.; Olsbye, U.; Lillerud, K. P. Defect Engineering: Tuning the Porosity and Composition of the Metal–Organic Framework UiO-66 via Modulated Synthesis. *Chem. Mater.* **2016**, *28*, 3749–3761.
- (319) Gonçalves, T. P.; Huang, K.-W. Metal–Ligand Cooperative Reactivity in the (Pseudo)-Dearomatized PN_x(P) Systems: The Influence of the Zwitterionic Form in Dearomatized Pincer Complexes. *J. Am. Chem. Soc.* **2017**, *139*, 13442–13449.
- (320) Zhang, Y.; Chen, X.; Zheng, B.; Guo, X.; Pan, Y.; Chen, H.; Li, H.; Min, S.; Guan, C.; Huang, K.-W.; Zheng, J. Structural Analysis of Transient Reaction Intermediate in Formic Acid Dehydrogenation Catalysis Using Two-Dimensional IR Spectroscopy. *Proc. Natl. Acad. Sci.* **2018**, *115*, 12395–12400.


- (321) Park, S.; Brookhart, M. Hydrosilylation of Carbonyl-Containing Substrates Catalyzed by an Electrophilic N1-Silane Iridium(III) Complex. *Organometallics* **2010**, *29*, 6057–6064.
- (322) Metsänen, T. T.; Hrobárik, P.; Klare, H. F. T.; Kaupp, M.; Oestreich, M. Insight into the Mechanism of Carbonyl Hydrosilylation Catalyzed by Brookhart's Cationic Iridium(III) Pincer Complex. *J. Am. Chem. Soc.* **2014**, *136*, 6912–6915.
- (323) Raya-Barón, Á.; Oña-Burgos, P.; Fernández, I. Iron-Catalyzed Homogeneous Hydrosilylation of Ketones and Aldehydes: Advances and Mechanistic Perspective. *ACS Catal.* **2019**, *9*, 5400–5417.
- (324) Iglesias, M.; Fernández-Alvarez, F. J.; Oro, L. A. Non-Classical Hydrosilane Mediated Reductions Promoted by Transition Metal Complexes. *Coord. Chem. Rev.* **2019**, *386*, 240–266.
- (325) Fuchs, J.; Klare, H. F. T.; Oestreich, M. Two-Silicon Cycle for Carbonyl Hydrosilylation with Nikonov's Cationic Ruthenium(II) Catalyst. *ACS Catal.* **2017**, *7*, 8338–8342.
- (326) Cao, L.; Lin, Z.; Peng, F.; Wang, W.; Huang, R.; Wang, C.; Yan, J.; Liang, J.; Zhang, Z.; Zhang, T.; Long, L.; Sun, J.; Lin, W. Self-Supporting Metal–Organic Layers as Single-Site Solid Catalysts. *Angew. Chem. Int. Ed.* **2016**, *55*, 4962–4966.
- (327) Sawano, T.; Lin, Z.; Boures, D.; An, B.; Wang, C.; Lin, W. Metal–Organic Frameworks Stabilize Mono(Phosphine)–Metal Complexes for Broad-Scope Catalytic Reactions. *J. Am. Chem. Soc.* **2016**, *138*, 9783–9786.
- (328) Zhang, X.; Sun, J.; Wei, G.; Liu, Z.; Yang, H.; Wang, K.; Fei, H. In Situ Generation of an N-Heterocyclic Carbene Functionalized Metal–Organic Framework by Postsynthetic Ligand Exchange: Efficient and Selective Hydrosilylation of CO₂. *Angew. Chem. Int. Ed.* **2019**, *58*, 2844–2849.
- (329) Zhang, Z.; Bai, L.; Hu, X. Alkene Hydrosilylation Catalyzed by Easily Assembled Ni(II)-Carboxylate MOFs. *Chem. Sci.* **2019**, *10*, 3791–3795.
- (330) Li, H.; Gonçalves, T. P.; Zhao, Q.; Gong, D.; Lai, Z.; Wang, Z.; Zheng, J.; Huang, K.-W. Diverse Catalytic Reactivity of a Dearomatized PN₃P*–Nickel Hydride Pincer Complex towards CO₂ Reduction. *Chem. Commun.* **2018**, *54*, 11395–11398.
- (331) Li, H.; Gonçalves, T. P.; Hu, J.; Zhao, Q.; Gong, D.; Lai, Z.; Wang, Z.; Zheng, J.; Huang, K.-W. A Pseudodearomatized PN₃P*Ni–H Complex as a Ligand and σ -Nucleophilic Catalyst. *J. Org. Chem.* **2018**, *83*, 14969–14977.
- (332) Prabhakaran, B.; Santhi, N.; Emayavaramban, M. Synthesis and Spectral Studies of Ru(II) Carbonyl Schiff Base Complexes. *Int. Lett. Chem. Phys. Astron.* **2013**, *8*, 53–66.
- (333) Hwang, T. L.; Shaka, A. J. Water Suppression That Works. Excitation Sculpting Using Arbitrary Wave-Forms and Pulsed-Field Gradients. *J. Magn. Reson. Ser. A* **1995**, *112*, 275–279.
- (334) Giboulot, S.; Baldino, S.; Ballico, M.; Nedden, H. G.; Zuccaccia, D.; Baratta, W. Cyclometalated Dicarboxyl Ruthenium Catalysts for Transfer Hydrogenation and Hydrogenation of Carbonyl Compounds. *Organometallics* **2018**, *37*, 2136–2146.

Appendix

Permissions to Reprint

[Home](#) [Help](#) [Email Support](#) [Sign in](#) [Create Account](#)

 **Improved Catalytic Activity and Stability of a Palladium Pincer Complex by Incorporation into a Metal–Organic Framework**

Author: Samantha A. Burgess, Abebu Kassie, Sarah A. Baranowski, et al
Publication: Journal of the American Chemical Society
Publisher: American Chemical Society
Date: Feb 1, 2016

Copyright © 2016, American Chemical Society

PERMISSION/LICENSE IS GRANTED FOR YOUR ORDER AT NO CHARGE

This type of permission/license, instead of the standard Terms & Conditions, is sent to you because no fee is being charged for your order. Please note the following:

- Permission is granted for your request in both print and electronic formats, and translations.
- If figures and/or tables were requested, they may be adapted or used in part.
- Please print this page for your records and send a copy of it to your publisher/graduate school.
- Appropriate credit for the requested material should be given as follows: "Reprinted (adapted) with permission from (COMPLETE REFERENCE CITATION). Copyright (YEAR) American Chemical Society." Insert appropriate information in place of the capitalized words.
- One-time permission is granted only for the use specified in your request. No additional uses are granted (such as derivative works or other editions). For any other uses, please submit a new request.

Burgess, S. A.; Kassie, A.; Baranowski, S. A.; Fritzsching, K. J.; Schmidt-Rohr, K.; Brown, C. M.; Wade, C. R. *J. Am. Chem. Soc.* **2016**, *138*, 1780-1783.

Postsynthetic Metal Exchange in a Metal–Organic Framework Assembled from Co(III) Diphosphine Pincer Complexes**Author:** Abebu A. Kassie, Pu Duan, Eric T. McClure, et al**Publication:** Inorganic Chemistry**Publisher:** American Chemical Society**Date:** Mar 1, 2019

Copyright © 2019, American Chemical Society

PERMISSION/LICENSE IS GRANTED FOR YOUR ORDER AT NO CHARGE

This type of permission/license, instead of the standard Terms & Conditions, is sent to you because no fee is being charged for your order. Please note the following:

- Permission is granted for your request in both print and electronic formats, and translations.
- If figures and/or tables were requested, they may be adapted or used in part.
- Please print this page for your records and send a copy of it to your publisher/graduate school.
- Appropriate credit for the requested material should be given as follows: "Reprinted (adapted) with permission from (COMPLETE REFERENCE CITATION). Copyright (YEAR) American Chemical Society." Insert appropriate information in place of the capitalized words.
- One-time permission is granted only for the use specified in your request. No additional uses are granted (such as derivative works or other editions). For any other uses, please submit a new request.

Kassie, A. A.; Duan, P.; McClure, E.; Schmidt-Rohr, K.; Woodward, P.; Wade, C. R. *Inorg. Chem.* **2019**, *58*, 3227-3236.

**Synthesis and Reactivity of Zr MOFs Assembled from PNNNP-Ru Pincer Complexes**

Author: Abebu A. Kassie, Pu Duan, Matthew B. Gray, et al

Publication: Organometallics

Publisher: American Chemical Society

Date: Sep 1, 2019

Copyright © 2019, American Chemical Society

**PERMISSION/LICENSE IS GRANTED FOR YOUR ORDER AT NO CHARGE**

This type of permission/license, instead of the standard Terms & Conditions, is sent to you because no fee is being charged for your order. Please note the following:

- Permission is granted for your request in both print and electronic formats, and translations.
- If figures and/or tables were requested, they may be adapted or used in part.
- Please print this page for your records and send a copy of it to your publisher/graduate school.
- Appropriate credit for the requested material should be given as follows: "Reprinted (adapted) with permission from (COMPLETE REFERENCE CITATION). Copyright (YEAR) American Chemical Society." Insert appropriate information in place of the capitalized words.
- One-time permission is granted only for the use specified in your request. No additional uses are granted (such as derivative works or other editions). For any other uses, please submit a new request.

Kassie, A. A.; Duan, P.; Gray, M. B.; Schmidt-Rohr, K.; Woodward, P.; Wade, C. R. *Organometallics*. **2019**, *38*, 3419-3428.